

Optically-Resonant Nanostructure-Based Systems for Spectral Selectivity

Dissertation
zur Erlangung des akademischen Grades
doctor rerum naturalium (Dr. rer. nat.)

vorgelegt dem Rat der Physikalisch-Astronomischen Fakultät
der Friedrich-Schiller-Universität Jena

von Jonas Berzinš
geboren am 16. Oktober 1991 in Klaipėda, Litauen

Gutachter:

1. Prof. Dr. Thomas Pertsch,
Friedrich-Schiller-Universität Jena, Germany
2. Prof. Dr. Boris Chichkov,
Leibniz Universität Hannover, Germany
3. Prof. Dr. Saulius Juodkazis,
Swinburne University of Technology, Australia

Tag der Disputation: 20. April 2021

Contents

Introduction	1
1 Spectrally-selective Mie-resonant metasurfaces	6
1.1 General properties	6
1.1.1 Mie scattering	6
1.1.2 Color science	13
1.2 Nanostructure-based color filters	17
1.2.1 Concept	18
1.2.2 Methods	18
1.2.3 Design and numerical optimization	20
1.2.4 Experimental realization	23
1.2.5 Specifications	25
1.3 Chapter summary	28
2 Nanostructure-modulated Fabry–Pérot resonators	30
2.1 General properties	31
2.1.1 Properties of Fabry–Pérot resonators	31
2.1.2 Effective medium theory	33
2.1.3 Tailoring of effective refractive index	35
2.2 Spectral filters for blood oxygen sensing	37
2.2.1 Concept	37
2.2.2 Methods	39
2.2.3 Design and numerical optimization	40
2.2.4 Experimental realization	43
2.2.5 Specifications	46
2.2.6 Integration on a CMOS sensor	49
2.3 High spectral resolution spectropolarimeter	50
2.3.1 Concept	51
2.3.2 Design and numerical optimization	52
2.3.3 Experimental realization	54
2.3.4 Specifications	61
2.3.5 Extended design considerations	63

2.4	Chapter summary	64
3	Laser-induced tailoring and structuring of metasurfaces	65
3.1	Photothermal tailoring of metasurfaces	66
3.1.1	Photothermal effects	66
3.1.2	Methods	69
3.1.3	Crystallization of metasurface elements	70
3.1.4	Controlled reshaping of metasurface elements	74
3.2	Direct laser interference patterning	79
3.2.1	Laser–matter interaction	79
3.2.2	Methods	83
3.2.3	Patterning of large-area metasurfaces	85
3.2.4	Tailoring of metasurface elements	90
3.2.5	Spectral analysis and Mie resonances	93
3.3	Chapter summary	96
4	Conclusions and outlook	98
	List of scientific contributions	101
	Bibliography	124
	Appendix A Refractive index database	125
	Abbreviations	129
	Deutschsprachige zusammenfassung	130
	Ehrenwörtliche Erklärung	131

Introduction

Two-dimensional arrays of subwavelength nanostructures, so-called metasurfaces, have emerged as the new generation of optical elements [1]. A careful material selection and alteration of nanostructures size, shape, density, and distribution pattern may result in marvelous ultra-thin optical components, which can alter phase, polarization, and amplitude of light [1]. High-index materials, such as silicon (Si), have been established as an alternative to plasmonic materials in the field of nanophotonics [2–5]. In contrast to plasmonics, high-index nanostructures provide a reasonable solution towards lossless optical systems while maintaining precise control of their spectral features [6–13]. In particular, low-loss and high-index dielectrics pave a direct path to efficient photonic devices for imaging [14–21], sensing [22, 23], light emission [24], light harvesting [25, 26], light directing, guiding and switching [27], and many other applications. Mie-resonant dielectric nanostructures, so-called Mie resonators, support electric and magnetic resonances [28], which enable a wavelength-dependent optical response tailored for a specific functionality via control of their shape and size [8], as well as period, if the nanostructures are assembled into a metasurface [7]. The physical phenomena governing the light–nanostructure interaction is the focus of this thesis.

The potential of metasurfaces is undeniable, yet there are still many obstacles to face before their actual real-life applications. To some extent, metasurfaces are competing with conventional optical elements, which are well-defined and are easy to manufacture, such as plastic optics [29]. Thus, for the industry to raise an eyebrow, one has to define some significant advantages of using metasurfaces. This work highlights several such advantages, which include but are not limited to the spatial variation of metasurface elements, and their multifunctionality. Extensive numerical and experimental tools are used for physics implementation into the novel and application-oriented designs. Several applications, like color imaging, biomedical imaging, and spectropolarimetry, are discussed. Furthermore, the reader of this work will be introduced to novel nanofabrication and postprocessing techniques, which are supposed to bring the metasurfaces closer to the industrial-scale fabrication. Many times great scientific ideas remain within the realm of scientific laboratories; thus, the thesis is dedicated to developing the metasurfaces a small step closer to real-life applications.

Scattering and absorption of light dictate how an object is perceived [30]. Mie theory describes the absorption and scattering of plane electromagnetic waves by a spherical nanoparticle in a uniform isotropic dielectric medium [28], but the Mie resonator term has been since transferred to other shapes as well. The first part of this thesis, Chapter 1, brings attention to Mie-resonant nanostructures and their wavelength-dependent spectral properties, emphasizing the spectral selectivity in the visible spectral range. Recently, there has been a great interest in generating the so-called structural colors using Mie-resonant dielectric nanostructures [30, 31]. The concept of structural colors is common in nature, e.g., blue Morpho butterfly

wings are not pigmented, but are seen in bluish color because the incident light is spectrally dispersed by the nanostructured pattern on the wings [32, 33]. This principle was quickly adapted in man-made structures using plasmonic nanoparticles [34–42]. However, the free-electron oscillations in metals are accompanied by a significant optical loss, which led to the investigation of high refractive index dielectric materials, such as Si, titanium dioxide (TiO_2), and gallium phosphide (GaP), and others [43]. Dielectric materials have low intrinsic losses; thus, they can be used to obtain structural colors with high luminosity, making such nanostructures suitable for applications like color printing [44–53]. Accordingly, they have been successfully used to create a full palette of colors in reflection [44–46]. Thus, a similar spectral discrimination is anticipated in transmission – the nanostructures may exhibit the same functionality as transmissive color filters. The first demonstrations of nanostructure-based transmissive color filters were done using Si nanowires [16–18]. Later, structural filters were shown using Si nanodisks [19], and Si nanoholes [20].

As digital imaging is continuously developing, steady improvement is observed in the spatial resolution of color imaging devices [54–61]. This technological outburst is mainly driven by daily-use hand-held devices, such as mobile phones and compact optical cameras, but the high resolution also serves a role in industrial and environmental imaging [62]. For many applications, high resolution is desirable, consequently requiring small spectral filters. The use of complementary metal–oxide–semiconductor (CMOS) image sensors with pigmented and dye-based color filters allows pixels as small as $1\ \mu\text{m}$ [54–56]. However, the further decrease in pixel size is not a straightforward process. Conventional filters require new materials and complicated multi-step fabrication [63]. In addition to that, they rely on absorption, which requires relatively high thickness [63]. Moreover, as the filters are arranged side-by-side, limitations such as crosstalk come into play [64]. An alternative is the use of the aforementioned optically resonant nanostructure-based systems, producing the structural colors due to their usually strong dispersion. By varying the dielectric nanostructure geometry, the positions of the electric dipole (ED) and magnetic dipole (MD) resonances can be tuned throughout the visible spectral range and beyond [6–13]. Such an approach has been successfully used in producing a variety of transmissive filters, including the realization of color filter arrays in red, green, and blue (RGB) [20], cyan, magenta, and yellow (CMY) [19], and multispectral patterns [14, 17, 18, 65]. Chapter 1 employs Si metasurfaces to demonstrate a full palette of colors in transmission. The metasurfaces are optimized for RGB pattern, resulting in state-of-the-art $0.5\ \mu\text{m}$ RGB filters.

Regardless of the spatial resolution, techniques such as multispectral imaging and spectropolarimetry provide substantially more information on the imaged scene or the object of interest than the conventional tricolor imaging [66–69]. Information on the polarization state of the collected light enables a better understanding of surface topography and scattering. Accordingly, it is widely used for detection and biomedical applications [67], while high-resolution spectral information provides details on material composition for the assessment of food quality, artwork authentication, and many other applications [68, 69]. The large size and functionality limitation of conventional optical components motivate the search for alternatives, and nanostructure-based systems seem to fit the need. Thus far, nanostructures have been successfully applied in compact polarimeters [70–74], spectral filters and spectrometers [75–79], and even spectropolarimeters [80–83]. However, there are still several obstacles to overcome, e.g., it is crucial to obtain a high spectral resolution for the maximum gain of the spectral information. Even though the previously

introduced Mie resonances can be used and extended to other than the visible spectral range, an alternative system with a high-quality factor – Fabry–Pérot (FP) resonator – is extensively explored in Chapter 2.

The standard way to tailor the FP resonances is changing the physical thickness of the resonator [84–86]. The thickness variation allows tuning the resonant wavelength across a wide spectral range without a significant spectral response degradation. Such an approach has been applied in RGB filters [84], while maintaining a few times smaller thickness compared to the conventional dye-based color filters [63]. However, the step-profile FP resonators within a single chip require a complex fabrication with multiple etching steps [85]. Thus, a novel approach came into existence, which suggests that one may change the effective optical thickness by simply changing the effective index of the medium [87]. Such a concept was first shown for multispectral filters in the visible spectral range [88] and later extended to the near-infrared [89]. It has been demonstrated that FP resonators can be tailored by inclusions of plasmonic nanostructures [79,90] and high-index dielectric nanostructures [70,76,87–89,91,92].

Slowly but steadily, multispectral imaging is finding its place in the field of biomedicine [93], e.g., for monitoring oxygen in our blood. Low oxygen levels in blood may indicate heart conditions such as heart defects, lung conditions such as asthma, emphysema, or bronchitis, sleep apnea, inflammation, and scarring of the lung tissue [94]. Accordingly, it is essential to monitor the level of oxygen transported by blood throughout our bodies. In order to build a compact optical system for remote sensing, nanostructure-based FP filters are analyzed in Chapter 2. Furthermore, using similar but polarization-sensitive nanostructures embedded in the FP cavity, one may create a spectropolarimetric system, which is the topic of the second part of Chapter 2. One of the main applications of spectropolarimetry is Earth observation [67], where the properties of aerosols, e.g., their size, shape, and refractive index, can be remotely identified using the polarization and spectral information. In general, astronomical instruments on board of satellites have stringent constraints in terms of mass and volume. As the number of nano- and cube-satellites is rapidly increasing [95], any innovative solution that enables compact instruments is highly desirable. Accordingly, there is an increasing demand for optical components to be miniaturized. However, despite many efforts, current spectropolarimetric systems in space still consist of multiple thick optical elements and result in cumbersome payloads [96,97]. Thus, both medicine and space applications are the perfect application fields for nanostructure-based systems.

Even though nanostructure-based optical systems open new horizons in optics and can replace conventional optical components, they often remain inferior to their conventional counterparts not just because of the performance but also because of the size-limited and complex fabrication [98]. Thus, for the nanostructure-based systems to be applied in mass-production devices, it is necessary to create new nanofabrication techniques or significantly improve the existing ones, which is the goal of the final part of this thesis, Chapter 3.

A variety of metasurface-based applications led to a necessity of an efficient large-scale fabrication technique. However, up to now, there has been no large-area and low-cost fabrication of Mie-resonant metasurfaces. Si is a well-known and CMOS-compatible material, but Si metasurfaces are usually fabricated by complex lithographic techniques, such as electron-beam lithography (EBL) followed by reactive ion etching [99] or focused ion beam (FIB) lithography [100]. Despite the precision offered, these techniques are limited to a small scale due to low-throughput and high cost. Other pattern transfer techniques

like interference lithography [101, 102], mask aligner lithography [103], nanosphere lithography [104], or nanoimprint [105] offer a greater flexibility in scaling-up but require multiple lengthy steps. In contrast, chemical synthesis [106] can be a relatively fast and large-scale technique but cannot ensure the periodic distribution of nanoparticles, similar to laser ablation in liquids [107], grinding and milling [108], or spontaneous dewetting [109–111]. An alternative approach was introduced using pulsed laser radiation, which by means of point-by-point material transfer [112–114], or direct writing [115, 116] enables the formation of ordered metasurfaces. In the steps of developing such ideas further, this work proposes several other laser-based techniques, which contribute towards a realization of metasurface-based devices.

An intriguing way to obtain non-uniform metasurfaces is using laser-induced thermal effects [117], where a lithographically preprocessed uniform metasurface is modified by laser irradiation. The absorption of the irradiation results in heating of the nanostructures. After sufficient energy is deposited, this leads to a crystallization of the material [118–123], which is followed by a drop in the refractive index. Furthermore, the increase of laser energy initiates the reshaping of the nanostructures, which is governed by surface diffusion of the molten material to minimize its surface energy [118, 119]. As the optical resonances are size- and shape-dependent [7, 8], this enables a vivid control of the optical response. Laser-induced reshaping was experimentally demonstrated in plasmonic [37, 124–130], dielectric [52, 131], and hybrid nanostructures [132–134]. In particular, resonant dielectric metasurfaces possess a strong electromagnetic field inside the volume of its elements [8]. Depending on the resonant mode and material absorption, this provides a specific field distribution and a corresponding absorption profile, which may be used for spatial selectivity of thermal effects. However, up to now, this has been barely addressed. Higher-order resonances were chosen for the melting of Si nanostructures using a continuous-wave (CW) laser [131], and the resonant behavior was used for resonant laser printing of germanium (Ge) metasurfaces with nanosecond laser pulses [52]. However, such tailoring was spatially limited as thermal diffusion length is proportional to the pulse duration [135]. Therefore, Chapter 3 demonstrates how the ultrashort laser pulses are used to confine the heat and access the full potential of the spatial-selectivity.

Spatially-selective tailoring builds new grounds in applications such as spectral filtering, but requires a preprocessed template and is limited by the repetition rate of pulsed lasers. To overcome this limitation, the final part of the thesis, Chapter 3, proposes a high-throughput and cost-effective technique for the direct fabrication of Mie-resonant metasurfaces – direct laser interference patterning. Direct patterning using high-peak-power laser interference has been previously shown as a suitable tool for large-area microstructuring of metals [136–145], organic materials [146–148], and even Si [149–156]. It does not require resist, etching, or any other postprocessing steps. Thus it is relatively fast and simple. Although direct laser interference patterning has been used to achieve submicrometer resolution, as shown in the case of a bulk Si [152, 156], the technique has never been exploited to obtain high-index metasurfaces. In Chapter 3, it is experimentally demonstrated that Si-based Mie-resonant metasurfaces can be fabricated in a single step by single-pulse laser interference.

As noted, this thesis consists of several scientific tasks, which conclude in the following results and statements. Chapter 1 confirms that the scattering of dielectric metasurfaces can be optimized for color selectivity. More importantly, it is shown that the optimized metasurfaces are both numerically and experimentally built into an RGB or any other color pattern and downscaled to a submicrometer pixel size,

potentially providing previously unattainable resolution for digital color imaging. Chapter 2 indicates that FP resonators remain one of the most promising spectrally-selective systems as inclusion of high-index dielectric nanostructures in the cavity provides an additional degree of freedom in their tunability. The inclusions change the effective optical thickness and the subsequent resonant wavelengths. Furthermore, the inclusion of polarization-sensitive nanostructures opens new grounds for multifunctional optical systems. Nanostructure-based systems for blood sensing and spectropolarimetry are designed, fabricated, and spectrally analyzed. Chapter 3 proves that laser irradiation can be successfully applied for both modification and structuring of dielectric metasurfaces. The laser pulses are used to post-process large-area metasurfaces by changing their crystallinity and spatial properties, which results in spatial and spectral tunability. Last but not least, the direct laser interference patterning is experimentally demonstrated as a lithography-free technique for patterning of Mie-resonant metasurfaces. Such a technique results in thousands of dielectric nanostructures by a single laser pulse. The obtained metasurfaces are optically, spectrally, and topographically analyzed, as well as compared to numerical results.

Naturally, the majority of the work presented in this thesis was done by the author, Jonas Berzinš, under the supervision by Dr. Frank Setzpfandt and Prof. Dr. Thomas Pertsch from Friedrich Schiller University Jena (FSU Jena), and Dr. Stefan Bäumer from Netherlands Organisation for Applied Scientific Research (TNO). However, here, it is also an excellent opportunity to highlight the key contributions from other colleagues. To start with, the experimental results of Mie resonators in Chapter 1 were obtained using Si samples nanostructured by Stefan Fasold from FSU Jena, who also did the rest of the EBL in this work. The first part of Chapter 2, Section 2.2, was initiated by a number of fruitful discussions with Jan Sperrhake from FSU Jena, and Markus Walther, Carsten Stock, and Dr. Thomas Siefke from FSU Jena, who integrated the FP filters on a CMOS camera. Similarly, the idea of Section 2.3 was built in a collaborative effort with L. Pjotr Stoevelaar, Dr. Fabrizio Silvestri, and, especially, Prof. Dr. Giampiero Gerini from TNO and Eindhoven University of Technology, who supervised that particular project. Specifically, L. Pjotr Stoevelaar made a substantial contribution by building the mathematical grounds for the spectropolarimetric system and carried out the analysis on the condition number. Last but not least, Chapter 3 would not be the same without a substantial contribution by Dr. Simonas Indrišiūnas and Dr. Paulius Gečys from Center for Physical Sciences and Technology, who have provided the laser equipment and assisted in the experiments. All of this work was done within the NOLOSS project, H2020 Marie Skłodowska-Curie Actions (675745).

In summary, this work presents two different approaches for spectrally-selective nanostructure-based systems with their specific advantages and disadvantages; see Chapter 1 for spectrally-selective Mie-resonant metasurfaces, and Chapter 2 for nanostructure-modulated FP resonators. Furthermore, to bridge the gap between fundamental science and industry, novel fabrication techniques – laser-induced tailoring and structuring of metasurfaces – are presented; see Chapter 3. All things considered, this work is not intended to revolutionize optics. Still, it is written with a bit of hope to put a small step in the development of nanophotonics and its applicability in real-world applications.

Chapter 1

Spectrally-selective Mie-resonant metasurfaces

This chapter discusses Mie-resonant dielectric nanostructures and their unique wavelength-dependent spectral properties. Mie theory and numerical tools are used to investigate the light–nanostructure interaction. The basics of color science are introduced to highlight applications in the visible spectral range, particularly, color imaging.

The spatial resolution is one of the most important parameters in digital color imaging. For many applications, a high spatial resolution is desirable, consequently requiring small spectral filters. In this chapter, the nanostructure-based filters are developed and assembled in a Bayer pattern and the lateral size of each color filter is spatially downscaled to obtain submicrometer spectral filters. Scattering properties are varied and localized by simply changing the lateral geometry of the nanostructures. As the scattering of a single nanostructure is already spectrally-selective [157], a high density of different spectral functions is expected, especially as an increased number of dots-per-inch (DPI) has been demonstrated in color printing [46].

This chapter will answer whether Mie resonances can be applied for a high spatial resolution in color filter arrays. In particular, the chapter presents metasurfaces based on Si nanodisks. They provide spectral functions with the transmission of 70–90% and bandwidth in the range of hundred nanometers – well suitable for RGB or CMY color filter arrays. Computational methods such as finite element method (FEM) and finite-difference time-domain (FDTD) are used to tune the ED and MD resonances for subsequent optimization of the metasurfaces. Different strategies are considered for improving color gamut and color quality.

The main results presented in this chapter are published in Proc. SPIE [S2] and ACS Photonics [S4]. These results inspired several other publications though not all are reflected in the thesis. Another publication [S12] is in preparation at the moment of writing this work.

1.1 General properties

1.1.1 Mie scattering

Scattering and absorption of light dictate how an object is perceived [30]. Mie theory describes the absorption and scattering of plane electromagnetic waves by a homogeneous and isotropic spherical nanoparticle, placed in a uniform isotropic dielectric medium. Originally proposed by Gustav Mie in 1908 [28], it has

been one of the most widely used theories in the field of optics. The optical resonances of non-spherical nanoparticles are also often labeled as Mie-type resonances, even though the shape restricts the direct applicability of the theory. Here, the very basics of Mie theory will be introduced, providing a glimpse into analytical and numerical approaches and different Mie-type resonances apparent in dielectric nanostructures. For a full mathematical basis, refer to [158].

1.1.1.1 Mie theory

The aim of Mie theory is to describe the optical response of the nanostructure by the Mie efficiency factors of absorption Q_{abs} , scattering Q_{scat} and extinction Q_{ext} , which follow the relation:

$$Q_{\text{ext}} = Q_{\text{scat}} + Q_{\text{abs}}. \quad (1.1)$$

Analytically, the extinction efficiency Q_{ext} and the scattering efficiency Q_{scat} for a sphere of arbitrary radius r and refractive index n are expressed as follows [158, 159]:

$$Q_{\text{scat}} = \frac{2}{x^2} \sum_{n=1}^{\infty} (2n+1) (|a_n|^2 + |b_n|^2), \quad (1.2)$$

$$Q_{\text{ext}} = \frac{2}{x^2} \sum_{n=1}^{\infty} (2n+1) \text{Re}(a_n + b_n), \quad (1.3)$$

while the absorption efficiency Q_{abs} can be calculated using the relation from Equation 1.1. Note that $x = 2\pi r/\lambda$ is a size parameter, while a_n and b_n are expansion coefficients, expressed in terms of Bessel functions:

$$a_n = \frac{m^2 j_n(mx) [x j_n(x)]' - j_n(mx) [mx j_n(mx)]'}{m^2 j_n(mx) [x h_n^{(1)}(x)]' - h_n^{(1)}(mx) [mx j_n(mx)]'}, \quad (1.4)$$

$$b_n = \frac{j_n(mx) [x j_n(x)]' - j_n(mx) [mx j_n(mx)]'}{j_n(mx) [x h_n^{(1)}(x)]' - h_n^{(1)}(mx) [mx j_n(mx)]'}. \quad (1.5)$$

Here, $j_n(x)$ and $h_n^{(1)}$ are the spherical Bessel functions, and m is the relative refractive index $m = n/n_0$, with n being the refractive index of the nanosphere, and n_0 – the refractive index of the surrounding medium. In Equations 1.4–1.5, permeabilities of the nanostructure and the medium are considered equal, thus are not factored in [158]. Plasmonic resonances correspond to the enhancement of the electric Mie coefficients a_n , while dielectrics enhance both a_n and b_n coefficients [160]. Unfortunately, the analytical solution for non-spherical nanostructures is a great challenge to this day. Thus, numerical tools are used in this work, as discussed next.

1.1.1.2 Numerical approach

The numerical analysis of scattering by an arbitrary-shape nanostructure may start from the assumption that the total electromagnetic field is expressed as a composition of the incident and scattered fields:

$$\mathbf{E} = \mathbf{E}_{\text{inc}} + \mathbf{E}_{\text{scat}}, \quad (1.6)$$

$$\mathbf{H} = \mathbf{H}_{\text{inc}} + \mathbf{H}_{\text{scat}}, \quad (1.7)$$

where the electric and magnetic fields \mathbf{E} and \mathbf{H} are calculated by some of the widely accessible numerical methods such as FEM or FDTD.

Then, the integration of the directional energy flux, the Poynting vector \mathbf{S}_{scat} , results in the total power scattered by the structure P_{scat} [161]. A common practice is to integrate over an imaginary sphere, which is small enough so the source is outside of it, but big enough to accommodate the nanostructure itself. Thus, the scattered power P_{scat} is calculated as follows [162]:

$$P_{\text{scat}} = \iint \mathbf{S}_{\text{scat}} \cdot \mathbf{n} dS = \frac{1}{2} \iint \text{Re}[\mathbf{E}_{\text{scat}} \times \mathbf{H}_{\text{scat}}^*] \cdot \mathbf{n} dS \quad (1.8)$$

where \mathbf{n} is the unit vector normal to the imaginary sphere.

By using the calculated scattering power P_{scat} , its cross section σ_{scat} is calculated by normalizing the scattered power P_{scat} to the incident energy flux P_{inc} :

$$\sigma_{\text{scat}} = 2 \sqrt{\frac{\mu_0}{\epsilon_0 \epsilon_{\text{host}}}} \frac{P_{\text{scat}}}{|\mathbf{E}_{\text{inc}}|^2}, \quad (1.9)$$

where \mathbf{E}_{inc} is the incident electric field. Then, the scattering efficiency Q_{scat} is obtained by normalizing the scattering cross-section σ_{scat} to the geometric cross-section σ_{geom} :

$$Q_{\text{scat}} = \frac{\sigma_{\text{scat}}}{\sigma_{\text{geom}}}. \quad (1.10)$$

Similarly, the power absorbed by the nanostructure is calculated and, accounting the losses of material, the absorption efficiency Q_{abs} is obtained. The extinction efficiency Q_{ext} is calculated as the sum of both, see Equation 1.1.

The following example presents the Mie efficiency factors of a Si-based nanosphere with a diameter of $D = 150$ nm in vacuum/air. The Si nanosphere is illuminated by a broadband plane-wave source in order to calculate its scattering Q_{scat} , absorption Q_{abs} , and extinction Q_{ext} efficiencies. As shown in Figure 1.1(a), the scattering and absorption of such a particle are highly wavelength-dependent. Such optical response is caused by electric and magnetic Mie-type resonances, as explained in Section 1.1.1.3. Si is widely known as a semiconductor, but it is classified as a dielectric in the field of nanophotonics, and this work. More so, it is a high-refractive index material in the visible and near-infrared spectral ranges (see Appendix A for the wavelength-dependent refractive index). Note from the relation of refractive index and Mie scattering coefficient, Equation 1.4, that having a high-index is the key for Mie resonances. The more significant is

the refractive index relative to the medium the nanostructure is embedded in – the stronger the confinement of the electromagnetic fields – the stronger the resonances [10].

It should be noted that the scattering efficiency Q_{scat} tells only half of the story – it represents the far-field response but not the near-field origins. Essentially it is a superposition of different resonant modes. Thus, the other half of the story is told by the analysis of the resonant modes, a technique known as mode decomposition; see Section 1.1.1.4. This is particularly important for dielectrics, where not only electric but also magnetic resonances are apparent [8, 13]; see Section 1.1.1.3 for a detailed discussion.

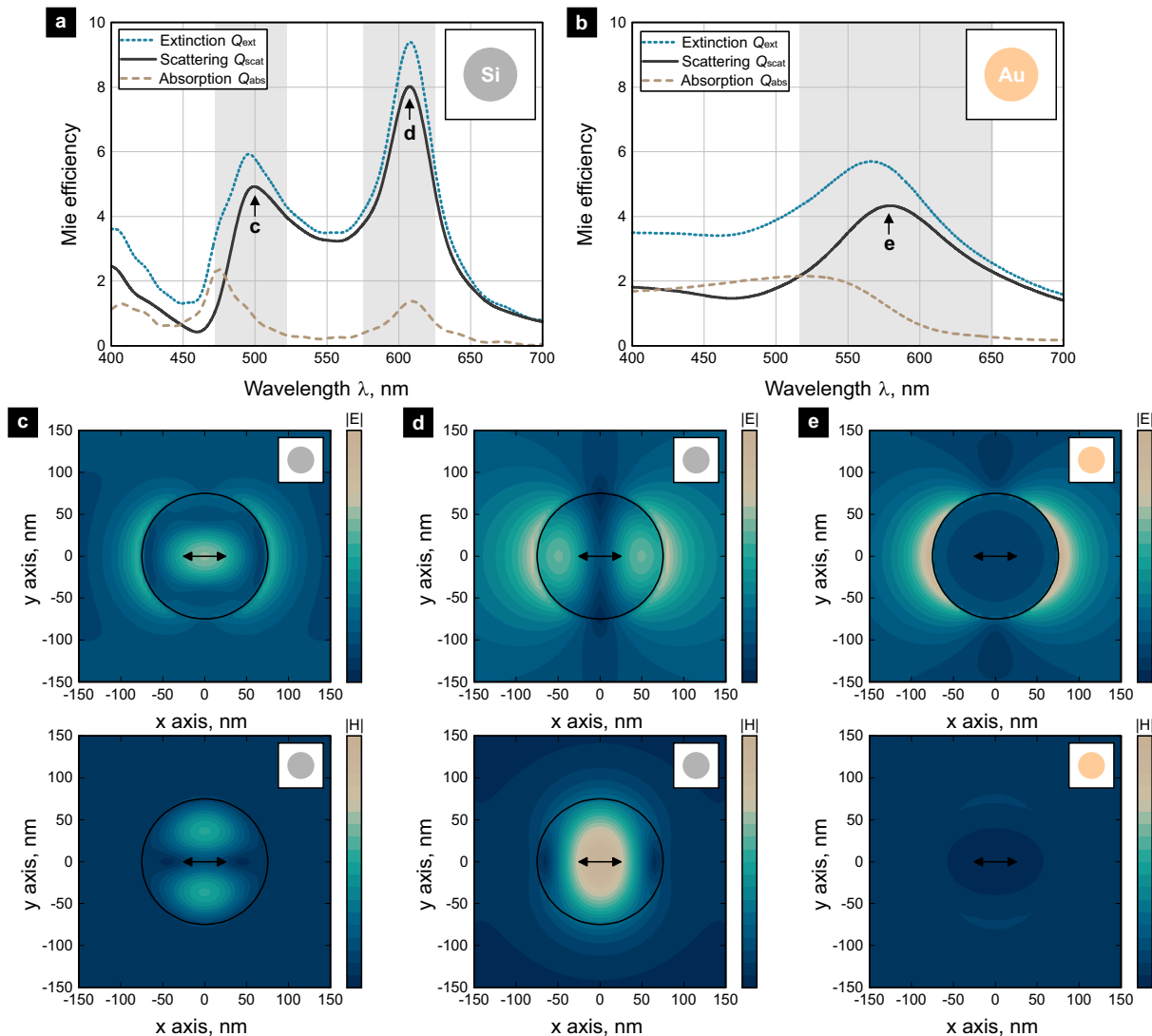


Figure 1.1: Comparison of Mie efficiency of Si and Au nanospheres with a diameter of $D = 150$ nm. (a) Scattering, absorption, and extinction of Si nanosphere. (b) Scattering, absorption, and extinction of Au nanosphere. (c, d) Electric (top) and magnetic (bottom) fields at x-y cross-section of Si nanosphere; at resonances, indicated in (a). (e) Electric (top) and magnetic (bottom) fields at x-y cross-section of Au nanosphere; at the resonance, shown in (b). Black arrows in (c-e) depict the polarization of the incident electromagnetic wave.

1.1.1.3 Dielectrics versus plasmonics

Next, the previously introduced scattering and absorption of the spherical Si-based dielectric nanostructure is compared to a plasmonic nanostructure. In particular, gold (Au) is selected as a widely known plasmonic

material. Using both, Si and Au, single nanospheres are constructed and their scattering Q_{scat} , absorption Q_{abs} , and extinction Q_{ext} efficiencies are simulated numerically. In both cases, the calculation is done using a single nanosphere with a diameter of $D = 150$ nm.

The Mie efficiency, shown in Figure 1.1(a,b), indicates not only the fact that dielectrics have lower losses, if any, as noted by a significantly lower absorption efficiency Q_{abs} , but also some other intriguing advantages. First, following the discussion from the previous section (see Section 1.1.1.2) dielectric nanostructures have multiple peaks/dips in their spectra due to additional magnetic resonances. The electric and magnetic resonances can be tailored independently of each other, which gives more degrees of freedom in control of the optical response. Second, as can be seen in Figure 1.1(a), the resonances in dielectrics are relatively narrow; thus, they enable higher spectral selectivity compared to plasmonics. The electric and magnetic field at the resonances of Si and Au nanospheres are indicated in Figure 1.1(c-e).

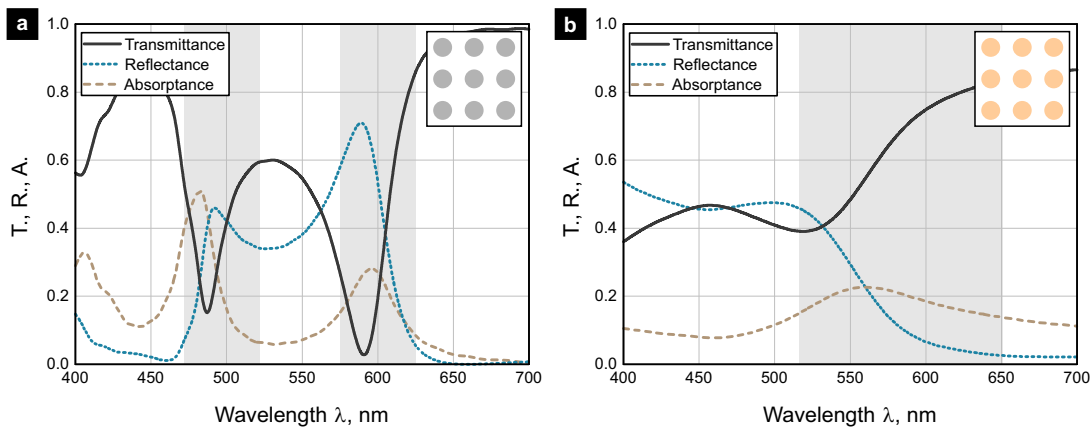


Figure 1.2: Transmittance, reflectance, and absorptance of nanosphere arrays – metasurfaces. (a) Crystalline Si metasurface with nanospheres in a rectangular lattice with a period of $P = 300$ nm. (b) Au metasurface, period $P = 300$ nm. Metasurfaces are embedded in air/vacuum. Insets illustrate the infinite arrays of the nanospheres. Grey areas indicate approximate spectral positions of the resonances.

If one builds a two-dimensional array of such nanospheres – a metasurface – it is then described by transmittance, reflectance, and absorptance. High transmittance of a metasurface relates to a forward scattering or a lack of scattering. In contrast, the reflectance is related to the backward scattering. At the same time, the absorptance is based on intrinsic losses – basically, all of the light that does not come out of the metasurface. To obtain a metasurface, the nanospheres with $D = 150$ nm are distributed in a rectangular array with period $P = 300$ nm; see the spectra of Si and Au metasurfaces in Figure 1.2(a) and Figure 1.2(b), respectively. Similar to previous findings, dielectric nanostructures have lower losses; thus, also higher transmittance outside of the resonances. The resonances in plasmonics are quite broad and due to losses the transmission does not go to zero. Accordingly, the spectral selectivity, equivalent to the bandwidth of the spectral peaks/dips, is quite broad. For many applications, including the spectral filters discussed in this work, the spectral selectivity is essential. Thus, the dielectric nanostructures have the upper hand and will be used from now on in this work.

1.1.1.4 Mode decomposition

In order to understand the fundamentals of Mie resonances, the scattering of a particle is decomposed into the contributing modes. The scattering efficiency of various modes can be computed from the current density [163]. Here, the contributions of electric and magnetic dipoles, electric and magnetic quadrupoles, as well as toroidal components, are considered. However, octupoles and other higher-order modes are not included due to their negligible impact, according to [164].

The polarization induced current density $\mathbf{J}(r)$ of a nanoparticle in a host medium is related to the electric field $\mathbf{E}(r)$ by the following expression:

$$\mathbf{J}(r) = i\omega(\varepsilon_{\text{particle}} - \varepsilon_{\text{host}})\mathbf{E}(r). \quad (1.11)$$

Using it, the electric dipolar moments p and magnetic dipolar moments m of the nanoparticle can be expressed as:

$$p_j = \frac{i}{\omega} \int_{\mathbf{v}} J_j \, d\mathbf{v}, \quad (1.12)$$

$$m_j = \frac{1}{2} \int_{\mathbf{v}} (\mathbf{r} \times \mathbf{J})_j \, d\mathbf{v}. \quad (1.13)$$

The toroidal dipole moments can be split into toroidal electric dipole $T^{(e)}$, along with a second-order correction term $T^{(2e)}$, and toroidal magnetic dipole $T^{(m)}$:

$$T_j^{(e)} = \frac{1}{10} \int_{\mathbf{v}} [(\mathbf{J} \cdot \mathbf{r})r_j - 2r^2 J_j] \, d\mathbf{v}, \quad (1.14)$$

$$T_j^{(2e)} = \frac{1}{280} \int_{\mathbf{v}} [3r^4 J_j - 2r^2 (\mathbf{r} \cdot \mathbf{J})r_j] \, d\mathbf{v}, \quad (1.15)$$

$$T_j^{(m)} = \frac{i\omega}{20} \int_{\mathbf{v}} r^2 (\mathbf{r} \times \mathbf{J})_j \, d\mathbf{v}. \quad (1.16)$$

The electric quadrupoles $Q^{(e)}$ and magnetic quadrupoles $Q^{(m)}$ are symmetrized traceless tensors, expressed as:

$$\bar{\bar{Q}}_{jk}^{(e)} = \frac{i}{\omega} \int_{\mathbf{v}} [r_j J_k + r_k J_j - \frac{2}{3} \delta_{jk} (\mathbf{r} \cdot \mathbf{J})] \, d\mathbf{v}, \quad (1.17)$$

$$\bar{\bar{Q}}_{jk}^{(m)} = \frac{1}{3} \int_{\mathbf{v}} [(\mathbf{r} \times \mathbf{J})_j r_k + (\mathbf{r} \times \mathbf{J})_k r_j] \, d\mathbf{v}. \quad (1.18)$$

The toroidal electric quadrupoles $\bar{\bar{T}}^{(Qe)}$ and toroidal magnetic quadrupoles $\bar{\bar{T}}^{(Qm)}$ are also symmetrized and expressed as:

$$\bar{\bar{T}}_{jk}^{(Qe)} = \frac{1}{42} \int_{\mathbf{v}} [4(\mathbf{r} \cdot \mathbf{J})r_j r_k + 2(\mathbf{J} \cdot \mathbf{r})r^2 \delta_{jk} - 5r^2 (r_j J_k + r_k J_j)] \, d\mathbf{v}, \quad (1.19)$$

$$\bar{\bar{T}}_{jk}^{(Qm)} = \frac{i\omega}{42} \int_{\mathbf{v}} r^2 [r_j (\mathbf{r} \times \mathbf{J})_k + (\mathbf{r} \times \mathbf{J})_j r_k] dv, \quad (1.20)$$

where j, k represents the coordinates $\{1, 2, 3\}$ for the coordinates $\{x, y, z\}$, δ_{jk} is the Kronecker delta, \mathbf{r} is the position vector, given by $\mathbf{r} = r_x \hat{x} + r_y \hat{y} + r_z \hat{z}$, and r^2 is the modulus square of the position vector, given by $r^2 = r_x^2 + r_y^2 + r_z^2$.

The scattered power can be decomposed into various multipoles. As the scattered power by toroidal magnetic dipoles $T^{(m)}$, toroidal electric quadrupoles $\bar{\bar{T}}^{(Qe)}$, and toroidal magnetic quadrupoles $\bar{\bar{T}}^{(Qm)}$ is small, they are included as a correction factors in magnetic dipolar moments m , electric quadrupoles $\bar{\bar{Q}}^{(e)}$, and magnetic quadrupole $\bar{\bar{Q}}^{(m)}$, respectively. Octupoles and other higher order modes are ignored. The following equations are used for scattering decomposition:

$$P_{\text{scat}}^{(e)} = \frac{k^4 \sqrt{\epsilon_{\text{host}}}}{12\pi \epsilon_0^2 c \mu_0} \sum_{j=1}^3 |p_j|^2, \quad (1.21)$$

$$P_{\text{scat}}^{(Te)} = \frac{k^4 \sqrt{\epsilon_{\text{host}}}}{12\pi \epsilon_0^2 c \mu_0} \sum_{j=1}^3 \left| \frac{ik \epsilon_{\text{host}}}{c} T_j^{(e)} + \frac{ik^3 \epsilon_{\text{host}}^2}{c} T_j^{(2e)} \right|^2, \quad (1.22)$$

$$P_{\text{scat}}^{(m)} = \frac{k^4 \sqrt{\epsilon_{\text{host}}^3}}{12\pi \epsilon_0 c} \sum_{j=1}^3 \left| m_j + \frac{ik \epsilon_{\text{host}}}{c} T_j^{(m)} \right|^2, \quad (1.23)$$

$$P_{\text{scat}}^{(Qe)} = \frac{k^6 \sqrt{\epsilon_{\text{host}}^3}}{160\pi \epsilon_0^2 c \mu_0} \sum_{k=1}^3 \sum_{j=1}^3 \left| \bar{\bar{Q}}_{jk}^{(e)} + \frac{ik \epsilon_{\text{host}}}{c} \bar{\bar{T}}_{jk}^{(Qe)} \right|^2, \quad (1.24)$$

$$P_{\text{scat}}^{(Qm)} = \frac{k^6 \sqrt{\epsilon_{\text{host}}^5}}{160\pi \epsilon_0 c} \sum_{k=1}^3 \sum_{j=1}^3 \left| \bar{\bar{Q}}_{jk}^{(m)} + \frac{ik \epsilon_{\text{host}}}{c} \bar{\bar{T}}_{jk}^{(Qm)} \right|^2. \quad (1.25)$$

As example, the metasurface constituted of Si nanospheres is analyzed next. The scattering contributions of ED, MD, as well as electric quadrupole (EQ), and magnetic quadrupole (MQ), in the case of a Si nanosphere with diameter $D = 150$ nm in an array with period $P = 300$ nm, are shown in Figure 1.3(a). As indicated, the peak at $\lambda = 485$ nm corresponds to the ED resonance, while the peak at $\lambda = 595$ nm relates to the MD resonance. The contributions of EQ and MQ resonances are smaller by more than an order of magnitude. The contribution of MQ is positioned at $\lambda = 475$ nm, while no significant contribution of EQ is visible in the spectral range of interest. The mode decomposition is done using an array of Si instead of a single nanosphere; thus, the scattering spectral positions are slightly different from the scattering of a single nanosphere, shown in Figure 1.1(a). Moreover, the scattering efficiency is slightly enhanced. Both effects are induced by the coupling of neighboring nanospheres. The coupling can be noted by the fields of a single nanosphere extending beyond the spatial size of a unit cell; see Figure 1.1(c-e). Based on the mode decomposition, the electric and magnetic fields at horizontal cross-sections of the Si nanosphere, shown in Figure 1.1(c), can now be related to the ED resonance, similarly, Figure 1.1(d) – MD resonance. The spectral positions of the fundamental ED and MD resonances perfectly coincide with the spectral dips in

the transmittance of the Si metasurface, shown in Figure 1.2.

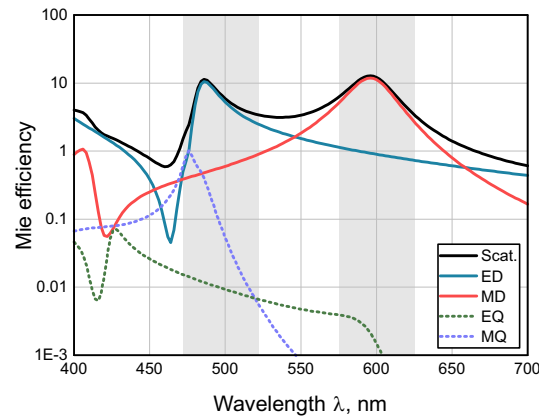


Figure 1.3: Resonant modes of Si nanospheres in an array. The total scattering is shown by the black solid line. It is decomposed into ED (blue solid line), MD (red solid line), EQ (green dotted line), and MQ (purple dotted line) resonances. The logarithmic scale is used to enhance the visibility of lower-order resonances. The diameter of the nanospheres is $D = 150$ nm; the array period is $P = 300$ nm.

The metasurfaces or single nanostructures may be engineered to have strong EQ or MQ resonances in the spectral range of interest [165]. Similarly, one can utilize even higher-order resonances [166]. However, this chapter will focus on the fundamental ED and MD resonances due to their robustness, easy access, and control. Next, the reader will be introduced to the basics of color science and will steadily answer how the Mie resonances, shown here, can be applied in color imaging.

1.1.2 Color science

Conventional color imaging is based on human color perception. The mechanism relies on three color channels, e.g., RGB, as realized in the Bayer sensor [167]. A color is essentially a particular spectral function in the visible spectral range. To identify the filter function which fits the targeted color, one must define a color reference and a figure of merit. There are several ways to optimize RGB filter functions, such as optimization towards particular wavelength ranges [35], optimization in comparison to reference filters [20], or the CIE color-matching functions [53]. A new approach is used for all experiments and simulations in this chapter. Thus, it will be shortly introduced in the following section.

1.1.2.1 Chromaticity and color spaces

The spectral composition of visible light can be characterized by the color matching functions $S_x(\lambda)$, $S_y(\lambda)$, and $S_z(\lambda)$, from the CIE standard colorimetric system [168–170]. A typical yet randomly selected spectral function $T(\lambda)$ and corresponding color is given in Figure 1.4(a). The color matching functions are shown in Figure 1.4(b). Each of the color matching functions are independent from each other and are used to

transform the spectral function $T(\lambda)$ to tristimulus values X , Y , and Z by the following equations:

$$X = \int T(\lambda) \times P_{D65}(\lambda) \times S_x(\lambda) d\lambda, \quad (1.26)$$

$$Y = \int T(\lambda) \times P_{D65}(\lambda) \times S_y(\lambda) d\lambda, \quad (1.27)$$

$$Z = \int T(\lambda) \times P_{D65}(\lambda) \times S_z(\lambda) d\lambda. \quad (1.28)$$

In this work, the spectral function $T(\lambda)$ is usually the transmittance of the designed metasurface. It is multiplied by the normalized spectral day-light distribution $P_{D65}(\lambda)$, assuming the standard illumination conditions; see spectral distribution in Figure 1.4(b). Such calculation provides the tristimulus values X , Y , and Z , allowing us to numerically identify the color from any measured or simulated spectra and accurately reproduce it, as discussed next.

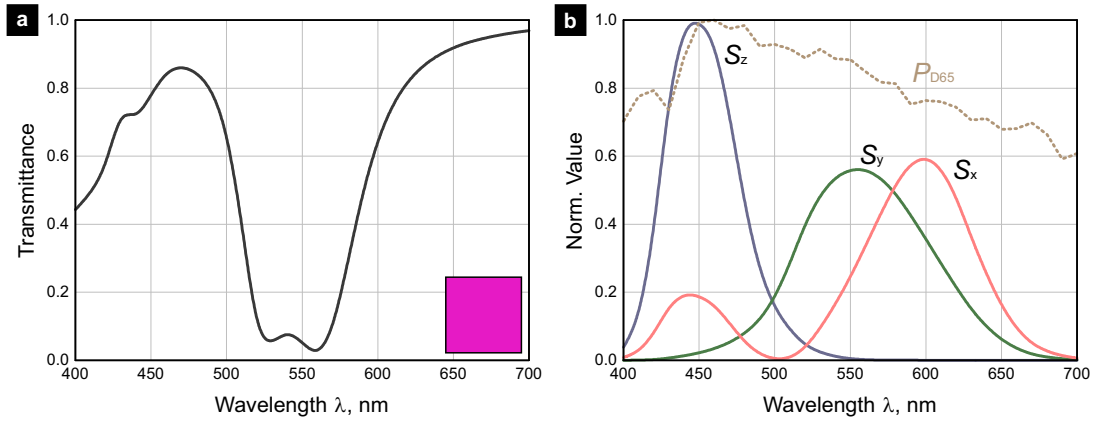


Figure 1.4: Example of typical spectra and spectral functions used in color science. (a) Typical randomly selected spectral function (transmittance) and its corresponding color, shown in the inset. (b) Normalized color matching functions $S_x(\lambda)$, $S_y(\lambda)$, and $S_z(\lambda)$, and spectral power distribution of day-light $P_{D65}(\lambda)$.

Since the perceived color depends only upon the relative magnitudes, the tristimulus values X , Y , and Z are normalized to obtain so-called chromaticity coordinates:

$$x = \frac{X}{X+Y+Z}, \quad y = \frac{Y}{X+Y+Z}. \quad (1.29)$$

The chromaticity diagram is commonly used to evaluate the color gamut. The outer boundary of the gamut represents the limits of human vision, but usually, one limits himself to a certain color space used by the detector. The sRGB color system is taken in this instance, as it is one of the most popular RGB color spaces. The assumption is that, if the color chromaticity is within the boundary, the color may be reproduced by that device or represented by that color system. However, here it should be noted that the chromaticity diagram is only two-dimensional and does not include the luminance. Because of this, using only the chromaticity diagram to determine the color is an incomplete solution. Thus, color spaces are introduced.

The color spaces provide a complete description of the true color. The values in a certain color space

are achieved by multiplying the tristimulus values by the matrix of the chosen color space, e.g., sRGB:

$$\begin{bmatrix} R \\ G \\ B \end{bmatrix}_{\text{sRGB}} = \begin{bmatrix} M \end{bmatrix}_{\text{sRGB}} \begin{bmatrix} X \\ Y \\ Z \end{bmatrix} = \begin{bmatrix} 3.2406255 & -1.537208 & -0.4986286 \\ -0.9689307 & 1.8757561 & 0.0415175 \\ 0.0557101 & -0.2040211 & 1.0569959 \end{bmatrix} \begin{bmatrix} X \\ Y \\ Z \end{bmatrix}. \quad (1.30)$$

In this work, the use of HSV color space is recommended as it includes not only RGB colors but also CMY. The HSV color space can be obtained by transforming tristimulus values to RGB, and then by several operations to the values of HSV (hue, saturation, and value). The particular operations will be described next. First, the values of R , G , and B are normalized:

$$R' = \frac{R}{255}, \quad G' = \frac{G}{255}, \quad B' = \frac{B}{255}. \quad (1.31)$$

Then, one selects the largest and the smallest among them, m_{\max} and m_{\min} , respectively, as well as the difference between the two Δ :

$$m_{\max} = \max(R', G', B'), \quad (1.32)$$

$$m_{\min} = \min(R', G', B'), \quad (1.33)$$

$$\Delta = m_{\max} - m_{\min}. \quad (1.34)$$

In HSV color space, hue represents the type of color, and is defined in terms of an angle with R color at 0° , G color at 120° , and B color at 240° , etc. The hue of a color is described as follows:

$$H = 60 \times \begin{cases} \text{undefined}, & \text{if } \Delta = 0, \\ \frac{G-B}{\Delta} + 0, & \text{if } m_{\max} = R, \\ \frac{B-R}{\Delta} + 2, & \text{if } m_{\max} = G, \\ \frac{R-G}{\Delta} + 4, & \text{if } m_{\max} = B, \end{cases} \quad (1.35)$$

where $H = H + 360$, if $H < 60$. Then the saturation is calculated, which represents the vibrancy of the color:

$$S = \begin{cases} 0, & \text{if } m_{\max} = 0, \\ \frac{\Delta}{m_{\max}}, & \text{if } m_{\max} \neq 0, \end{cases} \quad (1.36)$$

and then, finally, the value, which represents the brightness of the color – basically, the amplitude of the signal. It is expressed as:

$$V = m_{\max}, \quad (1.37)$$

which will be further used to obtain the figure of merit used in this chapter – the color quality Q_ξ ; see the following section.

1.1.2.2 Color quality

The figure of merit for optimizing the color filters takes into account the saturation and the value of the color while emphasizing the hue, which is critical in color imaging. As mentioned before, color optimization algorithms used up to now rely on the integration over a particular spectral range directly [35], comparison to reference filters [20], or the CIE color-matching functions to obtain color coordinates [53]. These coordinates can be transformed into the coordinates of a variety of color spaces, as discussed before. However, they will always form a set of numbers that do not allow direct access to the information on whether the optimization result resembles the target color. For example, the transformation of the spectrum from Figure 1.4 results in the tristimulus values $X = 0.54$, $Y = 0.32$, and $Z = 0.76$. The tristimulus values are used to obtain RGB values $R' = 0.90$, $G' = 0.10$, and $B' = 0.77$, if the sRGB model is used. However, even though one can already guess the shade of the color, it is difficult to assign it to a specific color, red or magenta.

It may be convenient to use the CIE color difference methods, which utilize the distance between the obtained and the target colors, calculated in three-dimensional CIELAB or CIELUV color spaces [171,172]. However, distances may vary significantly for different RGB and CMY primary colors used. In particular, if one optimizes not a single but a set of filters at once, as it is here, a direct comparison of the filters is required in the full set. Accordingly, a single value must be used as an optimization criterion. Such a figure of merit was first proposed in [S2], and updated in [S4]. The figure of merit – the color quality Q_ξ – is defined as:

$$Q_\xi = \begin{cases} 0, & \text{if } \Delta H_\xi = \frac{\pi}{n} \\ \sqrt[3]{(1 - \frac{n}{\pi} \times \Delta H_\xi) \times S \times V}, & \text{otherwise,} \end{cases} \quad (1.38)$$

where primary colors are indexed by $\xi \in (R, G, B, C, M, Y)$, $\Delta H_\xi = |H_\xi - H|$ is the hue difference from the chosen target primary color (in radians), S is the saturation, and V is the value of the color obtained from the transmittance or reflectance. These values used for calculation of color quality Q_ξ are graphically depicted in HSV color space in Figure 1.5.

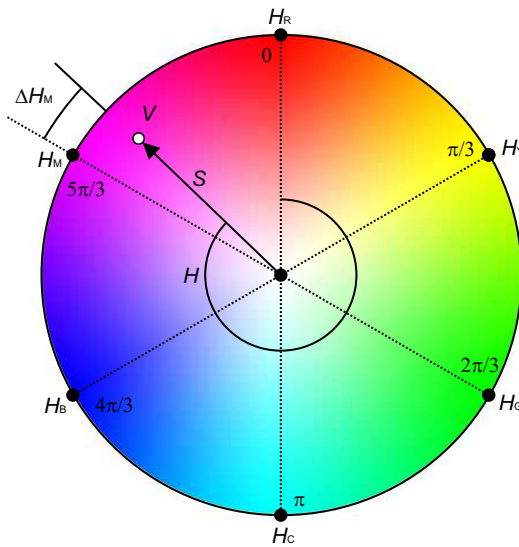


Figure 1.5: HSV color space with indicated values for color quality Q_ξ calculation: hue difference ΔH_ξ , value V , and saturation S . In this case $\xi = M$, which stands for magenta. Other primary colors included in the optimization are: red (R), yellow (Y), green (G), cyan (C), and blue (B). The figure is adapted from [S2].

The color quality Q_ξ results in a positive value for only one color index ξ , assigning the generated color to the closest primary color. The proposed figure of merit has a certain threshold to ensure that the color is manifested in the structure. For example, in the R filter optimization, the color quality will be positive $Q_R > 0$ only if the transmitted color is of a red shade. If the realized color is closer to any other color – the color quality is equal to zero $Q_R = 0$. Continuing with the case from Figure 1.4, the RGB values $R' = 0.90$, $G' = 0.10$, and $B' = 0.77$ result in color quality $Q_R = 0$, same for all other RGB/CMY colors except $Q_M = 0.82$. Thus, as it turns out, the spectral function, shown in Figure 1.4, provides a magenta color. Accordingly, when Q_ξ is non-zero, its actual values can be used to optimize the experimentally or numerically obtained spectrum towards the target primary color.

The rigorous optimization is especially important if the material used is not lossless in the visible spectral range with transmittance over a wide range of spectra. For example, in RGB filters based on Si gratings [20], the blue filter function has high transmittance in the blue spectral region but also exhibits very high values in red. This may imply that the actual color is not blue, but most likely of a magenta shade. It would be difficult to confirm such an assumption by just looking at the spectral function, simply integrating over particular spectral ranges, or comparing the color spaces.

Finally, before moving further, it should be noted that the CIE chromaticity diagram is occasionally used as evidence of high-quality colors. However, as mentioned, it is not entirely correct, as it does not factor in the luminosity. Thus, even if it is a very pure color, it will not necessarily be bright enough due to the lack of spectral power gathered by the image detector. On the contrary, the proposed figure of merit – the color quality – considers the luminosity equally valued to the saturation of colors [S2, S4]; see Equation 1.38. Note that in the color quality algorithm, the transmittance of the target color is the highest, while it is equally low for the others, obtaining the best saturation, the best value, and the correct hue. Such a feature will be specifically embraced in the following optimization of nanostructure-based color filters.

1.2 Nanostructure-based color filters

Mie-resonant dielectric nanostructures are used to build a spectrally-selective optical system for digital imaging, an RGB color filter array. Experimental and numerical tools are used to explore the spatial and angular limits of the nanostructured color filter arrays. Light scattering and coupling of the dielectric nanostructures are rigorously optimized for the best overall performance, showcasing Mie-resonant systems as a potential alternative to conventional color filters.

The target structure is schematically introduced in Figure 1.6(a). It consists of submicrometer RGB filters constituted of all-dielectric nanostructures placed on top of a CMOS image sensor with a spacer in-between. To realize different filter functions, the lateral geometry of nanostructures is varied. Amorphous Si, one of the most commonly used high refractive index and CMOS compatible materials, is used. Even though it is a lossy material in the visible spectral range, it is sufficient for conceptual demonstration. An example of a realized uniform periodic array of nanostructures is presented in Figure 1.6(b). The inset of Figure 1.6(b) schematically depicts a unit-cell of the polarization-insensitive disk-shape nanostructures, indicating the main geometrical parameters: diameter D , height H , and period P .

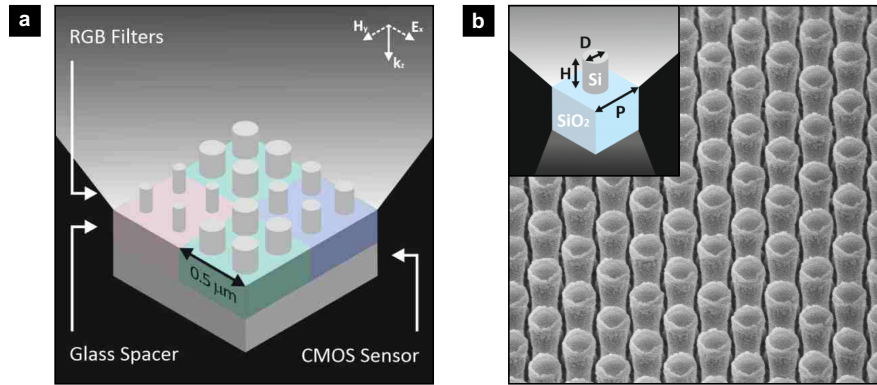


Figure 1.6: Proposed submicrometer dielectric nanostructure-based filters. (a) Graphic illustration of the implementation of sub-micrometer dielectric nanostructure-based RGB filters on top of a CMOS image sensor. (b) SEM image of amorphous Si nanostructures on top of a glass substrate. The inset shows the main geometrical parameters of the filters: height H , diameter D of the nanodisks, and period P . The figure is adapted from [S4].

1.2.1 Concept

In analogy to Mie theory for spherical particles, the MD resonance occurs when the wavelength of incident light is comparable to the optical size of the nanostructure [8, 13]. Even though a full analytical solution is not available for non-spherical nanostructures, the spectral positions of the fundamental ED and MD resonances can be estimated and optimized for a specific spectral selectivity.

The excitation of ED resonance requires a collective linear polarization induced by the electric field of the incident light, while the excitation of the MD is driven by the electric field of light that couples to displacement current loops [8]. This displacement current loop induces the MD moment, oriented perpendicularly to the electric field polarization. It is known that the spectral position of Mie resonances scales with the physical dimensions of nanostructures, as shown in Figure 1.7. Here, the diameter D is varied from 50 nm to 200 nm while having the period P set to 250 nm and height H fixed at 175 nm. The spectral representation of such parameter variation is given in Figure 1.7(a,b). The scaling of nanostructures is mainly limited by their fabrication, e.g., the smallest manufacturable size and/or the smallest gap between the nanostructures. Despite these limits, by optimizing an array of nanostructures, one may obtain various spectral bands in the visible spectral range, and subsequent colors; see the spectral representation in the chromaticity diagram in Figure 1.7(c,d).

1.2.2 Methods

1.2.2.1 Numerical methods

Numerical simulations were carried out using FDTD (Lumerical). The initial optimization of the dielectric nanostructure-based filters was done using a 3D model of an infinite array of amorphous Si nanostructures (see the refractive index in Appendix A), placed on top of a glass substrate, considering air as the covering medium. The model implemented periodic boundary conditions (PBCs) on the sides and perfectly matched layers (PMLs) on the top and the bottom of the simulation domain. The mesh accuracy was set to $\lambda/22$. Frequency domain field and power monitors recorded the electric and magnetic fields. The integration of

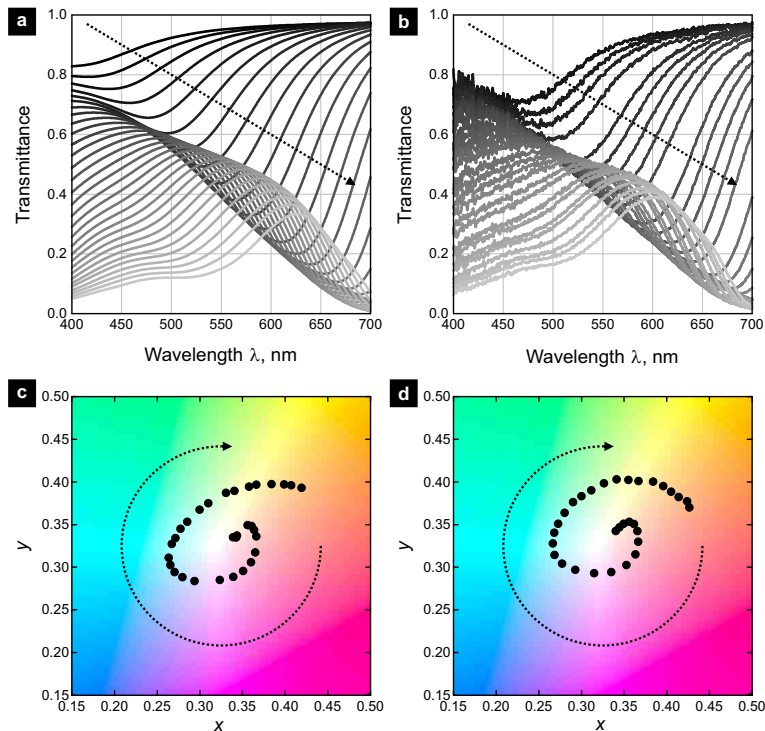


Figure 1.7: Spectral tunability of metasurface by increase of nanostructure diameter. (a) Simulation. (b) Experiment. (c,d) Simulation and experimental data in CIE 1931 chromaticity diagram. Height is fixed at $H = 175$ nm, period is set to $P = 250$ nm. The figure is adapted from [S4].

the power density over the monitor area provides transmission and reflection as functions of wavelength. For most simulations, the structure was excited by a normal-incidence plane wave source with a spectrum covering the visible spectral range. Furthermore, oblique incidence simulations were carried out using a broadband fixed angle source technique (BFAST) to ensure a constant angle for all of the wavelengths. The color filter array simulations were done using the same PBC and PML boundaries, but extending the simulation domain to a pixel array of 2×2 pixels [173]. The simulation considers a semi-infinite substrate. For monitoring the incident power, separate monitors were put in a distance of $0.1 \mu\text{m}$ from the color pixels illuminated by a normally-incident plane-wave source.

1.2.2.2 Fabrication method

The amorphous Si nanostructures were made from a commercial amorphous Si layer (Tafelmaier Dünnschicht-Technik) with a thickness of 500 nm on top of a glass substrate. The Si layer was etched step-by-step to the target height of 175 nm by argon (Ar) ion beam etching (Oxford Ionfab 300, Oxford Instruments). After each etching step, the sample thickness was measured by an optical transmission setup and, subsequently, compared to simulation data. Then, a 30 nm chromium (Cr) layer was deposited by ion beam deposition (Oxford Ionfab 300, Oxford Instruments). After the spin-coating of 100 nm electron beam resist (EN038, Tokyo Ohka Kogyo), the sample was exposed by a variable-shaped electron-beam lithography (EBL) system (Vistec SB 350, Vistec Electron Beam). The resist was developed for 30 s at room temperature, and the created mask was transferred in the Cr layer by ion beam etching (Oxford Ionfab 300, Oxford Instruments). Finally, the Cr mask was transferred in the Si layer by inductively coupled plasma reactive ion etching

(Sentech SI-500 C, Sentech Instruments). The reactive gas was tetrafluoromethane (CF_4). After etching, the remaining resist and Cr mask were removed by acetone and a Cr etchant.

1.2.2.3 Characterization methods

The fabricated sample was analyzed visually by a white-light optical microscope (Axio Imager 2, Carl Zeiss) with an installed 5-megapixel camera (AxioCam MRc 5, Carl Zeiss). The white-light adjusted optical images were taken using a $100\times$ magnification high numerical aperture $\text{NA} = 0.9$ objective (EC Epiplan-Neofluar DIC M27, Carl Zeiss). The scanning electron microscope (SEM) images were taken using FIB/SEM dual-beam system (Helios NanoLab G3 UC, FEI). The spectral analysis was done with a plane-wave illumination using an inverted optical microscope system (Axio Observer D1, Carl Zeiss) with integrated broadband VIS/IR imaging spectrometer (iHR320, Horiba).

1.2.3 Design and numerical optimization

1.2.3.1 Shape and size dependence

Before describing the optimization of the design, it is important to select the shape of the metasurface elements. Some publications have noted that structures like extruded crosses have more degrees of freedom for the tunability of Mie resonances than disks or crosses [53]. However, it is only partially true. Crosses have more geometric parameters, but their flexibility is quite limited, simply because of the nature of dielectric resonances. The dielectric resonances arise mainly from the volumetric effects rather than the particular shapes or features. For example, as long as a disk or a cube has the same volume and a similar aspect ratio as a cross, it is expected to have a similar optical response; see Figure 1.8, where the transmittance is compared for disks/pillar, cubes/squares, and crosses, as a function of the area the particular shapes constitute in the unit cell of the metasurface. From these plots, it is clear that regardless of the shape, the fundamental ED and MD resonances maintain an almost identical relation to the surface area (or volume, as their height is fixed at $H = 175$ nm). Of course, these assumptions are for symmetric nanostructures, while any asymmetry would induce a polarization-sensitive response.

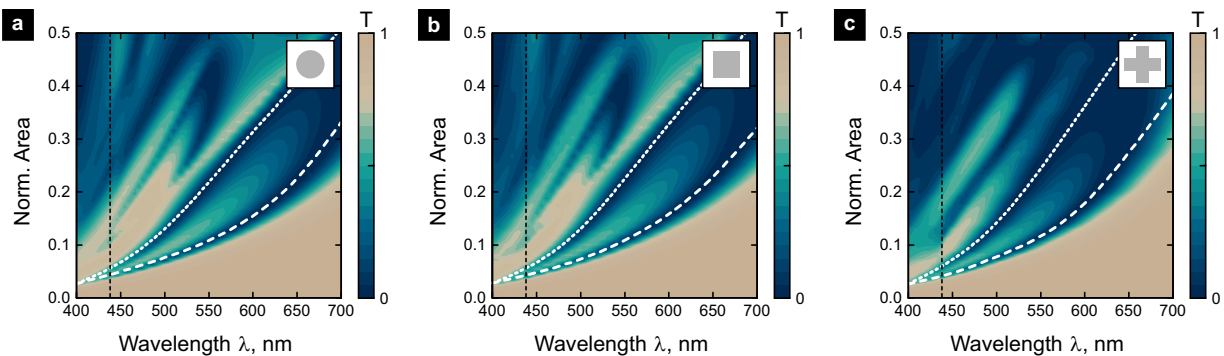


Figure 1.8: Transmittance of metasurfaces with different-shape elements: (a) disks, (b) squares, (c) crosses, reflecting rather similar optical response. The size is normalized to area. Approximate spectral position of ED and MD resonances are indicated by dotted and dashed lines, respectively. Period is set to $P = 300$ nm, height to $H = 175$ nm

It is possible to describe any shape mathematically, yet it is not recommended to use complex-shape

nanostructures because of the feature-size limits of EBL or other existing nanofabrication techniques. It is well-documented that the whole metasurface science has started from radio waves, and only in the past few decades was successfully downscaled to the optical spectral range. Such a trend directly relates to manufacturing capabilities. Even to this day, sharp sub-50 nm features remain a challenge for highly developed EBL. Thus, if there is no significant drawback, it is worth using shapes and geometries that are as simple as possible. Following such logic, this Chapter 1 utilizes the shape of a disk/pillar.

Furthermore, besides the shape of nanostructures, their arrangement can play a role in the optical response. The small distance between the nanostructures may cause electromagnetic coupling, as shown in the following sections. Ordered arrays possess array resonances [S3], but to some surprise, the disorder may also provide unique control of dispersion [174]. In the mean-time, spectral selectivity can be enhanced by nanostructure mixing [175] or stacking [176] of metasurfaces; for more details, refer to [S2].

1.2.3.2 Optimization algorithm

In the optimization of nanostructure-based filters with color quality Q_ξ as the figure of merit, the material and the environment are known and kept constant. Accordingly, the Si metasurface has only three variables: height H and diameter D of nanostructures, and lattice period P . Naturally, sophisticated evolutionary and genetic algorithms may be used for efficient optimization [177], but for such a limited amount of variables it is sufficient to vary the parameters and look for local minima or maxima. The variables can be visually represented as a parameter cube; see Figure 1.9. When tuning these parameters, the optical response is monitored. The transmission spectra are transformed into color and color quality, as described in Section 1.1.2. In the algorithm shown below, one is looking for the maximum color quality of the separate colors. However, specific requirements are also coming from the optical system, e.g., setting the same height H for all structures. Then, the critical aspect is to obtain the best RGB colors, as shown in Figure 1.9. One has to ensure that the quality of the worst filter would be as high as possible; thus, securing the best performance for the full set of filters.

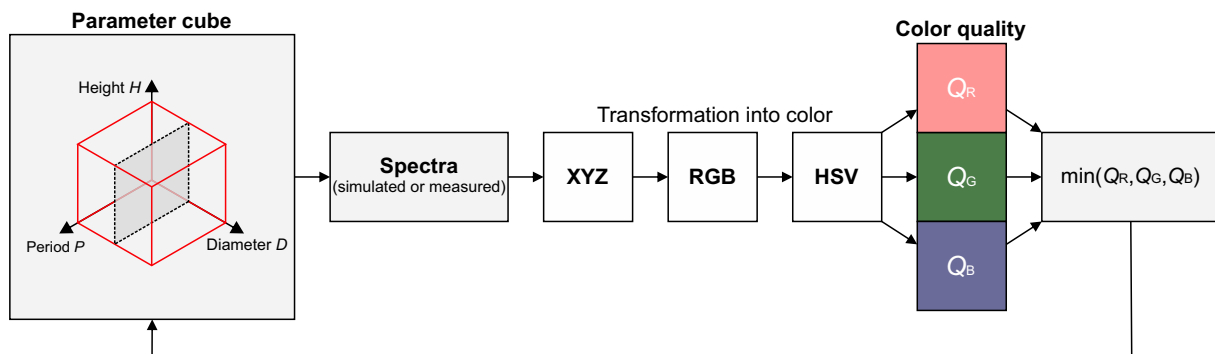


Figure 1.9: Schematic representation of parameter selection (optimization) algorithm. From a parameter sweep to the color quality via spectral information transformation into color. The figure is adapted from [S4].

During the optimization of the filter functions, specific requirements coming from the system engineering and nanostructure fabrication have to be met. As mentioned, a crucial factor in using nanostructured arrays is the uniform height, which is required to utilize an efficient transverse patterning, i.e. use single-step EBL instead of a cumbersome multi-step process. Accordingly, to determine the optimal height H

for the simultaneous realization of all three primary RGB colors, transmission spectra are calculated for homogeneous periodic arrays of nanostructures varying in height H , diameter D , and period P . During the optimization also other conditions, e.g., the limited resolution of EBL [178], are taken into account.

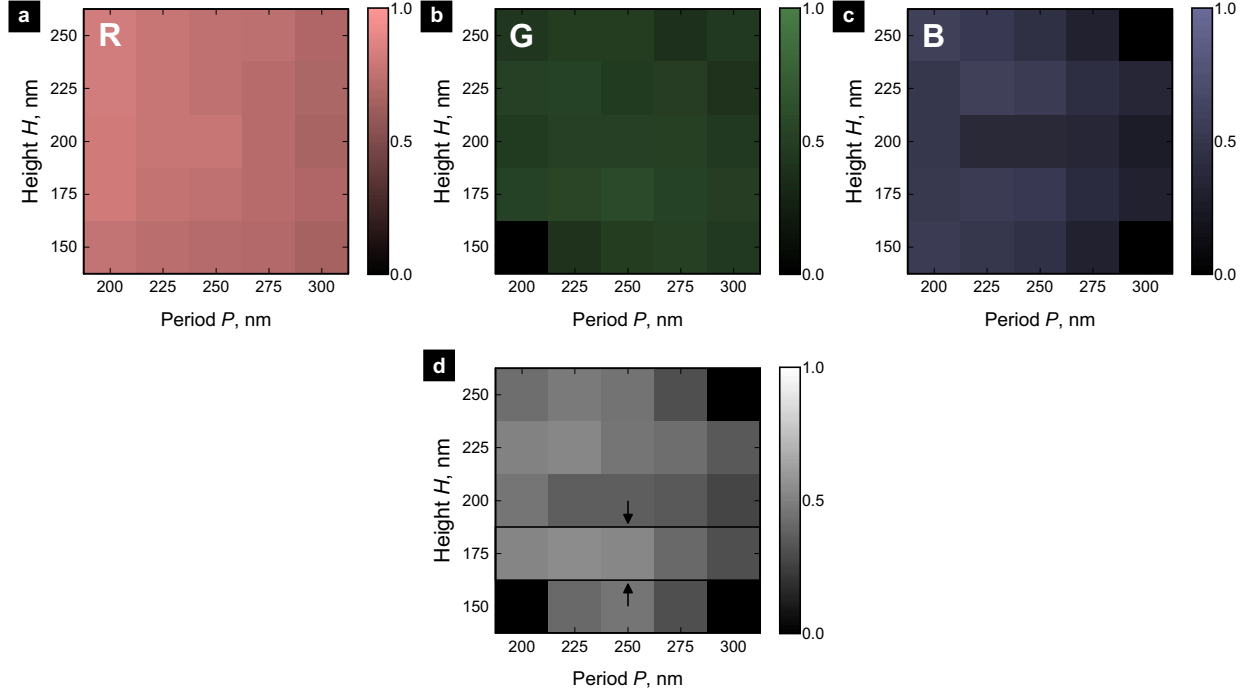


Figure 1.10: Selection of geometrical parameters. The highest RGB color quality values Q_ξ in the matrix of height H and period P , after sweeping the diameter D of the nanostructure for (a) R, (b) G, and (c) B filters. (d) Highest minimum Q_ξ values of RGB as the function of height H and period P . The selected height is $H = 175$ nm. The figure is adapted from [S4].

The dependence on some of the metasurface parameters, particularly, height H and period P , is shown in Figure 1.10. In each of the matrix values, the diameter D is varied from a minimum of 50 nm to 50 nm less than the period. In Figure 1.10, variation of the color quality Q_ξ is shown. It can be noticed that the optimal values of the R filter are almost constant; see Figure 1.10(a). In contrast, the color quality of G filter changes at the boundaries of the selected range, and even higher fluctuations are noted in the case of B; see Figure 1.10(b) and Figure 1.10(c), respectively. In this particular case, if the highest minimum value of color quality is calculated, the plot has two peaks at $H = 175$ nm and $H = 225$ nm; see Figure 1.10(d). A smaller deviation of color quality appears with the change of period P at the smaller height, $H = 175$ nm. Taking this into consideration, then the period is selected. The values between $P = 200$ nm and $P = 250$ nm are relatively similar. However, at the end, the period of $P = 250$ nm is selected due to the significance of G filter in the Bayer pattern. It is a square pattern, which consists of R filter, B filter, and two G filters [167]. Accordingly, from a technological perspective, obtaining a better G filter is of a higher importance than R and B filters. Even though it is not essential to use the same periodicity setting for all filters, a significant change in the color quality is not expected. In contrast, an equal periodicity over all filters reduces the degrees of freedom in the fabrication. Next, the numerical results will be presented in detail with a comparison to the experimental realization.

1.2.4 Experimental realization

The experimental demonstration of nanostructure-based color filters was based on a commercially available amorphous Si layer on top of a glass substrate; see Appendix A for dispersion parameters. The Si layer was etched to the target height $H = 175$ nm and then nanostructured by EBL and reactive ion etching (see Section 1.2.2 for more details on experimental methods).

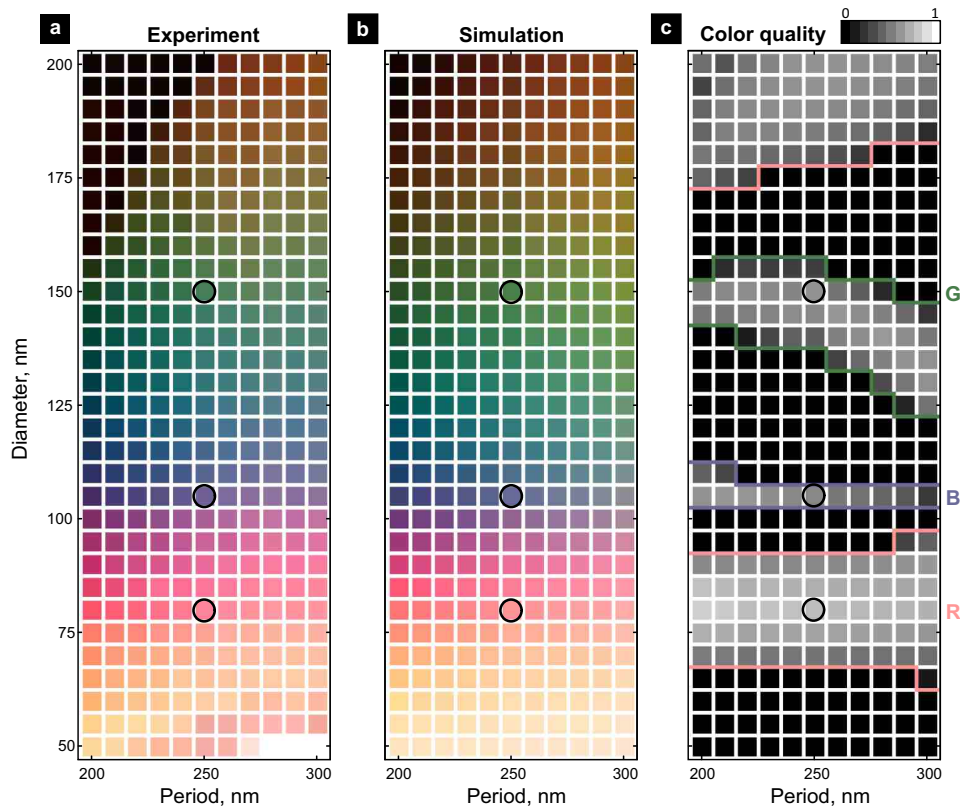


Figure 1.11: Visible spectral range nanostructure-based filters using amorphous Si nanostructures. (a) Measured transmissive colors in dependence of period and diameter of the nanodisks with a height of 175 nm. (b) Simulated colors, transformed from calculated spectra using CIE 1931 color matching functions and the sRGB primary color basis. (c) Color quality Q_{ξ} calculated from the simulation data with the regions bigger than zero for R, G and B colors highlighted and the optimal RGB colors circled. The figure is adapted from [S4].

Nanostructures were first realized in patches of $100 \times 100 \mu\text{m}^2$, which is a sufficient size to neglect the boundary effects and observe the true color realized by the semi-infinite nanostructure arrays. Figure 1.11(a) shows a matrix of color patches obtained from the measured spectra and arranged by their geometrical parameters. The colors obtained from the corresponding simulations are shown in Figure 1.11(b) and agree well with the measurements. Hence, the simulated spectra are further used to calculate the color quality; see Figure 1.11(c). Here, the regions for which Q_R , Q_G , and Q_B are larger than zero, are indicated by the respectively colored boundaries.

The color quality ranges indicate the limitations and tolerances of such filters. As shown in Figure 1.11(c), the R filter seems to be relatively consistent, while the B filter diameter has a tolerance of less than 5 nm. In contrast, the G filter seems to be more tolerant to the variation in diameter but is strongly influenced by the change of period. The color quality dependence on the period can be related to the density change and the near-field coupling of the neighboring nanostructures. The saturation of the structural

colors and the color quality tend to increase with the density of nanostructures; however, for a very small spacing between the nanostructures, e.g., a gap smaller than 100 nm, the color quality Q_ξ drops. Such a drop is directly related to the coupling between the neighboring nanostructures. As the spectral positions of resonances depend on the size of the nanostructures [8, 13], tuning their lateral geometry allows to select particular non-transmissive wavelengths throughout the full spectral range of the visible light, enabling the creation of the transmissive colors required for the RGB color filter arrays. The calculated and measured spectra of the optimal RGB filters, denoted by circles in Figure 1.11, are plotted in Figure 1.12(a). Experiment and simulation have an excellent quantitative agreement. The small mismatches can be attributed to the fabrication errors and the formation of a Si oxide outer-layer [47]. The mode decomposition of the respective structures highlights the spectral positions of fundamental ED and MD resonance; see Figure 1.12(b). They are distinguishable at the minima of transmission functions.

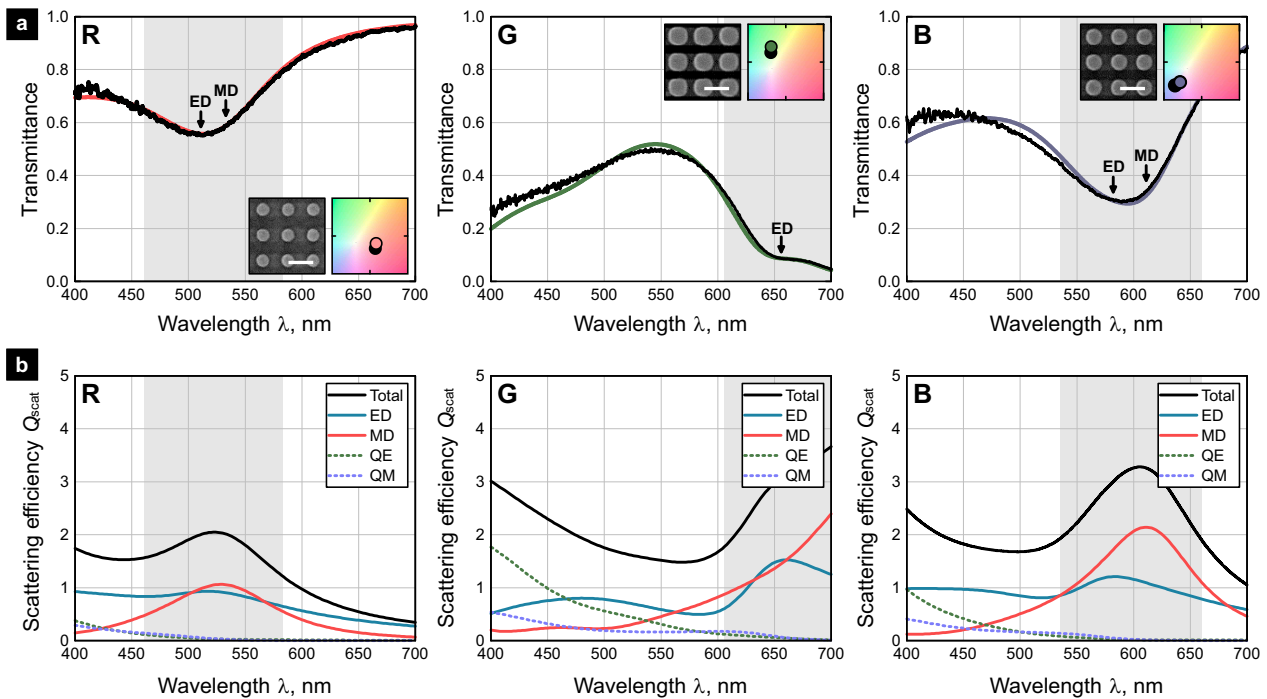


Figure 1.12: Optimized RGB spectral functions based on amorphous Si nanostructures. (a) Measured (black line) and simulated (colored line) transmission spectra of optimal nanostructures for red (left), green (middle), and blue (right) color. The grey-shaded areas depict the central positions of the ED and MD resonances. The insets show the SEM images of the corresponding Si nanostructures (scale bar – 250 nm) and the relative positions of the obtained colors in the chromaticity diagram. This part of the figure is adapted from [S4]. (b) Mode decomposition of the corresponding nanostructures for red (left), green (middle) and blue (right) color: total scattering, as well as ED, MD, EQ, and MQ contributions are indicated.

The maximum transmittance of the structures is approximately 90% for the R filter at $\lambda = 650$ nm, 50% for G at $\lambda = 550$ nm, and 60% for B at $\lambda = 450$ nm. The corresponding color quality values of the optimal filters are $Q_R = 0.74$, $Q_G = 0.59$, and $Q_B = 0.52$. In comparison, pigmented color filters can achieve slightly higher values: $Q_R = 0.94$, $Q_G = 0.82$, and $Q_B = 0.76$ [179]. However, considering the fabrication and scalability advantages of Si nanostructures as well as their insensitivity to strong illumination and non-degradation in case of ultraviolet light illumination, they are a viable alternative to the established color filter technologies. Some of the key specifications will be discussed next.

1.2.5 Specifications

1.2.5.1 Angle tolerance

One of the main limitations of Mie-resonant planar nanostructures, or planar nanostructures in general, is the dependence on the incident angle. The transmission spectra of the optimized RGB filters were calculated for the incidence angle θ up to 45° , see Figure 1.13(a). While only small changes are observed for the R filter, the transmission spectra of the other two other filters, G and B, change significantly: a new maximum appears while an existing minimum vanishes. Such changes are due to the angle-dependent excitation cross-section of ED and MD resonances, their spectral shift and separation enabled by the nanostructure coupling [99], as well as the excitation of higher-order modes in the spectral range of interest.

Even though incident light does not scatter into higher diffraction orders for normal incidence, this becomes apparent at oblique incidence. The spectral position of the first diffraction order scales with the angle of incidence according to the following relation:

$$\lambda_d = (n + \sin \theta) \times P, \quad (1.39)$$

where n is the refractive index of the surrounding medium. To analyze the influence on the color quality Q_ξ , it is calculated at different angles and plotted in Figure 1.13(b) for R, G, and B, respectively. As expected, the color quality Q_ξ decreases with the increase of incident angle. However, up to an angle of 25° – a limit set by the B filter – color reconstruction can still be achieved, and all filters produce distinguishable target colors. For the G filter, the maximum incidence angle is 40° , and for the R filter, it is larger than 45° .

The results of filters illuminated by linearly polarized light coincide with the unpolarized illumination due to rotational symmetry; see [S4] for more information. In contrast to normal-incidence, the electric field distribution and electric field lines change inside the nanostructure because the nanostructures are of a relatively small height H . With the increase of the angle θ , the light impinges at the different-size nanostructure cross-sections.

It should be noted that conventional dye-based color filters are also angle-sensitive. Their performance relies on the wavelength-dependent absorption. Thus, the increase of the light path due to oblique incidence results in subsequently modified transmission spectra.

1.2.5.2 Spatial resolution

The filters, arranged as small pixels in Bayer pattern [167], are analyzed to understand the effect of lateral pixel-size and the limit of spatial resolution. To study this numerically, a model of a backside-illuminated CMOS image sensor [180] is used. It is depicted in Figure 1.6(a). For simplicity, a perfect absorber [58, 181, 182] is emulated at the photodiode interface, neglecting reflection, and interference effects. Such a condition means that the light, which passes the filter array, is fully absorbed by the photodiode. The optimum parameters determined earlier (see Section 1.2.3.2) are used for the nanostructures within the RGB pixels. The spacer layer ($n_s = 1.46$) between the filters and the photodiode is set to a thickness of $0.1 \mu\text{m}$.

The lateral pixel size was decreased from $4 \mu\text{m}$, equal to 16 periods of the nanostructure array, down

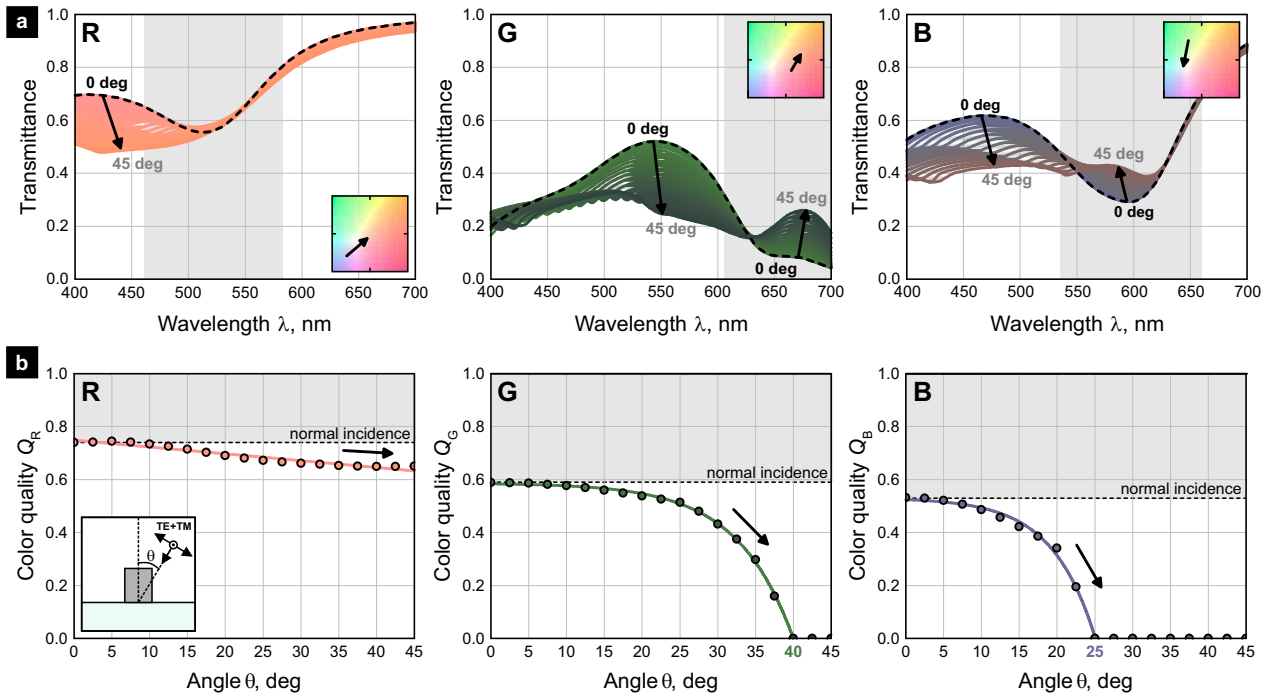


Figure 1.13: Angle tolerance analysis of optimized dielectric nanostructure-based RGB filters. (a) The transmittance of red (left), green (middle), and blue (right) filters and their change by the increase of the angle of incidence. The arrows highlight the transition from 0° (black dashed line) to 45° in the incidence angle. The colors of the lines correspond to the transmitted colors. The chromaticity change is depicted in the chromaticity diagrams shown in the insets. The filters are illuminated by unpolarized light. (b) Color quality Q_ξ change for red (left), green (middle), and blue (right) filters, compared to the normal incidence case (dashed line). The figure is adapted from [S4].

to $0.25 \mu\text{m}$, equivalent to a single period. Figure 1.14(a) shows how the transmission changes with the change of pixel size. For each wavelength, all four color pixels are illuminated. The transmission of each pixel is defined by a fraction of the total incident power of light. It is noticed that additional features arise in the spectra with the decrease of the pixel size. The most significant change can be seen when working at the submicrometer scale. This change is related to the scattering from the neighboring filters. The newly developed spectral dips can be assigned to a particular neighboring filter by comparing the positions of the fundamental ED and MD resonances of the corresponding nanostructures. These resonances were shown in the transmission spectra of semi-infinite arrays; see Figure 1.6(d). For reference, their spectral positions are indicated in Figure 1.14(a) by the colored bars above the spectra. Furthermore, one can see an increase in transmission at the position of the primary resonances. Thus, it can be concluded that the effectiveness of the filters gradually decreases with their size. In addition to the scattering, a sharp feature appears at $\lambda_w = 516 \text{ nm}$ for $0.25 \mu\text{m}$ pixel size, corresponding to the first order Wood anomaly [183, 184] from the periodicity of the Bayer pattern. The change of spectra results in a subsequent change in colors. In Figure 1.14(b), the color quality is plotted for the R, G, and B filters versus the filter size. For $4 \mu\text{m}$ filter size, the calculated values are equal to the ones obtained in the case of infinite arrays: $Q_R = 0.74$, $Q_G = 0.59$, and $Q_B = 0.52$. For $0.5 \mu\text{m}$ filters retain positive values of $Q_R = 0.74$, $Q_G = 0.39$, and $Q_B = 0.36$, meaning that the indexed colors could still be successfully discriminated. Hence, the analysis predicts that submicrometer color filters of $0.5 \mu\text{m}$ size, corresponding to just 2×2 nanostructures, would be applicable. Unfortunately, with the selected R, G, and B unit cells, going below $0.5 \mu\text{m}$ size is complicated due to the

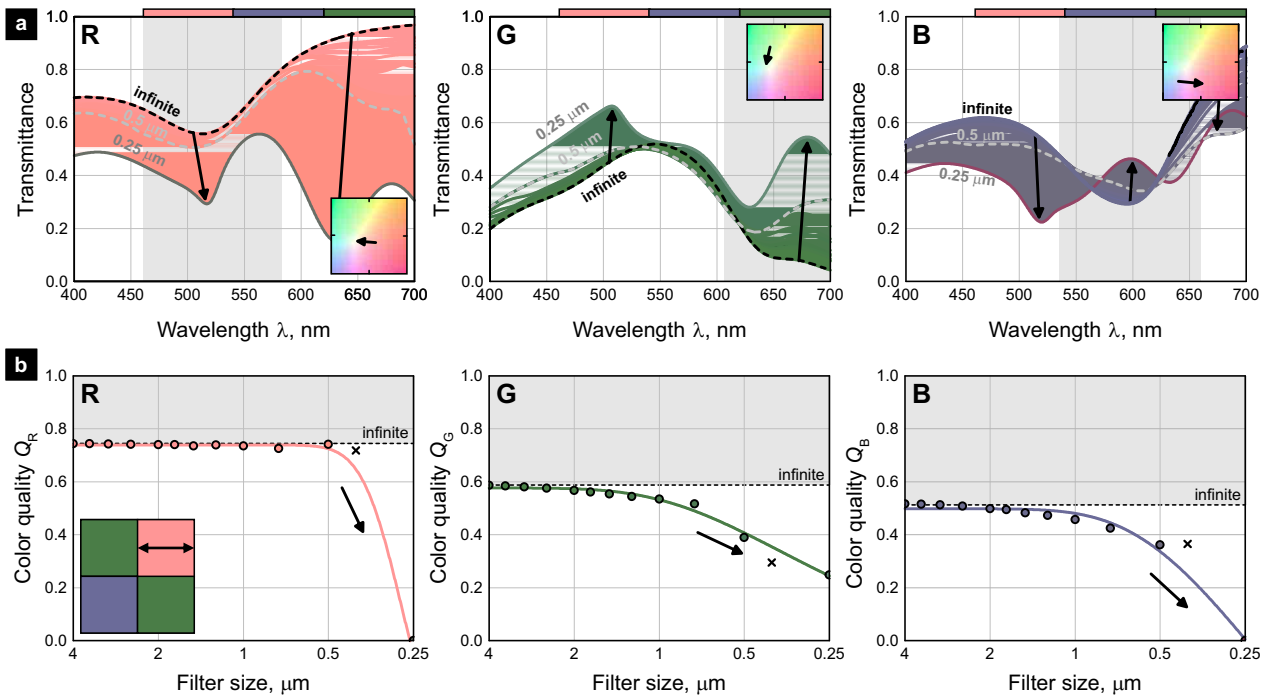


Figure 1.14: RGB filter array spectral response and crosstalk analysis based on color quality Q_ξ . (a) Transmission of red (left), green (middle), and blue (right) filters, measured $0.1 \mu\text{m}$ below of all three color filters. Arrows and the color coordinate change in the CIE chromaticity diagram in the insets show the spectral change by decreasing the pixel size. The infinite array case is highlighted by the black dashed line. The grey dashed line depicts the transmission functions of the $0.5 \mu\text{m}$ filters. Colored tabs show approximate positions of resonances from neighboring filters. (b) Color quality Q_ξ dependence on the pixel size for red (left), green (middle), and blue (right) filters, keeping the initial geometrical parameter. A cross depicts the color quality of $0.4 \mu\text{m}$ filters with tuned transversal parameters. The figure is adapted from [S4].

light diffraction and coupling. In correspondence to the spectral analysis, color qualities for $0.25 \mu\text{m}$ filter size drop significantly, with R and B diminishing to zero, meaning that the targeted colors are no longer distinguishable.

For experimental verification of numerical predictions, color filter arrays are fabricated in Bayer pattern, consisting of two G, one R, and one B pixels each. The same pattern was repeated by reducing the size of the filters from $4 \mu\text{m}$ by a factor of two until a color pixel of the single nanostructure is reached, resulting in the pixel sizes of $4, 2, 1, 0.5,$ and $0.25 \mu\text{m}$. The transmissive white-light microscope images, taken with a high numerical aperture ($\text{NA} = 0.9$) objective, are shown in Figure 1.15(a), together with SEM images of the structures in Figure 1.15(b). It is visible that the R, G, and B colors can be discriminated for the pixels down to $0.5 \mu\text{m}$ in size, which confirms the numerical results. For $0.25 \mu\text{m}$ pixel size, the different filters cannot be coupled to the far-field due to the diffraction limit [185], and no conclusions on the colors can be drawn.

According to the diffraction theory, the smallest resolvable object size is $\lambda/(2\sin\theta)$. If one selects a typical wavelength of the red color, $\lambda \approx 630 \text{ nm}$, this results in a resolvable pixel size of $0.315 \mu\text{m}$ or more and $0.350 \mu\text{m}$ if the $\text{NA} = 0.9$ objective is used. However, to discuss the effects appearing when integrating the proposed filters with CMOS sensors, the collection angle of the individual detectors is the limiting factor. In our setup, the resolvable size also depends on the periodicity and the spacer between pixel and

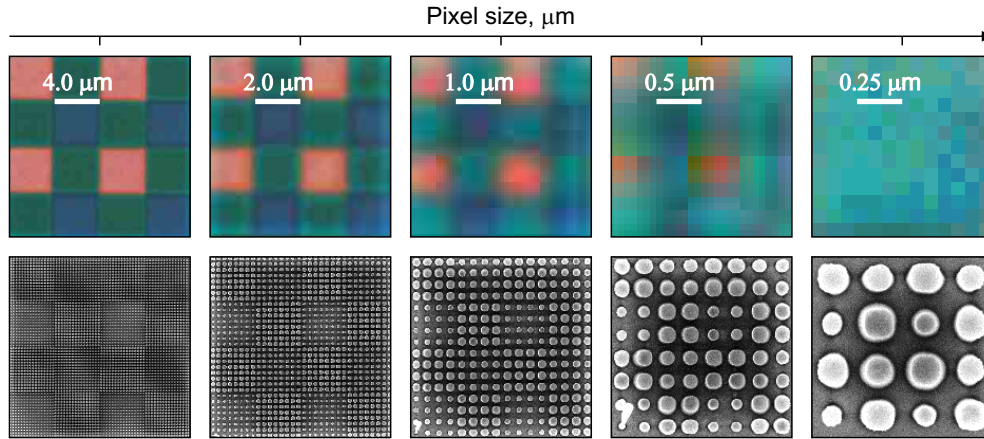


Figure 1.15: Downscaling of RGB color filters assembled in Bayer pattern. Optical microscope images of the 4, 2, 1, 0.5, and 0.25 μm filters (top); imaged with 100 \times (NA = 0.9) objective. The scale bars are shown in the microscope images. SEM images of the filters (bottom), same scales as in (a) are maintained. The figure is adapted from [S4].

detector. Potentially, it can be reduced by reducing the thickness of the spacer, but if 0.1 μm spacer is used, the collection angle $\theta \approx 51^\circ$ results in a minimal resolvable pixel size of 0.403 μm , which is close to the demonstrated RGB color filters using Si nanostructures.

Finally, to understand the potential of further miniaturization, a filter with a size smaller than 0.5 μm was found numerically possible by a denser distribution of the 2×2 nanostructures. Transversal geometry re-optimization results in a decrease of the period for all filters, from 250 to 200 nm, and a slight change in diameter of nanostructures composing G filters, from 150 to 160 nm. As shown by the crosses in Figure 1.14(b), a positive color quality for all of the RGB colors can be produced using 0.4 μm nanostructure-based filters.

1.3 Chapter summary

In summary, submicrometer dielectric nanostructure-based RGB filters were successfully demonstrated both numerically and experimentally. The fundamental ED and MD resonances of nanostructures were tuned using their diameter and height, as well as metasurface period. The spectral position of ED resonances was shown to be most sensitive to changing the diameter, MD resonances – the height of nanostructures. However, even if the height is fixed, the diameter still allows tuning the resonances throughout the visible spectral range.

A step-by-step optimization of metasurface elements was carried out to realize RGB color filter array. For this reason, a figure of merit – color quality – was introduced. Although amorphous Si is not ideal for such filters due to the broadband absorption losses limiting the maximum transmission in the short wavelength range, the realized filters show colors comparable to conventional filters. They also potentially provide many advantageous properties, e.g., robustness against high-intensity illumination and a well-developed CMOS-compatible fabrication process. Considering the experimentally achieved state-of-the-art 0.5 μm filters and their potential to be reduced even further by improving fabrication techniques, Mie-resonant nanostructures present an intriguing opportunity for increasing the digital imaging resolution.

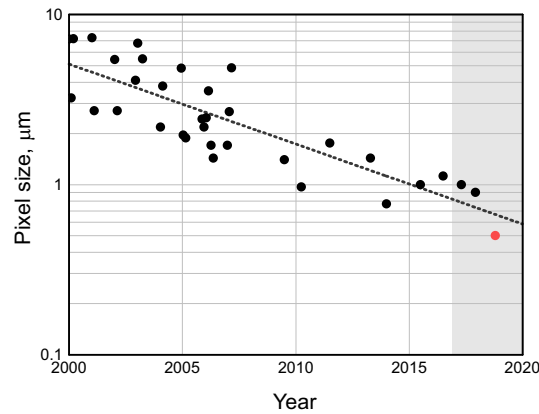


Figure 1.16: The RGB pixel size evolution in the last two decades and the position of the obtained $0.5 \mu\text{m}$ spectral filters. The adapted data points shown in black dots till the date of thesis submission, only filters arranged in color filter arrays are considered [20, 35, 40, 55–57, 59–61]. The black dashed line represent a linear fit of the dots. The red dot highlights the current result of $0.5 \mu\text{m}$ spectral filters. The grey area depicts the period of doctoral studies. The figure is adapted from [S4].

It should be noted that the successfully obtained $0.5 \mu\text{m}$ filters are significantly smaller than the previously reported color filters set in color filter arrays; see Figure 1.16, where our structures are compared to results of the last two decades [20, 35, 40, 55–57, 59–61]. Different types of Si, such as c-Si, a-Si, and a-Si:H [S2], as well as other high-index materials, such as TiO_2 and GaP [43], could further improve the nanostructured filters, increasing the transmitted color quality and, subsequently, improving the discrimination of RGB, CMY, and even multispectral colors.

The results on nanostructure-based transmissive color filters are published in Proc. SPIE [S2] and ACS Photonics [S4]. The knowledge on Mie resonators was used to create coupled Mie resonators for surface-enhanced Raman spectroscopy, published in Scientific Reports [S3] and Proc. SPIE [S7], but not included in the thesis. Furthermore, the numerical experience contributed to a project on scanning near-field optical microscope (SNOM), resulting in several publications in CLEO proc. [S5] and Rev. Sci. Instrum. [S6]. Another publication [S12] is in preparation at the moment of writing this work.

Chapter 2

Nanostructure-modulated Fabry–Pérot resonators

The Mie resonators, used as color filters in Chapter 1, can be used in other spectral ranges, but they do not provide a high spectral selectivity, which is desired for the multispectral imaging [186]. This implies a need for another optically resonant system. Accordingly, the spotlight of Chapter 2 is on a well known optically resonant high-quality system – a Fabry–Pérot (FP) resonator. Proposed more than a century ago [187], FP resonators have found their way into numerous applications in microwave [188] and optical technologies [189].

This chapter introduces the essential properties, definitions, and physics of the FP resonators. First, the reader will be taken through the basics, including the effective medium theory, and introduced to different ways of using high-index dielectric nanostructures inside the FP resonator to tailor its spectral response. The second part is an applicability-study of FP resonators for biomedical sensing. The basic configuration of the FP filters with silver (Ag) mirrors are used to obtain a simple, low-cost, and ultra-thin multispectral platform, which is optimized for remote blood-oxygen sensing in the visible and near-infrared spectral ranges. The pixelated FP filter arrays are experimentally realized and integrated on a CMOS sensor. Furthermore, to further carry the physics, the final part of this chapter presents a study on spectropolarimetry. Polarization-sensitive high-index nanostructures and DBRs are used to design and experimentally demonstrate a 7- μm -thick spectropolarimetric system for three spectral bands and two linear polarization states. The spectropolarimetric system enables the applicability in a variety of miniaturized optical devices, including but not limited to satellites for Earth observation.

The results on polarization-insensitive FP filters with Ag mirrors and TiO_2 nanostructures, presented in Section 2.2, are in the process to be published at the time of thesis writing [S11]. The concept of spectropolarimeter with DBRs and embedded polarization-sensitive Si nanostructures, presented in Section 2.3, is patented [T1] and published in Optics Express [S9].

2.1 General properties

2.1.1 Properties of Fabry–Pérot resonators

A typical FP resonator consists of two mirrors separated by a medium with an optical length L , as illustrated in Figure 2.1(a). For convenience, it is assumed that both mirrors are planar, and their reflectivities are equal, $R = R_1 = R_2$, while the losses generated by scattering and absorption are negligible. Then the FP resonator provides a Lorentzian-shaped transmission peak, centered at the wavelength λ_0 , as shown in Figure 2.1(b), for which the following condition holds [189]:

$$\lambda_0 = \frac{2L}{q}, \quad (2.1)$$

where q is an integer number, representing the order of the resonant mode.

Ideally, the transmission exhibits a periodic sequence of the peaks. The central wavelengths of the peaks λ_0 can be tailored by the optical distance between the mirrors $L = L_0 n_{\text{eff}}$, which relies on the geometrical length (distance) L_0 and the effective refractive index of the medium n_{eff} ; see further discussion on tailoring of the FP resonances in Section 2.1.3.

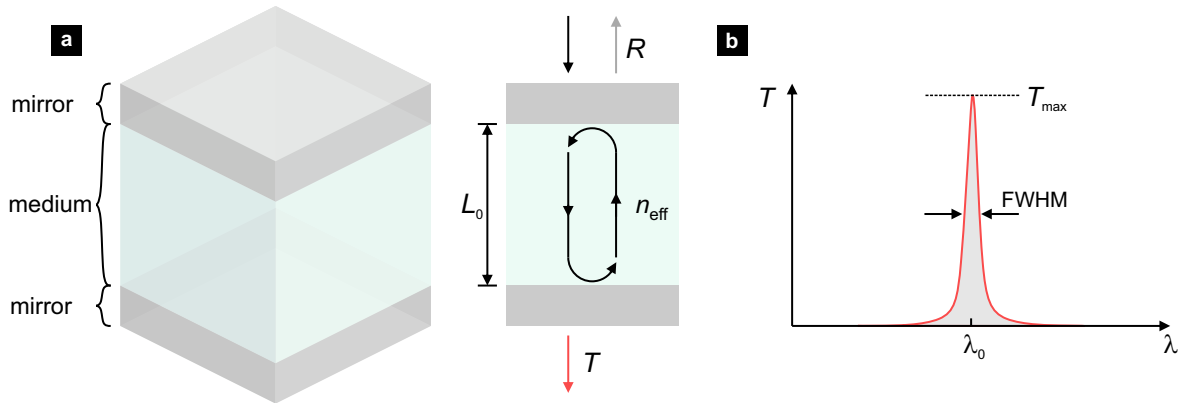


Figure 2.1: Schematic illustration. (a) FP resonator constituted of mirrors with reflectivity $R = R_1 = R_2$ spaced by a medium with optical length $L = L_0 n_{\text{eff}}$. Part of incident light is reflected by the first mirror, while the other part goes through, resonates between the mirrors, and is transmitted if the resonant condition is met. (b) Spectral resonance with highlighted properties such as the maximum transmittance T_{max} , the bandwidth (FWHM), and the central wavelength λ_0 . The figure is partially adapted from [S9].

In practice, using real mirrors, e.g., Ag mirrors, extra phase shifts induced by mirrors have to be accounted for [190]. Accordingly, Equation 2.1 is modified to the following expression:

$$\lambda_0 = \frac{2L}{q - \frac{\varphi_1 + \varphi_2}{2}}, \quad (2.2)$$

where φ_1 and φ_2 are the extra phase from the top and the bottom Ag mirrors, respectively; with $\varphi_1 = \varphi_2$, if identical mirrors are used. The beam propagation inside the resonator can be described by means of geometrical optics. Also, now, the losses generated by scattering and absorption of the mirror may be

incorporated into the resonator model by placing a medium with a loss factor V between the mirrors. The loss factor represents the fraction of incident light intensity that is transmitted by the medium.

If monochromatic light with wavelength λ , and intensity I_0 (electric field E_0) is incident on a FP resonator, it will be partially reflected by the first mirror, while the rest will propagate into the resonator. There the light gets reflected back and forth between the two mirrors, each time partially coupling out of the FP resonator in both, the forward and the backward, directions. Summation of all waves coupled out yields the transmission T and the reflectance R of the FP resonator. If r_1 and r_2 denote the reflection coefficients, and t_1 and t_2 are the corresponding transmission coefficients of the two mirrors, the reflected field E_r and the transmitted field E_t are expressed by the following equations [190]:

$$E_r = E_0 \left[r_1 - t_1^2 v^2 r_2 \exp[i2kL] \sum_{n=0}^{\infty} (v^2 r_1 r_2 \exp[i2kL])^n \right], \quad (2.3)$$

$$E_t = -E_0 t_1 t_2 v \exp[ikL] \sum_{n=0}^{\infty} (v^2 r_1 r_2 \exp[i2kL])^n. \quad (2.4)$$

By calculating the intensities from Equation 2.3 and Equation 2.4, the fraction of the incident intensity I_0 being transmitted and reflected by the FP resonator is determined as:

$$R = \frac{(\sqrt{R_1} - \sqrt{R_2}V)^2 + 4\sqrt{R_1 R_2}V \sin^2(kL)}{(1 - \sqrt{R_1 R_2}V)^2 + 4\sqrt{R_1 R_2}V \sin^2(kL)}, \quad (2.5)$$

$$T = \frac{(1 - R_1)(1 - R_2)V}{(1 - \sqrt{R_1 R_2}V)^2 + 4\sqrt{R_1 R_2}V \sin^2(kL)}, \quad (2.6)$$

where $R_i = |r_i|^2$ is the reflectivity of mirror, $V = |v|^2$ is the loss factor per transit (v is the amplitude loss factor), and $k = 2\pi/\lambda$ is the wavenumber. Accordingly, the maximum transmission (amplitude at λ_0) is given by:

$$T_{\max} = \begin{cases} 1, & \text{if } R_1 = R_2, V = 1, \\ \frac{(1 - R_1)(1 - R_2)V}{(1 - \sqrt{R_1 R_2}V)^2}, & \text{otherwise.} \end{cases} \quad (2.7)$$

Another important aspect of the filters based on the FP resonators is the full width at half maximum (FWHM) of the transmission peaks, which directly relates to the spectral resolution of the system. Following the assumption that both mirrors have the same reflectivity R , the FWHM is expressed by the following equation [191]:

$$\text{FWHM} = \frac{\lambda(1 - R)}{q\pi\sqrt{R}}. \quad (2.8)$$

Thus, the higher the reflectivity of the mirrors, the higher the spectral resolution. Accordingly, an important characteristic of all resonant systems is defined - the so-called quality factor Q :

$$Q = \frac{\text{FWHM}}{\lambda_0}. \quad (2.9)$$

All definitions presented will be further used in the following sections.

2.1.2 Effective medium theory

The tailoring of FP resonators in this chapter is largely based on changing the effective refractive index of the medium. This is done by adding high refractive index nanostructures into a lower index medium of the resonator; thus, changing the effective refractive index of the medium. The effective index calculation is not as simple as it seems, as simple geometric averaging does not provide accurate results. Thus, different effective medium theories were developed [192, 193]. The idea of the effective medium theory is to represent a system of different materials as a homogeneous structure, described by a particular dielectric function. The most known effective medium approximations are Maxwell Garnett [194] and Bruggeman [195]. They are introduced in Section 2.1.2.1 and Section 2.1.2.2, respectively. Other notable effective medium theories are Looyenga [196], Monecke [197], and aggregate equivalent [198, 199].

2.1.2.1 Maxwell Garnett approximation

One of the most famous effective medium approximations is the Maxwell Garnett approximation [194]. The derivation of the Maxwell Garnett approximation starts from the concept of Lorentz field. The assumption is that the local field \mathbf{E}_{loc} experienced by a molecule is not the macroscopically averaged field. To evaluate this field, a sphere, which is macroscopically small but microscopically large, is defined around the molecule. The local field \mathbf{E}_{loc} is then expressed as [192]:

$$\mathbf{E}_{\text{loc}} = \mathbf{E}_0 + \mathbf{E}_d + \mathbf{E}_s + \mathbf{E}_{\text{near}}, \quad (2.10)$$

where \mathbf{E}_0 is the external field, \mathbf{E}_d is the depolarization field due to the bound charges on the outer surface of the dielectric medium, \mathbf{E}_s is the field due to bound charges on the surface of the sphere, and \mathbf{E}_{near} is due to the configuration of nearby molecules. The external field \mathbf{E}_0 and its resulting depolarization field \mathbf{E}_d are equal to the macroscopic field \mathbf{E} , the spherical polarization field can be rewritten as $\mathbf{E}_s = (4\pi/3)\mathbf{P}$, while the contribution of \mathbf{E}_{near} vanishes in the cubic symmetry [200]. Thus, the final expression of the local field \mathbf{E}_{loc} simplifies to:

$$\mathbf{E}_{\text{loc}} = \mathbf{E} + \frac{4\pi}{3}\mathbf{P}, \quad (2.11)$$

which is the so called Lorentz local field relation. It is used to obtain the Clausius–Mossotti relation [201], which relates a macroscopic property with a microscopic property, e.g., the dielectric constant ϵ with the molecular polarizability α . Its proof consists of identifying the connection between the dipole moment of the molecule with the local field \mathbf{E}_{loc} via the molecular polarizability α . Then, the Lorentz field relation is used to derive the macroscopic polarization \mathbf{P} and hence the susceptibility χ in terms of polarizability α . The dipole moment of a molecule \mathbf{p} is given by:

$$\mathbf{p} = \alpha\mathbf{E}_{\text{loc}}, \quad (2.12)$$

where α is the polarizability. Then, using Equation 2.11 the polarization \mathbf{P} is expressed as:

$$\mathbf{P} = \sum_j N_j \mathbf{p}_j = \sum_j N_j \alpha_j \mathbf{E}_{\text{loc}}(j) = \sum_j N_j \alpha_j \left(\mathbf{E} + \frac{4\pi}{3} \mathbf{P} \right). \quad (2.13)$$

The sum is over all molecules j , whose polarizabilities α_j are with the local field $\mathbf{E}_{\text{loc}}(j)$ at that site, and N_j is the number of molecules per unit volume, assuming that the local field is identical for all sites. Next, the dielectric susceptibility is expressed as:

$$\chi = \frac{\mathbf{P}}{\mathbf{E}} = \frac{\sum_j N_j \alpha_j}{1 - \frac{4\pi}{3} \sum_j N_j \alpha_j}. \quad (2.14)$$

The Clausius–Mossotti relation is written in terms of dielectric constant $\varepsilon = 1 + 4\pi\chi$. It is obtained by rearranging Equation 2.14 [201]:

$$\frac{\varepsilon - 1}{\varepsilon + 2} = \frac{4\pi}{3} \sum_j N_j \alpha_j, \quad (2.15)$$

which directly shows the relation between the macroscopic ε and the microscopic α_j , and is a key relation for the approximations of the effective medium theory.

It is assumed that a microscopic polarizability α for a spherical inclusion with dielectric constant ε_i and radius a is expressed as [200]:

$$\alpha = \left(\frac{\varepsilon_i - 1}{\varepsilon_i + 2} \right) a^3. \quad (2.16)$$

If Equation 2.16 and the Clausius–Mossotti relation, Equation 2.15, is combined, one obtains:

$$\left(\frac{\varepsilon_{\text{eff}} - 1}{\varepsilon_{\text{eff}} + 2} \right) = f \left(\frac{\varepsilon_i - 1}{\varepsilon_i + 2} \right), \quad (2.17)$$

where ε_{eff} is the effective dielectric constant of the medium, ε_i is the dielectric constant of the inclusions, and f is the volume fraction of the inclusions [192]. Finally, the Maxwell Garnett formula can be rewritten for a host medium of dielectric constant ε_m with inclusions of dielectric constant ε_i :

$$\left(\frac{\varepsilon_{\text{eff}} - \varepsilon_m}{\varepsilon_{\text{eff}} + 2\varepsilon_m} \right) = f \left(\frac{\varepsilon_i - \varepsilon_m}{\varepsilon_i + 2\varepsilon_m} \right). \quad (2.18)$$

Solving for the effective dielectric constant ε_{eff} leads us to [193]:

$$\varepsilon_{\text{eff}} = \varepsilon_m \frac{\varepsilon_i + 2\varepsilon_m + 2f(\varepsilon_i - \varepsilon_m)}{\varepsilon_i + 2\varepsilon_m - f(\varepsilon_i - \varepsilon_m)}. \quad (2.19)$$

2.1.2.2 Bruggeman approximation

Another famous effective medium theory was derived by Bruggeman [195]. Here, a binary system with fraction f of dielectric constant ε_i and $(f - 1)$ of dielectric constant ε_m is considered, as before. Brugge-

man's greatest contribution is the hypothesis that the average flux deviation should be zero:

$$f\Delta\Phi_i + (f-1)\Delta\Phi_m = 0. \quad (2.20)$$

Here the flux deviation $\Delta\Phi_i$ is given by the following expression:

$$\Delta\Phi_i = 2\pi \left(\int_0^a dr \varepsilon_i E_{\text{inside}} - \int_0^a dr \varepsilon_i E_0 \right) = 2\pi a^2 \varepsilon_{\text{eff}} E_0 \left(\frac{\varepsilon_i - \varepsilon_{\text{eff}}}{\varepsilon_i + 2\varepsilon_{\text{eff}}} \right), \quad (2.21)$$

where r is the coordinate unit in spherical system, E_0 and E_{inside} are the fields far from the particle and inside of it, respectively, and a is the radius of the particle. Accordingly, for a single particle (inclusion) the following formula is obtained:

$$f \left(\frac{\varepsilon_i - \varepsilon_{\text{eff}}}{\varepsilon_i + 2\varepsilon_{\text{eff}}} \right) + (f-1) \left(\frac{\varepsilon_m - \varepsilon_{\text{eff}}}{\varepsilon_m + 2\varepsilon_{\text{eff}}} \right). \quad (2.22)$$

A detailed derivation is provided in [192]. Using the Bruggeman formula, one can also solve for the effective dielectric constant ε_{eff} :

$$\varepsilon_{\text{eff}} = \frac{1}{4} \left(\beta + \sqrt{\beta^2 + 8\varepsilon_i \varepsilon_m} \right), \quad (2.23)$$

where $\beta = (3f-1)\varepsilon_i + (3(1-f)-1)\varepsilon_m$ for a medium constituted of two different materials with corresponding dielectric constants, ε_m and ε_i .

In the case of the presented effective medium theories, a certain size and filling factor limitations have to be considered, e.g., the presented Bruggeman approximation holds for spherical inclusions only up to $f = 1/3$ [192], and similar limitations are found for Maxwell Garnett approximation [193, 202]. For larger or more complex-shaped inclusions, Maxwell Garnett and Bruggeman effective medium theories cease to work. They can still be used for a rough estimation of the effective refractive index, which is expressed as:

$$n_{\text{eff}} = \sqrt{\varepsilon_{\text{eff}}}. \quad (2.24)$$

However, more sophisticated models have to be used for accurate results, especially when the optical size becomes comparable to the wavelength of irradiation, and nanostructures start to resonate [10]. The validity of the effective medium theories will be tested in Section 2.3.2.

2.1.3 Tailoring of effective refractive index

The most common approach to tailor the FP resonances is to change the physical length of the resonator L_0 [84–86]. However, it has been also demonstrated that inclusions, such as arrays of high-index nanostructures, might be used to modulate the effective index n_{eff} and, subsequently, the optical thickness of the resonator [87]. Here, different ways of tailoring FP resonators with high-index dielectric nanostructures will be introduced.

The FP resonator provides a Lorentzian-shaped peak in transmission, centered at the wavelength λ_0 , as introduced in Section 2.1.1 and shown in Figure 2.2(a). The inclusion of high-index nanostructures

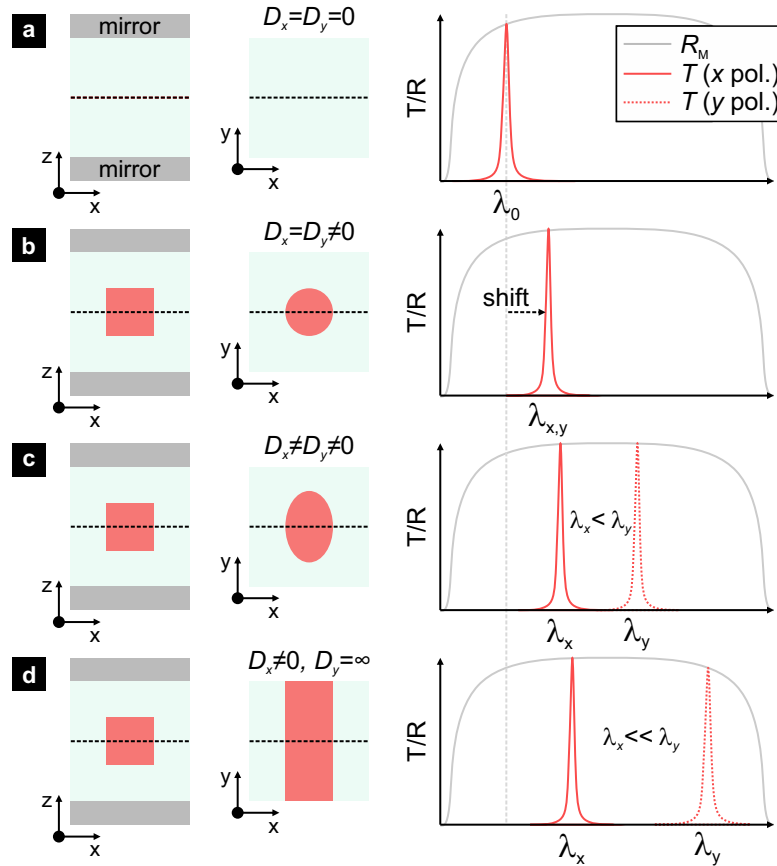


Figure 2.2: Tailoring of FP resonators by high-index nanostructures: (a) empty resonator (without inclusion) producing a single peak at the spectral range of interest; (b) resonator modulated by polarization-insensitive nanostructure, producing a single red-shifted peak; (c) resonator modulated by polarization-sensitive nanostructure, two different peaks at λ_x and λ_y ($\lambda_x < \lambda_y$) for two linear polarization states; (d) resonator modulated by grating, two different peaks at λ_x and λ_y ($\lambda_x \ll \lambda_y$) for two linear polarization states, x and y , respectively. The transmittance of x -polarized light is depicted by the red solid line, the transmittance of y -polarized – the red dashed line, the reflectivity of mirrors – the grey line. The figure is adapted from [S9].

increases the effective refractive index n_{eff} ; see Section 2.1.2. Such an inclusion adds a phase shift to the resonator and a subsequent red-shift of the resonant peak, see Figure 2.2(b). Furthermore, suppose the diameter in one axis D_x of the nanostructures is chosen differently than the diameter in another D_y . In that case, the resonator will produce two different transmission peaks for two orthogonal linear polarization states: one corresponding to a case where the electric field of the incident light aligns with the width of the nanostructure (x -polarized light), the other - when the field aligns with the length of the nanostructure (y -polarized light) [T1], as shown in Figure 2.2(c,d).

The spectral distance between the peaks can be controlled by altering the aspect ratio D_x/D_y of the nanostructures. The most significant spectral separation of the peaks is achieved by a linear grating, as in Figure 2.2(d), since it has an infinite aspect ratio. In any case, it is essential that the optical size of the nanostructures is significantly smaller than the wavelength of operation ($nD_{x,y} < \lambda$). As described in Section 2.1.2, then, the dielectric nanostructures are expected to be non-resonant, and the modulation of the resonator is based only on the change of the effective refractive index [192]. Also, the period of the

nanostructure array should be sub-wavelength to avoid the diffraction of light.

Next, the FP resonances and tailoring of them using high-index dielectric nanostructures will be employed for specific functionalities in spectral imaging and spectropolarimetry.

2.2 Spectral filters for blood oxygen sensing

Spectral imaging is applied in various applications as the spectral information provides details on the material composition. Such information is useful in assessing food quality, artwork authentication, and many other applications [68, 69]. Slowly but steadily, the multispectral imaging is also finding its place in the field of biomedicine [93].

Oxygen is vital to our bodies. Low oxygen levels in our blood may indicate heart conditions such as heart defects, lung conditions such as asthma, emphysema, or bronchitis, sleep apnea, inflammation, and scarring of the lung tissue [94]. Thus, it is essential to monitor the level of oxygen transported by blood throughout our bodies. The first spectrophotometric analysis of oxygen saturation in tissue was presented more than half a century ago [203]. A few years later, the methodology was implemented in a device [204], which was called oximeter [205]. Since then, it has endured extensive development to what is now known as a pulse oximeter [206, 207]. A typical oximeter uses two light-emitting diodes for illumination and a photodiode to detect the light reflected from a test subject. One of the light-emitting diodes emits red light, the other – near-infrared light. Absorption of light at these particular spectral ranges differs significantly between the blood with oxygen and the blood lacking it. The oximeters were usually fixed to a fingertip or an earlobe but have been recently also built-in smartwatches [208]. Moreover, it has been demonstrated that identification of oxygen level can be made remotely using ambient light and capturing its reflected part by a set of cameras with dedicated filters [209, 210].

In order to build a compact optical system for remote sensing, nanostructure-based filters are analyzed. The filters are used in array configuration with the potential to detect the signals from multiple spectral ranges on a single CMOS sensor. To some extent, the previously introduced Mie-resonant metasurfaces could be extended to the near-infrared spectral range. However, such biomedical applications would benefit from a high signal-to-noise (SNR) ratio. Thus, alternative optically resonant systems – FP resonators – are investigated. In this section, a design of nanostructured multispectral FP filters is demonstrated. They will be optimized towards blood-oxygen sensing, and their performance will be analyzed in terms of spectral resolution, spatial resolution, and other crucial parameters.

2.2.1 Concept

The protein inside red blood cells that bounds to oxygen is called hemoglobin (Hb). If the hemoglobin molecule is bound to oxygen, it is called oxy-hemoglobin (HbO₂). Accordingly, the saturation of oxygen is expressed as follows [211]:

$$S_{O_2} = \frac{C_{HbO_2}}{C_{Hb} + C_{HbO_2}}, \quad (2.25)$$

where C_{Hb} and C_{HbO_2} are the concentrations of Hb and HbO₂, respectively. Hb and HbO₂ have different wavelength-dependent absorption [212]. The molar extinction coefficient as a function of wavelength for both, Hb and HbO₂, are shown in Figure 2.3. There are at least five spectral ranges, where one can identify a high difference between the spectra. At the beginning of oximetry, it was quite difficult to isolate those spectral ranges [205], but because of highly improved light sources and/or spectral filters, it became feasible.

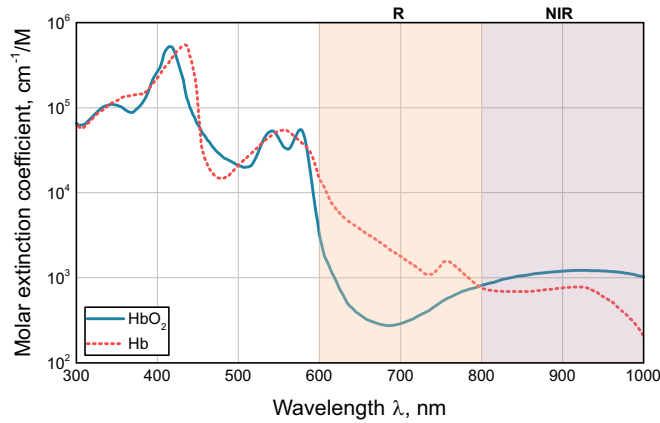


Figure 2.3: Molar extinction coefficient of Hb and HbO₂ as a function of wavelength. Two spectral ranges of interest are indicated: from 600 nm to 800 nm (R band; see sand color area), and from 800 nm to 1000 nm (NIR band; see violet area). The spectra are adapted from [212].

Initially, oximeters used one spectral range around red light for oxygen saturation measurement and another around green light, which is at a relatively neutral position, to designate the total density of blood [205]. Later, the irradiation of the second source was moved further to the near-infrared [211, 213]. As can be seen in Figure 2.3, the extinction of Hb is stronger in the spectral range from 600 to 800 nm, and it is the other way around from 800 to 1000 nm. It can be also noticed that there is a number of spectral ranges below 600 nm, which seem to also fit the required difference between Hb and HbO₂, but the use of short wavelengths is limited by high absorption of melanin [214].

There have been a multiple demonstrations of multispectral imaging [215, 216] or even a single wavelength detection [217, 218], but using red and near-infrared spectral ranges have prevailed for measurement of the relative oxygen level. The following equation [213] governs the relation of oxygen saturation and the ratio of collected light at red (R) and near-infrared (NIR) wavelengths:

$$S_{\text{O}_2} = A + B \times (\alpha_{\text{R}}/\alpha_{\text{NIR}}), \quad (2.26)$$

where A and B are constants dependent on physiological characteristics of the sensor and blood, and α_{NIR} and α_{R} are the signals (intensities) of the reflected light collected at NIR and R spectral ranges, respectively.

In remote sensing using ambient light and spectral filters, the signals are attenuated by the transmission bands of those filters. Thus it is important to have spectral selectivity in the bands of interest but also sustain as high transmission as possible. In this section, the FP resonators will be optimized for R and NIR bands. The bandpass of the filters has to be broad enough to collect as much as possible light at the targeted spectral range, but also back-reflect the parasitic light, especially the light from the other band of interest. Next, the design considerations, optimization, fabrication steps, and estimates for spectral and spatial resolution will

be presented.

2.2.2 Methods

2.2.2.1 Numerical simulations

The design of FP filters for blood-oxygen sensing was created using the FDTD method (Lumerical). A 3D model of an infinite array of TiO₂ nanostructures in a FP resonator was emulated by a unit cell with PBC on the sides and PML on the top and the bottom of the simulation domain. An extremely fine mesh ($\Delta x < \lambda/100$) was used for the Ag mirrors to ensure converged results. The unit cell was illuminated by a normally-incident linearly-polarized plane-wave source. Frequency domain field and power monitors were used to record transmittance and reflectance of the cavity.

2.2.2.2 Sample Fabrication

The fabrication was carried out in the following steps: the deposition of the bottom mirror, the formation of the alignment markers, the nanostructuring and the formation of the cavity, and the deposition of the top mirror.

First, a 30 nm Ag layer was deposited on a glass wafer by electron beam evaporation (Vacom V700, custom-made). The sample was immediately transported to the ion-beam machine (Oxford Ionfab 300, Oxford Instruments), where 10 nm of Ag was etched to remove the potentially oxidized layer, and 15 nm of Al₂O₃ was deposited. Before structuring the cavity, alignment markers have to be created for the bonding procedure, described in Section 2.2.6. For this reason, a resist (EN038, Tokyo Ohka Kogyo) was spin-coated, which was then patterned by electron beam (Vistec SB 350, Vistec Electron Beam) and developed for 30 s at room temperature. The Al₂O₃ and Ag were etched with an ion beam (Oxford Ionfab 300, Oxford Instruments). Afterward, the resist was removed by 5 min exposure of oxygen plasma (Sentech SI-500 C, Sentech Instruments).

Then, the nanostructuring of the cavity was done by a lift-off technique. First, a two-layer resist (ARP617 and ARP6200) was spin-coated, exposed by electron beam (Vistec SB 350, Vistec Electron Beam), and developed for 30 s at room temperature. Then, the TiO₂ was deposited by electron beam evaporation without background pressure (Vacom V700, custom-made). Finally, the excess material was lifted-off in acetone. The height of the nanostructures was determined to be equal to 100 nm. After the nanostructuring, the nanostructures were covered with SiO₂ by atomic layer deposition (ALD). The desired thickness of the oxide layer was adjusted by back-etching. The sample was not planarized by a chemical–mechanical polishing process [92], but an additional layer of the resist was deposited to reduce the local waviness and roughness of the layer. The resist and SiO₂ were back-etched to 115 nm by ion beam etching (Oxford Ionfab 300, Oxford Instruments).

Finally, the top Ag mirror was deposited using the same steps as the bottom mirror. The sample was covered with a 100 nm SiO₂ layer to provide an effective hydrogen barrier for environmental sealing.

2.2.2.3 Characterization

The fabricated sample was visually inspected using a white-light optical microscope (Axio Imager 2, Carl Zeiss) with an installed 5-megapixel camera (AxioCam MRc 5, Carl Zeiss). The spectral analysis was done with a plane-wave illumination using an inverted optical microscope system (Axio Observer D1, Carl Zeiss) with an integrated broad-band VIS/IR imaging spectrometer (iHR320, Horiba), and SEM images were taken (Helios NanoLab G3 UC, FEI).

2.2.3 Design and numerical optimization

Next, one will be introduced to design considerations of nanostructure-modulated FP resonators. Both conventional and nanostructured filters will be used to obtain an array of filters required for blood-oxygen sensing.

2.2.3.1 Material considerations

The critical elements of a FP resonator are its mirrors. The mirrors can be metallic [84] or dielectric [87]; the latter being often preferred due to lower intrinsic losses, but the former consist of only a single layer, enabling thinner and simpler construction of the FP resonator.

Several different metals have been used in the construction of FP resonators, in particular Ag [57, 70, 84, 219, 220], Au [221], and aluminium (Al) [78]. The selection of the metal relies on its reflectance and losses. For simplicity, one can assume the reflectance of a bulk metal, which has zero transmittance. In such case, the normal incidence reflectance of a metal surface according to Fresnel equations is [222]:

$$R = \frac{(n-1)^2 + k^2}{(n+1)^2 + k^2}, \quad (2.27)$$

where n and k are the refractive index and the extinction coefficient, respectively. Accordingly, one can calculate and compare the reflectance of different metals; see Figure 2.4.

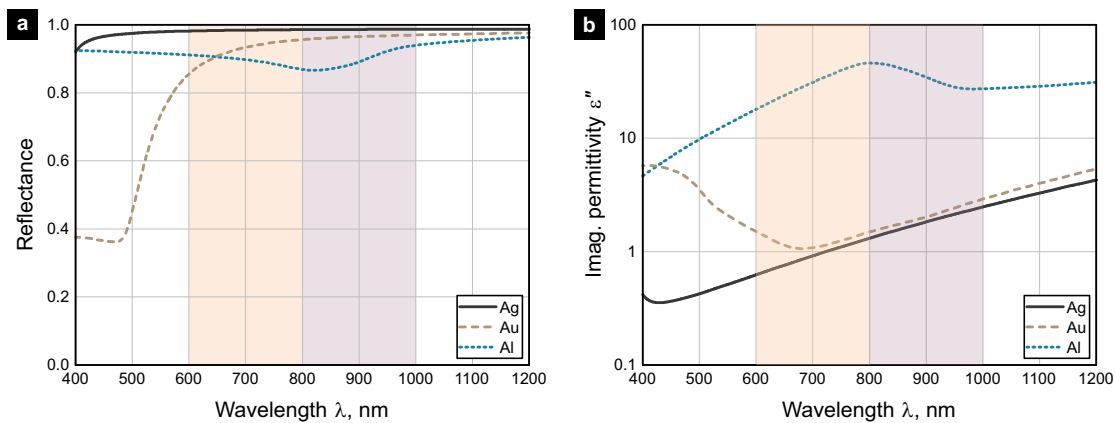


Figure 2.4: Comparison of different metals (Ag, Au, and Al) for the construction of FP mirrors. (a) The reflectance of bulk materials as a function of wavelength λ . (b) The imaginary part of permittivity ϵ'' as a function of wavelength λ , corresponding to the absorption of materials. Spectra of Ag are marked by the solid red line, Au – the dashed blue line, Al – the dotted brown line. The sand-color area corresponds to the R band, the purple area – NIR band.

Moreover, using the refractive index n , and the extinction coefficient k , the imaginary part of the permittivity can be calculated:

$$\varepsilon'' = 2nk, \quad (2.28)$$

which resembles the losses in the material; see Figure 2.4. Here, it can be seen that the reflectance of Ag in the visible spectral range for Ag is higher than that of Au or Al. Also, the imaginary part of the permittivity is lower compared to others. Both aspects indicate Ag as the best choice. The dispersion of a thin Ag film may differ from the bulk material; thus, it was measured [219]; see Appendix A. The top and the bottom Ag mirrors are made the same way and are optimized for the maximum transmission, as required by Equation 2.7. The cavity is constituted of SiO₂ with TiO₂ inclusions, the latter being the high index material of the medium. Both materials exhibit negligible losses in the visible spectral range; see dispersion parameters in Appendix A.

2.2.3.2 Figure of merit

Next, a figure of merit for the optimization of FP filters will be introduced. For color filters it is convenient to use the figure of merit of color quality Q_ξ as it indicates both, the color difference ΔE and the SNR. Here, the exact spectral location does not matter as much as the total amount of light transmitted by the filter, the relative power detected by the sensor α_{signal} , and its ratio with noise – the SNR. The signal at the band of interest is the integral of the filter function $T(\lambda)$:

$$\alpha_{\text{signal}} = \int_{\lambda_{\min}}^{\lambda_{\max}} T(\lambda) d\lambda, \quad (2.29)$$

where λ_{\min} and λ_{\max} depict the boundaries of the spectral band of interest. Subsequently, the SNR is:

$$\text{SNR} = \frac{\alpha_{\text{signal}}}{\alpha_{\text{noise}}} = \frac{\int_{\lambda_{\min}}^{\lambda_{\max}} T(\lambda) d\lambda}{\int_{\lambda_0}^{\lambda_{\min}} T(\lambda) d\lambda + \int_{\lambda_{\max}}^{\lambda_{\infty}} T(\lambda) d\lambda}, \quad (2.30)$$

where α_{noise} is the unwanted signal from the spectral components outside of band of interest, yet still transmitted through the filter.

In case of blood-oxygen sensing, the spectral range can be reduced to only two spectral bands, R band (from 600 nm to 800 nm) and NIR band (from 800 nm to 1000 nm). Subsequently, the calculation of SNR simplifies to:

$$\text{SNR}_R = \frac{\alpha_R}{\alpha_{\text{NIR}}} = \frac{\int_{600}^{800} T(\lambda) d\lambda}{\int_{800}^{1000} T(\lambda) d\lambda}, \quad (2.31)$$

$$\text{SNR}_{\text{NIR}} = (\text{SNR}_R)^{-1}. \quad (2.32)$$

2.2.3.3 Conventional resonators

The simplest way to tune a FP resonator is to change its physical length (thickness) L_0 . To reduce the complexity of the final system, the design starts from a conventional empty cavity. It will be the filter at the

shorter wavelengths, the R band. The central wavelength of the resonance λ_0 is linearly dependent on the cavity length (thickness) L_0 , as defined by Equation 2.1. Thus, the physical cavity length L_0 is varied in the search for the highest SNR_R . From Figure 2.5(a), this turned out to be at the thickness L_0 of only 170 nm. In such a case, the operation is with the lowest order mode ($q = 1$).

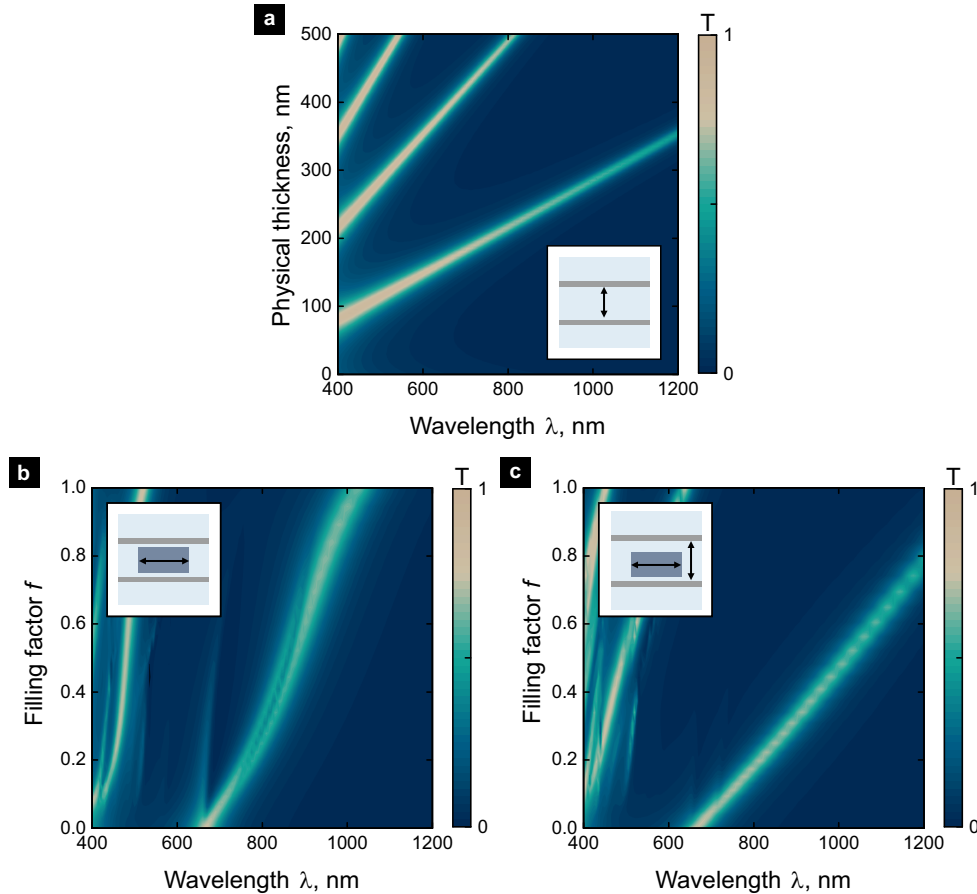


Figure 2.5: Three different types of FP spectral filters. (a) Conventional FP filter with an empty cavity, where only the physical thickness of the cavity is varied; such type of a filter is used to get the R band. (b) Nanostructure-modulated but planarized filter, where high index nanostructures (TiO_2) are embedded in the cavity and later planarized to obtain 15 nm SiO_2 spacers between the nanostructure and both top and bottom mirror. The filling factor (fraction) f of the nanostructure is varied from an empty cavity to a cavity consisting only TiO_2 with only thin SiO_2 spacers. (c) Nanostructure modulated but unplanarized, where the thickness of the top spacer also depends on the filling factor of the nanostructure, accordingly the resonance shift is bigger than for the planarized filter; such type of a filter is used for NIR band.

If L_0 is increased further, higher-order modes ($q > 1$) appear at shorter wavelengths. Here, it is also important to note that using Ag for the construction of mirrors ensures high reflection in the infrared spectral range. Thus, if the lowest order mode ($q = 1$) is used, only shorter wavelengths have to be stopped by an additional spectral filter.

2.2.3.4 Nanostructured resonators

Next, the periodic array of rectangular TiO_2 nanostructures is embedded into the FP resonator. In such a way the FP resonances can also be tailored to obtain multispectral filters, and then one of the bands is used as our NIR filter.

During the fabrication (see Section 2.2.2.2), the nanostructure size has an effect on the total thickness of the cavity. If one considers that the ALD process covers the whole nanostructured TiO₂ layer uniformly with SiO₂, the thickness of the cavity at different patches is expressed by the following equation:

$$L_0 = H(1 + f) + 2L_{\text{spac}}, \quad (2.33)$$

where L_{spac} is the thickness of the spacer, H is the height of the nanostructure, and f is the filling factor of the high-index nanostructure within the unit cell, expressed as $f = D^2/P^2$ with D being the diameter of the nanostructure, and P – period. In this particular configuration, the thickness of both, Al₂O₃ spacer and SiO₂ spacer, is considered constant and equal to $L_{\text{spac}} = 15$ nm. The thickness of the pixelated area with nanostructured FP cavities is usually planarized by a chemical-mechanical polishing process [92] in order to have the same physical thickness for the empty and the nanostructured resonators, but the unplanarized sample can be actually used to an advantage.

Taking the filling factors from $f = 0$ to $f = 1$, the planarized FP filters cover the spectral range from $\lambda_0 = 665$ nm to $\lambda_0 = 1024$ nm ($\Delta\lambda_0 \approx 360$ nm), while the unplanarized FP filters cover the spectral range from $\lambda_0 = 665$ nm to $\lambda_0 = 1434$ nm ($\Delta\lambda_0 \approx 770$ nm); see Figure 2.5. Thus, the spectral range obtainable with the unplanarized sample is larger than for the planarized one by at least a factor of 2. See more details on exact spectral properties in the following section.

In the meantime, the maximum thickness of the unplanarized nanostructured FP filter reaches $L_0 = 230$ nm, while for the conventional FP filter resonant at $\lambda_0 = 1434$ nm one would require a thickness of $L_0 = 434$ nm. Accordingly, it can be concluded that the high-index inclusions enable not only a single-lithography-step fabrication, but also physically thinner optical elements, which is of convenience in miniature optical devices.

2.2.4 Experimental realization

The nanostructure arrays inside the nanostructure-modulated FP resonators were fabricated by a lift-off technique described in Methods; see Section 2.2.2. The $300 \times 300 \mu\text{m}^2$ patches, shown in Figure 2.6(a), vary in the diameter of nanostructures from 60 to 300 nm. Note that the color in the transmission is a product of the FP resonances. They relate to the first-order FP resonance or a combination of the first and the second order. However, for the current application, the colors have to be considered carefully. Part of the investigated spectra, as shown further, is in NIR, which is not fully resembled by the colors.

The nanostructures used in the big patches were also used for construction of pixelated arrays with a pixel size $d_{\text{pixel}} = 17.92 \mu\text{m}$; see Figure 2.6(b). Similarly, the pixelated patches differ in the diameter of nanostructures D , but due to a higher etching rate, the positions of the geometric parameters are slightly shifted. The highlighted pixelated patch consists of optimized pixels. The pixels are arranged in a checkerboard pattern. Half of the pixels are based on empty FP resonators (sand color), and another half – FP resonators with nanostructure inclusions (purple color). The constituents of the resonators are explicitly shown in Figure 2.6(c–e). Here, one can note a horizontal cross-section of an empty cavity in Figure 2.6(c), where a grain-like surface is observed as a result of Ag degradation. The deposited Ag layer was back-etched to

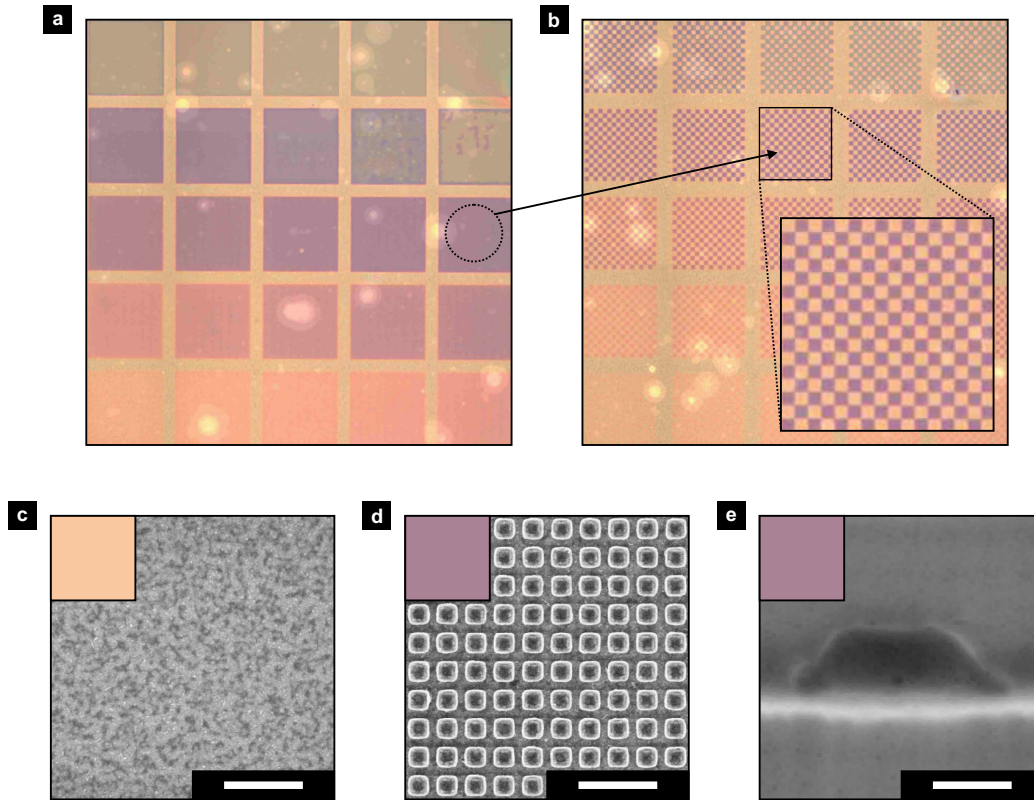


Figure 2.6: Experimentally obtained patches of FP filters with different size inclusions: (a) uniform patches, D varies from 60 to 300 nm. (b) same but pixelated patches, with pixels equal to $17.94 \mu\text{m}$. (c) SEM image of top view of an empty cavity before top mirror deposition. Scale bar is equal to $1 \mu\text{m}$. Oxidation of bottom Ag mirror is clearly visible. (d) SEM image of top view of a nanostructured cavity before top mirror deposition. Scale bar is equal to $1 \mu\text{m}$. (e) SEM image of side view of a single TiO_2 nanostructure (darker shade) on Ag mirror (bright shade). Scale bar is equal to 100 nm . Colored insets correspond to the optically visible colors in transmission.

avoid the oxidized layer, but as discussed next, such a process was found to be insufficient. The nanostructures are also shown; see SEM image of the square-like nanostructures from the top in Figure 2.6(d), while the vertical cross-section of a unit cell before the deposition of the top Ag mirror is shown in Figure 2.6(e).

Due to the irregular shape of sidewalls of the nanostructures, the filling factor of the nanostructures f was found via fitting of the numerical results. The previously introduced design was adjusted to the changes in geometry. In particular, the cavity's physical thickness was found to be only $L_0 = 130 \text{ nm}$, compared to the design cavity with $L_0 = 170 \text{ nm}$. Thus, the resonant peaks are blue-shifted. The spectral response as a function of the high-index filling factor is shown in Figure 2.8. Here, the positions of the experimentally obtained values are indicated by the white dots.

The FP resonances of the measured systems are strongly damped due to the absorption in the oxidized Ag mirrors; see Figure 2.7 for spectral comparison of the experimentally and numerically obtained optimal pixels. Here, a significant drop in transmittance is noted, i.e., the maximum transmittance for the empty cavity goes from 69% to roughly 14%, for the nanostructured cavity – from 65% to only 10%. Accordingly, the SNR_R drops from a theoretical value of 15.4 to 1.4, while the SNR_{NIR} drops from 10.3 to 1.5. Moreover, the first-order peak of the empty cavity is blue-shifted by $\Delta\lambda \approx 100 \text{ nm}$, from $\lambda_0 = 665 \text{ nm}$ to $\lambda_0 = 560 \text{ nm}$, which reassures that the thickness of the fabricated resonator L is smaller than anticipated. The blue-shift

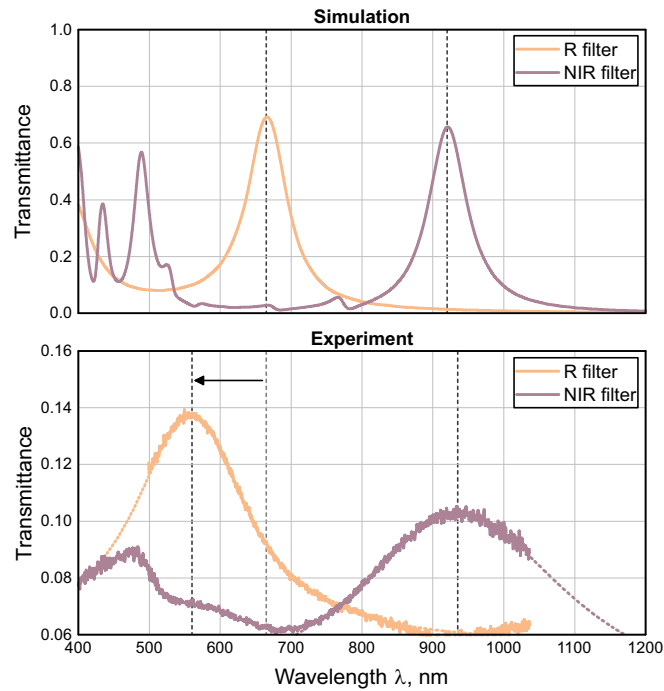


Figure 2.7: Comparison of optimal peaks for both simulation (top) and experiment (bottom). The peaks are strongly damped for the experimental case, the peaks are shifted, but retain $\text{SNR} > 1$. Vertical dashed lines depict the central positions of the peaks λ_0 . The arrow notes the blue-shift of the R filter. Dotted lines indicate the Lorentzian-fit of the peaks.

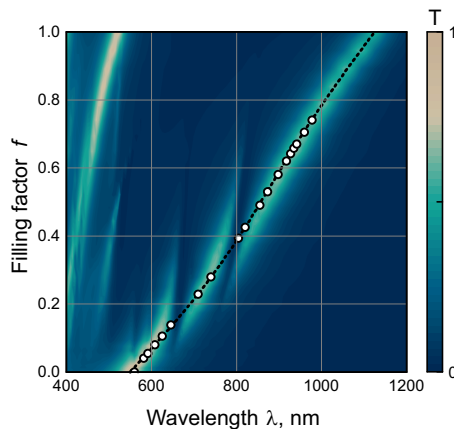


Figure 2.8: Simulated spectral response of the blue-shifted FP filter with respect to filling factor f . The dashed line indicates the central wavelength of the FP resonance, the white dots depict central wavelengths λ_0 of the experimentally obtained filters.

is not observed for the nanostructured FP filter, as it was freely picked from a set of filters to match the designed NIR filter. Even though the initial design proposed the filling factor of $f = 0.31$, due to a thinner cavity, the filling factor of $f = 0.65$ is used. Naturally, the freely selected NIR filter is close to the design. The experimentally obtained peak is at $\lambda_0 = 938$ nm, while the design peak was at $\lambda_0 = 920$ nm. Despite the attenuated performance, the experimentally fabricated sample is sufficient for the proof of concept. Next, several other specifications will be discussed in detail.

2.2.5 Specifications

2.2.5.1 Angle tolerance

It is known that the transmission peak of the FP resonator blue-shifts with the increase of the incident angle [190]. The shift is described by a cosine relation; thus, Equation 2.2 can be modified to obtain the following form [190, 223]:

$$\lambda_0 = \frac{2L \cos \theta}{q - \varphi_{1,2}}, \quad (2.34)$$

where θ is the angle of incidence, L is the optical length of the resonator, q is the integer defining the order of the resonance, $\varphi_{1,2}$ is the phase shift by the Ag mirror.

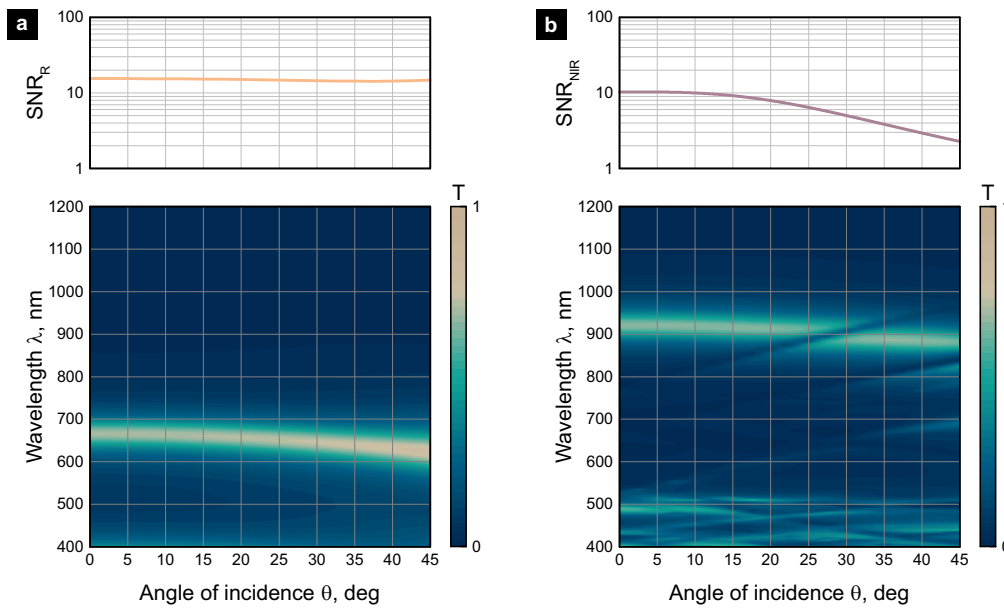


Figure 2.9: Angle tolerance of FP filters. (a) R filter, an empty resonator operating from 600 nm to 800 nm, (b) NIR filter, a nanostructured resonator operating from 800 nm to 1000 nm. The spectral information (bottom) is integrated over specified spectral bands to obtain the SNR (top).

The exact spectral response is found numerically. The polarization of the incident light is set at the axis of the varied angle (p -polarized light). The transmission spectra were calculated for the angle θ up to 45° for both R and NIR filters; see Figure 2.9(a) and Figure 2.9(b), respectively. Despite the shift, the peaks remain mostly within the spectral bands of interest. Thus the change of SNR is minimal. In the numerical analysis, the SNR_R maintains its value, while SNR_{NIR} experiences a slight decrease but remains well above 1, proving that FP cavities with Ag mirrors are quite tolerant to oblique incidence.

Furthermore, the proposed FP filters can be used in various optical systems because the blue-shift of the peak can be compensated by increasing the size of the embedded nanostructures [224]. In the standard imaging system, the chief ray angle increases from the center to the edges of the sensor from normal incidence up to $25\text{--}30^\circ$. As the central wavelength of the peak λ_0 relates to the incident angle θ by a cosine relation (see Equation 2.34). This means that the optical thickness of the cavity should be proportionally increased in order to compensate for the spectral shift.

2.2.5.2 Spectral resolution

FP filters using metallic mirrors cannot provide a high transmission and a narrow FWHM simultaneously due to the aforementioned absorption of the mirrors [225]. The FWHM of the peak decreases with the increase of mirror thickness at the expense of maximum transmission; see Figure 2.10. Here, the performance of both an empty resonator (R filter) and a nanostructured resonator (NIR filter) is observed, while gradually increasing the thickness of the Ag mirrors, from 5 nm up to 50 nm. Subsequently, in the case of the R filter, the FWHM decreases from 584 nm down to 10 nm, see Figure 2.10(a), but, at the same time, the transmission maximum drops from 90% to 19%; see Figure 2.10(b). A similar trend is noted for the NIR filter.

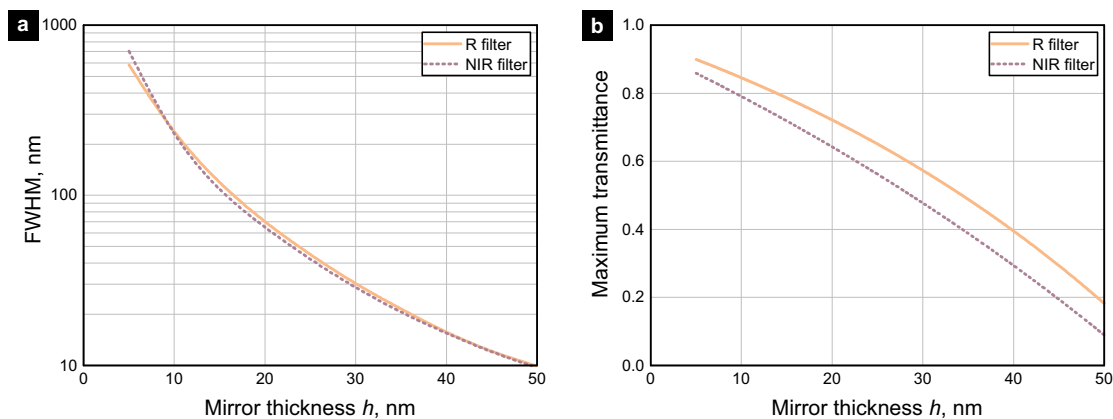


Figure 2.10: Spectral resolution and transmittance dependence on the thickness of Ag mirrors, constituting the FP resonator. (a) FWHM, which directly corresponds to the spectral resolution, as a function of mirror thickness h . (b) Maximum transmittance as a function of mirror thickness h . Due to wavelength-dependent refractive index of Ag, the values for R and NIR filters differ, though the trend is identical.

The designed filters with Ag mirrors of $h = 20$ nm, presented in Section 2.2.3, have a spectral resolution of $\text{FWHM}_R = 69$ nm and $\text{FWHM}_{\text{NIR}} = 66$ nm with the maximum transmission at 73% and 66%, respectively. In addition to mirror thickness, higher spectral sensitivities may be reached with a double resonator design [57, 219, 226], but this requires multiple deposition steps. Thus, if a high spectral resolution is desired, the DBRs are the better option, as shown in Section 2.3.4.

2.2.5.3 Spatial resolution

Similarly to color filters, the smaller the lateral size of the FP filters, the more of them can be fitted on a sensor, which ideally results in more information on the imaged object. A typical pixel size of multi- and hyperspectral cameras ranges from 5.5 to 15 μm [85, 186]. However, the limits of spatial resolution have never been tested for nanostructure-modulated FP filters.

To analyze the limits of the spatial resolution, numerical tests are done with the previously optimized FP filters in a checker-board pattern, gradually decreasing the lateral size of the filters. The SiO_2 spacer layer between the filters and the detector was set to a thickness of 0.1 μm . Pixel sizes were considered from approx. 4 μm , equal to 11×11 nanostructures inside the resonator, down to 0.36 μm , a single nanostructure. In the case of an empty resonator (R filter), the SNR remains above 1 for all pixel sizes; from $\text{SNR}_R = 15.4$

for infinite size pixel it reduces to $SNR_R = 3.0$ for a pixel with its transversal size equal to a single period of $P = 0.36 \mu\text{m}$; see Figure 2.11(a). Furthermore, the results for nanostructured pixel (NIR filter) have a similar trend, but it goes down to $SNR_R = 0.3$ for a single period; see Figure 2.11. Thus, larger pixels have to be used. In particular, numerical simulations suggest that pixels of at least $0.72 \mu\text{m}$ (2×2 nanostructures) have to be employed, resulting in $SNR_R = 3.6$ and $SNR_{NIR} = 2.2$.

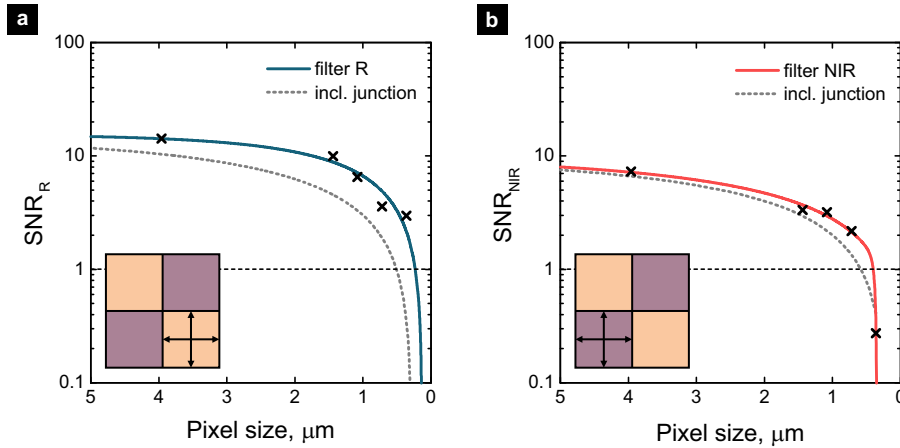


Figure 2.11: Theoretical assessment of spatial resolution of FP filters. (a) R filter, (b) NIR filter. Filters are downscaled to submicrometer range, the effect of junction increases the minimum obtainable functional filter size.

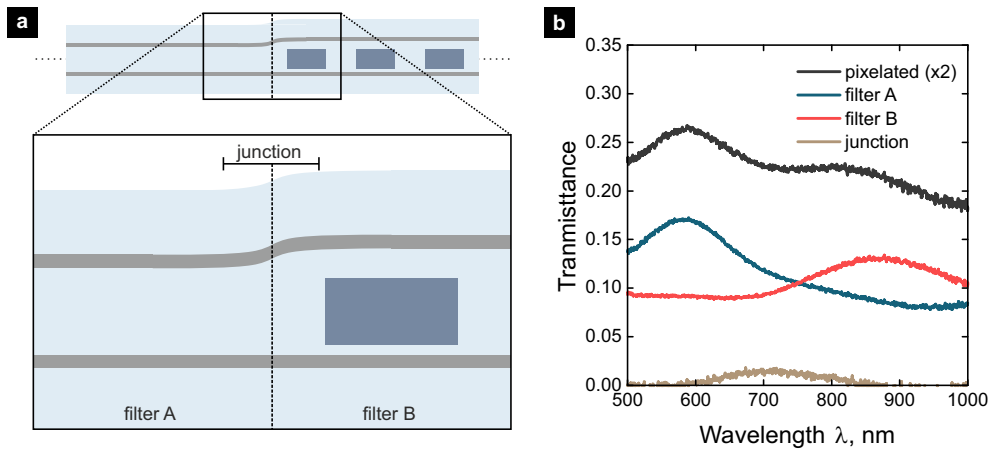


Figure 2.12: Junction between pixels and its corresponding effect. (a) Two-dimensional schematic depiction of the junction due to different heights of R and NIR filters. (b) Transmittance result from the junction when comparing separate pixels and pixelated area.

Up to now, the assumption was that neighboring FP filters are structurally independent of each other. However, this is not fully correct. Experimentally, the top SiO_2 and Ag layers are uniformly deposited on all of the samples. Due to a vastly different filling factor of the TiO_2 nanostructures in the cavities, $f_R = 0$ and $f_{NIR} = 0.31$ for R filter and NIR filter, respectively, not only the total thickness will differ at the spatial positions of different filters, but a thickness gradient will be observed at the junctions of the filters [227]; see Figure 2.12(a). This is experimentally investigated by measuring and comparing the spectrum of the pixelated filter area to the respective filters’ spectra. The arithmetic operation results in a small peak in the middle of the main peaks, which is due to the gradient thickness at the junction; see Figure 2.12(b). For

filters of $d_{\text{pixel}} = 17.92 \mu\text{m}$, it is approx. 1.35% of the total signal. The percentage relates to the ratio of the junction and the total filter area. Thus the size of the junction is calculated to be 120 nm in width.

The size of the junction is expected to remain similar regardless of the size of the pixels. Thus, results can be extrapolated for various size pixels. If accounted for, this slightly reduces the SNR for small pixels; see Figure 2.11. However, for $d_{\text{pixel}} = 2P$ the SNRs remain above 1: $\text{SNR}_{\text{R}} = 1.8$ and $\text{SNR}_{\text{NIR}} = 1.5$ for R filter and NIR filter, respectively.

2.2.6 Integration on a CMOS sensor

Some nanostructured filters, such as silicon-based Mie-resonant filters, are CMOS-compatible. Thus their fabrication may be carried out simultaneously with the fabrication of the CMOS sensor. However, filters can also be bonded on an already existing sensor. Here, the bonding process and initial tests of the previously introduced nanostructure-modulated FP filters will be presented.

The experiment was carried out using a Raspberry Pi camera module v2.1 [228]. The camera is equipped with a backside-illuminated 8-megapixel Sony IMX219 image sensor, featuring $1.12 \times 1.12 \mu\text{m}$ pixels. The total size of the sensor is $3.68 \times 2.76 \text{mm}^2$. For simplicity of the demonstration, the native RGB filters and microlenses are kept on the sensor.

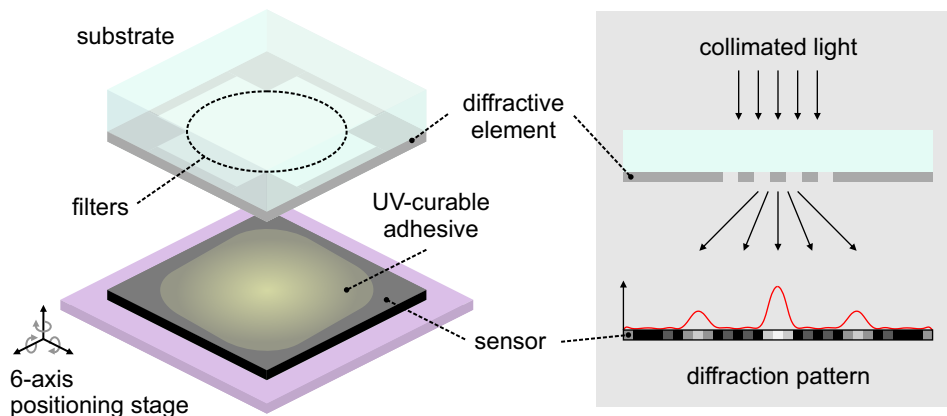


Figure 2.13: Scheme of filters integration on a CMOS sensor. The sample is bonded filters side down with UV-curable adhesive. Diffractive elements on the sides of the sample produce a diffraction pattern, which is monitored for accurate alignment. The sensor is spatially oriented by a 6-axis positioning system.

The wafer with FP filters is cut into small chips to fit the Raspberry Pi camera sensor area. During the bonding procedure, a chip is mounted above the camera with the filter side facing the camera sensor, as illustrated in Figure 2.13. Special alignment markers and diffractive optical elements (DOEs) are structured for the bonding procedure. The space between the filter and sensor is filled with a liquid UV-curable adhesive that matches the refractive index of the substrate. A collimated laser beam is directed to the setup perpendicularly to the camera sensor. Subsequently, the aforementioned diffractive elements generate a diffraction pattern on the sensor plane. From the signal registered, a relative position of the chip is evaluated such that the lateral shift, rotation, distance, and tilt can be robustly controlled. The camera is fixed on a 6-axis positioning stage with submicrometer precision.

The distance between the filters and the sensor can be adjusted from a few to tens of micrometers by the

pressure applied during the bonding procedure. However, it cannot be reduced lower than a micrometer, as in the previous section. Thus, for the bonding, large filters are used. The lateral filter size is $d_{\text{pixel}} = 17.92 \mu\text{m}$; it covers 16×16 camera pixels. After the bonding, the sensor was illuminated by a light source with narrow-band filters centered at $\lambda = 660 \text{ nm}$ and $\lambda = 830 \text{ nm}$; see Figure 2.14. The grey-scale image correlates with the expected behavior. For illumination at $\lambda = 660 \text{ nm}$, more light reaches the sensor through R filter, while at $\lambda = 830 \text{ nm}$, it is vice versa.

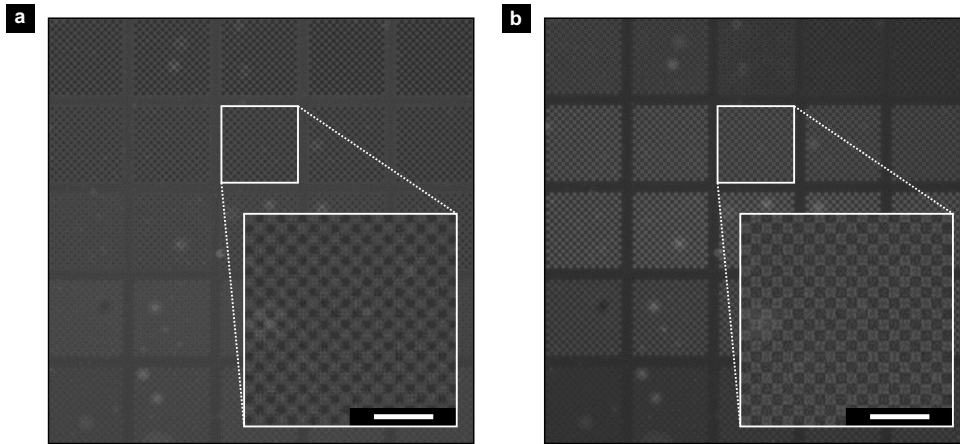


Figure 2.14: Camera test with bonded FP filters. Camera images of single-wavelength illumination at $\lambda = 660 \text{ nm}$ and $\lambda = 830 \text{ nm}$, (a) and (b), respectively. The 25 pixelated arrays with parameter variations are shown, the optical image is zoomed in. Scale bars are equal to $100 \mu\text{m}$.

2.3 High spectral resolution spectropolarimeter

Multifunctional imaging has emerged as new generation of digital imaging. It combines different technologies to obtain broader or even previously inaccessible information on the subject or scene of interest. In the previous section, an exciting example was introduced for imaging beyond the conventional color imaging; next, we extend it even further with an addition of polarization sensitivity. The technique that captures both spectrum and polarization falls under the term of spectropolarimetry [66].

The limitations of the conventional optical components results in metasurfaces being suggested as a technological solution for miniaturization and expanding of the functionalities. However, there are still several obstacles to overcome and challenges to be addressed. First, many multifunctional optical elements consist of a few transversely-variant layers on top of each other. Multiple layers cause quite a challenge in terms of spatial alignment, as even small misalignment results in errors of the detected information [82]. Furthermore, it is crucial to obtain a high spectral resolution for the maximum gain of the spectral information. However, up to now, the spectral resolution of spectropolarimetric systems was limited to the bands of RGB filters [82] or required a connection to an external spectrometer [80]. Last but not least, imaging systems should be integrated on a compact sensor. Thus, aspects such as sensor-compatibility of the pixels are of a high importance and have to be addressed.

In this section, the concept of a planar spectropolarimeter is introduced. It is based on a set of polarization-sensitive Si nanostructures embedded in a FP cavity. Such a system enables the reconstruction of the first

three Stokes parameters (S_0 , S_1 , S_2) with a high spectral resolution. This section presents a systematic design and experimental demonstration, the polarization reconstruction algorithm regarding its limitations, and optimization towards multiband spectropolarimetric design.

2.3.1 Concept

High-index inclusions, such as arrays of high-index nanostructures, can be used to modulate the effective index of the FP resonator n_{eff} , as introduced in Section 2.1.3. As mentioned, if the nanostructures have different diameter on x - and y -axis, D_x and D_y , two resonant peaks are obtained for x - and y -polarized light, respectively. The spectral distance between the peaks can be controlled by carefully altering the aspect ratio D_x/D_y . As long as the nanostructures are non-resonant, the modulation of the FP resonator is based only on the anisotropic change of the effective index [192].

Using different-size polarization-sensitive nanostructures inside the FP resonator, resonance peaks for different wavelength and polarization combinations can be obtained. As illustrated in Figure 2.15, by measuring intensities of a set of 6 pixels (I_1, \dots, I_6), one can retrieve both spectral and polarization information in the form of discrete intensities for two linear polarization states (I_x and I_y) at three wavelengths ($\lambda_1, \lambda_2, \lambda_3$) [T1]. For simplicity, it is assumed that the pixels have a transmission $T = \alpha_m^n$ at their peaks and $T = 0$ elsewhere, where n is the number corresponding to the detector pixel and m indicates the polarization state. Using this assumption, the following system of equations is formed:

$$\begin{pmatrix} I_1 \\ I_2 \\ I_3 \\ I_4 \\ I_5 \\ I_6 \end{pmatrix} = \begin{bmatrix} 0 & 0 & \alpha_x^1 & \alpha_y^1 & 0 & 0 \\ 0 & \alpha_x^2 & 0 & 0 & 0 & \alpha_y^2 \\ \alpha_x^3 & 0 & 0 & 0 & \alpha_y^3 & 0 \\ \alpha_x^4 & 0 & 0 & 0 & 0 & \alpha_y^4 \\ 0 & 0 & \alpha_x^5 & 0 & \alpha_y^5 & 0 \\ 0 & \alpha_x^6 & 0 & \alpha_y^6 & 0 & 0 \end{bmatrix} \begin{pmatrix} I_x^{\lambda_1} \\ I_x^{\lambda_2} \\ I_x^{\lambda_3} \\ I_y^{\lambda_1} \\ I_y^{\lambda_2} \\ I_y^{\lambda_3} \end{pmatrix}. \quad (2.35)$$

Unfortunately, this system of equations cannot be inverted. Thus, the spectropolarimetric reconstruction is impossible. However, it can be made invertible by removing one of the transmission peaks from the system of equations, e.g., by setting $\alpha_x^6 = 0$. This results in a set of spectropolarimetric pixels, schematically depicted in Figure 2.15(a). Their spectral functions are conceptually illustrated in Figure 2.15(b).

Furthermore, by including a second set of 6 pixels but with the nanostructures rotated by an angle of 45° , the intensity of light polarized along 45° and 135° can be measured. Then, a set of 12 pixels in total allows the retrieval of the first three Stokes parameters:

$$S_0 = I_x + I_y = I_{45^\circ} + I_{135^\circ}, \quad (2.36)$$

$$S_1 = I_x - I_y, \quad (2.37)$$

$$S_2 = I_{45^\circ} - I_{135^\circ}. \quad (2.38)$$

Such a system cannot retrieve all Stokes parameters [229], because it is unable to distinguish circularly polarized light from unpolarized light; the fourth Stokes parameter S_3 can not be retrieved. Also, the

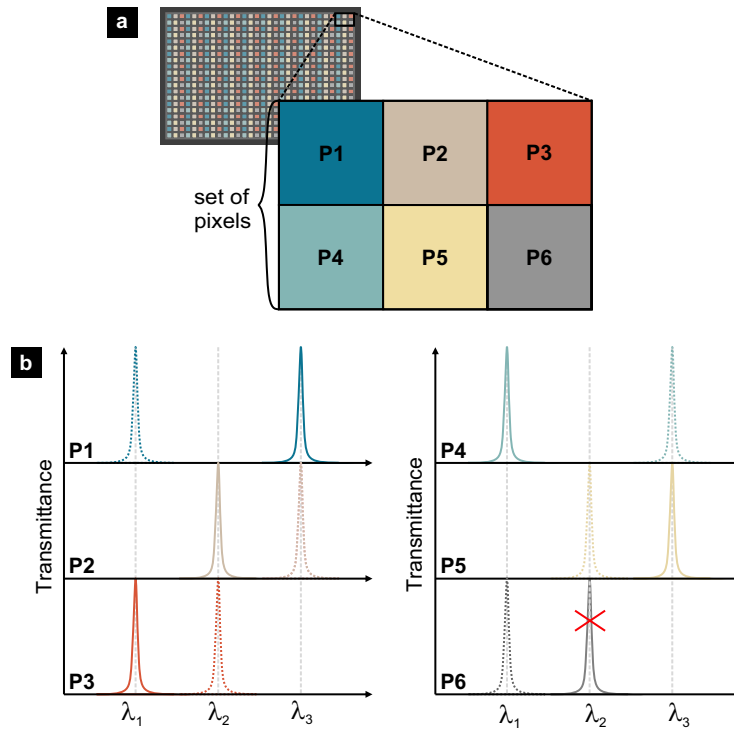


Figure 2.15: Concept of spectropolarimeter for linear-polarization. (a) Illustration of a set of 6 pixels, a super-pixel, integrated directly on a sensor. (b) Lorentzian-shape spectral functions for 3 wavelengths (λ_1 , λ_2 , λ_3) and two polarization states (x and y) using a set of 6 pixels (P1, \dots , P6). A single-pixel provides two peaks for the two states of linear-polarization, while one peak (P6) is cut-out for inversion of the matrix. The transmittance of x -polarized light is depicted by the solid line, while transmittance of y -polarized light is shown by the dashed line. The figure is adapted from [S9].

presence of circularly polarized light may disrupt the estimation of the first Stokes parameter. However, this is not critical for some applications, e.g., Earth observation, where the amount of circularly polarized light is negligible.

2.3.2 Design and numerical optimization

2.3.2.1 Effective medium theory

The effective medium approximations, introduced in Section 2.1.2, can be used to calculate the effective refractive index n_{eff} and, subsequently, the optical length of the resonator L , which defines the behavior of the FP resonator. Instead of the relatively complex numerical simulations and expensive computational resources, one can predict the spectral position of the peak. However, as mentioned in Section 2.1.2, the effective medium theory has certain size restrictions, which are tested here.

In this particular case, Si polarization-insensitive nanostructures are embedded in glass, which has a lower refractive index; see Appendix A for Si dispersion parameters. The diameter of the Si nanostructures is gradually increased. If the period is fixed, as in this case at $P = 500$ nm, this subsequently leads to an increase of the filling factor f . At each value, the effective refractive index is calculated using the Maxwell Garnett formulation, see Equation 2.18, and the Bruggeman formulation, see Equation 2.23. In addition, full-wave simulations are used (FDTD, Lumerical). As indicated in Figure 2.16, the effective index using

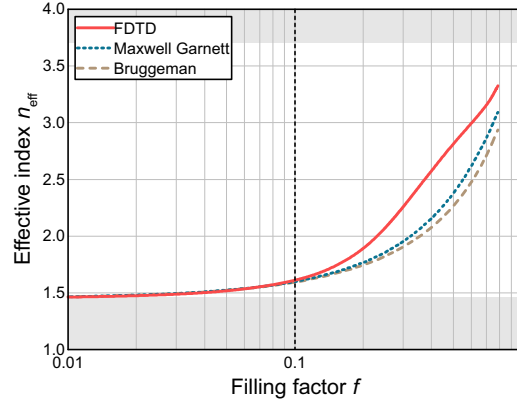


Figure 2.16: Effective medium theory limits with respect to numerical simulations. The effective index calculated by Maxwell Garnett effective medium theory is depicted by the blue dotted line, Bruggeman – the brown dashed line. The numerical simulations are done using FDTD method; see the red solid line. The areas outside of refractive index boundaries (from refractive index of SiO₂ to Si) are indicated by the grey shaded areas.

effective medium theories fits well to the numerical simulations only up to $f = 0.1$, which is equal to nanostructures with diameter of $D = 180$ nm in an array with period of $P = 500$ nm.

The limit means the effective medium theory can be used to some extent but with certain precautions. For larger filling factor, $f > 0.1$, the effective medium predictions can be used, but are no longer accurate, as the error (shift) of the wavelength $\Delta\lambda$ directly relates to the error (difference) of the refractive index Δn :

$$\lambda_0 + \Delta\lambda \propto n_{\text{eff}} + \Delta n, \quad (2.39)$$

where n is the refractive index predicted by effective medium theory.

2.3.2.2 Design considerations

The nanostructure-modulated FP-based spectropolarimeter design was based on the requirements of the spectropolarimeter for planetary exploration (SPEX) [230]. For initial selection of the FP parameters, the effective medium theory was used, but to enable the highest accuracy, the final design is carried out using numerical methods.

Similar to the previous design with Ag mirrors, the design of the spectropolarimeter starts from the mirrors. Thus, an important aspect is the spectral width of the FP resonance, which relates to the spectral resolution of the system. Following the assumption that both mirrors have the same reflectivity R , the FWHM is defined by Equation 2.8, which notes that the higher the reflectivity, the higher the spectral resolution. In order to obtain high spectral selectivity, distributed Bragg reflectors (DBRs) are used. In theory, if the DBR layers are made of lossless materials, there is no strict limitation to the number of layers and, subsequently, the FWHM [231]. However, here, the DBRs are restrained to 7 pairs of alternating SiO₂ ($n = 1.45$) and TiO₂ ($n = 2.285$ [232]) layers, with a reflection band centered at $\lambda = 1500$ nm. This configuration results in a reflectance of $R \approx 99.5\%$ and FWHM ≈ 1 nm (resonator quality factor $Q > 1000$). The mirrors are separated by an optical length L equal to the central wavelength of $\lambda = 1500$ nm. The physical length of the resonator was set to $L_0 = 985$ nm.

Arrays of polarization-sensitive Si nanostructures were constructed from amorphous hydrogenated Si (a-Si:H), which has a high refractive index and negligible intrinsic losses ($n = 3.7$ and $k = 0$ at $\lambda = 1500$ nm). The nanostructures were placed in the middle of the FP resonator in order not to alter the performance of the mirrors. SiO₂ ($n = 1.45$) was selected as the low-index material of the resonator. The control of the central wavelength λ_0 for x - and y -polarization is done by changing the diameter along the x -axis for two different cases: a polarization-sensitive inclusion and a grating; see Figure 2.17(a) and Figure 2.17(b), respectively. Regardless of the shape of the nanostructures inside the resonator, their optical size has a restriction to be smaller than the wavelength $\lambda = 1500$ nm, such that the nanostructures are non-resonant and provide transmission close to unity.

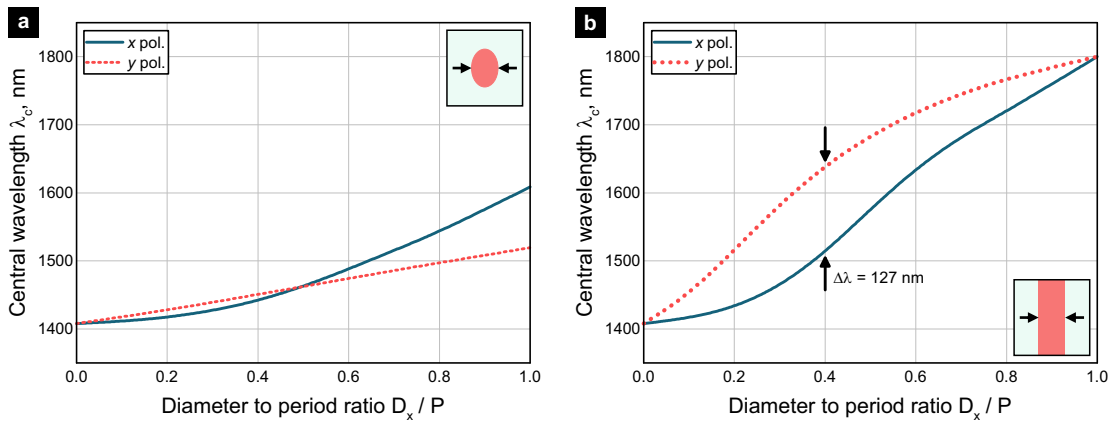


Figure 2.17: Spectral positions of transmission peaks for x and y polarization states as a function of width D_x of the inclusions. (a) The case of an array constituted of elliptical nanostructures with $D_y = 250$ nm, while D_x was varied from 0 nm to 500 nm. (b) The case of a linear grating with its width varied from 0 nm to 500 nm (equal to period P). The maximum separation of the peaks is 127 nm. The figure is adapted from [S9].

The optimal nanostructures were defined as extruded ellipses with a specific diameter along the x -axis D_x , diameter along the y -axis D_y , and height H . The nanostructures were distributed in a square lattice with a period of $P = 500$ nm. The height of the nanostructures was set to $H = 300$ nm. The diameters of the elliptical nanostructures, D_x and D_y , were optimized in the range of 140 – 360 nm to obtain three spectral bands centered at the following wavelengths: $\lambda_1 = 1480$ nm, $\lambda_2 = 1500$ nm, and $\lambda_3 = 1520$ nm. Moreover, to remove a transmission peak in the matrix, as mentioned in Section 2.3.1, one of the pixels with elliptical Si nanostructures was replaced by a subdiffractive linear Si grating. The grating is defined with an infinite aspect ratio, meaning a certain width of D_x , but $D_y = \infty$. The results of the final design are compared to the experimental demonstration in the following section.

2.3.3 Experimental realization

2.3.3.1 Fabrication

The sample fabrication was carried out in several steps: the deposition of the bottom mirror, the structuring of the resonator, and the deposition of the top mirror. Here, each step will be presented in detail, highlighting the challenges faced.

First, the bottom mirror was constructed by alternating SiO₂ and TiO₂ layers. The layers were deposited on top of a glass substrate by plasma-ion-assisted deposition (PIAD) [231]. In total, seven pairs of SiO₂/TiO₂ layers were deposited for high reflectivity at $\lambda = 1500$ nm; see Figure 2.18. The thicknesses of the layers were initially calculated as quarter-wavelength layers, but later tuned to $t_{\text{IL}} = 320$ nm and $t_{\text{IH}} = 120$ nm for SiO₂ and TiO₂, respectively, to reduce the thickness of TiO₂ layers in an attempt to avoid its polycrystalline growth, thus retaining smooth surfaces with low scattering and absorbance [233].

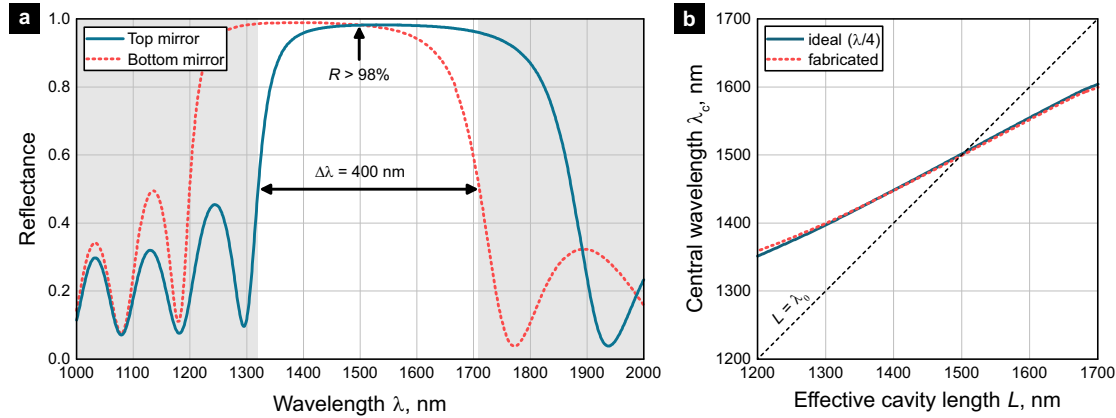


Figure 2.18: Reflectivity of the fabricated mirrors and their impact on the FP resonance. (a) Measured reflectance of the bottom and the top DBRs. Bandwidth and reflectance in the spectral range of interest are highlighted. Due to the mismatch of mirrors, the bandwidth is smaller than of an individual mirror. (b) Simulated central positions of the FP resonance depending on the effective length of the resonator, when different mirrors are used: ideal ($\lambda/4$, for 1500 nm), and fabricated. For comparison, a dashed line represents a case for which mirrors and effective length of the resonator are $\lambda/4$ and $\lambda/2$, respectively. The figure is adapted from [S9].

The nanostructures were made from a 300 nm layer of a-Si:H, deposited by plasma-enhanced chemical vapor deposition (PECVD) using SiH₄ gas as a source (Oxford Plasmalab 100 Dual Frequency, Oxford Instruments). Afterward, a 30 nm Cr layer was deposited by ion beam deposition (Oxford Ionfab 300, Oxford Instruments), and a 100 nm layer of electron beam resist (EN038, Tokyo Ohka Kogyo) was spin-coated on top. The sample was exposed by a variable-shaped EBL system (Vistec SB 350, Vistec Electron Beam). First, the resist was developed, and the mask was transferred in the Cr layer by ion beam etching (Oxford Ionfab 300, Oxford Instruments). Then, the Cr mask was transferred in the Si layer by inductively coupled plasma reactive ion etching (SI-500 C, Sentech Instruments) with CF₄ as the reactive gas. Finally, the remaining resist and Cr mask were supposed to be removed by acetone and Cr etchant. But eventually it turned out that some Cr mixed with resist and was not fully removed, as indicated in the colored SEM image in Figure 2.19(a). Cr has a high absorption ($n = 3.675$ and $k = 4.072$ at 1500 nm [234]). Thus, any amount of it in the resonator is undesirable. As determined by simulating Cr inclusions, the Cr volume of 0.3% of the total resonator volume already decreases the amplitude of the resonant peak to 55%. A bit higher concentration completely destroys the resonance; see Figure 2.19(b,c) for the transmittance and the FWHM dependence on Cr volume inside the resonator. For comparison, Si nanostructures constitute around 6% of the total resonator volume.

The nanostructured Si was embedded in a SiO₂ layer by ALD at a low growth rate of 1.19 Å/cycle, ensuring an air-gap-free resonator (Silayo ICP 330, Sentech Instruments). The Si nanostructures induce waviness in the upper layers; see Figure 2.20(a). Thus the embedding layer was planarized by ion-beam

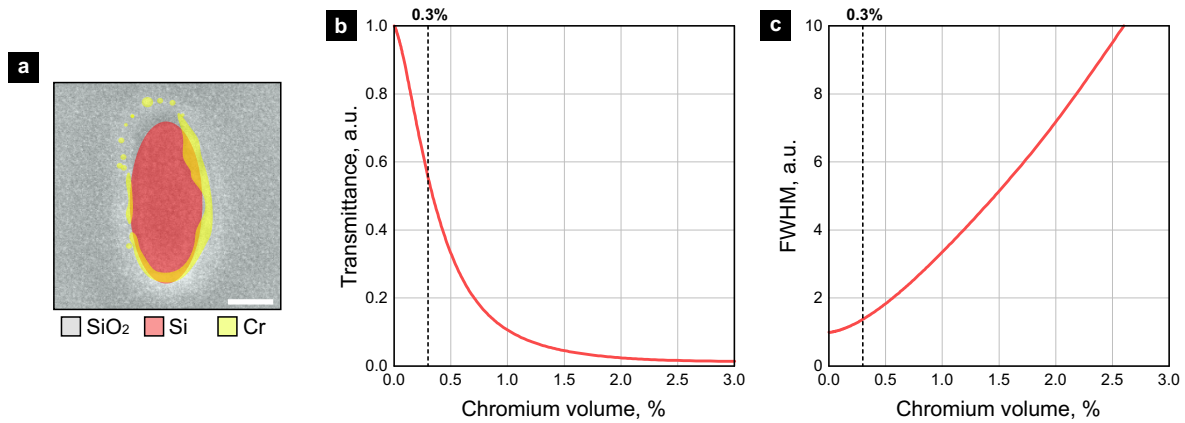


Figure 2.19: Impact of resonator contamination with Cr. (a) Colored SEM image of the horizontal cross-section of a single elliptical nanostructure inside the resonator. Si is red, SiO₂ is grey, and Cr is yellow. (b) Simulated relative peak transmittance (intensity) as a function of the volume of Cr in the resonator. Cr is considered elliptical for the simplicity of the model. (c) Simulated relative peak width (FWHM) as a function of the volume of Cr in the resonator. Dotted line highlights anticipated value. The figure is adapted from [S9].

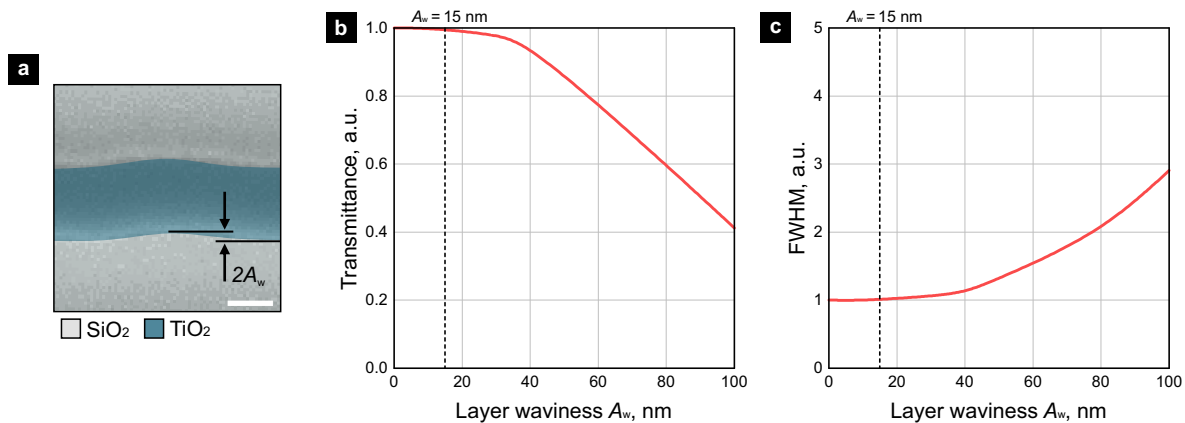


Figure 2.20: Impact of top mirror waviness. (a) Colored SEM image of a vertical cross-section of a single high-index DBR layer. TiO₂ is blue, SiO₂ is grey. The uneven surface can be described as sinusoidal surface with $A_w = 15$ nm. The scale bar is equal to 100 nm. (b) Simulated relative peak transmittance (intensity) as a function of waviness amplitude. (c) Simulated relative peak width (FWHM) as a function of waviness amplitude. Dotted line highlights anticipated value based on experimentally obtained $A_w = 15$ nm. The figure is adapted from [S9].

etching (Oxford Ionfab 300, Oxford Instruments). The waviness was reduced to $A_w = 15$ nm, which is significantly less than the operating wavelength and is not expected to deter the performance of the FP resonator; see Figure 2.20(b,c) for the transmittance and the FWHM dependence on Cr volume inside the resonator. During the process, the physical length of the resonator was reduced to $L_0 = 910$ nm; thinner than the original design value with $L_0 = 950$ nm.

Before the deposition of the top mirror, the SiO₂ cladding surface was pre-treated with Ar-ion plasma to create chemically active sites for better cross-link [235]. Similarly to the bottom, the top mirror was optimized for high reflectivity at $\lambda = 1500$ nm. However, due to different deposition conditions, the thicknesses changed. In particular, the top DBR was constituted of 7 pairs of SiO₂ and TiO₂ layers with thicknesses of $t_{2L} = 250$ nm and $t_{2H} = 170$ nm, respectively, and the last layer of SiO₂ set to 100 nm. Because of the different thicknesses, the reflection band of the top mirror shifted, but high reflectivity $R \approx 98\%$, comparable

to the initial design in the spectral range of interest, was still maintained, see Figure 2.18.

2.3.3.2 Characterization

Despite the complex fabrication, the designed FP resonators were successfully obtained. Their performance will be presented and compared to the numerical data.

First, vertical and horizontal cross-sections of the fabricated spectropolarimeter were obtained using FIB-cut and SEM; see images in Figure 2.21. The total thickness of the optical device is found to be only 7 μm . The horizontal cross-sections of all pixels (P1, \dots , P6) were imaged to evaluate the sizes of the nanostructures; see Figure 2.22. All nanostructures had a height of $H = 300$ nm, but varied in diameters, D_x and D_y . The measured transverse dimensions of the nanostructures are provided in Table 2.1. As can be seen from the standard deviation of the measured diameters σ , the proximity effect during electron beam exposure leads to certain errors. However, the error is homogeneously distributed in the whole measured area of $20 \times 20 \mu\text{m}^2$.

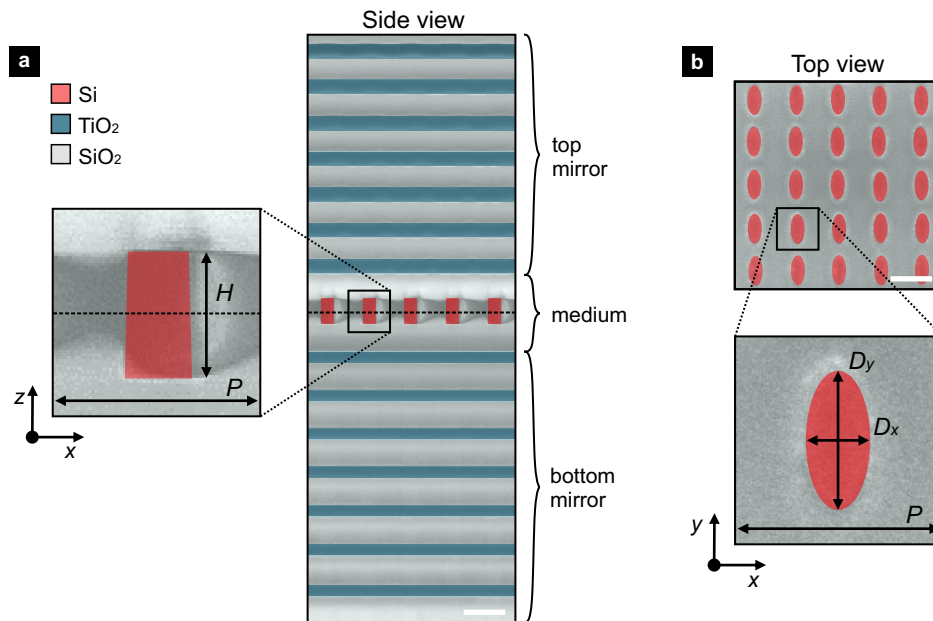


Figure 2.21: Exemplary pixel from the fabricated spectropolarimetric system: (a) side view, (b) top view. Colored SEM images of vertical and horizontal cross-sections of a pixel based on a FP resonator modulated by an array of Si nanostructures. Si is colored red, TiO₂ – blue, SiO₂ – grey. Si nanostructures are defined by their height H and diameter in x and y axis (D_x and D_y , respectively), and are distributed in a square lattice with a period P . Scale bars are equal to 500 nm. The figure is adapted from [S9].

The spectral measurements of the fabricated sample were carried out using a broadband halogen lamp (SLS301, Thorlabs). Its light was delivered to the sample via an optical system as a plane-wave illumination. A linear polarizer was mounted on a rotational stage (PR50CC, Newport) in front of the sample to control the incident light polarization. The sample was positioned, and the position angle was calibrated using a 5-axis positioning system (Aerotech). The transmitted light was collected via 20 μm aperture and a lens system to an optical spectrum analyzer with subnanometer spectral resolution (AQ6370B, Yokogawa). The measured transmittance of the six individual pixels, constituting elements of the super-pixel configuration,

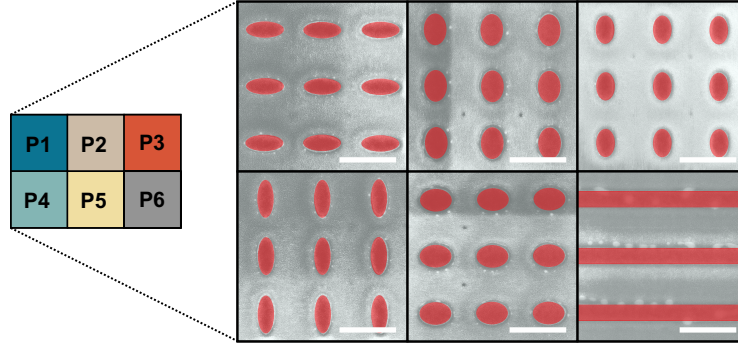


Figure 2.22: Set of the fabricated spectropolarimeter pixels and their exemplary distribution. SEM images of horizontal cross-sections of all pixels (P1, \dots , P6) show cuts 3×3 from the full arrays. Si is colored red; scale bars are equal to 500 nm.

Table 2.1: Measured transverse dimensions ($D_{x,y} \pm \sigma$) of Si nanostructures in the set of 6 pixels (P1, \dots , P6) and measured central wavelengths of their transmission peaks for x and y polarization.

	D_x , nm	D_y , nm	λ_x , nm	λ_y , nm
P1	335 ± 8	145 ± 6	1463	1431
P2	202 ± 5	282 ± 5	1445	1462
P3	162 ± 4	247 ± 4	1430	1446
P4	145 ± 6	335 ± 8	1431	1463
P5	282 ± 5	202 ± 5	1462	1445
P6	-	134 ± 5	-	1432

as shown in Figure 2.22, is presented and compared to simulations in Figure 2.23.

The measured peaks have an excellent agreement with the simulation results regarding their central wavelengths. Considering the reduction of the resonator length compared to the initial design, the anticipated spectral positions of the peaks blue-shifted to $\lambda_1 = 1430$ nm, $\lambda_2 = 1446$ nm, and $\lambda_3 = 1462$ nm. The central wavelengths of the measured peaks are given in Table 2.1, the standard deviation being less than 1 nm. Moreover, the measured peaks reach a transmission of 46%, while the simulated peaks are close to 92%. The width of the measured peaks are slightly broader, in average FWHM = 3.6 nm compared to FWHM = 1.6 in the case of the simulation. Such behavior is induced by the Cr-contamination of the resonator, as discussed in Section 2.3.3.1.

Now, in order to estimate the performance of the pixels, three spectral bands were selected, as described in Section 2.3.1. Since the FP resonances are of a Lorentzian-shape with long tails, they were spaced $\Delta\lambda = 16$ nm apart to minimize the cross-coupling. Accordingly, the three spectral bands of the system were: 1422–1438 nm, 1438–1454 m, and 1454–1470 nm. As can be seen in Figure 2.23(b), the measurements have a high noise floor, which comes from the detector of the spectrometer and is not inherent to the fabricated structures. Thus, prior analytical knowledge is used. Instead of the noisy measurement, the intensity for a given band and polarization state is computed from its Lorentzian fit. As demonstrated later, this enables a significant reduction in noise.

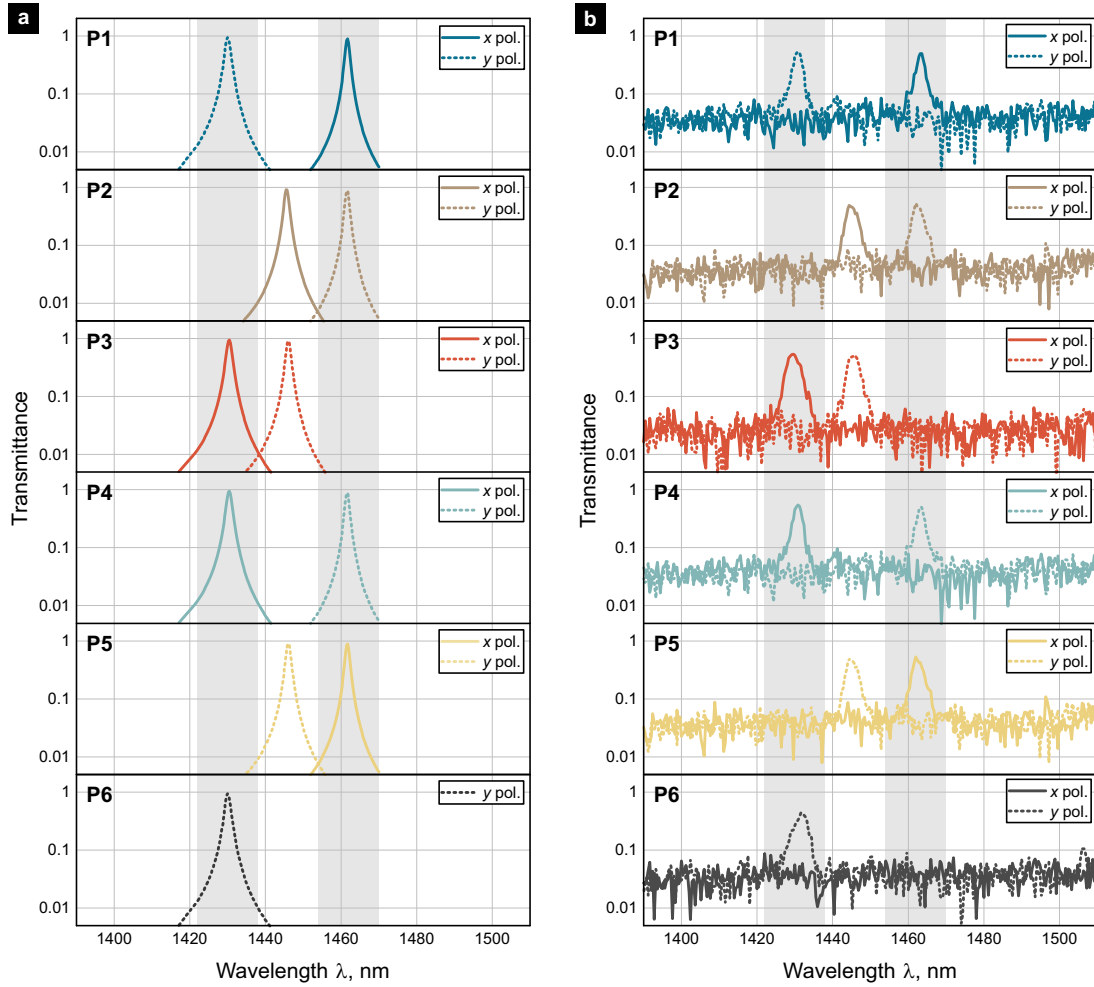


Figure 2.23: Pixels and their transmission spectra. (a) Simulated transmission of 6 pixels, introduced in Figure 2.15, with Lorentzian peaks centered at 1430 nm, 1446 nm, and 1462 nm and distributed in 3 spectral bands of $\Delta\lambda = 16$ nm. (b) Measured transmission of the corresponding pixels. Spectra for x-polarized light are shown in solid lines, for y-polarized – dashed lines. The figure is adapted from [S9].

The elements of the reconstruction matrix, Equation 2.35, are then obtained using the following integral:

$$\alpha = \int_{\lambda_{\min}}^{\lambda_{\max}} T_{pol}(\lambda) d\lambda, \quad (2.40)$$

where λ_{\min} and λ_{\max} are the boundaries of the spectral band, and $T_{pol}(\lambda)$ is the transmittance of a pixel for a given polarization state. Computing these integrals for the measured data at all spectral bands and polarization states results in the following matrix:

$$A = \begin{bmatrix} 0.017 & 0.076 & 2.002 & 2.229 & 0.112 & 0.021 \\ 0.170 & 2.457 & 0.124 & 0.029 & 0.136 & 2.478 \\ 2.877 & 0.160 & 0.034 & 0.147 & 2.577 & 0.126 \\ 2.229 & 0.112 & 0.021 & 0.017 & 0.076 & 2.002 \\ 0.029 & 0.136 & 2.478 & 0.170 & 2.457 & 0.124 \\ 0 & 0 & 0 & 2.432 & 0.239 & 0.042 \end{bmatrix}. \quad (2.41)$$

2.3.3.3 Performance analysis

In order to assess the performance of our spectropolarimeter, it is important to look at the noise propagation through the system. This allows the estimation of the SNR of measured Stokes parameters as a function of the sensor pixel SNR. For this analysis the condition number $k(A)$ is used, since it is a measure of the sensitivity to variations for a standard system of equations $A\mathbf{x} = \mathbf{b}$. The condition number $k(A)$ is defined as:

$$\frac{\|\delta\mathbf{x}\|}{\|\mathbf{x}\|} = k(A) \frac{\|\delta\mathbf{b}\|}{\|\mathbf{b}\|}, \quad (2.42)$$

where $\delta\mathbf{x}$ and $\delta\mathbf{b}$ are small variations on the corresponding vectors \mathbf{x} and \mathbf{b} . A common way to compute the condition number of matrix A , is to take the ratio of the largest singular value and the smallest singular value of the matrix A . As can be seen from Equation 2.42, the condition number $k(A)$ expresses the proportion between any variation of the known vector \mathbf{b} and the unknown vector \mathbf{x} . Thus, in the presented system, it relates the noise of the measured intensities (shot noise, read-out noise, etc.) to the noise of the reconstructed intensities. Using the relation between the polarized intensities and Stokes parameters, the expected value and standard deviation of the reconstructed Stokes parameters can be derived as [S9]:

$$E(\tilde{S}_0) = S_0, \quad E(\tilde{S}_1) = S_1, \quad E(\tilde{S}_2) = S_2, \quad (2.43)$$

$$\sigma(\tilde{S}_0) = \left(\frac{k(A)}{\text{SNR}} \right), \quad \sigma(\tilde{S}_1) = \sqrt{2} \left(\frac{k(A)}{\text{SNR}} \right), \quad \sigma(\tilde{S}_2) = \sqrt{2} \left(\frac{k(A)}{\text{SNR}} \right). \quad (2.44)$$

As can be seen, the reconstruction method is bias-free because the expected values are equal to the true values. Note that the standard deviation of \tilde{S}_0 is smaller than of other Stokes parameters since \tilde{S}_0 is measured twice, according to Equation 2.36. Since the standard deviation is inversely proportional to the SNR, it reduces by a factor of $k(A)$ after reconstruction. The matrix, shown in Equation 2.41, has a condition number of $k(A) = 8.43$. Thus the noise in the reconstructed signal will be increased by at most this factor. For comparison, ideally, with $\alpha_x^6 = 0$ and $\alpha_p^1 = 1$, one obtains $k(A) = 8.0552$.

Next, we will shortly compare the performance to other systems, e.g., the polarimeter reported in reference [71], which uses a metasurface as a polarization-sensitive lens. There, the different polarization states are focused on different parts of the sensor. Even though that system has a condition number of $k(A) = 3.6581$, the metasurface is spatially distanced from the sensor by a focal distance, making its integration difficult. Another example is the spectropolarimeter from reference [80], which achieves a condition number of $k(A) = 2.082$. However, an external spectrometer is needed in their setup. Despite the higher condition number, our nanostructure-modulated spectropolarimeter can be directly integrated on top of a sensor. Furthermore, it does not require external devices, resulting in a very robust and compact system.

Another factor that has to be taken into account is the shot noise. It depends on the total number of photons reaching the detector N_{phot} . In particular, the SNR of a shot-noise limited pixel is given by: $\text{SNR}_{\text{shot}} = \sqrt{N_{\text{phot}}}$. A transmission of 50% means that the number of photons that reach the detector is reduced by a factor of 2. Thus the SNR drops by a factor of $\sqrt{0.5}$. Therefore, a demonstrated system would have SNR reduced by -1.681 dB compared to an ideal system. However, the effect of lower transmission can be partially reduced by measuring longer, increasing the detector's integration time.

2.3.4 Specifications

2.3.4.1 Polarization rotation

In addition to the optical response to the inputs of x and y linear polarization states, the optical response was measured in dependence on the polar angle ϕ . Two different peaks centered at λ_x and λ_y are produced for the aforementioned x and y polarization, while the maximum transmittance of the peaks is a functions of the polar angle ϕ . As can be seen from Figure 2.24, the peak transmittances at λ_x and at λ_y follow the analytically predicted $\cos^2 \phi$ and $\sin^2 \phi$ functions, respectively.

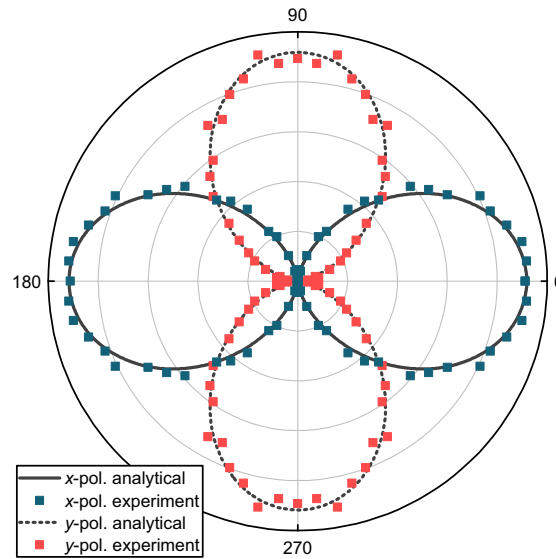


Figure 2.24: Spectral response dependence on polar angle ϕ . Normalized measured intensity at λ_x and λ_y as a function of polarization angle ϕ in case of arbitrarily selected pixel with nanostructure inclusion. The intensity follows analytically predicted $\cos^2 \phi$ and $\sin^2 \phi$ functions, respectively. The figure is adapted from [S9].

2.3.4.2 Angle tolerance

Next, we analyze how the transmittance behaves with increasing angle of incidence θ . This is of particular importance, as multi-layer systems are known for high angle dependence. In Figure 2.25, a blue-shift of the spectral peak is observed with the increase of the incidence angle θ in x -axis with respect to the surface normal for x - and y -polarization. Quantitatively similar results were observed for all of the pixels.

During the device implementation, the chief ray angle of the imaging optics must be taken into account. For a conventional optical system, this angle will increase radially from the center to the detector edge. The increasing incident angle leads to the blue-shift of the transmission peaks, as shown in Figure 2.25. However, this spectral shift can be compensated by the proportional scaling of the effective resonator length L , e.g., by scaling the size of the high-index inclusions [224]. Furthermore, a telecentric optical system can be used instead. Then, the chief ray angle is constant over the entire detector; thus, no blue-shift occurs. Also, a system with a low NA is recommendable since a high NA will increase the transmission peak width [191], thus reducing the spectral resolution of the system.

The presence of a focused beam may also influence the polarization reconstruction. When a linearly polarized beam is focused by an optical system, some of the light will become cross-polarized [236, 237].

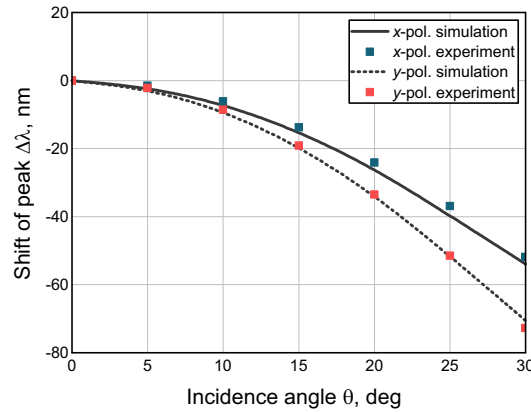


Figure 2.25: Spectral response dependence on incident angle θ . Blue-shift of the central wavelength of the peak λ_c for x - and y -polarization in case of an empty resonator. Simulations are shown in solid and dashed lines, while blue and red squares depict experimental points. The experimental points were measured in the first quarter, from 0° to 90° degrees and symmetrically replicated to other quarters. The figure is adapted from [S9].

From these considerations, it can be concluded that in order to minimize this effect, a telecentric and low NA optical system should be used.

2.3.4.3 Maximum bandwidth

The total bandwidth of the system is defined as the spectral distance of the nearest resonance. It is an important parameter for the imaging applications of interest as well [230]. As mentioned before, the bandwidth of the presented spectropolarimetric system depends on the reflection band of the mirrors and the maximum separation of the transmission peaks. The relative bandwidth of a DBR-mirror using quarter-wavelength sections is described by [238]:

$$\frac{\Delta f}{f_0} = \frac{4}{\pi} \arcsin(\rho), \quad (2.45)$$

with ρ being the Fresnel reflection coefficient. From this equation, it is clear that the mirror bandwidth depends only on the difference between the refractive indices of the two materials used in constructing DBRs. In our case, the mirrors limit the bandwidth to roughly 400 nm; see Section 2.3.2. However, using more advanced mirror designs [239], it is possible to obtain a wider reflection band. Therefore, bandwidth limitations due to the mirrors can be mitigated.

Thus, in practice, the total bandwidth is limited by the maximum achievable separation of two linear polarization peaks. This separation between the peaks ultimately determines the maximum achievable total bandwidth of the system, since one of the transmission peaks has to be outside of the reconstruction bands. As illustrated in Section 2.3.2, in our design the maximum separation of the two peaks is equal to 127 nm. It can be achieved with a subdiffractive grating of 200 nm width. This results in one row of the matrix having only one peak, which is the necessary condition for the spectropolarimetric retrieval. Hence, the maximum number of bands can be computed using:

$$N = \left\lfloor \frac{\text{BW}}{\Delta\lambda} \right\rfloor - 1, \quad (2.46)$$

where BW is the total bandwidth of the system, and $\Delta\lambda$ is the width of a single spectral band.

2.3.4.4 Spectral resolution

In the spectropolarimetric system, the spectral positions and the width of the spectral bands have to be chosen carefully for the best performance. By decreasing the width of a spectral band one can increase the number of total spectral bands and, subsequently, the spectral resolution. However, as shown in Figure 2.26, reducing the width of spectral band $\Delta\lambda$ below the FWHM increases the condition number and, in turn, decreases the SNR of the system. The increase of the condition number $k(A)$ can be attributed to the spectral overlap of the neighboring peaks. This translates to smaller differences between the rows of the reconstruction matrix, making equations more linear dependent. It is recommended to use $\Delta\lambda = \text{FWHM}$, limiting the spectral resolution to the FWHM.

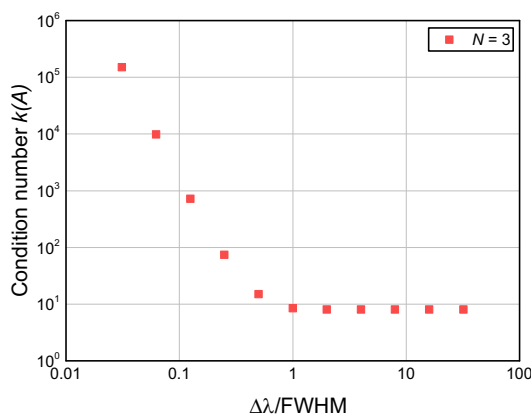


Figure 2.26: Condition number $k(A)$ of 3 bands versus spectral resolution. Condition number $k(A)$ of reconstruction matrix is shown in cases of different ratios between the single bandwidth $\Delta\lambda$ and the transmission peak width FWHM, assuming Lorentzian-shape peaks. The figure is adapted from [S9].

2.3.5 Extended design considerations

Using the design limitations discussed before, meaning the maximum bandwidth of 127 nm and spectral resolution of 1 nm ($\Delta\lambda = \text{FWHM}$), one can consider an ideal spectropolarimetric sensor with 126 bands (42×3). Then, as described in the Section 2.3.1 for the system to be able to retrieve the first three Stokes parameters (S_1, S_2, S_3), it would have to consist of 504 pixels in total. Such a system would have a condition number of 14.57; see [S9] for more details.

For implementing the presented nanostructure-modulated FP-based spectropolarimetric system in an actual imaging device, telecentric optics are recommended. The measured wavelengths will vary along the image plane. An optical system with a low NA is also recommended if narrow peak widths are required since higher NA will increase the peak width of the transmission peaks [191].

Since our system effectively uses 4 pixels per spectral band, the spatial resolution is equal to a quarter of a standard spectral system (1 pixel per spectral band). This is also in accordance with a typical spectropolarimeter where 4 pixels are used to determine the polarization state. The reduction in spatial resolution arises from an increased amount of obtained information per spatial location while keeping the number

of pixels on the detector fixed. This factor is independent of the presented system and will occur for any spectropolarimetric system.

2.4 Chapter summary

The key idea of the Chapter 2 was to prove that FP resonators can be tailored by using high index dielectric nanostructures as inclusions. In particular, the nanostructures were used to modulate the effective index of the cavity and tailor the FP resonator. The phenomena were successfully applied to create filters for blood oxygen sensing and the conceptual demonstration of a spectropolarimeter.

The first part of Chapter 2 presented ultra-thin polarization-insensitive FP filters for biomedical applications. A multispectral performance was demonstrated, while the filters were optimized for the highest SNR in two spectral bands for blood-oxygen sensing. Even though similar FP systems have been presented before [70, 76, 87–89, 91, 92], they were not optimized towards the indicated biomedical application. Here, it was also demonstrated how usually the unwanted error of using nanostructures inside a cavity – uneven layer due to varying filling factors – could be utilized to increase the spectral bandwidth by a factor of 2. The numerically optimized filters were fabricated and integrated on an actual CMOS sensor, proving that the nanostructured FP resonators can be implemented in a real optical device. Despite the lower transmission in the fabricated samples, the results are sufficient for conceptual demonstration.

The second part of Chapter 2 shows the feasibility of a planar spectropolarimeter. As a proof of concept, a set of 6 pixels with transmission peaks of 50% and FWHM = 3.6 nm is experimentally demonstrated. The peaks were separated into three spectral bands with $\Delta\lambda = 16$ nm and sorted by their polarization state. Using the measured data in the reconstruction matrix, a condition number of $k(A) = 8.43$ is obtained, which is extremely close to the theoretical limit of $k(A) = 8.06$. Finally, the design could be scaled to other spectral ranges by changes in material selection, e.g., using TiO_2 instead of Si in the visible spectral range to minimize intrinsic losses. Using several different cavities at once, this would allow a broadband sensor. The system would also benefit from a more anisotropic inclusion inside the cavity in place of the grating to increase the bandwidth. Finally, the system could be extended with additional layers of retarders to enable the measurements of circularly polarized light, allowing the retrieval of the full Stokes vector.

The results on polarization-insensitive FP filters with Ag mirrors and TiO_2 nanostructures (for blood-oxygen sensing), discussed in Section 2.2, are in the process to be published at the time of writing this thesis [S11]. The concept of spectropolarimeter with DBRs and embedded polarization-sensitive Si nanostructures, presented in Section 2.3, is patented [T1], while the experimental demonstration is published in Optics Express [S9].

Chapter 3

Laser-induced tailoring and structuring of metasurfaces

Nanostructure-based systems have a great potential to be implemented in optical systems, as shown previously. However, optically resonant metasurfaces often remain inferior to their conventional counterparts not just because of the performance but also because of the size-limited and complex fabrication [98]. Hence, for metasurface-based elements to be applied in mass-production devices, it is necessary to create new fabrication techniques or significantly improve the existing ones, which is the goal of Chapter 3.

In the first part of this chapter, Section 3.1, a complementary technique for post-processing of large-area metasurfaces is presented. The method is based on ultrashort laser pulses with a duration of $\tau_p \leq 10$ ps, which are used to induce local functionalities within or even beyond the capabilities of the conventional two-dimensional fabrication. It will be demonstrated how the resonant behavior of the preprocessed dielectric metasurface elements can be exploited to engineer a specific absorption profile, which leads to a spatially-selective heating and a customized modification. In particular, two different photothermal effects, crystallization and reshaping, are utilized, while localizing the heat with a tightly focused laser beam. Two distinct study cases will be explicitly demonstrated: first, a spatial pixelation of a large-area metasurface and, second, a height modification of metasurface elements, demonstrating the potential to reduce the complexity in the fabrication of non-uniform metasurface-based optical elements, which is otherwise quite expensive and complex task.

The second part of this chapter, Section 3.2, introduces a technique for the fabrication of Mie-resonant metasurfaces. Here, single-pulse laser interference is used for direct patterning of a homogeneous amorphous Si film into an array of Mie resonators with a few hundred nanometers in diameter. The proposed technique is based on laser-interference-induced dewetting. Precise control of the laser pulse energy enables the fabrication of ordered dielectric metasurfaces in areas spanning tens of micrometers and thousands of hemispherical nanoparticles with a single laser shot. The fabricated nanoparticles exhibit a wavelength-dependent optical response with a strong electric dipole signature. Variation of the predeposited Si film thickness allows tailoring of the resonances in the targeted visible and infrared spectral ranges.

The results presented in Section 3.1 and Section 3.2 were successfully published in *Optics Express* [S8] and *ACS Nano* [S10], respectively.

3.1 Photothermal tailoring of metasurfaces

An intriguing way to obtain non-uniform metasurfaces is using laser-induced thermal effects [117], where a lithographically preprocessed uniform metasurface is locally modified by laser irradiation, as illustrated in Figure 3.1(a,b).

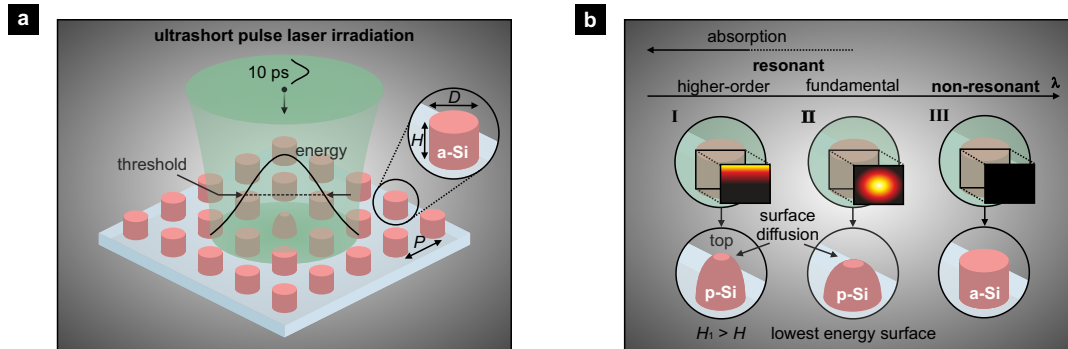


Figure 3.1: Illustration of laser-induced tailoring of amorphous Si metasurfaces using a pulsed laser. (a) Spatial positioning of a focused laser beam. Sufficient pulse energy results in a phase change; at higher temperatures, the material melts. Metasurface elements are defined by diameter D , height H , and period P . (b) Spatially-selective heating engineered by electromagnetic field distribution in the metasurface elements and the material absorption. Different regimes: (I) high absorption at high-order resonances, $\lambda \ll nD$, with hotspot at the top, resulting in height increase, $H_1 > H$; (II) high absorption at fundamental resonances, $\lambda \approx nD$, with a hotspot in the center and reshaping towards global lowest energy surface; (III) non-absorptive and non-resonant regime, $\lambda \gg nD$. The figure is adapted from [S9].

In this section, laser-induced thermal effects are utilized for flexible and large-scale post-processing of dielectric metasurfaces. In particular, laser irradiation is used to locally modify (pixelate) nanostructure-based transmissive spectral filters. Moreover, the spatial selectivity is used to obtain an additional degree of freedom in the spatial control of Si metasurface elements. The laser-matter interaction is investigated employing geometry analysis, linear and Raman spectroscopy, and complemented by numerical simulations. The use of ultrashort pulses is shown as a promising complementary technique for dielectric metasurfaces beyond the limits of planar fabrication, thus opening new possibilities in the field of nanophotonics.

3.1.1 Photothermal effects

3.1.1.1 Spatially-selective absorption

Laser-induced thermal effects depend on many different parameters: the optical and thermal properties of the target material, the environment it is being modified in, and the parameters of the irradiation source such as spectrum, pulse duration, spatial energy distribution, and energy density [156, 240]. In addition, nanostructured materials tend to obtain wavelength-dependent optical properties. Si nanostructures, as well as other high-index nanostructures, possess strong fundamental ED and MD resonances at the wavelengths close to their optical size, $\lambda \approx nD$ [8]. Furthermore, higher-order resonances appear at shorter wavelengths, $\lambda \ll nD$. Each resonant mode is associated with a particular electromagnetic field distribution in the nanostructure volume, thus enabling a spatial control of energy dissipation. If accounted for, this provides an additional degree of freedom in post-processing of the uniform dielectric metasurfaces.

The investigation of laser-induced tailoring is based on Si metasurfaces fabricated from a thin film of amorphous Si on top of a glass substrate; see Appendix A for dispersion parameters. Using EBL and reactive ion etching, the film was structured into polarization-insensitive disk-shaped nanostructures, illustrated in Figure 3.1. Multiple metasurfaces were fabricated with a diameter of their elements D varying from 55 to 165 nm, a period P ranging from 200 to 300 nm, and a height H fixed at 175 nm. The diameter variation within the given range results in metasurfaces with their fundamental ED and MD resonances in the visible spectral range; as seen in the transmission spectrum in Figure 3.2(a). Furthermore, a metasurface with the following parameters was investigated: a diameter $D = 560$ nm, a period $P = 794$ nm, and a height $H = 220$ nm, which results in the fundamental resonances in infrared spectral range; see transmission spectrum in Figure 3.2(d).

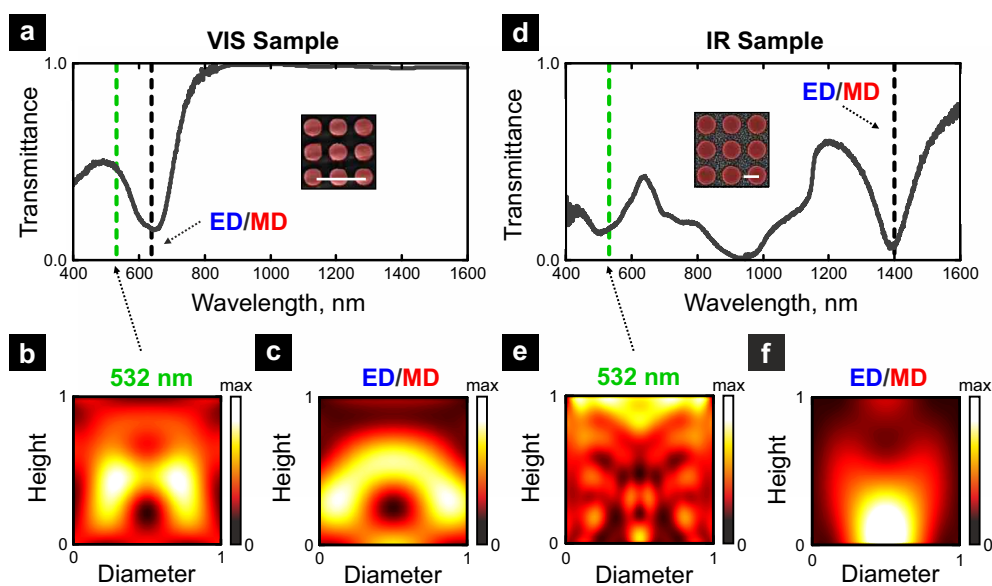


Figure 3.2: Optical response of Si metasurfaces before the photothermal treatment. (a) Measured transmittance of Si metasurface with ED and MD resonances in the visible region ($D = 140$ nm, $P = 250$ nm, $H = 175$ nm). (b,c) Calculated absorption profile at the cross section of an element of metasurface from (a), when irradiated at: (b) $\lambda = 532$ nm, (c) $\lambda = 640$ nm. (d) Measured transmittance of Si metasurface with ED and MD resonances in the infrared ($D = 560$ nm, $P = 794$ nm, $H = 220$ nm). (e,f) Calculated absorption profile at the cross section of an element of metasurface from (d), when irradiated at: (e) $\lambda = 532$ nm, (f) $\lambda = 1400$ nm. The insets in (a,d) show colored SEM images of the respective samples, the scale bars are equal to 500 nm. The figure is adapted from [S9].

For the post-processing, first, an overview of the linear optical properties of pre-processed samples is obtained to estimate their influence on the process. In Figure 3.2, one can note measured transmission spectra and calculated spatial distributions of absorption for two optically distinct Si metasurfaces. In particular, in Figure 3.2(a), the transmission spectrum is shown for a metasurface with its resonances in the visible spectral range ($D = 140$ nm, $P = 250$ nm, $H = 175$ nm). The transmittance minimum denotes the resonances at $\lambda = 640$ nm, which is associated with the closely spaced ED and MD resonances [S4]. In order to gauge how the laser energy could be deposited in the metasurface elements, the spatial distribution of the absorbed laser power is calculated at the wavelength of irradiation λ ; see Figure 3.2(b). As the irradiation wavelength is spectrally close to the fundamental dipolar resonances, the largest absorption is observed in the middle of the nanostructure. For comparison, irradiation directly at the resonance would

yield a qualitatively comparable energy distribution, as shown in Figure 3.2(c). However, a somewhat different behavior is found in the metasurface, which has its fundamental ED and MD resonances in the infrared ($D = 560$ nm, $P = 794$ nm, $H = 220$ nm), as shown in the transmittance in Figure 3.2(d). Here, the fundamental resonances and the excitation wavelength $\lambda = 532$ nm are further apart, with the latter coinciding with a high absorption range and higher-order optical resonances. As shown in Figure 3.2(e), this leads to absorption primarily at the top of the nanostructure. This is substantially different from the previous case and the excitation at the fundamental resonances, presented in Figure 3.2(f).

Our simulations indicate a spatial control of the onset of the laser-induced thermal effects. The optical simulations were carried out by FDTD; see details in Section 3.1.2. The absorbed power at the cross-sections of the metasurface elements shows distinct hot-spots, where the material threshold F_0 is reached first, inducing the anticipated modification. The smallest spatial scale of thermal effects is estimated by the thermal diffusion length [135]:

$$L_{\text{th}} \propto \sqrt{2\alpha\tau_p}, \quad (3.1)$$

where τ_p is the laser pulse duration, and α is the thermal diffusivity. The thermal diffusivity is calculated as $\alpha = k/(\rho c_p)$, where k is the thermal conductivity, ρ is the density, and c_p is the specific heat. As noted in Equation 3.1, the length-scale is directly related to the pulse duration; the longer the duration, the larger the thermal diffusion length. Thus, a laser source is chosen with relatively short pulses, $\tau_p = 10$ ps. Using a single pulse, this allows a spatial resolution as high as 4 nm, considering that amorphous Si has the density of $\rho = 2280$ kg/m³, specific heat of $c_p = 880$ J/(kg K), and a relatively low thermal conductivity of $k = 1.8$ W/(mK) [241, 242]. In contrast, a longer duration of operation, e.g., using nanosecond pulses or a CW irradiation would induce heat penetration throughout the whole Si nanostructure without the possibility to obtain small features.

3.1.1.2 Laser damage threshold

Next, an experimental study is performed to find the laser damage threshold F_{th} for the thermal modifications to take place. It is known that the fluence threshold of homogeneous amorphous Si thin-films using a Gaussian laser beam is in the range from 100 to 220 mJ/cm² [243–246]. However, there was no in-depth investigation in the case of metasurfaces of Si or any other materials, especially considering their geometry.

To experimentally determine the laser damage threshold F_{th} , each investigated metasurface was irradiated with a set of laser pulses and a step-wise increase of the pulse energy. At each step, the diameter of the modified area d is measured from the SEM images. It is considered that the modification is either intrinsic if the nanostructure is heated above the crystallization temperature T_c , or shape-related, if the temperature gets close to or above the melting temperature T_m . Using the measurements, the threshold F_{th} can be calculated from the well-defined relation between the diameter of the modified area d , and the energy density F [247]:

$$d^2 = d_{\text{spot}}^2 \ln(F/F_{\text{th}}), \quad (3.2)$$

where d_{spot} is the laser spot diameter.

The obtained threshold F_{th} values are plotted against the diameter to period ratio D/P for all of the

investigated samples; see Figure 3.3(a). Here, the threshold of Si metasurface F_{th} is found to be similar or smaller than the damage threshold of a homogeneous Si thin film [243–246]. Moreover, if normalized to the metasurface absorption at $\lambda = 532$ nm, the obtained threshold values follow a linear trend; see Figure 3.3(b). This is linked to the material surface to air ratio and the high index contrast to the environment. The obtained dependence on the diameter to period ratio D/P helps to predict the required energy for precise tailoring of the nanostructured samples.

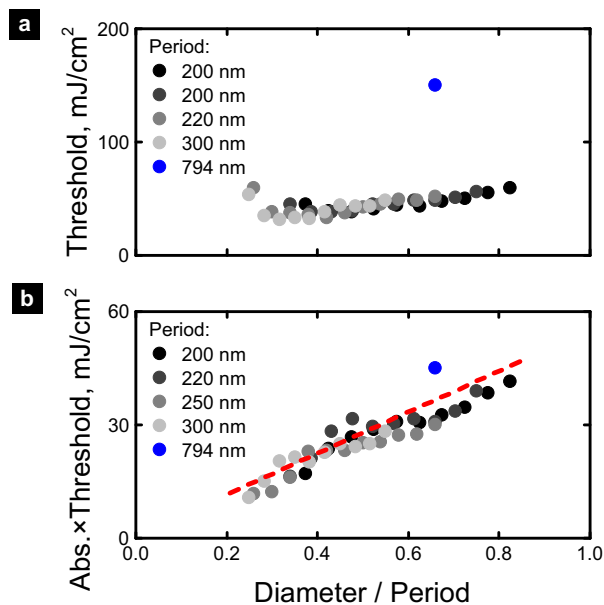


Figure 3.3: Energy density threshold of Si metasurfaces vs diameter to period ratio: (a) calculated from measured data, according to [247], (b) same values, but normalized to the absorption of the corresponding samples at $\lambda = 532$ nm. The samples are color coded by their period P : 200, 220, 250, 300, and 794 nm. The threshold grows with the size of the metasurface elements. The dashed line represents a linear fit of the normalized experimental points. The figure is adapted from [S9].

3.1.2 Methods

3.1.2.1 Experimental setup

As the irradiation source, a high peak power picosecond laser (Ekspla) was chosen. The laser has a pulse duration of $\tau_p = 10$ ps, and a pulse repetition rate up to $\nu = 1024$ kHz. The fundamental wavelength $\lambda = 1064$ nm was transformed into a second harmonic with wavelength $\lambda = 532$ nm in the resonant spectral range of the investigated samples and the high-absorption of amorphous Si. The diameter of the Gaussian-shape laser beam was $d_1 = 5$ mm, as measured at $1/e^2$ level of intensity. The laser beam was focused by a $f = 50$ mm lens into a spot-size of $d_{spot} = 5.6$ μ m, calculated by the pulsed beam spot-size measurements [247]. The samples were positioned by a high-precision multi-axis stage (Aerotech). The experiments were carried out in ambient conditions.

3.1.2.2 Sample characterization

The spectral analysis was done with a plane-wave illumination using an inverted optical microscope system (Axio Observer D1, Carl Zeiss) with an integrated broad-band VIS/IR imaging spectrometer (iHR320, Horiba). In addition, SEM images were taken (Helios NanoLab G3 UC, FEI), and the surface topography was measured by an AFM with integrated peak force tapping technology (Dimension Edge, Bruker). The Raman spectra were taken using a commercially available confocal Raman system (WITec) equipped with a 785 nm laser. The light was focused onto the sample, and the scattered light was collected with the same microscope objective (NA = 0.95). The measurements were taken with a laser power of 1 mW and an integration time of 1 s with five accumulations. Measured spectra were background corrected using the statistics-sensitive non-linear iterative peak-clipping (SNIP) algorithm with 100 iterations.

3.1.2.3 Numerical simulations

Optical simulations were carried out using FDTD (Lumerical). The simulations were done using a 3D model of an infinite array of amorphous Si nanostructures. The unit cell model was implemented with PBC on the sides and PML on the top and bottom of the simulation domain. The unit cell was illuminated by a normally incident plane-wave source. Frequency domain field and power monitors were placed to record the electric and magnetic fields and the transmittance of the nanostructures. The FDTD method was also used to obtain the optical power absorbed by the Si nanostructure and transfer it further for FEM-based thermal simulations for calculating the heat diffusion. Here, the step-like heat source was set to the duration of the laser pulse, $\tau_p = 10$ ps.

3.1.3 Crystallization of metasurface elements

Next, it will be demonstrated how the laser-induced spatially-selective internal and shape changes of the metasurface elements can be harnessed for control of their optical response. The laser-induced tailoring is applied to amorphous Si metasurfaces with their fundamental ED and MD resonances close to the irradiation wavelength $\lambda = 532$ nm. Because of wavelength-dependent absorption and scattering, such structures can be used as dielectric nanostructure-based transmissive color filters, shown in Chapter 1 as a promising alternative to conventional dye-based filters. However, their fabrication is usually done on a small-scale by lithography techniques. Thus, a complementary technique is proposed – laser pixelation – which is similar to laser printing [248] in the sense that it allows using a large-scale fabrication technique for an initial homogeneously nanopatterned template and then locally post-process it for the required functionality. The technique utilizes reshaping and crystallization of the amorphous material, as illustrated in Figure 3.4.

3.1.3.1 Shape dynamics and thermal regimes

For the proof of concept, a nanostructure-based G (green) color filter is chosen. It is based on a uniform amorphous Si metasurface ($D = 140$ nm, $H = 175$ nm, $P = 250$ nm). The absorption of metasurface elements at the wavelength of irradiation is shown in Figure 3.2(b,c). First, a uniform energy distribution over a large area is obtained to investigate the laser-induced thermal effects systematically. This was carried out by a

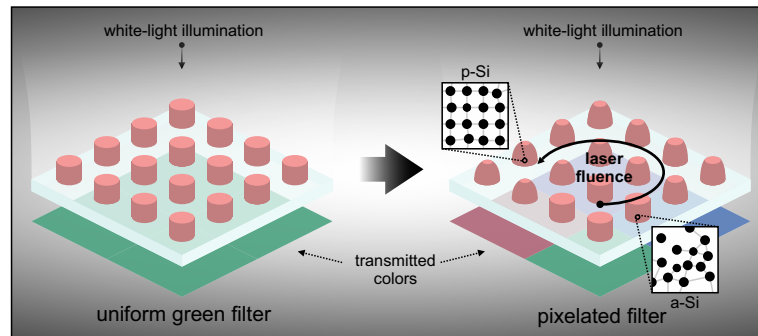


Figure 3.4: Illustration of laser pixelation, where the uniform nanostructure-based filter is spatially tailored by increasing the laser fluence for specific functionality, e.g., the green filter is modified to adhere to a pixelated multi-color pattern. The modification is not just the reshaping but also the crystallization of a-Si, as indicated by the artistic impression of the atom distribution.

partial overlap of several laser shots in a hexagonal configuration, which corresponds to the densest packing of the circular laser spots. The laser energy density at $\lambda = 532$ nm was increased in several steps until the nanostructures became completely molten, thus moving from their initial position, subsequently disordering the lattice. Note that while disordered metasurfaces offer some intriguing properties [174], within this work, the disorder generated by laser irradiation will not be further characterized. Thus, regimes are analyzed up to shortly before the appearance of disorder. Figure 3.5(a) shows SEM images of experimentally modified metasurface elements after irradiation with laser energy density F of 50, 56, 71, and 170 mJ/cm², respectively, together with resulting transmissive colors and approximate thermal regimes, determined by spectroscopic measurement, geometric analysis, and visual observation.

In general, it is known that the crystallization of amorphous Si starts at $T_c = 900$ K [123], whereas Si melts at $T_m = 1420$ K [249]. Furthermore, when the average temperature of the metasurface elements exceeds the melting temperature of T_m , they melt completely, and a chaotic conglomeration is observed, extinguishing the functionality of the metasurface. Even though a clear threshold for the latter was not distinguished, for the investigated filter, it is predicted at $F \approx 100$ mJ/cm². Figure 3.5(b) shows measured diameters and heights, as well as calculated volumes of several analyzed metasurface elements at different thermal regimes. The increase of energy density results in a slight growth of the average diameter D from 142 ± 4 nm to 146 ± 5 nm, while the height H decreases from 176 ± 6 nm to 166 ± 6 nm. As anticipated by the mechanism of dewetting [119], corners of the metasurface elements become rounder at higher energies. However, only minimal change is anticipated in the volume, see Figure 3.5(b), as long as the ablation regime is not reached.

3.1.3.2 Spectral and modal analysis

The post-processed metasurfaces are spectrally characterized. Measured transmission spectra of the metasurfaces are shown in Figure 3.6(a). One can find a dip in all of the spectra due to the fundamental ED and MD resonances. Although it is not strongly pronounced because of the high absorption of amorphous Si in the visible spectral range, the resonances and the subsequent dip blue-shift by $\Delta\lambda \approx 100$ nm with the increase of the laser energy density F ; see Figure 3.6(a). However, such a significant shift of the optical

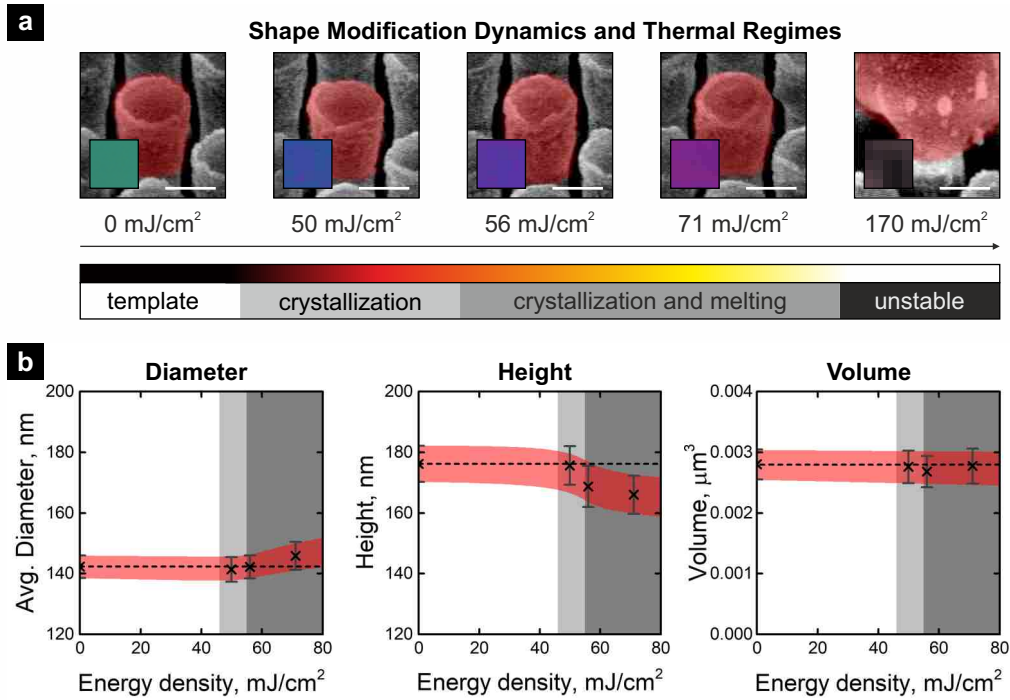


Figure 3.5: Shape modification and modification dynamics due to laser pixelation of Si metasurface elements with ED and MD resonances in the visible spectral range. (a) SEM images of a unit cell after irradiation with different energy densities and respectively identified thermal regimes via shape and Raman measurements. The scale bars denote 100 nm. The insets show the transmitted colors of the metasurfaces. (b) Measured geometrical parameters after irradiation: average diameter (left), height (center), and volume of modified nanostructures (right). The dashed line highlights the values for the unmodified template. Crosses with error bars depict measurements after irradiation. The red shade denotes the interval of uncertainty. The different modified regimes defined in (a), crystallization, crystallization, and melting regime, are highlighted in light- and dark grey, respectively. The figure is adapted from [S9].

resonances cannot be explained only by the geometry changes mentioned above.

In contrast to the reshaping-based laser printing [52], the spectral blue-shift is attributed to the intrinsic changes of the amorphous material – the crystallization. The difference in the refractive index of amorphous Si and crystalline Si is relatively large in the visible spectral range, i.e., $\Delta n \approx 0.3$ at $\lambda = 532$ nm (see Appendix A for refractive index of Si). Raman spectroscopy is a common tool to determine the phase of Si. Thus, the Raman spectra of the Si sample are measured before and after the irradiation; see plots in Figure 3.6(b). Raman measurements were performed using a commercially available confocal Raman system; see Section 3.1.2 for more details. For the template, a broad maximum is noted at $\nu = 480$ cm⁻¹, which corresponds to a vibrational mode of amorphous Si. A peak at $\nu = 510$ cm⁻¹ appears after the irradiation of the template and can be attributed to the formation of grain boundaries and nanocrystals. In contrast, the peak of crystalline Si is expected slightly further at $\nu = 520$ cm⁻¹ [250–252]. As the laser energy density F increases, the FWHM of the peak drops from $\Delta\nu \approx 53$ cm⁻¹ to $\Delta\nu \approx 20$ cm⁻¹. Therefore, the phase transition to the polycrystalline phase is assigned as a key contributor to the change of optical response.

To justify this further, a numerical simulation is done, where the refractive index was fixed and just the aforementioned geometry changes are considered. Then, the ED and MD resonances were tracked and compared to the experimentally obtained dips. Figure 3.6(c) shows the comparison, where it seems that

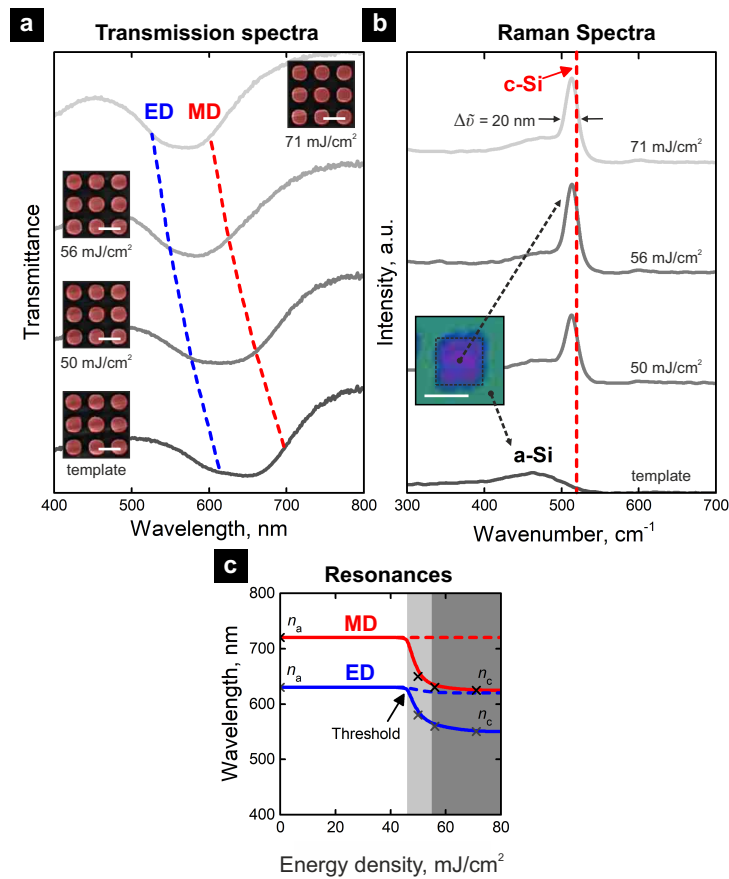


Figure 3.6: Modification of optical resonances based on crystallization. (a) Transmittance before and after photothermal reshaping of nanostructure-based G color filter. Insets show SEM images. The scale bar is 250 nm. Central wavelengths of ED and MD resonances are highlighted by blue and red dashed lines, respectively (b) Raman spectra measurements of the samples with a-Si and c-Si fingerprints highlighted. (c) Spectral positions of ED and MD resonances depending on the laser energy density applied. The crosses show points where full analysis was carried out. Dashed lines show simulation results of amorphous Si with the same geometry. The figure is adapted from [S9].

there is almost no change at all, if the refractive index is fixed, while the change is significant if one applied the change of the material properties. Accordingly, this confirms that prediction of crystallization.

3.1.3.3 Laser pixelation

Up to now, it has been shown that it is possible to modify the lithographically pre-processed G filter to shift its optical resonances and subsequently change its transmissive color. To further emphasize the applicability, laser-induced thermal effects are used to create user-defined patterns and individual color pixels, i.e., pixelate the metasurface.

By using the same laser energies as in Figure 3.6, a multispectral filter array is designed. In Figure 3.7, experimentally realized transmissive colors are shown, as depicted in a CIE 1931 chromaticity diagram. They correspond to different laser energies applied. Here, the chromaticity range is limited by the aforementioned $\Delta\lambda \approx 100$ nm blue-shift of the dipole resonances. A broader color range could be achieved with more templates, e.g., nanostructure-based R filter tailored to transmit yellow. Furthermore, a white-light transmission microscope image of a pixelated green filter is shown in the inset of Figure 3.6. Its pixel size is equal to 50 μm . The high precision of the laser beam permits a square-shape of the pixels and an accurate

position to each other. Each of the uniform pixels consists of 450 partially overlapped laser shots. Despite a large number of laser shots (pulses), a laser source with a high repetition rate and a fast positioning table permits this within seconds.

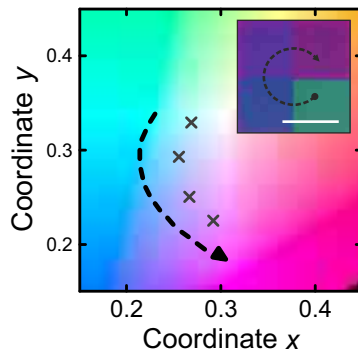


Figure 3.7: Filter colors realized by laser modification denoted in the CIE 1931 chromaticity diagram. The inset shows realized multispectral filters from the G filter template, as imaged by transmitted light microscope. The pixel size and scale bar is $50\ \mu\text{m}$. The figure is adapted from [S9].

Moreover, even though the circular spot-size limited the laser pixelation resolution in our proof-of-concept experiments, it is sufficient to achieve semi-square $5\ \mu\text{m}$ pixels by control of laser energy in respect to the threshold and partial overlap of 4 laser shots. Besides the G filter, this was also done for templates of R and B filters, as shown in Figure 3.8, which proves that the laser-induced tailoring may be applied to post-process nanostructure-based filters of all colors of the standard RGB pattern.

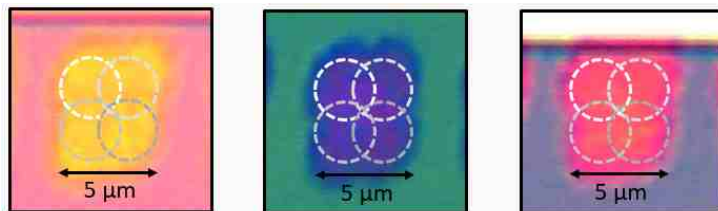


Figure 3.8: Pixelation of nanostructure-based color filters using 4 overlapped Gaussian spots. $5\ \mu\text{m}$ pixels on R, G, and B samples using the spot overlap, as imaged by transmission optical microscope. Scale bar – $5\ \mu\text{m}$.

In perspective, the size of the laser spot could be reduced even further using a high NA objective or a shorter irradiation wavelength. This would enable using the laser as a single nanostructure manipulation tool, as demonstrated by using other techniques such as AFM-assisted reshaping [128].

3.1.4 Controlled reshaping of metasurface elements

In the experiments discussed so far, the fundamental dipole resonances of the dielectric metasurface elements are used to tailor their refractive index without a firm control of the shape. Laser-induced reshaping of the nanostructures was initially demonstrated in plasmonics [127]. Later, a particular field distribution was used for an anisotropic reshaping of plasmonic nanostructures [128, 130], but was never utilized in dielectric metasurfaces. Here, it will be demonstrated how, by engineering the absorbed power profile and using ultrashort pulses, one can obtain a spatially selective reshaping of dielectric metasurface elements.

3.1.4.1 Shape modification dynamics and thermal regimes

In order to obtain spatially-selective reshaping, one has to select a metasurface with access to higher-order resonances. Thus, a sample with the larger metasurface elements was selected: $D = 560$ nm, $P = 794$ nm, $H = 220$ nm. Laser irradiation at $\lambda = 532$ nm excites higher-order resonances and is absorbed predominantly at the top of the elements, as shown in Figure 3.9. Here, the normalized temperature in the metasurface is indicated at different times steps after irradiation by a 10 ps pulse.

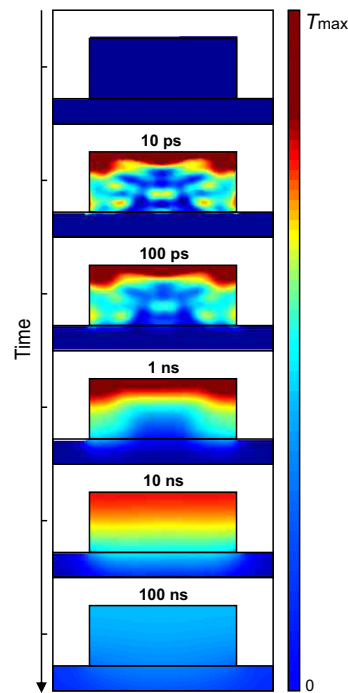


Figure 3.9: Normalized temperature maps of Si unit cell after $\tau_p = 10$ ps irradiation at $\lambda = 532$ nm. Sample parameters: diameter $D = 560$ nm, period $P = 794$ nm, and height $H = 220$ nm. Logarithmic timescale goes from 0 s (template) to 10 ps, 100 ps, 1 ns, 10 ns, and 100 ns. The maps show x - y cross-sections.

The template was irradiated by a set of single pulses while steadily increasing the energy until the ablation. The laser-induced thermal effects were analyzed by observation of shape and spectral response. Figure 3.10(a) shows SEM images of the metasurface elements irradiated by different laser energies, together with a sketch denoting the thermal regimes. For laser energy densities below $F \approx 150$ mJ/cm² the geometry remains unchanged, while its further increase results in temperatures close to the melting point $T_m = 1420$ K [249]. The nanostructures develop curved corners, which is happening exclusively at the top of nanostructures. Such spatial confinement is attributed to the unique absorption profile with the hot-spot at the top; see Figure 3.2(e). The induced heat remains strongly localized during the pulse duration of $\tau_p = 10$ ps because it takes tens of nanoseconds for the heat to diffuse throughout the amorphous Si nanostructures; see Figure 3.9.

Accordingly, a substantial increase of the vertical dimensions is noted for the modified nanostructures, while the diameter at the bottom seems to be sustained, as shown in Figure 3.10(a). From the template up to the unstable case, the height H increases almost by a factor of 2, from 220 ± 13 nm to 434 ± 54 nm, while the average diameter D decreases from 560 ± 5 nm to 300 ± 42 nm; see Figure 3.10(b). The nanostructure becomes somewhat conical rather than hemispherical, which was the case in the examples of CW [131] or

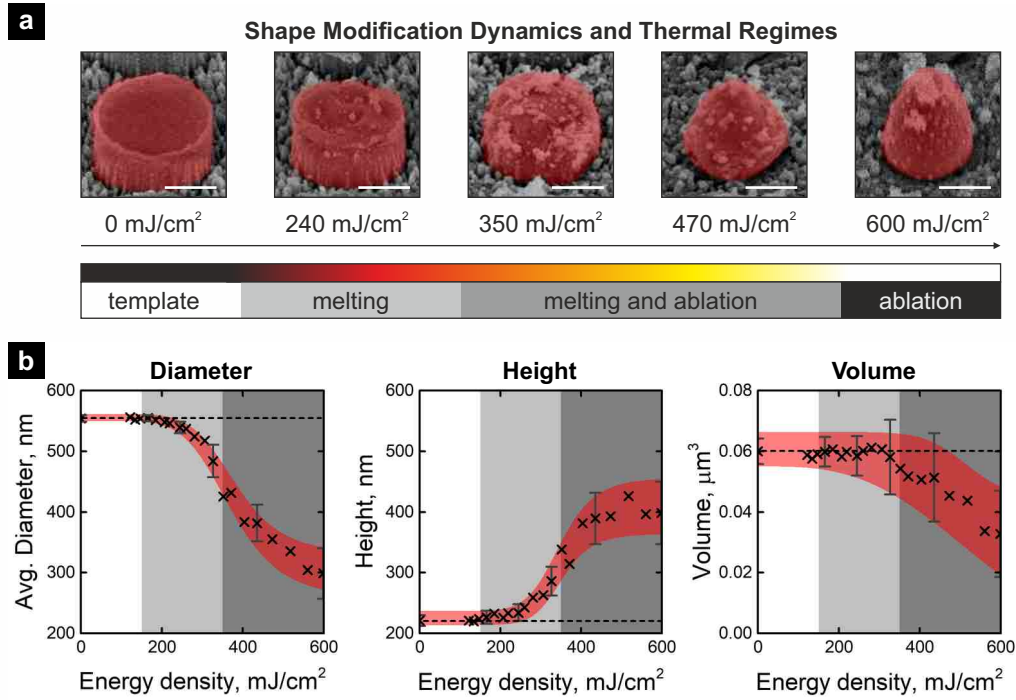


Figure 3.10: Shape dynamics due to laser-induced tailoring of Si metasurface elements with ED and MD resonances in the IR. (a) SEM images of a typical unit cell after irradiation using different energy density and from the shape measurements identified thermal regimes. (b) Measured geometrical parameters after irradiation: average diameter (left), height (center), and volume of the metasurface elements (right). Crosses depict measured values, and red shading denotes the interval of uncertainty. The dashed lines highlight the geometry values of the template. Melting as well as melting with ablation are highlighted in light- and dark grey, respectively. The figure is adapted from [S9].

nanosecond pulse-induced heating [52].

Also, certain previously neglected aspects should be noted here. First, the crystallization of Si is taking place again, but the difference in the refractive index between amorphous and crystalline Si is negligible in the infrared spectral range (see Appendix A). Second, the heating leads to a decrease in the volume of the nanostructures starting at $F \approx 350$ mJ/cm², due to part of the sample reaching evaporation temperature of $T_v = 2654$ K [241]. Some of the evaporated material is redeposited on the surface, but the debris particles are significantly smaller than the metasurface elements. Thus, their influence on the optical response is also negligible in the investigated spectral range.

3.1.4.2 Spectral and modal analysis

The template and the reshaped samples were spectrally characterized using a broadband spectrometer. As shown in Figure 3.11(a), the dip in the transmission spectra, corresponding to the fundamental ED and MD resonances, tends to broaden and blue shift with the increase of the applied laser energy. As crystallization does not significantly affect the optical material properties of Si in the infrared spectral range, this behavior can be directly related to the change of geometry, which affects the Mie-type electric and magnetic resonances.

The subsequent optical simulations of the periodic conical metasurface elements provide identical spectral functions and confirm the positions of the fundamental ED and MD resonances; see Figure 3.11(b). In

Figure 3.11(c), the measured central wavelength of the resonances is plotted as a function of the diameter D scaled to the period P of the metasurface. The ED resonance blue-shifts, while the MD resonance maintains its position. As the ED resonance is due to the collective polarization induced in the nanostructure, it is sensitive to the changes in the lateral dimensions, i.e., the nanostructure diameter. On the other hand, the MD resonance is driven by the electric field coupling to displacement current loops, which are partially compensated by the increase of height.

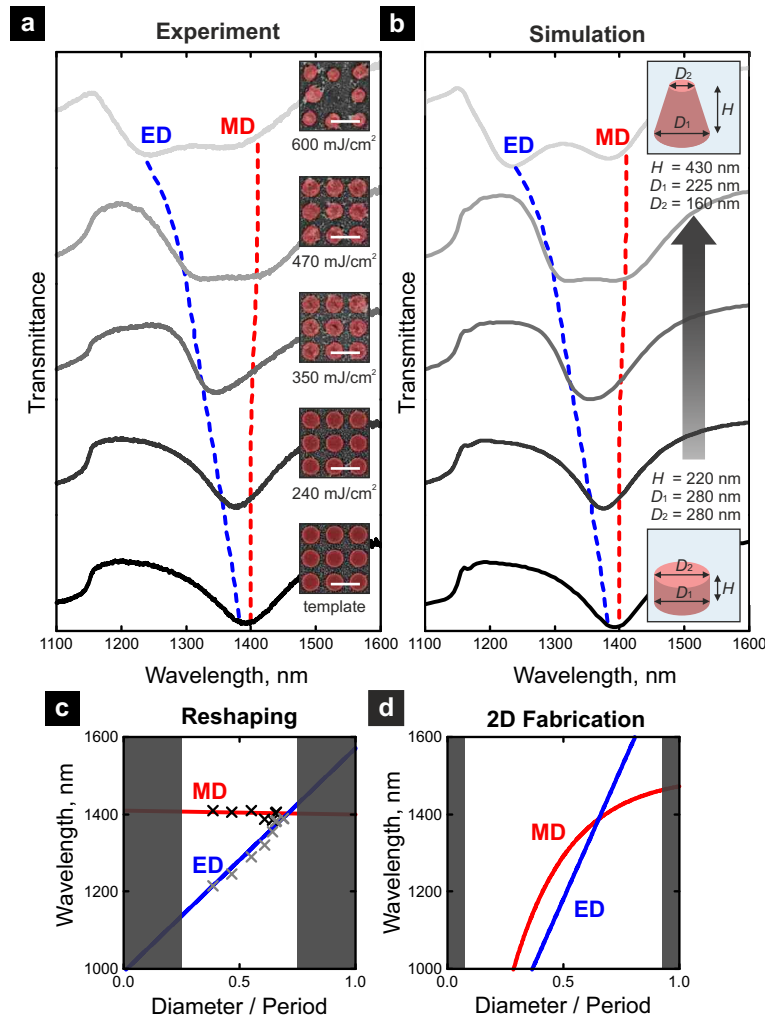


Figure 3.11: Control of optical resonances based on metasurface reshaping beyond two-dimensions. (a) Transmittance measurements of an infrared metasurface reshaped by increasing laser energy density, where ED and MD resonances are highlighted by the blue and red lines, respectively. The insets show SEM pictures of the measured arrays. The scale bars denote 1 μm . (b) Simulated transmittance of the arrays, with highlighted ED and MD resonances. Insets show the initial and the largest conical metasurface elements used. The structure is described by its height H , and diameter at the bottom D_1 and at the top D_2 . (c) The measured spectral position of ED and MD resonances as a function of diameter, scaled to the period, for the sample from (a). The crosses denote measurement results; the lines are linear fits. (d) The simulated spectral position of ED and MD resonances versus the diameter to period ratio, for metasurfaces realized by two-dimensional fabrication technologies with height $H = 220$ nm and period $P = 794$ nm. Black areas in (c,d) depict experimentally unattainable parameters. The figure is adapted from [S9].

In order to demonstrate the flexibility of the laser-induced reshaping for control of optical resonances, simulations are carried out for the spectral positions of ED and MD resonances of dielectric metasurfaces with a fixed height of $H = 220$ nm and period $P = 794$ nm while varying a diameter D , within limits allowed

by fabrication using standard two-dimensional lithography. The results are plotted in Figure 3.11(d) in dependence on the diameter D , and they can be compared directly to the result of the laser-induced thermal reshaping in Figure 3.11(c). In the case of a fixed height, both ED and MD resonances blue-shift with the decrease of the diameter, whereas in the case of laser-induced thermal reshaping, the ED resonance can be varied independently of the MD. Thus a prior unattainable control of optical resonances is obtained. Such control of the ED and MD resonances paves the way for various applications, e.g., broadband band-stop filters and absorbers. Regarding the former, using the spectral data shown in Figure 3.11(a,b), it can be said that the bandwidth of fundamental resonances can be flexibly adjusted and increased by as much as a factor of 2, from 120 to 240 nm.

3.1.4.3 Height transformation

Finally, the actual physical height changes are measured and compared to a maximum height of a geometrically calculated hemisphere. The largest experimentally obtained height is significantly larger than predicted by the shape transition to a hemispherical shape; see Figure 3.12. Here, a basic geometry transformation is used to find the height of the hemisphere after reshaping H_{new} . The volume of a disk with a particular height H and diameter D is transformed into a hemisphere with its radius $R = H_{\text{new}}$. Naturally, such results vary with the aspect ratio of the disk D/H , and at low aspect ratio values, one gets the increase of height. Thus, the change in height is obtainable with a conventional reshaping, but the limits of reshaping may be broadened using ultrashort laser pulses.

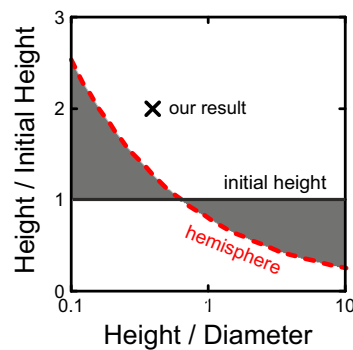


Figure 3.12: Comparison of the obtained height to the generally predicted height transition from the initial to the hemispherical shape, plotted in respect to an aspect ratio. The figure is adapted from [S9].

Furthermore, by adjusting the laser irradiation's wavelength, the demonstrated spatially-selective reshaping could be applied to dielectric metasurfaces with their elements of different sizes, e.g., the previously discussed smaller nanostructures with their resonances in the visible spectral range. In general, laser technologies open broad possibilities and could be used not just for tailoring but also for structuring the metasurfaces, which is the topic of the following section.

3.2 Direct laser interference patterning

A variety of metasurface-based applications led to the necessity of an efficient large-scale fabrication technique. Laser-based techniques, such as point-by-point material transfer [112–114], or direct writing [115, 116], enable the formation of ordered metasurfaces. These methods are direct and provide sufficient control of the periodicity. Still, their efficiency is limited to the repetition rate of the pulsed laser, as each laser pulse produces only a single metasurface element. To overcome this limitation and obtain high-throughput and cost-effectiveness, direct laser interference patterning is proposed.

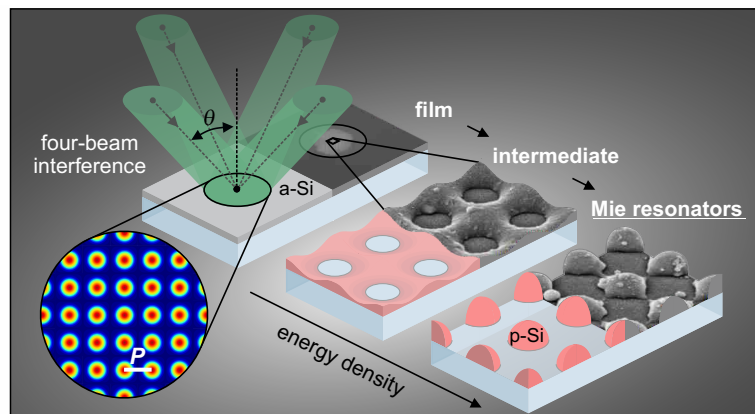


Figure 3.13: Graphical illustration of direct laser interference patterning of Si film into Mie-resonators using four-beam interference. The figure is adapted from [S10].

In this section, laser interference is applied for direct patterning of Si films. It is demonstrated that Si-based Mie-resonant metasurfaces can be fabricated in a single step by single-pulse laser interference; see illustration in Figure 3.13. The obtained hemispherical Mie resonators are distributed in a regular square lattice with a submicrometer period. Their size can be tailored in the range of a few hundred nanometers by controlling the irradiation conditions and initial film thickness. The structural and spectral analysis of the fabricated metasurfaces is used to evaluate the scalability and applicability of the proposed technique. It is shown that single-pulse laser interference is a technique for direct and high-throughput fabrication of dielectric metasurfaces, and guidelines are introduced for its potential applications.

3.2.1 Laser–matter interaction

3.2.1.1 Laser interference

The mechanism of laser interference patterning of thin films can be understood as a templated dewetting, but instead of pre-patterning by ion milling [118, 253], EBL [254], or photolithography and subsequent wet-etching [255], the interference pattern itself is used as a template for the required configuration of nanostructures; see Figure 3.14(a) for schematic depiction and Section 3.2.1.2 for a detailed discussion on thermal effects. Now, let us focus on the interference itself.

In general, interference of electromagnetic waves appears when two or more coherent laser beams overlap with each other. For a number of beams N with the same optical frequency, the interference intensity

profile can be expressed as [256]:

$$I(\mathbf{r}) \propto \frac{1}{2} \sum_{i=1}^N |\mathbf{E}_{0i}|^2 + \sum_{j<i}^N \sum_{i=1}^N \mathbf{E}_{0i} \cdot \mathbf{E}_{0j} \times \cos(\mathbf{k}_i \cdot \mathbf{r} - \mathbf{k}_j \cdot \mathbf{r} + \varphi_i - \varphi_j), \quad (3.3)$$

where \mathbf{E}_{0i} and \mathbf{E}_{0j} represent the electric fields, \mathbf{k}_i and \mathbf{k}_j are the wavevectors, and φ_i and φ_j are the phases of the respective interfering laser beams.

The laser interference for patterning was realized using a picosecond laser with a pulse duration $\tau_p = 300$ ps and a wavelength $\lambda = 532$ nm, generated by second-harmonic generation from a 1064 nm laser system. The laser beam was split into four beams by a diffractive optical element (DOE). The four in-phase beams were transferred to the sample plane by a confocal optical system, ensuring equal incidence angles θ of each beam with respect to the surface normal of the sample [137, 257]; see Section 3.2.2 for more details on experimental setup. This results in a cos-shaped intensity pattern periodic in the x - and y -directions. Such an intensity pattern is used to obtain nanostructures with the corresponding spatial arrangement. The experimental demonstration is done using amorphous Si films deposited on glass substrates; see Appendix A for dispersion parameters. By increasing the laser energy density F with respect to the material threshold F_{th} , different nanostructures can be obtained. In this work, the focus is on the regime of Mie-resonant nanoparticles (Mie resonators), see Figure 3.14(c), considering nanohole-like nanostructures as the intermediate regime, see Figure 3.14(b).

Short-pulse lasers are known for a high-peak-power, which enables efficient micro- and nanostructuring of materials [258, 259]. However, several other considerations have to be made in the selection of the optimal source. The different physical phenomena involved in generating the nanopatterned surface will be explained next. First, thermal diffusion is playing a crucial role when the interference period goes down to the submicrometer range [156]. The thermal diffusion length is proportional to the pulse duration [135]; thus, short pulse duration is required for small features to be obtainable. The pulse duration of $\tau_p = 300$ ps was chosen to ensure a short laser-matter interaction time, but still produce a significantly large patterned area, as the shorter the pulses, the smaller the interference area over which they overlap [257]. Second, the lattice constant (period) of the interference pattern P is a wavelength-dependent parameter. The period of the interference intensity pattern P depends on the wavelength of irradiation λ , the number of interfering beams N , and the angle of incidence with respect to the surface normal θ . It is expressed as [260]:

$$P = \kappa_N \frac{\lambda}{\sin \theta}, \quad (3.4)$$

where κ_N is a coefficient related to the number of interfering beams N : $\kappa_2 = 1/2$, $\kappa_3 = 2/3$, $\kappa_4 = 1/\sqrt{2}$, and $\kappa_6 = 2/\sqrt{3}$. Accordingly, the period P of the four-beam interference pattern is expressed as follows [260]:

$$P = \frac{\lambda}{\sqrt{2} \sin \theta}. \quad (3.5)$$

The period P can be adjusted by changing the incident angle θ or the wavelength of irradiation λ . The incidence angle of the interfering beams θ using the four-beam interference system is dependent on the

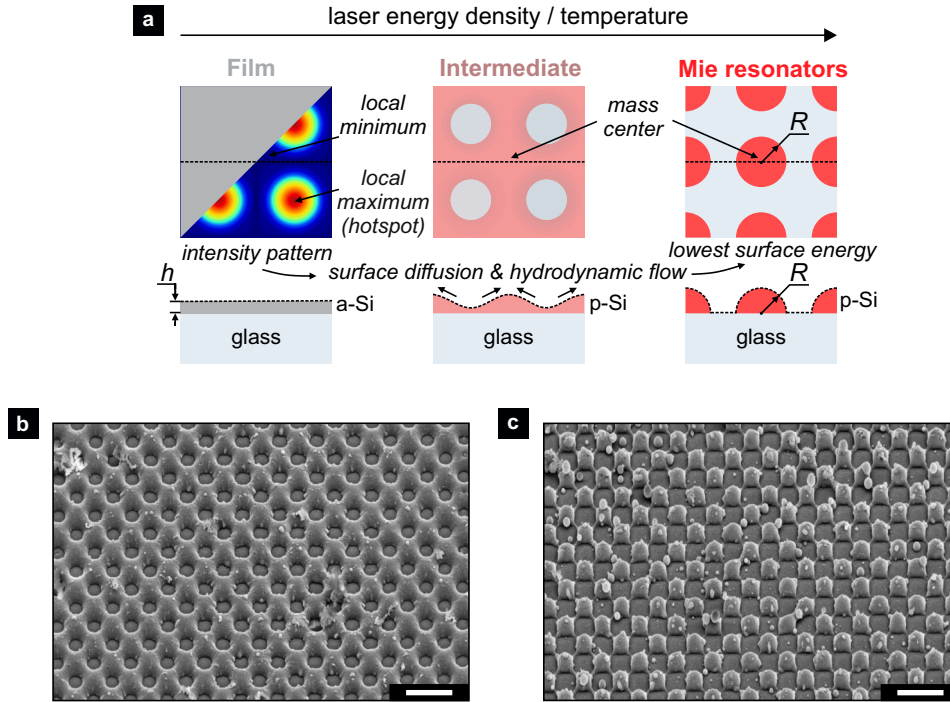


Figure 3.14: Concept of patterning Mie resonant metasurfaces by single-pulse laser interference. (a) Mechanism of dewetting using the interference intensity pattern as a template with respect to the laser energy density. Si film with thickness h reshapes via surface diffusion and hydrodynamic flow into a hemispherical shape with radius R to minimize its surface energy. During heating, a-Si crystallizes into p-Si. (b) Bird’s-eye view of an array of nanoholes (intermediate regime) patterned from Si film with $h = 70$ nm. SEM image, scale bar is equal to $1 \mu\text{m}$. (c) Bird’s-eye view of an array of nanoparticles (Mie resonators regime) patterned from Si film with $h = 70$ nm. SEM image, scale bar – $1 \mu\text{m}$. The figure is adapted from [S10].

angle between the first-order beams split by the diffractive optical element, the focal length of the first lens f_1 and the focal length of the second lens f_2 by the following equation [140]:

$$\theta = \arctan\left(\frac{f_1}{f_2} \tan \theta_0\right), \tag{3.6}$$

where θ_0 is the half-angle between the first-order beams split by the diffractive optical element. In theory, incident angles θ are possible up to 90° , which sets the limit to $P_{\min} = \lambda/\sqrt{2}$. In the experimental demonstration, all four laser beams were incident at $\theta \approx 41^\circ$ with respect to the surface normal of the sample; thus, a submicrometer period of $P = 570$ nm was obtained, which is sufficient for applications in the visible and near-infrared spectral range.

3.2.1.2 Thermal processes

The selected laser pulse duration is substantially longer than the electron–phonon relaxation time in Si, which is less than 300 fs [261], thus the laser–matter interaction can be approximated by relatively simple thermal processes.

The intensity peaks of interference pattern correspond to hotspots, as indicated in Figure 3.14(a). Here, more energy is deposited in the Si film by absorption, and it heats up faster than in the interference minima,

leading to melting. As surface tension of the molten material is a temperature-dependent parameter, it is lower in the interference maxima (hotspots) and is higher in the interference minima (colder zones) [262]. Subsequently, Si flows from the interference maxima to the minima due to surface tension. If the material melting temperature is reached, the mass transport is also governed by a hydrodynamic flow, as described by the mechanism of liquid-state dewetting [110, 119]. The irradiated material exhibits large temperature gradients and using the same interference pattern, but controlling the laser energy density with respect to the material damage threshold – one may obtain diverse patterns [137, 144].

In the case of thin films, the film-substrate interfacial free energy γ_{fs} determines the shape of the surface. The morphology of isotropic films is defined by Young's equation [263, 264]:

$$\cos \vartheta = \frac{(\gamma_s - \gamma_{fs})}{\gamma_f}, \quad (3.7)$$

where ϑ is the equilibrium contact angle, γ_f and γ_s are the surface tensions of the film and the substrate, respectively. When heated to sufficiently high temperatures, the continuous film breaks into nanohole-like periodic structures; shown in Figure 3.14(b). If the laser energy density is increased further, the film agglomerates to minimize the total free energy of the system [265], thus forming an array of hemispherical nanoparticles ($\vartheta = 90^\circ$); see Figure 3.14(c). Furthermore, if the ablation threshold is reached, a part of the sample gets locally ablated, while some of the material gets redeposited on the surface. The redeposited particles are spread irregularly based on the chaotic nature of evaporation and are significantly smaller compared to the ordered elements of the metasurface. Thus their influence on the optical response is negligible. The ablation does not have a prominent influence unless the majority of the material is evaporated, subsequently destroying the ordered metasurface.

Properly chosen laser irradiation conditions result in a large-area Mie-resonant metasurface, see exemplary SEM image of $20 \times 20 \mu\text{m}^2$ area in Figure 3.15(a). The dependence of the metasurface parameters on the laser irradiation is discussed in detail in the following chapters. AFM measurements confirm the prediction of a hemispherical shape of the individual nanoparticles, as shown in Figure 3.15(b) by a typical cross-section of a patterned 70-nm-thick Si film patterned using laser energy density $F = 3.75 \text{ J/cm}^2$. A semi-circle function is used to approximate the vertical cross-section of a single nanoparticle.

In addition, the heat-affected amorphous Si tends to crystallize [123, 250–252]. The crystallization starts before Si film starts to melt [123]. Accordingly, the patterned area becomes polycrystalline, as confirmed by Raman spectroscopy measurements. Note the Raman spectra of the structured and unstructured sample in Figure 3.15(c). For the unstructured Si film, a broad peak is observed at a Raman shift of $\nu = 480 \text{ cm}^{-1}$, which corresponds to a Raman scattering of amorphous Si [251]. A polycrystalline peak at $\nu = 510 \text{ cm}^{-1}$ appears only after the patterning. Moreover, the Raman peaks become significantly sharper: from $\Delta\nu = 104.0 \text{ cm}^{-1}$ at FWHM in case of the unstructured film to $\Delta\nu = 23.6 \text{ cm}^{-1}$ after exposure using a laser energy density of $F = 3.75 \text{ J/cm}^2$.

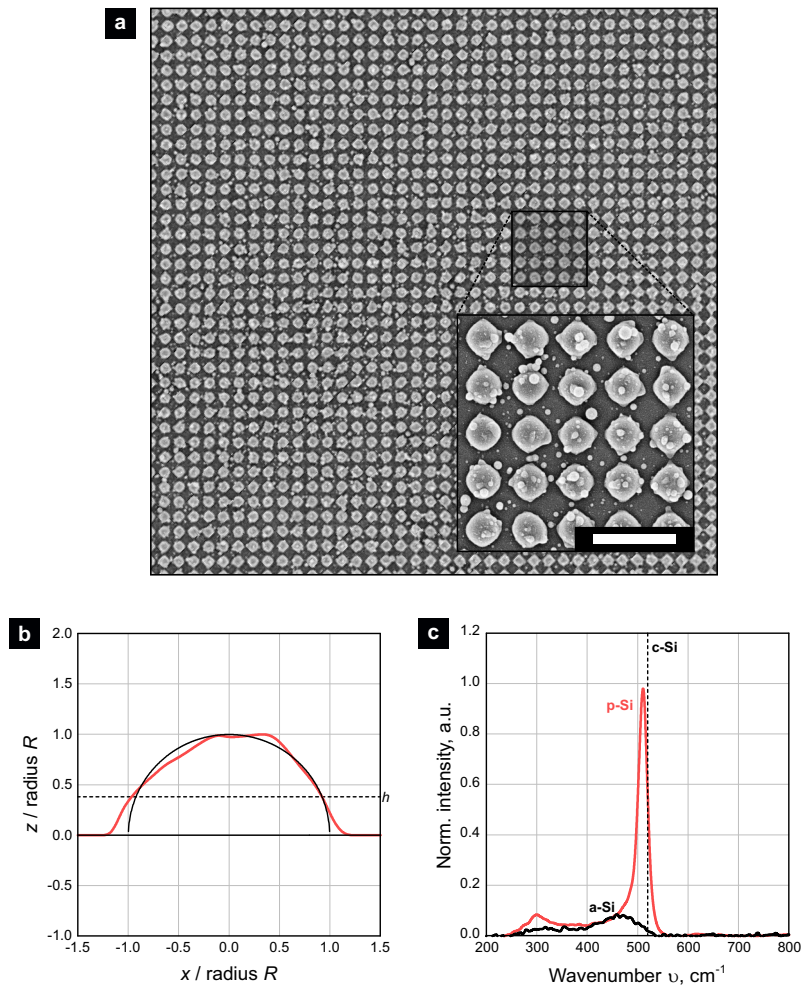


Figure 3.15: General properties of the fabricated metasurfaces. (a) SEM image of a $20 \times 20 \mu\text{m}^2$ area, constituted of Si-based Mie resonators. Scale bar is equal to $1 \mu\text{m}$. (b) Cross-section of a single Mie resonator (red dotted line), compared to initial Si film with thickness $h = 70 \text{ nm}$ (black dashed line). The profile is fitted by a semi-circle (black solid line). (c) Raman spectra indicating the transition from amorphous Si film with a peak at $\nu = 480 \text{ cm}^{-1}$ (black line) to polycrystalline Mie resonators with a peak at $\nu = 510 \text{ cm}^{-1}$ (red dotted line). The crystalline Si (c-Si) peak is at $\nu = 520 \text{ cm}^{-1}$ (black dashed line). The figure is adapted from [S10].

3.2.2 Methods

3.2.2.1 Experimental setup

The experimental setup is schematically depicted in Figure 3.16. The experiments were done using a high-power picosecond laser (Atlantic HE, Ekspla) with a pulse duration of $\tau = 300 \text{ ps}$ and a repetition rate of $\nu = 1 \text{ kHz}$. The fundamental wavelength of 1064 nm was transformed into its second harmonic of 532 nm to be in the high-absorption range of amorphous Si. The Gaussian beam diameter at the output was $d_{\text{out}} \approx 1.9 \text{ mm}$ at $1/e^2$, as measured with a CCD camera, but expanded by a factor of 2 using an optical telescope. The laser beam was divided into multiple beams using a multi-spot DOE with a 10° full angle (HOLOEYE Photonics). The 1st order beams were directed to the sample plane using a system composed of two plano-convex spherical lenses ($f_1 = 100 \text{ mm}$ and $f_2 = 15 \text{ mm}$), while a metal aperture blocked the 0th diffraction order and the higher-order beams. The laser power was controlled by an attenuator based on a half-wave plate, a beam splitter, and a beam dump.

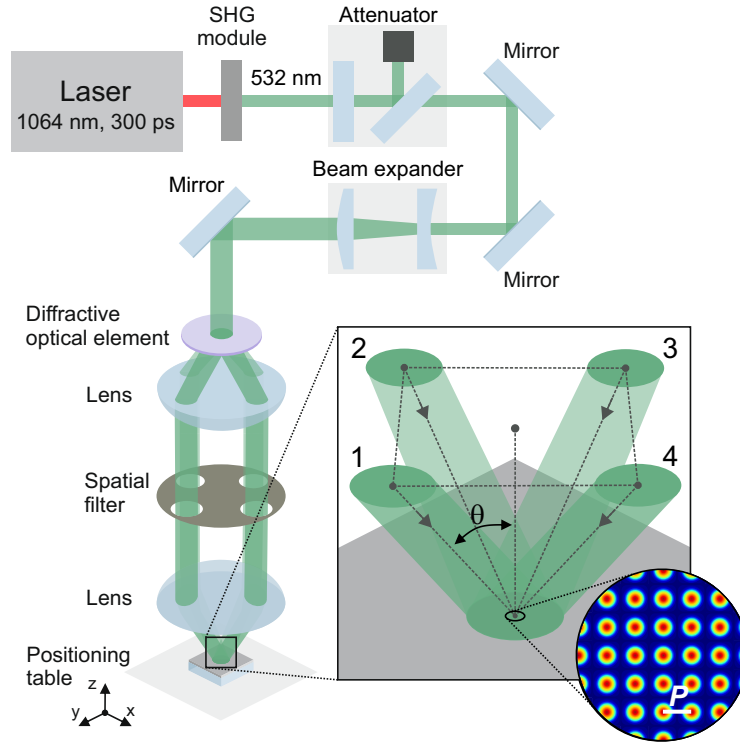


Figure 3.16: Schematic representation of the four-beam interference setup for direct laser interference patterning. The DOE splits the beam into four, which are further propagated through a $4f$ lens system to the sample plane, forming a square lattice intensity pattern with a period P . The figure is adapted from [S10].

The setup was used to pattern Si films of four different thicknesses: 30, 50, 70, and 90 nm, which were fabricated on top of glass substrates by ion-beam deposition. The samples were positioned using a translation stage (Aerotech). All of the experiments were carried out in ambient conditions.

3.2.2.2 Sample characterization

The spectral analysis was done with a plane-wave illumination using an inverted optical microscope system (Axio Observer D1, Carl Zeiss) with an integrated broad-band VIS/IR imaging spectrometer (iHR320, Horiba). Also, SEM images were taken (Helios NanoLab G3 UC, FEI), and the surface topography was measured by an AFM with incorporated peak force tapping technology (Dimension Edge, Bruker). The Raman spectra were taken using a commercially available confocal Raman system (WITec) equipped with a 785 nm laser. The light was focused and collected with the $NA = 0.95$ microscope objective. The measurements were taken with the laser power of 1 mW. Measured spectra were background corrected using the SNIP algorithm with 100 iterations.

3.2.2.3 Numerical simulations

The optical response was simulated using FDTD (Lumerical). As usual, a 3D model of an infinite array of amorphous Si nanostructures was created. The unit cell was illuminated by a normally-incident linearly-polarized plane-wave source. Frequency domain field and power monitors were placed to record transmittance and reflectance. The Mie resonators were constructed as ideal hemispheres with a certain ra-

dius R . The intermediate regime of nanoholes was implemented using a surface, characterized by a period P in the transverse directions, a distance from the glass surface z , and an amplitude A of the sine function. The refractive index of Si is given in Appendix A. The refractive index of glass was set to $n = 1.46$. The electromagnetic fields for the mode decomposition were calculated using the FEM package (COMSOL). The scattering efficiency of various modes were computed from the current density (see Section 1.1.1.4 for details).

3.2.3 Patterning of large-area metasurfaces

3.2.3.1 Interference spot and damage thresholds

A technique to determine the beam spot size and the material damage threshold using pulsed Gaussian beams was introduced by Liu [247].

The spatial envelope of interference resembles the shape of the interfering beams [266]; see illustration in Figure 3.17. Thus, the technique is also valid for the interference patterning. The Gaussian intensity distribution is given by:

$$I(r) = I_0 \exp\left(-r^2/\rho^2\right), \quad (3.8)$$

where I_0 is the peak intensity, r is the radial coordinate, and ρ is the spatial radius at the $1/e$ level of intensity. Here, the diameter is defined at the $1/e$ level of intensity as the diameter of the laser spot, $d_{1/e} = d_{\text{spot}}$. The intensity and the energy are related linearly, thus by substitution one may obtain [247]:

$$d^2 = d_{\text{spot}}^2 \ln(E/E_{\text{th}}), \quad (3.9)$$

where E_{th} is the threshold pulse energy. Note that the same relation can be expressed for energy density, as indicated in Equation 3.2.

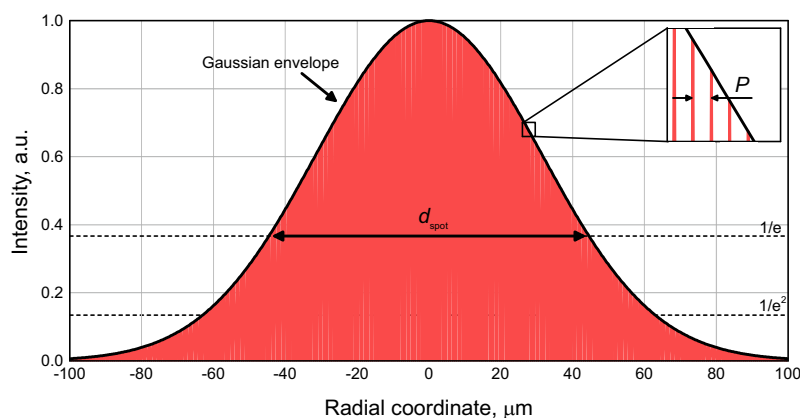


Figure 3.17: Interference intensity distribution using Gaussian beams. The intensity distribution (red) has a Gaussian envelope (black line), while it is modulated periodically, $P = 570$ nm (see the inset). The diameter of the interference spot $d_{\text{spot}} = 99$ μm is found at the $1/e$ level of intensity. The figure is adapted from [S10].

Based on the Equation 3.9, the Gaussian beam spot diameter d_{spot} can be determined by measuring the diameter d of the laser-induced damage by using different pulse energies E . The sample of Si film with a

thickness of $h = 70$ nm was exposed using laser interference at different spatial positions while gradually increasing the laser pulse energy E . The total diameters of the patterned areas were measured and plotted as $d^2 \propto \ln E$; see Figure 3.18(a). The slope is obtained from a linear fit of the measured data, which corresponds to the laser spot diameter squared d_{spot}^2 . Accordingly, as shown in Figure 3.18(a), the interference spot is found to be equal to $d_{\text{spot}} = 99$ μm . The interference spot is expected to be maintained regardless of the Si film's thickness if no changes are applied to the laser or the optical system.

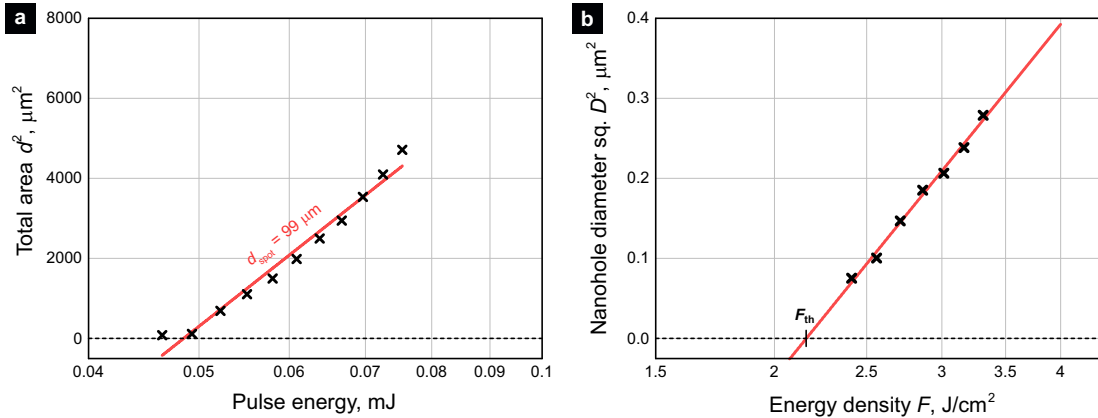


Figure 3.18: Interference spot and threshold analysis. (a) Patterned area (diameter squared d^2) dependence on the laser pulse energy E . The slope of the linear approximation (red line) represents the laser spot with $d_{\text{spot}} = 99$ μm . (b) Relation of the nanohole size d^2 to the calculated laser energy density F . Laser energy density threshold F_{th} is indicated at $d^2 = 0$. The patterned film has a thickness of $h = 70$ nm. The figure is adapted from [S10].

By using the diameter of the laser spot d_{spot} one can simply calculate the area of the spot $S_{\text{spot}} = \pi d_{\text{spot}}^2/4$, which allows us to determine the energy per area – the laser energy density F :

$$F = N \frac{E}{S_{\text{spot}}} = N \frac{4E}{\pi d_{\text{spot}}^2}. \quad (3.10)$$

The measurements of the total patterned areas are not as precise as measurements of single nanostructures, thus to determine the patterning threshold, the metasurface elements are analyzed, in particular, nanoholes. The diameter squared d^2 of the nanoholes as a function of the laser energy density F is plotted in Figure 3.18(b). Here, the linear-fit of the experimental data is spanned to $d^2 = 0$, which indicates the threshold energy density F_{th} . The threshold for patterning of a Si film with thickness $h = 70$ nm was found to be at the laser energy density $F_{\text{th}} = 2.16$ J/cm^2 ; see Figure 3.18(b). Similarly, the threshold of other processes can be found, such as the threshold of the nanoparticle (Mie resonator) regime – $F_{\text{th}} = 3.30$ J/cm^2 . The laser spot diameter d_{spot} depends on the laser parameters as well as the optical system used but is independent of the sample [S8], while the damage threshold F_{th} not only depends on the irradiation parameters but also varies with the selection of the material and its thickness, thus the calculation of the thresholds has to be repeated for each of the Si thicknesses used.

3.2.3.2 Dependence on laser energy density

An essential advantage of direct laser interference patterning is obtaining a relatively large area of periodic structures from a thin film or a bulk material by just a single laser pulse. In general, the envelope of the

spatial energy distribution of the interference resembles the spatial energy distribution of the initial Gaussian beam [266], while the interference area is limited by the spatial and temporal overlap of the interfering beams [257].

Due to energy-dependent photothermal effects, the patterned area size also depends on the laser energy density with respect to the material threshold. The total patterned area may be distorted due to ellipticity of the initial beam or aberrations in the optical setup. Thus, for simplicity, an average diameter of d is used to define the total patterned area. The diameter d varies as a function of the total laser energy density up to the diameter of the interference spot d_{spot} , which is defined as the diameter of the spatial energy envelope at $1/e$ level; see Section 3.2.3.1. The nanostructured elements inside the area are described by their diameter D and height H , as well as period P of the rectangular lattice.

The first experimental demonstration is done using an amorphous Si film of $h = 70$ nm thickness. Si was deposited on a glass substrate (silicon dioxide, $n = 1.46$) by ion-beam deposition (see Appendix A for Si dispersion parameters). Figure 3.19(a) shows a SEM image of a Si film irradiated by an arbitrarily selected laser energy density $F = 2.70$ J/cm². Using this energy, a part of the Si film reaches the material melting threshold, Si melts and is reshaped into an array of nanostructures, which can be seen as a brighter color of the SEM image shown in Figure 3.19(a). At a slightly larger energy density $F = 3.75$ J/cm², accordingly larger patterned area is obtained; see Figure 3.19(b).

As anticipated, the diameter of the total patterned area d and the diameter of the area with Mie resonators d_{Mie} is coupled to the applied laser energy density F , as shown in Figure 3.20(a,b). It steadily grows towards the diameter of the interference spot $d_{\text{spot}} = 99$ μm obtained from the pulsed beam spot size measurements; see Section 3.2.3.1 for more details. The threshold of the patterning process for a Si film with thickness $h = 70$ nm was found to be at the laser energy density $F_{\text{th}} = 2.16$ J/cm², while nanoparticles start to form above the laser energy density of $F_{\text{Mie}} = 3.30$ J/cm². As depicted in Figure 3.20(a), for high laser energies up to a half of the patterned area consist of nanoparticles. Such area with $d_{\text{Mie}} = 55$ μm consists of almost 7500 nanoparticles distributed in a rectangular lattice with a period $P = 570$ nm. Considering this is achieved using only a single laser pulse, significantly higher fabrication efficiency is demonstrated compared to the pulse-by-pulse direct laser writing; see head-to-head comparison in Section 3.2.3.4.

3.2.3.3 Uniformity of patterned areas

The size of the metasurface correlates with the size of the metasurface elements. The development of the metasurface elements was investigated by observation of the central part of the patterned area while changing the applied laser energy density F ; see Figure 3.20(b), where the diameter of the nanostructures D is plotted as a function of the laser energy density F . A logarithmic growth of the nanoholes size is noted, starting from the threshold of $F_{\text{th}} = 2.16$ J/cm² up to the laser energy density of $F_{\text{Mie}} = 3.30$ J/cm². By increasing the laser energy density F further, the photothermally induced heat becomes sufficient to melt the Si film within the whole range of the unit cell. At such a condition, the surface of the Si film is discontinued, and an array of spherical nanoparticles is formed due to the surface tension, as in the previously introduced model of templated solid-state dewetting [118,253–255]. In the case of nanoparticles (Mie resonators), the further increase of the laser energy density F steadily decreases the diameter D of the

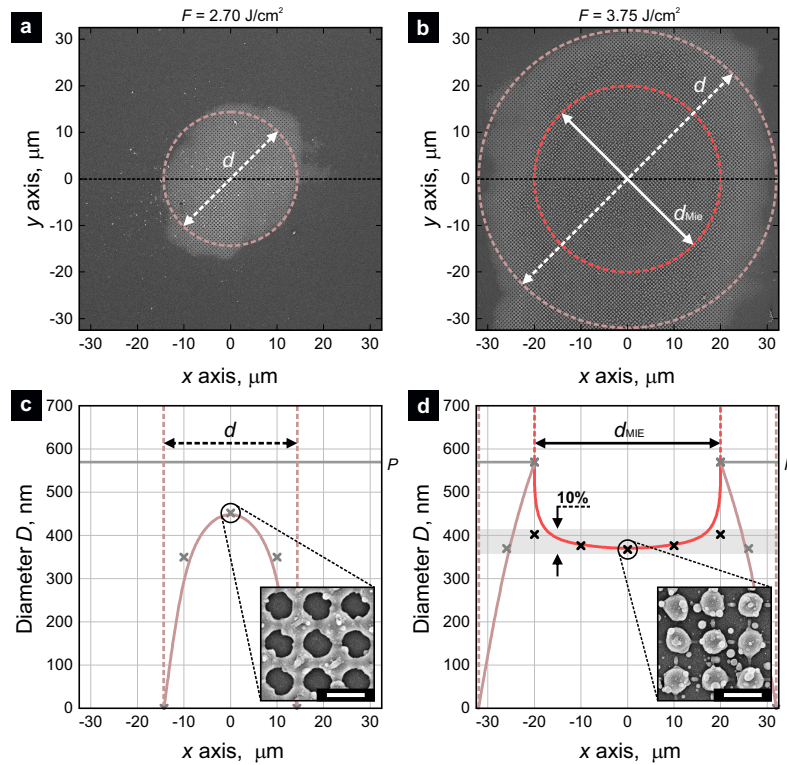


Figure 3.19: Examples of large-area metasurfaces and their submicrometer elements from Si film with $h = 70$ nm. (a) A patterned area with diameter $d = 28.6 \mu\text{m}$ (brown dashed line) using a laser energy density $F = 2.70 \text{ J/cm}^2$. (b) A patterned area using a laser energy density $F = 3.75 \text{ J/cm}^2$. The diameter of the total area $d = 64 \mu\text{m}$ is highlighted by brown dashed line, while nanoparticle area $d_{\text{Mie}} = 40 \mu\text{m}$ - red dashed line. (c) Structural analysis of the area from (a), along x -axis. Nanoholes are formed with a maximum diameter $D = 450$ nm, as shown in the SEM image, scale bar – 500 nm. (d) Structural analysis of the area from (b), along x -axis. Size of nanoholes increases till nanoparticles are formed. Diameter of nanoparticles D stays in 10 % range off the central value, $D = 2R = 368$ nm. Inset shows SEM image, scale bar – 500 nm. The figure is adapted from [S10].

nanoparticles till $D = 2R$. The $h = 70$ nm Si film was converted into hemispherical nanoparticles with a diameter $D = 2R = 368 \pm 10$ nm (from $F \approx 3.45 \text{ J/cm}^2$ to $F \approx 4.50 \text{ J/cm}^2$), as obtained from analysis of SEM images and AFM measurements (see Section 3.2.2 for more details on sample characterization). At and beyond the critical laser energy density F , which was found to be at $F_{\text{abl}} \approx 4.50 \text{ J/cm}^2$, the Si film is destroyed, as the material is ablated at the center of the interference spot.

A challenge for direct laser interference patterning is the homogeneity over a large area. It is fundamentally limited by the Gaussian spatial energy distribution of the laser beam. Nevertheless, even without a complex beam shaping approach, a significant part of the patterned area is uniform. For example, the patterning with the laser energy density $F = 2.70 \text{ J/cm}^2$ is at the fringe of the nanoparticle (Mie resonator) regime. The total patterned area with a diameter of $d = 28.6 \mu\text{m}$ is constituted only of nanoholes. Their diameter variation at the central cut of the patterned area is indicated in Figure 3.19(c). The diameter of the largest nanoholes in the center is equal to $D = 450 \pm 12$ nm, while it decreases fast when going away from the center till the nanoholes are no longer obtained due to insufficient laser energy. In contrast, the patterned film using a larger laser energy density $F = 3.75 \text{ J/cm}^2$ exhibits the regime of Mie resonators; see Figure 3.19(d). The Mie resonators seem to be spread more uniformly as all of the obtained structures in the area of $d_{\text{Mie}} = 40 \mu\text{m}$ fit into a 10 % range off the value at the central part, from $D_{\text{min}} = 368 \pm 10$ nm to

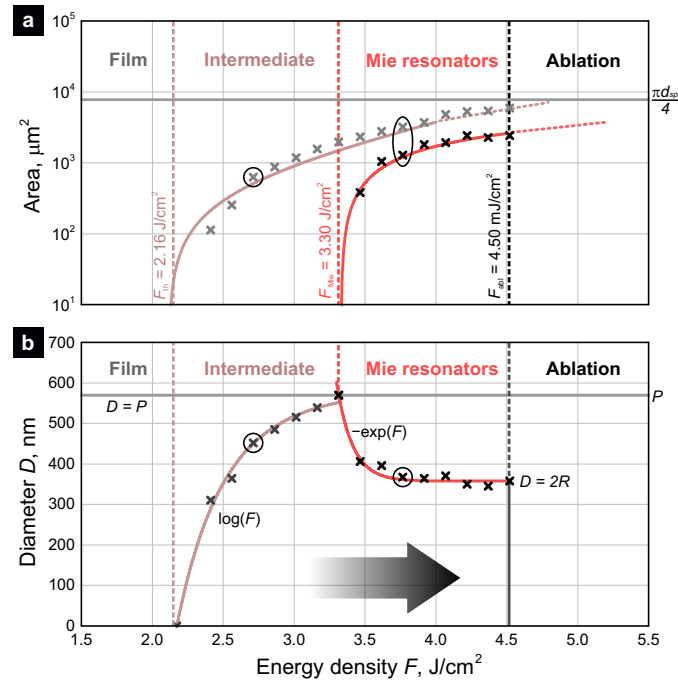


Figure 3.20: Metasurfaces and their elements as functions of energy density from Si film with $h = 70 \text{ nm}$. (a) Growth of the nanostructured area and the Mie-resonators area with respect to the applied laser energy density F . Thresholds are indicated for nanostructuring at $F_{th} = 2.16 \text{ J}/\text{cm}^2$, nanoparticles at $F_{Mie} = 3.30 \text{ J}/\text{cm}^2$, and ablation at $F_{abl} = 4.50 \text{ J}/\text{cm}^2$. (b) Transition from Si film to Mie-resonators *via* analysis of the metasurface elements. Crosses indicate experimental data, brown line - logarithmic growth of nanoholes, red line - exponential decay of the nanoparticles size till $D = 2R$. Circled data are represented in Figure 3.19. The figure is adapted from [S10].

$$D_{max} = 402 \pm 22 \text{ nm.}$$

It is worth noting that a metasurface of tens of micrometers in lateral size is already applicable in Raman spectroscopy, fluorescence, or refractometry measurements, but, if required, has the potential to be spatially extended further by a partial interference spot overlap [140, 145], as discussed next.

3.2.3.4 Comparison to direct laser writing

To have a better feeling of the throughput using laser interference, it is compared to direct laser writing. Direct laser writing enables point-by-point fabrication of Mie-resonant nanostructures [112]. However, to obtain a relatively large area of nanostructures, discussed previously, the technique requires a laser with a high pulse repetition rate and a sufficiently fast and precise positioning stage. Using laser interference, only a single laser pulse is required to pattern Si film (thickness $h = 70 \text{ nm}$) into an area consisting of almost 7500 nanoparticles distributed in a rectangular lattice with a period of $P = 570 \text{ nm}$. In contrast, direct laser writing would require exactly 7500 pulses; see the difference depicted in Figure 3.21(a).

To emphasize this, two main factors for the patterning rate are considered: the pulse repetition rate of the laser and the speed of the positioning stage. One or another is the limiting factor. For simplicity, the laser source with a repetition rate of 1 kHz and the positioning stage with a maximum speed of 500 mm/s are considered. Here, the positioning stage can keep up to the repetition rate of the laser. Thus the total time of direct laser writing of 7500 nanostructures is limited by the pulse repetition rate. The process would require 7.5 s, the patterning rate being equal to 1000 nanostructures per second.

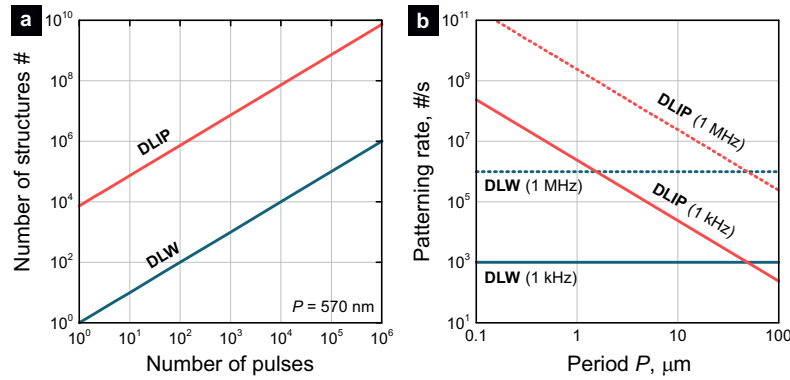


Figure 3.21: Comparison of direct laser interference patterning (DLIP) and direct laser writing (DLW). (a) Number of nanostructures versus number of laser pulses for DLIP (red line) and DLW (blue line), assuming the fabrication of 7500 Mie-resonant nanoparticles by single-pulse laser interference. (b) Patterning rate for both techniques as a function of period P . Cases of using lasers with a repetition rate of 1 kHz and 1 MHz are depicted by solid and dashed lines, respectively. The figure is adapted from [S10].

In comparison, using the same laser for direct laser interference patterning, only a single pulse/shot is needed, thus only 1 ms to pattern the same number of nanostructures. For patterning of a metasurface with a period of $P = 570 \text{ nm}$, direct laser writing requires a pulsed laser with a repetition rate of 4 MHz to be at the same rate as direct laser interference patterning with 1 kHz; see Figure 3.21(b). If the period of interference is increased, the number of nanostructures per area decreases. Thus, for a large period, direct laser writing could have the upper hand; see Figure 3.21(b). Otherwise, direct laser interference patterning may provide higher throughput.

3.2.4 Tailoring of metasurface elements

3.2.4.1 Size control by initial film thickness

In the intent to access a large parameter set of Mie-resonant metasurfaces, the methodology described in Section 3.2.3 was repeated for amorphous Si films of different thickness h . In total, Si films were deposited with the following thicknesses: 30, 50, 70, and 90 nm. The patterning was carried out using the same experimental conditions (see Section 3.2.2 for more details on experimental setup). At each thickness h , the laser energy density F was step-by-step increased at different spatial positions until the consecutive development of the Mie resonators.

The direct laser interference patterning process is dependent on the film thickness h , as is the laser ablation of thin films using a single Gaussian laser beam [135,267]. Even-though the patterning of metasurfaces was successful for all of the selected film thicknesses h , as shown in the SEM images of the samples patterned at explicitly chosen energy densities F , see Figure 3.22(a), the experimental results differ for varying thickness h . For example, a laser energy density $F \approx 3.15 \text{ J/cm}^2$ is sufficient for the formation of Mie resonators from Si film with $h = 30 \text{ nm}$, but such regime is not reached in the case of thicker films.

The experimentally obtained threshold for the intermediate regime, the regime of Mie resonators, and the ablation of Si are indicated for all of the thicknesses in Figure 3.22(b). There the experimental points are fitted by a linear function of the film thickness. According to the well-known Beer-Bouguer-Lambert law,

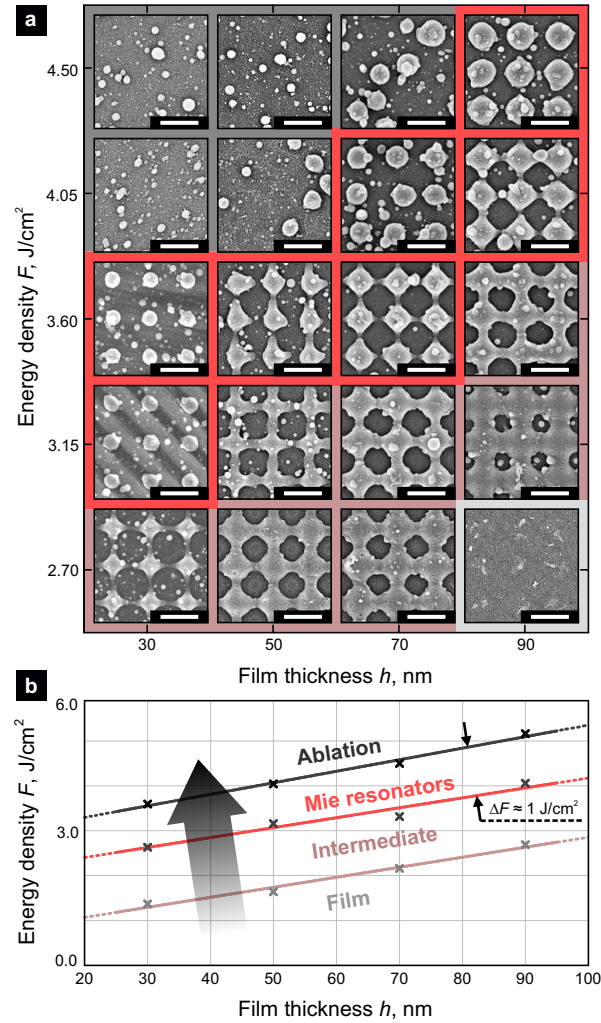


Figure 3.22: Tailoring of Si metasurfaces by film thickness and laser energy density. (a) SEM images of patterned samples in a matrix of the energy density and the film thickness h . (b) Laser energy density required for different regimes. Experimental points (crosses) are fitted linearly: brown line depicts the threshold of structuring, the red line – the Mie resonators regime, up to the ablation, see the black line. The figure is adapted from [S10].

the intensity of an electromagnetic wave decays exponentially while it propagates through a material. The penetration depth in Si at which the intensity of radiation decreases to $1/e$ of the incident light is $\delta \approx 5 \mu\text{m}$, based on the absorption coefficient $\alpha = 2.0729 \times 10^5 \text{ cm}^{-1}$ at radiation wavelength $\lambda = 532 \text{ nm}$ [268]. As long as the thin film thickness is significantly smaller than the penetration depth, $h \ll \delta$, the assumption of homogeneous energy distribution among the film thickness h is made [267]. This assumption allows a precise designation of the patterning regimes. As shown in Figure 3.22(b), the range of the laser energy density for the Mie-resonant nanostructures to be obtained is $\Delta F \approx 1 \text{ J/cm}^2$, which is the difference between the onset of the formation of the Mie resonators and the onset of ablation.

Next, an in-depth geometry analysis of the metasurfaces is performed. The high index metasurfaces were obtained with their elements varying in diameter D and height H , depending on the film thickness h and the laser energy density F . The geometry parameters after the patterning were determined by analysis of SEM images and complimentary AFM measurements (see Methods for more details). A typically measured cross-section of a unit cell is shown in Figure 3.15(b). As the patterned Mie resonators are in the shape of a hemisphere, the cross-sections were approximated by a semi-circle function, with its radius $R = H = D/2$.

This resulted in Mie resonators with their radius R equal to 129 ± 6 , 156 ± 8 , 184 ± 9 , and 195 ± 10 nm, when patterned from the Si films with thickness h equal to 30, 50, 70, and 90 nm, respectively.

As can be visually identified in Figure 3.22(a), the patterned metasurface elements increase in size with the increase of the initial film thickness, which is also predicted by a direct volume transformation:

$$V = V_f \cdot \xi, \quad (3.11)$$

The volume of a single hemisphere V is equal to a certain fraction ξ of the film volume within the unit cell, $V_f = P^2 \cdot h$. Subsequently, the radius R of the Mie resonator can be defined by a function:

$$R = \sqrt[3]{\frac{3}{2\pi} \cdot P^2 \cdot h \cdot \xi}, \quad (3.12)$$

in our case, with the period P being fixed and a cube-root relation to the film thickness h . The relation of diameter D and height H to the initial thickness h of the Si film are shown in Figure 3.23(a) and Figure 3.23(b), respectively. In particular, the same trend as shown in Figure 3.19(f) is found for all thicknesses h . By increase of laser energy density F , the diameter of the Mie resonators D changes from the size of the unit cell (period) P to the radius of a hemisphere R , see Figure 3.23(a), while the height H changes from the initial film thickness h to the radius R , see Figure 3.22(b). Based on the cube-root function, it is determined that at least half of the Si film volume is transformed into the Mie resonators, $\xi \approx 52\%$. In contrast, the other part either gets fully evaporated or is redeposited on the surface. The predicted volume relation to the initial Si film thickness is plotted in Figure 3.22(c). The experimental points are extrapolated for film thickness h from 0 to 285 nm. The obtainable nanostructure radius is limited for large thicknesses due to the conglomeration of neighboring nanostructures.

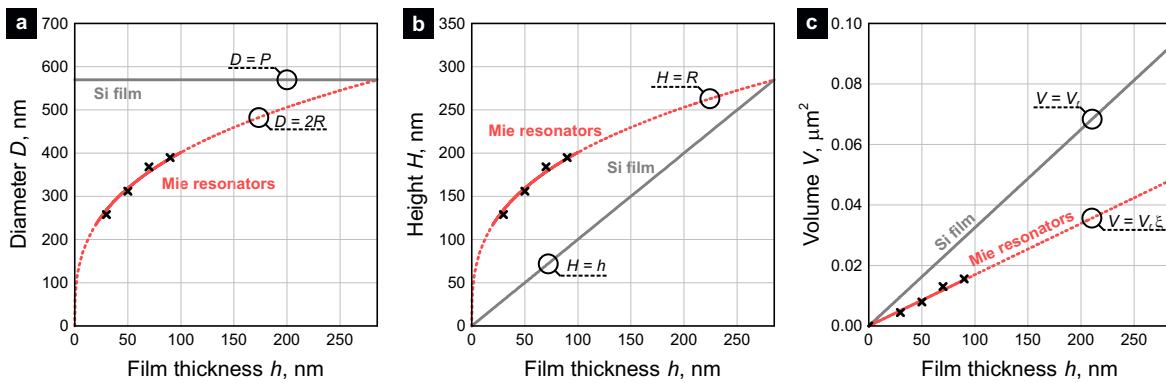


Figure 3.23: Geometry of tailored Si metasurfaces depending on the film thickness h . (a) Diameter of the fabricated Mie resonators D as a function of film thickness h (red line). The increase of energy density F results in reshaping the film (grey line) into hemispheres. (b) Height of the fabricated Mie resonators H as a function of film thickness h : from Si film with thickness h (grey line) to hemispheres with radius R (red line). Cube-root function is extrapolated from experimental points (crosses) with $\xi = 52\%$. (c) Mie resonator volume relation to the initial Si film thickness (red line), which is a fraction of the Si film volume within a unit cell (grey line). The figure is adapted from [S10].

Here, it should be noted that the volume fraction ξ is not equivalent to the patterning efficiency, meaning the amount (mass) of the material transformed into Mie resonators. The porous amorphous Si density is 5-25% lower than the crystalline Si density [269]. Thus the actual efficiency of Si film patterning into Mie

resonators using single-pulse laser interference patterning with a pulse duration of $\tau = 300$ ps is 55-65%.

3.2.4.2 Size control by periodicity

In the necessity of having multiple metasurfaces with different-size elements on the same sample, one may want to control the radius R of the Mie resonators by changing the period P instead of the initial film thickness h , which can be done by changing the radiation wavelength λ or the incidence angle θ , as noted in Section 3.2.1.1. On one hand, incident angles of interfering beams θ are theoretically possible up to 90° , which sets the lower boundary of the size of period, $P_{\min} = \lambda/\sqrt{2}$, while the upper boundary is in principle limitless, $P_{\max} = \infty$. For easier control of the angle of incidence θ , one may even consider a different interference setup like the beam splitter and mirrors setup [152], instead of a confocal optical system. However, it is less robust in spatial and temporal alignment. On the other hand, the wavelength change can be achieved using achromatic optical elements and different laser harmonics. For example, one may consider the same angle of $\theta \approx 41^\circ$ as in the experiments shown in this chapter. Then, the first three harmonics of the 1064 nm laser system: $\lambda_{\text{I}} = 1064$ nm, $\lambda_{\text{II}} = 532$ nm, $\lambda_{\text{III}} = 355$ nm, would result in three different periods: $P_{\text{I}} = 1140$ nm, $P_{\text{II}} = 570$ nm, and $P_{\text{III}} = 380$ nm, respectively. As the radius of the Mie-resonant elements R have a relation to the period P , see Equation 3.12, this would lead to three different sizes of Mie resonators patterned from the same 70 nm Si film: $R_{\text{I}} = 292$ nm, $R_{\text{II}} = 184$ nm, and $R_{\text{III}} = 116$ nm. Even broader tunability is potentially achievable by using tunable-wavelength sources, such as optical parametric amplifiers [270].

3.2.5 Spectral analysis and Mie resonances

3.2.5.1 Spectral response of different regimes

The optical response of Si film is wavelength-dependent, but even sharper spectral features appear after the patterning. This is demonstrated by the measured transmittance prior- and post-patterning of a Si film with thickness $h = 70$ nm, see Figure 3.24(a). Here, the transmittance of the film is compared to the transmittance of the samples irradiated by laser energy densities $F = 3.15$ J/cm² and $F = 3.75$ J/cm², which correspond to the intermediate regime and the Mie resonator regime, respectively. In Figure 3.24(b), the measured spectra are supported by the FDTD simulations. The nanoparticles (Mie resonators) are defined as hemispheres with a certain radius R , while a two-dimensional sinusoidal surface characterizes the nanoholes with a period P , a mean distance from the substrate z , and an amplitude of the sinusoidal wave A . The refractive index of Si is fitted between the refractive index of a-Si and c-Si due to its dependence on the crystallization state (see Appendix A for dispersion parameters).

Due to the sinusoidal interference intensity distribution, the nanoholes sidewalls are inclined; see the sketch in Figure 3.24(b). Accordingly, it is difficult to assign the peaks and dips of the transmission spectra in Figure 3.24(a,b) to a particular type of resonance, as they could be of a mixed nature, including but not limited to guided-mode resonances [271], and Mie resonances [7,8]. In contrast, in the case of well-defined-shape Mie resonators, the dips in the transmission spectra, such as a clearly pronounced dip at $\lambda \approx 950$ nm, can be assigned to Mie-type electric and magnetic resonances, as known from Chapter 1.

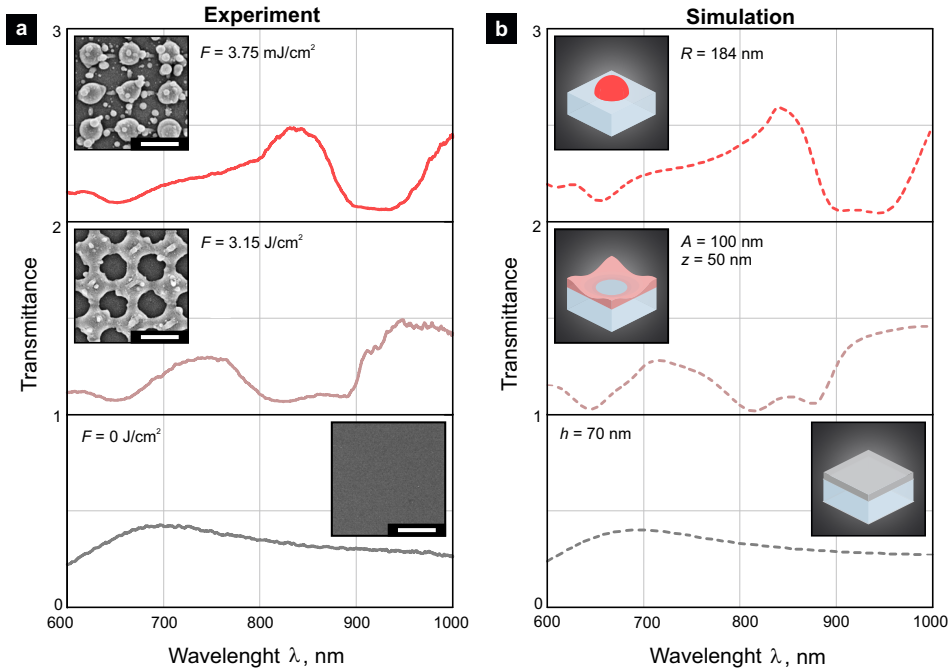


Figure 3.24: Spectral response of Si film prior and post patterning. (a) Measured spectra of unstructured 70 nm-thick film, nanoholes (intermediate regime) and nanoparticles (Mie resonators), obtained by irradiation of $F = 3.15 \text{ J/cm}^2$ and of $F = 3.75 \text{ J/cm}^2$, respectively. Insets show SEM images from the central parts of the patterned areas, scale bars are equal to 500 nm. (b) Numerically obtained spectra of the corresponding structures: film ($h = 70 \text{ nm}$), nanoholes (sinusoidal surface with amplitude $A = 100 \text{ nm}$, positioned $z = 50 \text{ nm}$ above the substrate), and hemispherical Mie resonators ($R = 184 \text{ nm}$). The insets show sketches of the unit cells. The figure is adapted from [S10].

3.2.5.2 Scattering contributions

For the Mie-type resonators, the origin of the strong scattering at $\lambda \approx 950 \text{ nm}$ is assigned to an ED based on the mode decomposition shown in Figure 3.25(a).

More precisely, the ED resonance is split into two resonances due to symmetry breaking when using optically non-identical materials for substrate and cladding, e.g., using a glass substrate in air [272]. Even though these resonances are partially overlapping, the distinction between them can be seen by observation of the electromagnetic fields inside the nanostructures shown in Figure 3.25(b–e), where the electric field distributions in the horizontal and vertical cross-sections of the Mie resonator are given. One of the ED resonances is identified at $\lambda = 910 \text{ nm}$ with the strongest field being at the bottom of the hemisphere, see Figure 3.25(b,c), while another peak, marked as ED', lies at $\lambda = 960 \text{ nm}$ with electric field concentrating at the top of the structure, see Figure 3.25(d,e).

The ED resonances originate from the collective polarization induced in the dielectric particle, while MD resonances are driven by the electric field coupling to displacement current loops. However, the latter is not as prominent when compared by the scattering efficiency Q_{scat} (scattering cross-section normalized to geometric cross-section), because of a relatively small height $H = D/2$ and intrinsic Si losses. Moreover, suppression of the ED scattering at $\lambda \approx 850 \text{ nm}$ may relate to a non-scattering anapole mode [163,273]. The optical response at shorter wavelengths is influenced by EQ and MQ; see Figure 3.25(a). Lattice resonances are indicated at the wavelengths of $\lambda = 570 \text{ nm}$ and $\lambda = 832 \text{ nm}$, based on the period P and the refractive index of air ($n = 1$) and glass ($n = 1.46$), respectively. Octopoles and other higher-order modes are neglected.

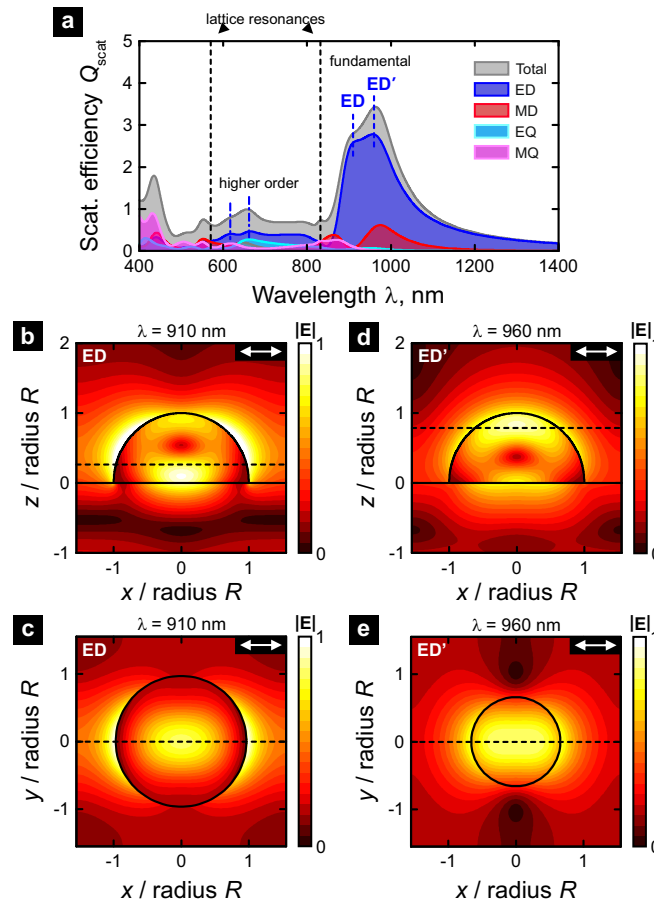


Figure 3.25: Mode decomposition. (a) Scattering efficiency Q_{scat} of metasurface consisting of Mie resonators with $R = 184$ nm (patterned from Si thin film of $h = 70$ nm): total scattering and contributions from ED, MD, EQ, and MQ modes. The ED resonance is split into ED and ED' because of symmetry breaking. Lattice resonances are indicated by black dashed lines. (b) Electric field at a vertical cross-section of a unit cell at $\lambda = 910$ nm, corresponding to ED. (c) Electric field at a vertical cross-section at $\lambda = 960$ nm, corresponding to ED'. (d) Electric field at a horizontal cross-section at $\lambda = 910$ nm, corresponding to ED. The cut is at $1/4$ of the height H , as shown in (b). (e) Electric field at a horizontal cross-section at $\lambda = 960$ nm, corresponding to ED'. The cut is at $3/4$ of the height H , as shown in (c). Electric field is x -polarized, its magnitude is normalized to 1. The figure is adapted from [S10].

3.2.5.3 Dependence on elements size

The spectral positions of the resonances are related to the optical size of the nanostructures [8]. In particular, a red-shift of the transmittance dips is observed in the measured spectra with the increase of the initial film thickness and, subsequently, the size of the Mie resonators, see Figure 3.26(a). The nanostructures patterned from Si film thicknesses of 30, 50, 70, and 90 nm, and their respective spectral functions were successfully reproduced numerically using the measured geometry, see Figure 3.26(b). Experimentally, the spectral features are slightly less pronounced due to slight irregularities in the metasurface and subsequent broadening of the resonances. Nevertheless, the mode decomposition of the periodic resonators confirms the spectral function trend and their correlation with the Mie resonances. Note the highlighted fundamental electric dipole resonances ED and ED' in both experimental and numerical results in Figure 3.26(a,b).

As the measured transmittance and the numerical simulations have a firm agreement, this enables a reliable emulation of the spectral behavior (transmittance, reflectance, and absorbance) within and even

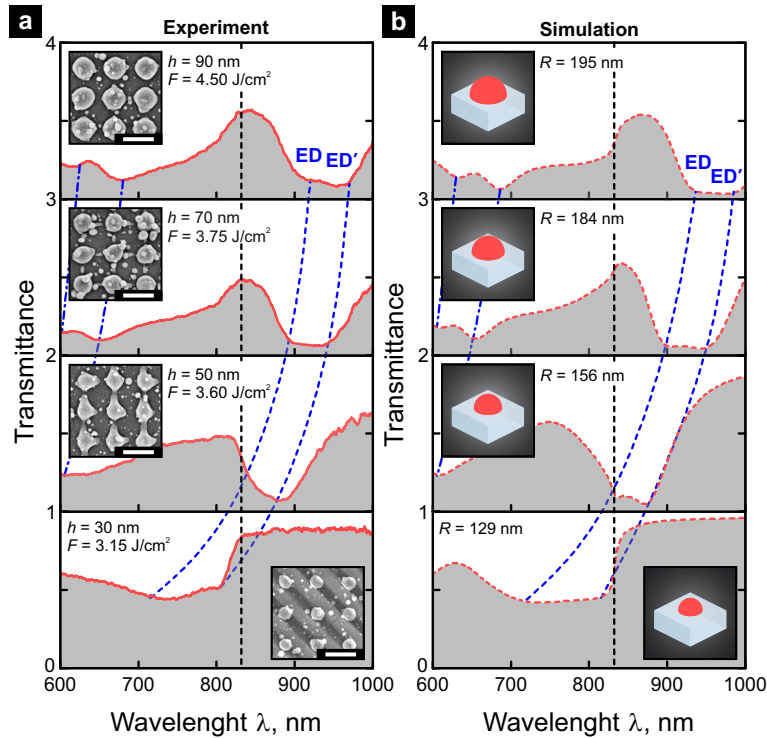


Figure 3.26: Spectral response of the Mie-resonant metasurfaces depending on their size. (a) Transmittance of the samples fabricated from Si films with varied thickness: 30 nm, 50 nm, 70 nm, and 90 nm. SEM images are shown in insets. Scale bars depict 500 nm. Dominant fundamental electric dipole modes, ED and ED', are highlighted by the blue dashed lines, higher-order – by blue dash-dot lines. (b) Numerically obtained spectra of the Mie resonators. Electric dipole modes are highlighted. Insets show sketches of resonators with a certain radius R . The figure is adapted from [S10].

outside of the experimentally observed spectral range plotted in Figures 3.27(a–c). It can be noted that the influence of the resonances becomes apparent only when the Mie resonators radius is sufficiently large, $R > 100$ nm. Up to that point, the structures fill only a tiny portion of the surface. Thus their density is too low considering the lattice configuration. In contrast, when $R > 250$ nm, another effect is adhered, because the gap between the neighboring metasurface elements reduces significantly and causes strong coupling and subsequent broadening of the resonances. As a result, in the demonstrated case, the optimal range of the radius is from $R = 100$ nm to $R = 250$ nm, in which a strong and wavelength-selective optical response is observed.

3.3 Chapter summary

In the first part of this chapter, ultrashort-pulse lasers are used for deterministic and spatially-selective tailoring of Si metasurfaces. The laser-induced thermal effects are applied for spatial customization, so-called laser pixelation, of a large-scale metasurface. The technique is mainly based on the crystallization of amorphous Si, which resulted in a $\Delta\lambda \approx 100$ nm blue-shift of the ED and MD resonances, sufficient to change the transmissive color of the nanostructure-based green filter to blue and, finally, red-shade. Such results indicate a simplification in the complex fabrication of the nanostructure-based color filter arrays and make a step towards their implementation into daily-use digital imaging devices. Second, a

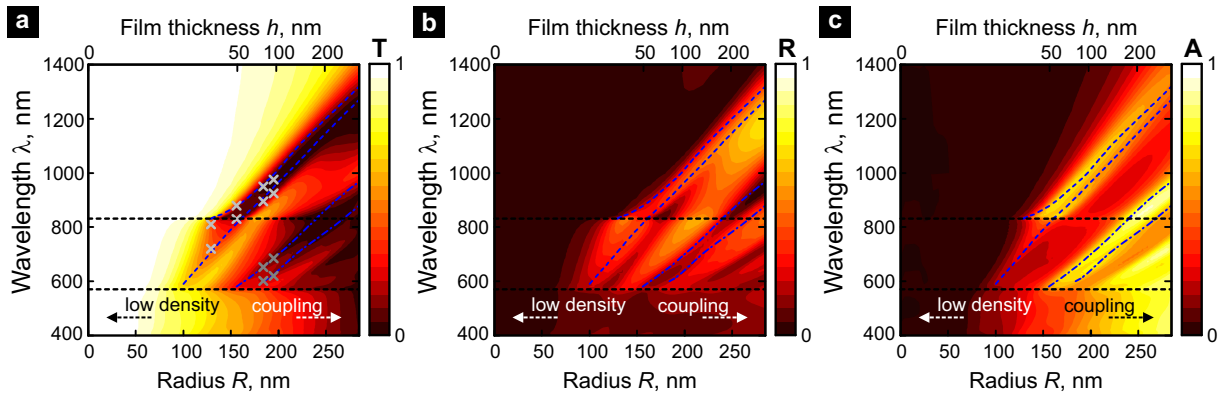


Figure 3.27: Extrapolated spectral response of the Mie-resonant metasurfaces. (a) Extrapolated transmittance map in dependence of Mie resonators radius R and the initial film thickness h . Electric dipole resonances are highlighted, crosses depict experimentally obtained transmittance dips. Similarly simulated maps of: (b) reflectance, (c) absorbance. At small radius R insufficient density of the resonators is observed, while at high values – coupling between neighboring resonators. Black dashed lines shows lattice resonances. The figure is adapted from [S10].

multi-dimensional reshaping technique for dielectric nanostructures is introduced. It is shown how high absorption and the selection of a resonance-associated field distribution allows us to spatially engineer the hotspot for the reshaping, while a 10 ps pulse duration enables spatial heat confinement. In the demonstrated example, we have shown an increase of nanostructure height by a factor of 2, while slightly shrinking its diameter. Such reshaping is followed by independent control of the ED and MD resonances, expanding the capabilities beyond the two-dimensional fabrication. The technique using ultrashort pulses is not surface energy limited as using continuous illumination or longer pulse duration. A great perspective is envisioned using even shorter pulses, spatial and temporal beam shaping approaches.

Furthermore, in the second part of this chapter, see Section 3.2, we have introduced a single-step technique for the fabrication of Mie-resonant metasurfaces. Direct laser interference patterning has been applied for the fabrication of high-index nanostructure arrays on a glass substrate. The area of the obtained metasurface spans across 10^2 – 10^4 μm^2 and, subsequently, consists of thousands of polycrystalline Si nanostructures distributed in an ordered rectangular lattice with a period $P = 570$ nm. The technique is carried out using only a single 300 ps laser pulse. Thus, it shows an enormous throughput compared to other existing laser-assisted fabrication techniques. Moreover, it was demonstrated that the hemispherical Mie resonators could be tailored by the preselection of the initial Si film thickness and control of the irradiation conditions. The film thickness variation allowed us to obtain Mie resonators with a diameter ranging from less than 260 nm to almost 400 nm, with their electric and magnetic resonances covering the visible and the near-infrared spectral range. While for complex shapes and patterns one may still consider laser-induced point-by-point material transfer [112–114] and direct writing [115, 116], the presented direct and high-throughput fabrication is a step towards a simple realization of spatially invariant metasurface-based devices.

The results on postprocessing dielectric nanostructures, presented in Section 3.1, are successfully published in *Optics Express* [S8]. Simultaneously, the results on direct laser interference patterning of Mie-resonant metasurfaces, discussed in Section 3.2, are published in *ACS Nano* [S10]. More publications on this topic are envisioned.

Chapter 4

Conclusions and outlook

This work is intended to take its reader through a small part of possibilities – spectral selectivity – using the physics of optically resonant high-index nanostructures and non-resonant nanostructures embedded in other-type resonant systems, and bring such structures a step closer to the real-life applications.

Chapter 1 is used for the analysis of Mie resonances and their applicability in spectral filtering. High-index dielectric nanostructures, exhibiting ED and MD resonances, provide a wavelength-dependent spectral response, which allowed the realization of color filter arrays. Moreover, the resonances can be tuned by lateral geometry, keeping it within the subwavelength range. Thus, the nanostructures can be assembled into flexible and miniature spectral filters. As a result, RGB filters as small as $0.5\ \mu\text{m}$ in lateral size were demonstrated. The use of the enhanced camera resolution enabled by the submicrometer pixels could potentially give access to hitherto hardly obtainable information. The nanostructure-based filters have the potential to replace conventional pigmented and dye-based color filters, and their consequent use can significantly improve the technologies of digital color imaging.

Silicon (Si) is the most frequently used high-index material because of its relatively low cost, compatibility with the CMOS process, and tolerable losses [234, 274]. Thus, amorphous Si was used for most demonstrations, disregarding the losses in the visible spectral range. Naturally, better performance and higher efficiency are envisioned with other materials, such as TiO_2 and GaP. Furthermore, the performance can be enhanced by vertical stacking, extending the gamut over the limits of sRGB, or horizontal mixing, which could improve the color quality without impinging additional technological steps [S2].

Chapter 2 explores the FP resonators, which is another optically resonant system. It was shown that the FP resonator can be tailored by inclusions of high index nanostructures to create multispectral filters and even extend the concept to polarization-sensitive structures. Conventional step-profile FP resonators within a single chip require a complex fabrication with multiple etching steps [85]. Also, the majority of multispectral and multifunctional nanostructure-based devices consist of a few transversely-variant layers on top of each other. Multiple layers cause quite a challenge in terms of alignment, as even small misalignment results in errors of the detected information [82]. In contrast, the proposed architecture – FP resonator with embedded nanostructures made from a high-index material – involves only a single lithography step. Thus the performance cannot be deteriorated by the aforementioned issues. The previously introduced Mie resonances can be extended to the infrared. However, biomedical applications and Earth observation

benefit from a high SNR (quality factor) provided by FP resonators have an edge. The spectral resolution of systems, presented in Chapter 2, is limited only by the reflectivity of the mirrors. Thus, subnanometer spectral resolution is possible. Moreover, the spatial resolution may reach a submicrometer scale, making the systems extremely compact but powerful.

The limits of the spectropolarimetric design were analyzed. With a spectral resolution of 1 nm, such a system could have a bandwidth of 127 nm separated in 126 bands. In the ideal case, the system would benefit from a more anisotropic inclusion inside the cavity to increase the bandwidth. Furthermore, the system could be extended with additional layers of retarders to enable circularly polarized light measurements, enabling the retrieval of the full Stokes vector. In perspective, more advanced tailoring of the FP resonances can be done by using multiple cavities [226, 275], nanostructuring the mirrors [78, 221], or embedding resonant nanostructures [79, 90].

Laser-based techniques for postprocessing and patterning of high-index nanostructures are proposed in Chapter 3. It was demonstrated that laser pulses might be used to spatially-tailor single nanostructures or large scale metasurfaces. The process was based on laser-induced thermal processes, crystallization of amorphous Si, and melting. It allowed the laser to pixelate the aforementioned nanostructure-based color filters and even control the height of the nanostructures – adding local functionalities to the sample.

Direct laser interference patterning was applied to create the whole metasurface from a homogeneous thin film using only a single laser pulse. The presented interference technique could be extended towards different and more complex shapes of the metasurface elements and their geometrical distribution by manipulation of amplitude and phase [144, 276, 277], control of polarization [154], or sub-period positioning of the sample [140]. Moreover, different lattice configurations could be obtained using a different number of interfering beams, e.g., three or six beams for hexagonal lattice and five, seven, or more beams for more exotic quasi-periodic patterns [278]. Furthermore, while the period is limited by the wavelength of the laser source used, the filling factor could be potentially increased and even doubled by manipulating the phase of the interfering beams [277, 278]. Also, the patterned area could be increased from tens of μm^2 to cm^2 , or even m^2 , by a partial spatial overlap of interference spots with a stitching error as low as 9% [140, 145]. The error could also be reduced further by the spatial modulation of the beams, e.g., by using a top-hat profile [279]. High repetition rates of pulsed lasers and speed of high-accuracy positioning stages already allow processing speeds within the mass-production scale, up to $1 \text{ m}^2/\text{min}$ [280]. At the same time, the fabricated large-scale uniform metasurface could be equipped with local functionalities by the complimentary process of photothermal reshaping [52, 129, 248].

Even though laser-induced thermal processes depend on Si parameters, they are also transferable to metasurfaces constituted of other high-index materials, e.g., TiO_2 , GaP, and others. At the same time, the selection of a pulsed laser with a high repetition rate as a light source gives the opportunity not only for the spatial but also for rapid and efficient postprocessing, which serves as a strong building block in bridging the gap between high-index dielectric metasurfaces and their implementation in mass-produced devices. A great perspective is envisioned using even shorter pulses, spatial and temporal beam shaping.

The comparison of the presented optically-resonant nanostructure-based systems is summarized in Table 4.1. Here, one can see that the RGB color filters, introduced in Chapter 1 and later modified by laser-induced processes in Chapter 3, have relatively broad resonances, which fit the requirements of the con-

Table 4.1: Summary of different optically resonant nanostructure-based systems presented in this work. The approximate values of FWHM and quality factors are taken from the numerical results.

	Key physics	Spectral range	FWHM, nm	Quality factor
RGB color filters (Chapter 1, Chapter 3)	Mie resonances	VIS	100–150 nm	2–5
FP oximeter (Chapter 2)	FP resonance and effective index	VIS/NIR	60–70 nm	8–14
Spectropolarimeter (Chapter 2)	FP resonance and effective index	IR	1–4 nm	>300
Laser-patterned (Chapter 3)	Mie resonances	NIR	120–170 nm	3–5

ventional tricolor imaging. The FP-based oximeter, shown in Chapter 2, have narrower resonances and, subsequently, a higher quality factor. Furthermore, such FP resonators tailored by high index nanostructures may be further improved using DBRs instead of metallic mirrors, if a higher spectral selectivity is required. This is the case for the spectropolarimeter, embracing a quality factor of > 300 . Finally, the lithography-free fabrication technique, proposed in Chapter 3, offers a decent solution for an easier Mie-resonant metasurface fabrication and subsequent implementation in optical devices. Even though at the moment their quality factor is relatively low, there is a lot of room for improvement.

Last but not least, in addition to the optical properties, discussed in this work, dielectric nanostructures and metasurfaces may serve several other roles depending on their physical size and geometry. This includes but is not limited to physical matrices for SERS [281] and other sensing applications [282, 283], surfaces for mechanical bactericidal effect [284], and other ingenious applications yet to be defined.

List of scientific contributions

Publications:

- [S1] M. Gedvilas, J. Mikšys, **J. Berzinš**, V. Stankevič, and G. Račiukaitis, “Multi-photon absorption enhancement by dual-wavelength double-pulse laser irradiation for efficient dicing of sapphire wafers,” *Scientific Reports* **7**, 1–10 (2017).
- [S2] **J. Berzinš**, F. Silvestri, G. Gerini, F. Setzpfandt, T. Pertsch, and S. M. Bäumer, “Color filter arrays based on dielectric metasurface elements,” *SPIE Proc.* **10671**, 106711F (2018).
- [S3] J. Černigoj, F. Silvestri*, L. P. Stoevelaar*, **J. Berzinš***, and G. Gerini*, “Lattice resonances and local field enhancement in array of dielectric dimers for surface enhanced raman spectroscopy,” *Scientific Reports* **8**, 1–7 (2018).
- [S4] **J. Berzinš**, S. Fasold, T. Pertsch, S. M. Bäumer, and F. Setzpfandt, “Submicrometer nanostructure-based RGB filters for CMOS image sensors,” *ACS Photonics* **6**, 1018–1025 (2019).
- [S5] N. Abbasirad, D. Arslan, **J. Berzinš**, S. Fasold, I. Staude, F. Setzpfandt, and T. Pertsch, “Mapping the near-field interaction of silicon nanodisc arrays by automated dual-tip scanning near-field optical microscopy,” in “CLEO/Europe-EQEC 2019,” (2019).
- [S6] N. Abbasirad, **J. Berzinš**, K. Kollin, S. Saravi, N. Janunts, F. Setzpfandt, and T. Pertsch, “A fully automated dual-tip scanning near-field optical microscope for localized optical excitation and detection in the visible and near-infrared,” *Review of Scientific Instruments* **90**, 053705 (2019).
- [S7] L. P. Stoevelaar*, J. Černigoj*, **J. Berzinš***, F. Silvestri, and G. Gerini, “Nanostructured dielectric surfaces for Raman spectroscopy: Design and thermal analysis,” *SPIE Proc.* **11080**, 110802U (2019).
- [S8] **J. Berzinš**, S. Indrišiūnas, S. Fasold, M. Steinert, O. Žukovskaja, D. Cialla-May, P. Gečys, S. M. Bäumer, T. Pertsch, and F. Setzpfandt, “Laser-induced spatially-selective tailoring of high-index dielectric metasurfaces,” *Optics Express* **28**, 1539–1553 (2020).
- [S9] L. P. Stoevelaar*, **J. Berzinš***, F. Silvestri, S. Fasold, K. Z. Kamali, H. Knopf, F. Eilenberger, F. Setzpfandt, T. Pertsch, S. M. B. Bäumer, and G. Gerini, “Nanostructure-modulated planar high spectral resolution spectro-polarimeter,” *Optics Express* **28**, 19818–19836 (2020).

- [S10] **J. Berzinš**, S. Indrišiūnas, K. van Erve, A. Nagarajan, S. Fasold, M. Steinert, G. Gerini, P. Gečys, T. Pertsch, S. M. B. Bäumer, and F. Setzpfandt, "Direct and high-throughput fabrication of Mie-resonant metasurfaces via single-pulse laser interference," *ACS Nano* **14**, 6138–6149 (2020).
- [S11] J. Sperrhake, **J. Berzinš**, M. Walther, C. Stock, S. Fasold, M. Steinert, S. M. B. Bäumer, F. Setzpfandt, T. Pertsch, "Nanostructured spectral filters for blood oxygen sensing," (in preparation).
- [S12] **J. Berzinš**, K. van Erve, G. Gerini, S. M. B. Bäumer, F. Setzpfandt, T. Pertsch, "Single-step nanostructure-based color filters: The quest for the best material," (in preparation).

*equal contribution.

Patents:

- [T1] F. Silvestri, **J. Berzinš**, Z. Deutschman, G. Gerini, and S. M. B. Bäumer, "Optical device and spectrometer comprising such a device," (2019). EP3543665A1, WO2019182444A1.

Conference presentations:

- [C1] **J. Berzinš**, "Sub-wavelength period structures and their formation by direct laser interference patterning", Open Readings 2017, 14.03.2017-17.03.2017 (Vilnius, Lithuania).
- [C2] **J. Berzinš**, F. Silvestri, G. Gerini, F. Setzpfandt, T. Pertsch, S. M. B. Bäumer, "Optical systems based on metasurface elements", 3rd ERP 3D Nanomanufacturing Dissemination Event, 06.11.2017 (Delft, Netherlands).
- [C3] **J. Berzinš**, F. Silvestri, G. Gerini, F. Setzpfandt, T. Pertsch, S. M. B. Bäumer, "Color filter arrays based on dielectric metasurface elements", SPIE Photonics Europe, 22.04.2018-26.04.2018 (Strasbourg, France).
- [C4] Z. K. Deutschman, F. Silvestri, **J. Berzinš**, S. M. B. Bäumer, G. Gerini, "Dielectric resonators surfaces for infrared filters and pleochroics", SPIE Photonics Europe, 22.04.2018-26.04.2018 (Strasbourg, France).
- [C5] N. Abbasirad, **J. Berzinš**, D. Arslan, S. Fasold, I. Staude, F. Setzpfandt, T. Pertsch, "Fully automated dual-probe SNOM for near-field excitation and characterization of nanodiscs arrays", 15th International Conference of Near-field Optics and Nanophotonics, 26.08.2018-31.08.2018 (Troyes, France).
- [C6] **J. Berzinš**, J. Andruseč, J. Černigoj, J. Sperrhake, P. Stoevelaar, F. Silvestri, G. Gerini, S. M. B. Bäumer, F. Setzpfandt, T. Pertsch, "Dielectric metasurfaces for sensing and imaging applications in visible and infrared spectral range", 7th Doctoral Conference DokDok 2018, 17.09.2018-21.09.2018 (Friedrichroda, Germany).

- [C7] N. Abbasirad, **J. Berzinš**, D. Arslan, S. Fasold, I. Staude, F. Setzpfandt, T. Pertsch, "Dual-probe SNOM for the near-field study of nanostructures", 21st Conference of Non-Contact Atomic Force Microscopy, 17.09.2018-21.09.2018 (Porvoo, Finland).
- [C8] **J. Berzinš**, S. Fasold, F. Silvestri, G. Gerini, F. Setzpfandt, T. Perstch, S. M. B. Bäumer, "RGB color filters using periodic arrays of silicon nanostructures", European Optical Society Biennial Meeting (EOSAM) 2018, 08.10.2018-12.10.2018 (Delft, Netherlands).
- [C9] J. Andrasec, P. Stoevelaar, F. Silvestri, **J. Berzinš**, G. Gerini, "Assessment study of spectro-polarimeter concepts based on Fabry-Perot cavities and nanostructures", European Optical Society Biennial Meeting (EOSAM) 2018, 08.10.2018-12.10.2018 (Delft, Netherlands).
- [C10] **J. Berzinš**, S. Fasold, S. Indrišiūnas, P. Gečys, S. M. B. Bäumer, F. Setzpfandt, T. Pertsch, "Laser pixelation of dielectric nanostructure-based spectral filters", 7th International Topical meeting on Nanophotonics and Metamaterials, 03-06.01.2019 (Seefeld, Austria).
- [C11] J. Černigoj, **J. Berzinš**, P. L. Stoevelaar, F. Silvestri, F. Setzpfandt, T. Pertsch, S. M. B. Bäumer, G. Gerini, "Low-loss all-dielectric SERS substrates", 2nd European Biosensor Symposium 2019, 18-21.02.2019 (Florence, Italy).
- [C12] **J. Berzinš**, S. Indrišiūnas, S. Fasold, O. Žukovskaja, M. Steinert, P. Gečys, S. M. B. Bäumer, F. Setzpfandt, T. Pertsch, "Direct laser interference patterning of silicon metasurfaces", ICNN 2019, 22.04.2019-26.04.2019 (Yokohoma, Japan).
- [C13] **J. Berzinš**, S. Fasold, T. Pertsch, P. Gečys, S. M. B. Bäumer, F. Setzpfandt, "Nanostructure-based color filter arrays", ICNN 2019, 22.04.2019-26.04.2019 (Yokohoma, Japan).
- [C14] N. Abbasirad, D. Arslan, **J. Berzinš**, S. Fasold, I. Staude, F. Setzpfandt, T. Pertsch, "Mapping the near-field interaction of silicon nanodisk arrays by automated dual-tip scanning near-field optical microscopy", CLEO Munich 2019, 23-27.06.2019 (Munich, Germany).
- [C15] P. Stoevelaar, J. Černigoj, **J. Berzinš**, G. Gerini, "Nanostructured dielectric surfaces for Raman Spectroscopy: Design and thermal analysis", SPIE Optics+Photonics 2019, 11-15.08.2019 (San Diego, USA).
- [C16] **J. Berzinš**, S. Fasold, G. Gerini, T. Pertsch, S. M. B. Bäumer, F. Setzpfandt, "Dielectric nanostructure-based spectral filters for high resolution imaging", Nanophotonics and Micro/Nano Optics International Conference, 04-06.09.2019 (Munich, Germany)

Bibliography

- [1] N. Yu and F. Capasso, “Flat optics with designer metasurfaces,” *Nature Materials* **13**, 139–150 (2014).
- [2] P. Genevet, F. Capasso, F. Aieta, M. Khorasaninejad, and R. Devlin, “Recent advances in planar optics: From plasmonic to dielectric metasurfaces,” *Optica* **4**, 139–152 (2017).
- [3] I. Staude and J. Schilling, “Metamaterial-inspired silicon nanophotonics,” *Nature Photonics* **11**, 274 (2017).
- [4] A. Barreda, J. Saiz, F. González, F. Moreno, and P. Albella, “Recent advances in high refractive index dielectric nanoantennas: Basics and applications,” *AIP Advances* **9**, 040701 (2019).
- [5] Z. Dong, T. Wang, X. Chi, J. Ho, C. Tserkezis, S. L. K. Yap, A. Rusydi, F. Tjiptoharsono, D. Thian, N. A. Mortensen, and J. K. W. Yang, “Ultraviolet interband plasmonics with Si nanostructures,” *Nano Letters* **19**, 8040–8048 (2019).
- [6] J. A. Schuller and M. L. Brongersma, “General properties of dielectric optical antennas,” *Optics Express* **17**, 24084–24095 (2009).
- [7] I. Staude, A. E. Miroshnichenko, M. Decker, N. T. Fofang, S. Liu, E. Gonzales, J. Dominguez, T. S. Luk, D. N. Neshev, I. Brener *et al.*, “Tailoring directional scattering through magnetic and electric resonances in subwavelength silicon nanodisks,” *ACS Nano* **7**, 7824–7832 (2013).
- [8] J. van de Groep and A. Polman, “Designing dielectric resonators on substrates: Combining magnetic and electric resonances,” *Optics Express* **21**, 26285–26302 (2013).
- [9] S. Jahani and Z. Jacob, “All-dielectric metamaterials,” *Nature Nanotechnology* **11**, 23 (2016).
- [10] M. A. van de Haar, J. van de Groep, B. J. Brenny, and A. Polman, “Controlling magnetic and electric dipole modes in hollow silicon nanocylinders,” *Optics Express* **24**, 2047–2064 (2016).
- [11] M. Decker, I. Staude, M. Falkner, J. Dominguez, D. N. Neshev, I. Brener, T. Pertsch, and Y. S. Kivshar, “High-efficiency dielectric Huygens’ surfaces,” *Advanced Optical Materials* **3**, 813–820 (2015).
- [12] A. García-Etxarri, R. Gómez-Medina, L. S. Froufe-Pérez, C. López, L. Chantada, F. Scheffold, J. Aizpurua, M. Nieto-Vesperinas, and J. J. Sáenz, “Strong magnetic response of submicron silicon particles in the infrared,” *Optics Express* **19**, 4815–4826 (2011).

- [13] A. I. Kuznetsov, A. E. Miroshnichenko, Y. H. Fu, J. Zhang, and B. Luk'Yanchuk, "Magnetic light," *Scientific Reports* **2**, 492 (2012).
- [14] I. Koirala, V. R. Shrestha, C.-S. Park, S. Gao, S.-S. Lee, and D.-Y. Choi, "All dielectric transmissive structural multicolor pixel incorporating a resonant grating in hydrogenated amorphous silicon," *Scientific Reports* **7**, 1–7 (2017).
- [15] C. Jin, M. Afsharnia, R. Berlich, S. Fasold, C. Zou, D. Arslan, I. Staude, T. Pertsch, and F. Setzpfandt, "Dielectric metasurfaces for distance measurements and three-dimensional imaging," *Advanced Photonics* **1**, 036001 (2019).
- [16] L. Cao, P. Fan, E. S. Barnard, A. M. Brown, and M. L. Brongersma, "Tuning the color of silicon nanostructures," *Nano Letters* **10**, 2649–2654 (2010).
- [17] K. Seo, M. Wober, P. Steinvurzel, E. Schonbrun, Y. Dan, T. Ellenbogen, and K. B. Crozier, "Multicolored vertical silicon nanowires," *Nano Letters* **11**, 1851–1856 (2011).
- [18] H. Park and K. B. Crozier, "Multispectral imaging with vertical silicon nanowires," *Scientific Reports* **3**, 2460 (2013).
- [19] C.-S. Park, V. R. Shrestha, W. Yue, S. Gao, S.-S. Lee, E.-S. Kim, and D.-Y. Choi, "Structural color filters enabled by a dielectric metasurface incorporating hydrogenated amorphous silicon nanodisks," *Scientific Reports* **7**, 1–9 (2017).
- [20] Y. Horie, S. Han, J.-Y. Lee, J. Kim, Y. Kim, A. Arbabi, C. Shin, L. Shi, E. Arbabi, S. M. Kamali *et al.*, "Visible wavelength color filters using dielectric subwavelength gratings for backside-illuminated CMOS image sensor technologies," *Nano Letters* **17**, 3159–3164 (2017).
- [21] S. Daqiqeh Rezaei, Z. Dong, J. You En Chan, J. Trisno, R. J. H. Ng, Q. Ruan, C.-W. Qiu, N. A. Mortensen, and J. K. Yang, "Nanophotonic structural colors," *ACS Photonics* (2020).
- [22] M. Caldarola, P. Albella, E. Cortés, M. Rahmani, T. Roschuk, G. Grinblat, R. F. Oulton, A. V. Bragas, and S. A. Maier, "Non-plasmonic nanoantennas for surface enhanced spectroscopies with ultra-low heat conversion," *Nature Communications* **6**, 1–8 (2015).
- [23] N. Bosio, H. Šípová Jungová, N. O. Länk, T. J. Antosiewicz, R. Verre, and M. Käll, "Plasmonic versus all-Dielectric nanoantennas for refractometric Sensing: A direct comparison," *ACS Photonics* **6**, 1556–1564 (2019).
- [24] A. Vaskin, R. Kolkowski, A. F. Koenderink, and I. Staude, "Light-emitting metasurfaces," *Nanophotonics* **8**, 1151–1198 (2019).
- [25] E. Slivina, A. Abass, D. Bätzner, B. Strahm, C. Rockstuhl, and I. Fernandez-Corbaton, "Insights into backscattering suppression in solar cells from the helicity-preservation point of view," *Physical Review Applied* **12**, 054003 (2019).

- [26] F. Uleman, V. Neder, A. Cordaro, A. Alù, and A. Polman, “Resonant metagratings for spectral and angular control of light for colored rooftop photovoltaics,” *ACS Applied Energy Materials* (2020).
- [27] T. Shibanuma, S. A. Maier, and P. Albella, “Polarization control of high transmission/reflection switching by all-dielectric metasurfaces,” *Applied Physics Letters* **112**, 063103 (2018).
- [28] G. Mie, “Beiträge zur Optik trüber Medien, Speziell Kolloidaler Metallösungen,” *Annalen der Physik* **330**, 377–445 (1908).
- [29] S. Bäumer, *Handbook of plastic optics* (John Wiley & Sons, 2011).
- [30] K. Baek, Y. Kim, S. Mohd-Noor, and J. K. Hyun, “Mie resonant structural colors,” *ACS Applied Materials & Interfaces* (2020).
- [31] F. Gildas and Y. Dan, “Review of nanostructure color filters,” *Journal of Nanophotonics* **13**, 020901 (2019).
- [32] S. Kinoshita, S. Yoshioka, and J. Miyazaki, “Physics of structural colors,” *Reports on Progress in Physics* **71**, 076401 (2008).
- [33] Y. Zhao, Y. Zhao, S. Hu, J. Lv, Y. Ying, G. Gervinskas, and G. Si, “Artificial structural color pixels: A review,” *Materials* **10**, 944 (2017).
- [34] K. Kumar, H. Duan, R. S. Hegde, S. C. Koh, J. N. Wei, and J. K. Yang, “Printing colour at the optical diffraction limit,” *Nature Nanotechnology* **7**, 557 (2012).
- [35] Y. Yu, Q. Chen, L. Wen, X. Hu, and H.-F. Zhang, “Spatial optical crosstalk in CMOS image sensors integrated with plasmonic color filters,” *Optics Express* **23**, 21994–22003 (2015).
- [36] Q. Chen, X. Hu, L. Wen, Y. Yu, and D. R. Cumming, “Nanophotonic image sensors,” *Small* **12**, 4922–4935 (2016).
- [37] X. Zhu, C. Vannahme, E. Højlund-Nielsen, N. A. Mortensen, and A. Kristensen, “Plasmonic colour laser printing,” *Nature Nanotechnology* **11**, 325 (2016).
- [38] S. J. Tan, L. Zhang, D. Zhu, X. M. Goh, Y. M. Wang, K. Kumar, C.-W. Qiu, and J. K. Yang, “Plasmonic color palettes for photorealistic printing with aluminum nanostructures,” *Nano Letters* **14**, 4023–4029 (2014).
- [39] T. Ellenbogen, K. Seo, and K. B. Crozier, “Chromatic plasmonic polarizers for active visible color filtering and polarimetry,” *Nano Letters* **12**, 1026–1031 (2012).
- [40] R. Rajasekharan, E. Balaur, A. Minovich, S. Collins, T. D. James, A. Djalalian-Assl, K. Ganesan, S. Tomljenovic-Hanic, S. Kandasamy, E. Skafidas *et al.*, “Filling schemes at submicron scale: Development of submicron sized plasmonic colour filters,” *Scientific Reports* **4**, 6435 (2014).

- [41] S. Yokogawa, S. P. Burgos, and H. A. Atwater, “Plasmonic color filters for CMOS image sensor applications,” *Nano Letters* **12**, 4349–4354 (2012).
- [42] X. Wang, A. Kuchmizhak, D. Storozhenko, S. Makarov, and S. Juodkazis, “Single-step laser plasmonic coloration of metal films,” *ACS Applied Materials & Interfaces* **10**, 1422–1427 (2018).
- [43] D. G. Baranov, D. A. Zuev, S. I. Lepeshov, O. V. Kotov, A. E. Krasnok, A. B. Evlyukhin, and B. N. Chichkov, “All-dielectric nanophotonics: The quest for better materials and fabrication techniques,” *Optica* **4**, 814–825 (2017).
- [44] V. Flauraud, M. Reyes, R. Paniagua-Dominguez, A. I. Kuznetsov, and J. Brugger, “Silicon nanostructures for bright field full color prints,” *ACS Photonics* **4**, 1913–1919 (2017).
- [45] Z. Dong, J. Ho, Y. F. Yu, Y. H. Fu, R. Paniagua-Dominguez, S. Wang, A. I. Kuznetsov, and J. K. Yang, “Printing beyond sRGB color gamut by mimicking silicon nanostructures in free-space,” *Nano Letters* **17**, 7620–7628 (2017).
- [46] Y. Nagasaki, M. Suzuki, and J. Takahara, “All-dielectric dual-color pixel with subwavelength resolution,” *Nano Letters* **17**, 7500–7506 (2017).
- [47] Y. Nagasaki, M. Suzuki, I. Hotta, and J. Takahara, “Control of Si-based all-dielectric printing color through oxidation,” *ACS Photonics* **5**, 1460–1466 (2018).
- [48] B. Yang, W. Liu, Z. Li, H. Cheng, S. Chen, and J. Tian, “Polarization-sensitive structural colors with hue-and-saturation tuning based on all-dielectric nanopixels,” *Advanced Optical Materials* **6**, 1701009 (2018).
- [49] Y. Nagasaki, I. Hotta, M. Suzuki, and J. Takahara, “Metal-masked Mie-resonant full-color printing for achieving free-space resolution limit,” *ACS Photonics* **5**, 3849–3855 (2018).
- [50] J. Proust, F. Bedu, B. Gallas, I. Ozerov, and N. Bonod, “All-dielectric colored metasurfaces with silicon Mie resonators,” *ACS Nano* **10**, 7761–7767 (2016).
- [51] A. K. González-Alcalde, R. Salas-Montiel, H. Mohamad, A. Morand, S. Blaize, and D. Macías, “Optimization of all-dielectric structures for color generation,” *Applied Optics* **57**, 3959–3967 (2018).
- [52] X. Zhu, W. Yan, U. Levy, N. A. Mortensen, and A. Kristensen, “Resonant laser printing of structural colors on high-index dielectric metasurfaces,” *Science Advances* **3**, e1602487 (2017).
- [53] V. Vashistha, G. Vaidya, R. S. Hegde, A. E. Serebryannikov, N. Bonod, and M. Krawczyk, “All-dielectric metasurfaces based on cross-shaped resonators for color pixels with extended gamut,” *ACS Photonics* **4**, 1076–1082 (2017).
- [54] R. Fontaine, “The state-of-the-art of mainstream CMOS image sensors,” in “Proceedings of the International Image Sensors Workshop,” (2015), pp. 6–12.

- [55] G. Agranov, R. Mauritzson, J. Ladd, A. Dokoutchaev, X. Fan, X. Li, Z. Yin, R. Johnson, V. Lenchenkov, S. Nagaraja *et al.*, “Pixel continues to shrink, pixel development for novel CMOS image sensors,” in “Proc. Int. Image Sensor Workshop,” (2009), pp. 69–72.
- [56] A. Theuwissen, “CMOS image sensors: State-of-the-art and future perspectives,” in “ESSDERC 2007-37th European Solid State Device Research Conference,” (IEEE, 2007), pp. 21–27.
- [57] L. Frey, P. Parrein, J. Raby, C. Pellé, D. Hérault, M. Marty, and J. Michailos, “Color filters including infrared cut-off integrated on CMOS image sensor,” *Optics Express* **19**, 13073–13080 (2011).
- [58] S. Yokogawa, I. Oshiyama, H. Ikeda, Y. Ebiko, T. Hirano, S. Saito, T. Oinoue, Y. Hagimoto, and H. Iwamoto, “IR sensitivity enhancement of CMOS Image Sensor with diffractive light trapping pixels,” *Scientific Reports* **7**, 1–9 (2017).
- [59] S. Nishiwaki, T. Nakamura, M. Hiramoto, T. Fujii, and M.-a. Suzuki, “Efficient colour splitters for high-pixel-density image sensors,” *Nature Photonics* **7**, 240 (2013).
- [60] J.-K. Lee, A. Kim, D.-W. Kang, and B. Y. Lee, “Efficiency enhancement in a backside illuminated 1.12 μm pixel cmos image sensor via parabolic color filters,” *Optics Express* **24**, 16027–16036 (2016).
- [61] S. Takahashi, Y.-M. Huang, J.-J. Sze, T.-T. Wu, F.-S. Guo, W.-C. Hsu, T.-H. Tseng, K. Liao, C.-C. Kuo, T.-H. Chen *et al.*, “A 45 nm stacked CMOS image sensor process technology for submicron pixel,” *Sensors* **17**, 2816 (2017).
- [62] T. Blaschke, “Object based image analysis for remote sensing,” *ISPRS Journal of Photogrammetry and Remote Sensing* **65**, 2–16 (2010).
- [63] H. Taguchi and M. Enokido, “Technology of color filter materials for image sensor,” in “2011 Int. Image Sens. Work.”, (2011), pp. 8–11.
- [64] L. Anzagira and E. R. Fossum, “Color filter array patterns for small-pixel image sensors with substantial cross talk,” *JOSA A* **32**, 28–34 (2015).
- [65] H. Park, Y. Dan, K. Seo, Y. J. Yu, P. K. Duane, M. Wober, and K. B. Crozier, “Filter-free image sensor pixels comprising silicon nanowires with selective color absorption,” *Nano Letters* **14**, 1804–1809 (2014).
- [66] D. Hillier, “Spectropolarimetry and imaging polarimetry,” in “Ultraviolet-Optical Space Astronomy Beyond HST,” (1999), p. 90.
- [67] F. Snik, J. Craven-Jones, M. Escuti, S. Fineschi, D. Harrington, A. De Martino, D. Mawet, J. Riedi, and J. S. Tyo, “An overview of polarimetric sensing techniques and technology with applications to different research fields,” *Proc. SPIE* **9099**, 90990B (2014).
- [68] D. Bannon, “Hyperspectral Imaging: Cubes and slices,” *Nature Photonics* **3**, 627–629 (2009).

- [69] M. J. Khan, H. S. Khan, A. Yousaf, K. Khurshid, and A. Abbas, “Modern trends in hyperspectral image analysis: A review,” *IEEE Access* **6**, 14118–14129 (2018).
- [70] W. Yue, S.-S. Lee, and E.-S. Kim, “Angle-tolerant polarization-tuned color filter exploiting a nanostructured cavity,” *Optics Express* **24**, 17115 (2016).
- [71] S. Wei, Z. Yang, and M. Zhao, “Design of ultracompact polarimeters based on dielectric metasurfaces,” *Optics Letters* **42**, 1580 (2017).
- [72] N. A. Rubin, A. Zaidi, M. Juhl, R. P. Li, J. B. Mueller, R. C. Devlin, K. Leósson, and F. Capasso, “Polarization state generation and measurement with a single metasurface,” *Optics Express* **26**, 21455 (2018).
- [73] E. Arbabi, S. M. Kamali, A. Arbabi, and A. Faraon, “Full-stokes imaging polarimetry using dielectric metasurfaces,” *ACS Photonics* **5**, 3132–3140 (2018).
- [74] C. Yan, X. Li, M. Pu, X. Ma, F. Zhang, P. Gao, K. Liu, and X. Luo, “Midinfrared real-time polarization imaging with all-dielectric metasurface,” *Applied Physics Letters* **114**, 161904 (2019).
- [75] M. Faraji-Dana, E. Arbabi, A. Arbabi, S. M. Kamali, H. Kwon, and A. Faraon, “Compact folded metasurface spectrometer,” *Nature Communications* **9**, 4196 (2018).
- [76] Y. Horie, A. Arbabi, E. Arbabi, S. M. Kamali, and A. Faraon, “Wide bandwidth and high resolution planar filter array based on DBR-metasurface-DBR structures,” *Optics Express* **24**, 11677 (2016).
- [77] W. Yue, S.-S. Lee, E.-S. Kim, and B.-G. Lee, “Uniformly thick tri-color filters capitalizing on an etalon with a nanostructured cavity,” *Applied Optics* **54**, 5866 (2015).
- [78] W. Yue, Y. Li, C. Wang, Z. Yao, S.-S. Lee, and N.-Y. Kim, “Color filters based on a nanoporous Al-AAO resonator featuring structure tolerant color saturation,” *Optics Express* **23**, 27474 (2015).
- [79] A. M. Shaltout, J. Kim, A. Boltasseva, V. M. Shalaev, and A. V. Kildishev, “Ultrathin and multicolour optical cavities with embedded metasurfaces,” *Nature Communications* **9**, 1–7 (2018).
- [80] W. T. Chen, P. Török, M. R. Foreman, C. Y. Liao, W.-Y. Tsai, P. R. Wu, and D. P. Tsai, “Integrated plasmonic metasurfaces for spectropolarimetry,” *Nanotechnology* **27**, 224002 (2016).
- [81] F. Ding, A. Pors, Y. Chen, V. A. Zenin, and S. I. Bozhevolnyi, “Beam-size-invariant spectropolarimeters using gap-plasmon metasurfaces,” *ACS Photonics* **4**, 943–949 (2017).
- [82] X. Tu, O. J. Spires, X. Tian, N. Brock, R. Liang, and S. Pau, “Division of amplitude RGB full-Stokes camera using micro-polarizer arrays,” *Optics Express* **25**, 33160–33175 (2017).
- [83] J. Li, H. Wu, and C. Qi, “Ultracompact focal plane snapshot spectropolarimeter,” *Applied Optics* **58**, 7603–7608 (2019).

- [84] Y.-T. Yoon and S.-S. Lee, "Transmission type color filter incorporating a silver film based etalon," *Optics Express* **18**, 5344–5349 (2010).
- [85] B. Geelen, N. Tack, and A. Lambrechts, "A compact snapshot multispectral imager with a monolithically integrated per-pixel filter mosaic," *Proc. SPIE* **8974**, 89740L (2014).
- [86] Y. Wang, M. Zheng, Q. Ruan, Y. Zhou, Y. Chen, P. Dai, Z. Yang, Z. Lin, Y. Long, Y. Li, N. Liu, C.-W. Qiu, J. K. W. Yang, and H. Duan, "Stepwise-nanocavity-assisted transmissive color filter array microprints," *Research* **2018**, 1–10 (2018).
- [87] S. Kaushik and B. R. Stallard, "Two-dimensional array of optical interference filters produced by lithographic alterations of the index of refraction," *Proc. SPIE* **2532**, 276–281 (1995).
- [88] K. Walls, Q. Chen, J. Grant, S. Collins, D. Cumming, and T. Drysdale, "Narrowband multispectral filter set for visible band," *Optics Express* **20**, 21917–21923 (2012).
- [89] L. Frey, M. Armand, and C. Pelle, "Optical filtering structure in the visible and/or infrared domain," (2017). US Patent 9,658,372.
- [90] I.-H. Lee, E.-S. Yu, S.-H. Lee, and S.-D. Lee, "Full-coloration based on metallic nanostructures through phase discontinuity in Fabry-Perot resonators," *Optics Express* **27**, 33098–33110 (2019).
- [91] W. Nakagawa and Y. Fainman, "Tunable optical nanocavity based on modulation of near-field coupling between subwavelength periodic nanostructures," *IEEE Journal of Selected Topics in Quantum Electronics* **10**, 478–483 (2004).
- [92] D. Lerose, E. K. S. Hei, B. C. Ching, M. Sterger, L. C. Yaw, F. M. Schulze, F. Schmidt, A. Schmidt, and K. Bach, "CMOS-integrated geometrically tunable optical filters," *Applied Optics* **52**, 1655–1662 (2013).
- [93] G. Lu and B. Fei, "Medical hyperspectral imaging: A review," *Journal of Biomedical Optics* **19**, 010901 (2014).
- [94] Lung Institute, "Blood oxygen level: What it means to you," (2016). (www.lunginstitute.com/blog/blood-oxygen-level; accessed: 2020.03.24).
- [95] E. Kulu, "Nanosats database," (2019). (www.nanosats.eu; accessed: 2019.12.10).
- [96] P.-Y. Deschamps, F.-M. Breon, M. Leroy, A. Podaire, A. Bricaud, J.-C. Buriez, and G. Seze, "The POLDER mission: Instrument characteristics and scientific objectives," *IEEE Transactions on Geoscience and Remote Sensing* **32**, 598–615 (1994).
- [97] G. van Harten, F. Snik, J. H. H. Rietjens, J. M. Smit, J. de Boer, R. Diamantopoulou, O. P. Hasekamp, D. M. Stam, C. U. Keller, E. C. Laan, A. L. Verlaan, W. A. Vliegthart, R. ter Horst, R. Navarro, K. Wielinga, S. Hannemann, S. G. Moon, and R. Voors, "Prototyping for the Spectropolarimeter for Planetary EXploration (SPEX): Calibration and sky measurements," *Polarization Science and Remote Sensing V* **8160**, 81600Z (2011).

- [98] G. Yoon, I. Kim, and J. Rho, “Challenges in fabrication towards realization of practical metamaterials,” *Microelectronic Engineering* **163**, 7–20 (2016).
- [99] D. Arslan, K. Chong, A. Miroshnichenko, D. Choi, D. Neshev, T. Pertsch, Y. Kivshar, and I. Staude, “Angle-selective all-dielectric Huygens’ metasurfaces,” *Journal of Physics D: Applied Physics* **50**, 434002 (2017).
- [100] M. Erdmanis and I. Tittonen, “Focused ion beam high resolution grayscale lithography for silicon-based nanostructures,” *Applied Physics Letters* **104**, 073118 (2014).
- [101] G. J. Lee, Y. P. Lee, K. R. Kim, M. I. Jang, C. S. Yoon, J. Ahn, Y. D. Son, and J. Jang, “Fabrication of two-dimensional periodic structures in an amorphous silicon film by four-beam interference lithography,” *Journal of the Korean Physical Society* **49** (2006).
- [102] J. De Boor, N. Geyer, J. V. Wittemann, U. Gösele, and V. Schmidt, “Sub-100 nm silicon nanowires by laser interference lithography and metal-assisted etching,” *Nanotechnology* **21**, 095302 (2010).
- [103] A. Vetter, R. Kirner, D. Opalevs, M. Scholz, P. Leisching, T. Scharf, W. Noell, C. Rockstuhl, and R. Voelkel, “Printing sub-micron structures using Talbot mask-aligner lithography with a 193 nm CW laser light source,” *Optics Express* **26**, 22218–22233 (2018).
- [104] Y. Lu and S. Chen, “Nanopatterning of a silicon surface by near-field enhanced laser irradiation,” *Nanotechnology* **14**, 505 (2003).
- [105] S. Y. Chou, C. Keimel, and J. Gu, “Ultrafast and direct imprint of nanostructures in silicon,” *Nature* **417**, 835–837 (2002).
- [106] L. Shi, J. T. Harris, R. Fenollosa, I. Rodriguez, X. Lu, B. A. Korgel, and F. Meseguer, “Monodisperse silicon nanocavities and photonic crystals with magnetic response in the optical region,” *Nature Communications* **4**, 1–7 (2013).
- [107] A. Simakin, V. Voronov, N. Kirichenko, and G. Shafeev, “Nanoparticles produced by laser ablation of solids in liquid environment,” *Applied Physics A* **79**, 1127–1132 (2004).
- [108] W. Chaâbani, J. Proust, A. Movsesyan, J. Béal, A.-L. Baudrion, P.-M. Adam, A. Chehaidar, and J. Plain, “Large-scale and low-cost fabrication of silicon Mie resonators,” *ACS Nano* **13**, 4199–4208 (2019).
- [109] M. Abbarchi, M. Naffouti, B. Vial, A. Benkouider, L. Lermusiaux, L. Favre, A. Ronda, S. Bidault, I. Berbezier, and N. Bonod, “Wafer scale formation of monocrystalline silicon-based Mie resonators via silicon-on-insulator dewetting,” *ACS Nano* **8**, 11181–11190 (2014).
- [110] C. V. Thompson, “Solid-state dewetting of thin films,” *Annual Review of Materials Research* **42**, 399–434 (2012).

- [111] A. S. Roberts, S. M. Novikov, Y. Yang, Y. Chen, S. Boroviks, J. Beermann, N. A. Mortensen, and S. I. Bozhevolnyi, “Laser writing of bright colors on near-percolation plasmonic reflector arrays,” *ACS Nano* **13**, 71–77 (2018).
- [112] U. Zywiets, A. B. Evlyukhin, C. Reinhardt, and B. N. Chichkov, “Laser printing of silicon nanoparticles with resonant optical electric and magnetic responses,” *Nature Communications* **5**, 1–7 (2014).
- [113] S. Makarov, L. Kolotova, S. Starikov, U. Zywiets, and B. Chichkov, “Resonant silicon nanoparticles with controllable crystalline states and nonlinear optical responses,” *Nanoscale* **10**, 11403–11409 (2018).
- [114] Q. Li, D. Grojo, A.-P. Alloncle, B. Chichkov, and P. Delaporte, “Digital laser micro- and nanoprinting,” *Nanophotonics* **8**, 27–44 (2018).
- [115] P. Dmitriev, S. Makarov, V. Milichko, I. Mukhin, A. Gudovskikh, A. Sitnikova, A. Samusev, A. Krasnok, and P. Belov, “Laser fabrication of crystalline silicon nanoresonators from an amorphous film for low-loss all-dielectric nanophotonics,” *Nanoscale* **8**, 5043–5048 (2016).
- [116] S. Syubaev, E. Mitsai, A. Porfirev, S. Khonina, S. Kudryashov, T. Katkus, S. Juodkazis, E. Gurevich, and A. Kuchmizhak, “Silicon microprotrusions with tailored chirality enabled by direct femtosecond laser ablation,” *Optics Letters* **45**, 3050–3053 (2020).
- [117] S. V. Makarov, A. S. Zalogina, M. Tajik, D. A. Zuev, M. V. Rybin, A. A. Kuchmizhak, S. Juodkazis, and Y. Kivshar, “Light-induced tuning and reconfiguration of nanophotonic structures,” *Laser & Photonics Reviews* **11**, 1700108 (2017).
- [118] M. Naffouti, T. David, A. Benkouider, L. Favre, A. Delobbe, A. Ronda, I. Berbezier, and M. Abbarchi, “Templated solid-state dewetting of thin silicon films,” *Small* **12**, 6115–6123 (2016).
- [119] J. Ye, D. Zuev, and S. Makarov, “Dewetting mechanisms and their exploitation for the large-scale fabrication of advanced nanophotonic systems,” *International Materials Reviews* **64**, 439–477 (2019).
- [120] M. Rahmani, L. Xu, A. E. Miroschnichenko, A. Komar, R. Camacho-Morales, H. Chen, Y. Zárate, S. Kruk, G. Zhang, D. N. Neshev *et al.*, “Reversible thermal tuning of all-dielectric metasurfaces,” *Advanced Functional Materials* **27**, 1700580 (2017).
- [121] T. Lewi, N. A. Butakov, and J. A. Schuller, “Thermal tuning capabilities of semiconductor metasurface resonators,” *Nanophotonics* **8**, 331–338 (2019).
- [122] L. Wang, M. Eliceiri, Y. Deng, Y. Rho, W. Shou, H. Pan, J. Yao, and C. P. Grigoropoulos, “Fast reversible phase change silicon for visible active photonics,” *Advanced Functional Materials* p. 1910784 (2020).
- [123] G. P. Zograf, Y. F. Yu, K. V. Baryshnikova, A. I. Kuznetsov, and S. V. Makarov, “Local crystallization of a resonant amorphous silicon nanoparticle for the implementation of optical nanothermometry,” *JETP Letters* **107**, 699–704 (2018).

- [124] X. Chen, Y. Chen, M. Yan, and M. Qiu, "Nanosecond photothermal effects in plasmonic nanostructures," *ACS Nano* **6**, 2550–2557 (2012).
- [125] G. González-Rubio, A. Guerrero-Martínez, and L. M. Liz-Marzán, "Reshaping, fragmentation, and assembly of gold nanoparticles assisted by pulse lasers," *Accounts of Chemical Research* **49**, 678–686 (2016).
- [126] A. Kuhlicke, S. Schietinger, C. Matyssek, K. Busch, and O. Benson, "In situ observation of plasmon tuning in a single gold nanoparticle during controlled melting," *Nano Letters* **13**, 2041–2046 (2013).
- [127] P. Zijlstra, J. W. Chon, and M. Gu, "White light scattering spectroscopy and electron microscopy of laser induced melting in single gold nanorods," *Physical Chemistry Chemical Physics* **11**, 5915–5921 (2009).
- [128] C. Zhang, T. Tumkur, J. Yang, M. Lou, L. Dong, L. Zhou, P. Nordlander, and N. J. Halas, "Optical-force-dominated directional reshaping of Au nanodisks in Al–Au heterodimers," *Nano Letters* **18**, 6509–6514 (2018).
- [129] M. S. Carstensen, X. Zhu, O. E. Iyore, N. A. Mortensen, U. Levy, and A. Kristensen, "Holographic resonant laser printing of metasurfaces using plasmonic template," *ACS Photonics* **5**, 1665–1670 (2018).
- [130] Y. Zhang, L. Shi, D. Hu, S. Chen, S. Xie, Y. Lu, Y. Cao, Z. Zhu, L. Jin, B.-O. Guan *et al.*, "Full-visible multifunctional aluminium metasurfaces by in situ anisotropic thermoplasmonic laser printing," *Nanoscale Horizons* **4**, 601–609 (2019).
- [131] M. Aouassa, E. Mitsai, S. Syubaev, D. Pavlov, A. Zhizhchenko, I. Jadli, L. Hassayoun, G. Zograf, S. Makarov, and A. Kuchmizhak, "Temperature-feedback direct laser reshaping of silicon nanostructures," *Applied Physics Letters* **111**, 243103 (2017).
- [132] C. M. Aguirre, C. E. Moran, J. F. Young, and N. J. Halas, "Laser-induced reshaping of metalodielectric nanoshells under femtosecond and nanosecond plasmon resonant illumination," *The Journal of Physical Chemistry B* **108**, 7040–7045 (2004).
- [133] D. A. Zuev, S. V. Makarov, I. S. Mukhin, V. A. Milichko, S. V. Starikov, I. A. Morozov, I. I. Shishkin, A. E. Krasnok, and P. A. Belov, "Fabrication of hybrid nanostructures via nanoscale laser-induced reshaping for advanced light manipulation," *Advanced Materials* **28**, 3087–3093 (2016).
- [134] S. Lepeshov, A. Krasnok, I. Mukhin, D. Zuev, A. Gudovskikh, V. Milichko, P. Belov, and A. Miroshnichenko, "Fine-tuning of the magnetic fano resonance in hybrid oligomers via fs-laser-induced reshaping," *ACS Photonics* **4**, 536–543 (2017).
- [135] E. Matthias, M. Reichling, J. Siegel, O. Käding, S. Petzoldt, H. Skurk, P. Bizenberger, and E. Neske, "The influence of thermal diffusion on laser ablation of metal films," *Applied Physics A* **58**, 129–136 (1994).

- [136] M. D'alessandria, A. Lasagni, and F. Mücklich, "Direct micro-patterning of aluminum substrates via laser interference metallurgy," *Applied Surface Science* **255**, 3210–3216 (2008).
- [137] B. Voisiat, M. Gedvilas, S. Indrišiūnas, and G. Račiukaitis, "Flexible microstructuring of thin films using multi-beam interference: Ablation with ultrashort lasers," *Journal of Laser Micro/Nanoengineering* **6** (2011).
- [138] Y. Nakata, K. Murakawa, N. Miyanaga, and K. Momoo, "Interfering ultraviolet femtosecond laser processing of gold thin film and prospect of shortest period," *Applied Physics Express* **5**, 102703 (2012).
- [139] Y. Nakata, Y. Matsuba, N. Miyanaga, and K. Murakawa, "Fabrication of metallic hole array meta-materials with 760 nm and 1930 nm lattice constant by interfering femtosecond laser processing," *Photonics and Nanostructures-Fundamentals and Applications* **17**, 10–14 (2015).
- [140] S. Indrišius, B. Voisiat, A. Žukauskas, and G. Račiukaitis, "Direct laser beam interference patterning technique for fast high aspect ratio surface structuring," *Proc. SPIE* **9350**, 935003 (2015).
- [141] M. Bieda, M. Siebold, and A. F. Lasagni, "Fabrication of sub-micron surface structures on copper, stainless steel and titanium using picosecond laser interference patterning," *Applied Surface Science* **387**, 175–182 (2016).
- [142] Y. Nakata, K. Murakawa, N. Miyanaga, A. Narazaki, T. Shoji, and Y. Tsuboi, "Local melting of gold thin films by femtosecond laser-interference processing to generate nanoparticles on a source target," *Nanomaterials* **8**, 477 (2018).
- [143] B. Voisiat, W. Wang, M. Holzhey, and A. F. Lasagni, "Improving the homogeneity of diffraction based colours by fabricating periodic patterns with gradient spatial period using direct laser interference patterning," *Scientific Reports* **9**, 1–9 (2019).
- [144] S. Indrišiūnas, B. Voisiat, M. Gedvilas, and G. Račiukaitis, "Two complementary ways of thin-metal-film patterning using laser beam interference and direct ablation," *Journal of Micromechanics and Microengineering* **23**, 095034 (2013).
- [145] A. I. Aguilar-Morales, S. Alamri, and A. F. Lasagni, "Micro-fabrication of high aspect ratio periodic structures on stainless steel by picosecond direct laser interference patterning," *Journal of Materials Processing Technology* **252**, 313–321 (2018).
- [146] T. Zhai, X. Zhang, Z. Pang, and F. Dou, "Direct writing of polymer lasers using interference ablation," *Advanced Materials* **23**, 1860–1864 (2011).
- [147] T. Zhai, Y. Wang, L. Chen, and X. Zhang, "Direct writing of tunable multi-wavelength polymer lasers on a flexible substrate," *Nanoscale* **7**, 12312–12317 (2015).
- [148] E. Stankevičius, E. Daugnoraitė, and G. Račiukaitis, "Mechanism of pillars formation using four-beam interference lithography," *Optics and Lasers in Engineering* **116**, 41–46 (2019).

- [149] M. Lorens, Y. Zabala, M. Krupiński, M. Perzanowski, K. Suchanek, K. Marszałek, and M. Marszałek, "Micropatterning of silicon surface by direct laser interference lithography," *Acta Physica Polonica A* **121**, 543–545 (2012).
- [150] A. Vinciunas, S. Indrišūnas, B. Voisiat, G. Raciukaitis, I. Simkiene, R. Suzanoviciene, A. Reza, and R. Mazeikiene, "Effect of laser patterning on properties of crystalline si photovoltaic cells and substrates," *Journal of Laser Micro Nanoengineering* **8**, 244 (2013).
- [151] D. Wang, Z. Wang, Z. Zhang, Y. Yue, D. Li, and C. Maple, "Direct modification of silicon surface by nanosecond laser interference lithography," *Applied Surface Science* **282**, 67–72 (2013).
- [152] V. Oliveira, R. Vilar, R. Serra, J. Oliveira, N. Polushkin, and O. Conde, "Sub-micron structuring of silicon using femtosecond laser interferometry," *Optics & Laser Technology* **54**, 428–431 (2013).
- [153] Y. Hu, Z. Wang, Z. Weng, M. Yu, and D. Wang, "Bio-inspired hierarchical patterning of silicon by laser interference lithography," *Applied Optics* **55**, 3226–3232 (2016).
- [154] S. Indrišūnas, B. Voisiat, M. Gedvilas, and G. Račiukaitis, "New opportunities for custom-shape patterning using polarization control in confocal laser beam interference setup," *Journal of Laser Applications* **29** (2017).
- [155] S. Indrišūnas, B. Voisiat, A. Rēza, I. Šimkienė, R. Mažeikienė, A. Selskis, and G. Račiukaitis, "Influence of surface modification by laser beam interference ablation on characteristics of p-Si solar cells," *Proc. SPIE* **9180**, 918007 (2014).
- [156] M. Gedvilas, S. Indrišūnas, B. Voisiat, E. Stankevičius, A. Selskis, and G. Račiukaitis, "Nanoscale thermal diffusion during the laser interference ablation using femto-, pico-, and nanosecond pulses in silicon," *Physical Chemistry Chemical Physics* **20**, 12166–12174 (2018).
- [157] E.-K. Lee, J.-H. Song, K.-Y. Jeong, J.-H. Kang, H.-G. Park, and M.-K. Seo, "Resonant light scattering from a single dielectric nano-antenna formed by electron beam-induced deposition," *Scientific Reports* **5**, 10400 (2015).
- [158] C. F. Bohren and D. R. Huffman, *Absorption and scattering of light by small particles* (John Wiley & Sons, 2008).
- [159] C. Mätzler, "MATLAB functions for Mie scattering and absorption," *IAP Res. Rep* **8**, 9 (2002).
- [160] D. Tzarouchis and A. Sihvola, "Light scattering by a dielectric sphere: Perspectives on the Mie resonances," *Applied Sciences* **8**, 184 (2018).
- [161] P. H. Moon and D. E. Spencer, *Foundations of electrodynamics* (Courier Corporation, 2013).
- [162] S. Yushanov, J. S. Crompton, and K. C. Koppenhoefer, "Mie scattering of electromagnetic waves," in "Proceedings of the COMSOL Conference," (2013).

- [163] E. A. Gurvitz, K. S. Ladutenko, P. A. Dergachev, A. B. Evlyukhin, A. E. Miroschnichenko, and A. S. Shalin, “The high-order toroidal moments and anapole states in all-dielectric photonics,” *Laser & Photonics Reviews* **13**, 1800266 (2019).
- [164] A. Nagarajan, K. van Erve, and G. Gerini, “Ultra-narrowband polarization insensitive transmission filter using a coupled dielectric-metal metasurface,” *Optics Express* **28**, 773–787 (2020).
- [165] V. E. Babicheva and A. B. Evlyukhin, “Metasurfaces with electric quadrupole and magnetic dipole resonant coupling,” *ACS Photonics* **5**, 2022–2033 (2018).
- [166] V. A. Zenin, C. E. Garcia-Ortiz, A. B. Evlyukhin, Y. Yang, R. Malureanu, S. M. Novikov, V. Coello, B. N. Chichkov, S. I. Bozhevolnyi, A. V. Lavrinenko *et al.*, “Engineering nanoparticles with pure high-order multipole scattering,” *ACS Photonics* **7**, 1067–1075 (2020).
- [167] B. E. Bayer, “Color imaging array,” (1976). US Patent 3,971,065.
- [168] T. Smith and J. Guild, “The CIE colorimetric standards and their use,” *Transactions of the optical society* **33**, 73 (1931).
- [169] N. Ohta and A. Robertson, *Colorimetry: Fundamentals and applications* (John Wiley & Sons, 2006).
- [170] J. Schanda, *Colorimetry: Understanding the CIE system* (John Wiley & Sons, 2007).
- [171] W. Burger, “Color space considerations for linear image filtering,” in “Proc. 34th Workshop of the Austrian Ass. for Pattern Recognition, Zwettl, Austria,” (2010), pp. 163–170.
- [172] B. Lindbloom, “How the color difference calculator works,” (2020). (www.brucelindbloom.com; accessed: 2020.03.10).
- [173] F. Hirigoyen, A. Crocherie, J. M. Vaillant, and Y. Cazaux, “FDTD-based optical simulations methodology for CMOS image sensor pixels architecture and process optimization,” *Proc. SPIE* **6816**, 681609 (2008).
- [174] A. Rahimzadegan, D. Arslan, R. Suryadharma, S. Fasold, M. Falkner, T. Pertsch, I. Staude, and C. Rockstuhl, “Disorder-induced phase transitions in the transmission of dielectric metasurfaces,” *Physical Review Letters* **122**, 015702 (2019).
- [175] W. Zhao, X. Leng, and Y. Jiang, “Fano resonance in all-dielectric binary nanodisk array realizing optical filter with efficient linewidth tuning,” *Optics Express* **23**, 6858–6866 (2015).
- [176] C. Menzel, J. Sperrhake, and T. Pertsch, “Efficient treatment of stacked metasurfaces for optimizing and enhancing the range of accessible optical functionalities,” *Physical Review A* **93**, 063832 (2016).
- [177] R. Melnikov, K. V. Baryshnikova, M. Petrov, V. Ulyantsev, A. B. Evlyukhin, and B. N. Chichkov, “Evolutionary and genetic algorithms for design of metadevices working on electric dipole resonance,” *Journal of Physics: Conference Series* **1461**, 012011 (2020).

- [178] C. Vieu, F. Carcenac, A. Pepin, Y. Chen, M. Mejias, A. Lebib, L. Manin-Ferlazzo, L. Couraud, and H. Launois, "Electron beam lithography: Resolution limits and applications," *Applied surface science* **164**, 111–117 (2000).
- [179] T. Kudo, Y. Nanjo, Y. Nozaki, K. Nagao, H. Yamaguchi, W.-B. Kang, and G. Pawlowski, "Pigmented photoresists for color filters," *Journal of Photopolymer Science and Technology* **9**, 109–119 (1996).
- [180] Y. Malinovich and E. Koltin, "Backside illuminated image sensor," (2001). US Patent 6,169,319.
- [181] M. Steglich, D. Lehr, S. Ratzsch, T. Käsebier, F. Schrepel, E.-B. Kley, and A. Tünnermann, "An ultra-black silicon absorber," *Laser & Photonics Reviews* **8**, L13–L17 (2014).
- [182] A. Nagarajan, K. Vivek, M. Shah, V. G. Achanta, and G. Gerini, "A broadband plasmonic meta-surface superabsorber at optical frequencies: Analytical design framework and demonstration," *Advanced Optical Materials* **6**, 1800253 (2018).
- [183] R. W. Wood, "On a remarkable case of uneven distribution of light in a diffraction grating spectrum," *Proceedings of the Physical Society of London* **18**, 269 (1902).
- [184] A. Hessel and A. Oliner, "A new theory of Wood's anomalies on optical gratings," *Applied Optics* **4**, 1275–1297 (1965).
- [185] E. Abbe, "A contribution to the theory of the microscope and the nature of microscopic vision," *Proc. Bristol Nat. Soc* **1**, 200–261 (1874).
- [186] IMEC, "Hyperspectral imaging," (2020). (www.imec-int.com/en/hyperspectral-imaging; accessed: 2020.03.10).
- [187] A. Perot and C. Fabry, "On the application of interference phenomena to the solution of various problems of spectroscopy and metrology," *The Astrophysical Journal* **9**, 87 (1899).
- [188] R. Sauleau, "Fabry-Perot resonators," *Encyclopedia of RF and microwave engineering* (2005).
- [189] N. Hodgson and H. Weber, *Optical resonators: Fundamentals, advanced concepts, applications* (Springer Science & Business Media, 2005).
- [190] H. A. Macleod, *Thin-film optical filters* (CRC press, 2017).
- [191] P. Atherton, N. K. Reay, J. Ring, and T. Hicks, "Tunable Fabry-Perot filters," *Optical Engineering* **20**, 206806 (1981).
- [192] T. C. Choy, *Effective medium theory: Principles and applications* (Oxford University Press, 2015).
- [193] G. A. Niklasson, C. Granqvist, and O. Hunderi, "Effective medium models for the optical properties of inhomogeneous materials," *Applied Optics* **20**, 26–30 (1981).

- [194] J. M. Garnett, "XII. Colours in metal glasses and in metallic films," *Philosophical Transactions of the Royal Society of London. Series A, Containing Papers of a Mathematical or Physical Character* **203**, 385–420 (1904).
- [195] V. D. Bruggeman, "Berechnung verschiedener physikalischer Konstanten von heterogenen Substanzen. I. Dielektrizitätskonstanten und Leitfähigkeiten der Mischkörper aus isotropen Substanzen," *Annalen der Physik* **416**, 636–664 (1935).
- [196] H. Looyenga, "Dielectric constants of heterogeneous mixtures," *Physica* **31**, 401–406 (1965).
- [197] J. Monecke, "Bergman spectral representation of a simple expression for the dielectric response of a symmetric two-component composite," *Journal of Physics: Condensed Matter* **6**, 907 (1994).
- [198] R. Stognienko, T. Henning, and V. Ossenkopf, "Optical properties of coagulated particles," *Astronomy and Astrophysics* **296**, 797 (1995).
- [199] T. Henning and R. Stognienko, "Dust opacities for protoplanetary accretion disks: Influence of dust aggregates," *Astronomy and Astrophysics* **311**, 291–303 (1996).
- [200] J. R. Reitz, *Foundations of electromagnetic theory* (Pearson Education India, 2009).
- [201] R. Clausius, *Die mechanische Behandlung der Electricität* (Springer-Verlag, 2013).
- [202] W. Lamb, D. Wood, and N. Ashcroft, "Long-wavelength electromagnetic propagation in heterogeneous media," *Physical Review B* **21**, 2248 (1980).
- [203] L. Nicolai, "Über Sichtbarmachung, Verlauf und chemische Kinetik der Oxyhämoglobinreduktion im lebenden Gewebe, besonders in der menschlichen Haut," *Pflüger's Archiv für die gesamte Physiologie des Menschen und der Tiere* **229**, 372–384 (1932).
- [204] K. Matthes, "Untersuchungen über die Sauerstoffsättigung des menschlichen Arterienblutes," *Naunyn-Schmiedebergs Archiv für experimentelle Pathologie und Pharmakologie* **179**, 698–711 (1935).
- [205] G. A. Millikan, "The oximeter, an instrument for measuring continuously the oxygen saturation of arterial blood in man," *Review of Scientific Instruments* **13**, 434–444 (1942).
- [206] J. W. Severinghaus and P. B. Astrup, "History of blood gas analysis. VI. Oximetry," *Journal of Clinical Monitoring* **2**, 270–288 (1986).
- [207] J. W. Severinghaus and Y. Honda, "History of blood gas analysis. VII. Pulse oximetry," *Journal of Clinical Monitoring* **3**, 135–138 (1987).
- [208] Fitbit, Inc., "How do I track my estimated oxygen variation in the Fitbit app?" (2020). (www.fitbit.com; accessed: 2020.04.10).

- [209] L. Kong, Y. Zhao, L. Dong, Y. Jian, X. Jin, B. Li, Y. Feng, M. Liu, X. Liu, and H. Wu, “Non-contact detection of oxygen saturation based on visible light imaging device using ambient light,” *Optics Express* **21**, 17464–17471 (2013).
- [210] S. Heist, J. Sperrhake, and A. Thoss, “Fast 3D imaging for industrial and healthcare applications,” *Laser Focus World* **55**, 27–30 (2019).
- [211] S. Takatani and J. Ling, “Optical oximetry sensors for whole blood and tissue,” *IEEE Engineering in Medicine and Biology Magazine* **13**, 347–357 (1994).
- [212] S. Prahl, “Optical absorption of hemoglobin,” (1999). (www.omlc.ogi.edu/spectra/hemoglobin; accessed: 2020.03.24).
- [213] M. L. Polanyi and R. Hehir, “New reflection oximeter,” *Review of Scientific Instruments* **31**, 401–403 (1960).
- [214] J. Moyle, *Pulse Oximetry* (Wiley, 2002).
- [215] P. J. Dwyer, R. R. Anderson, and C. A. DiMarzio, “Mapping blood oxygen saturation using a multi-spectral imaging system,” *Proc. SPIE* **2976**, 270–280 (1997).
- [216] T. W. Sawyer, C. Williams, and S. E. Bohndiek, “Spectral band selection and tolerancing for multi-spectral filter arrays,” in “Frontiers in Optics,” (Optical Society of America, 2019), pp. JW4A–126.
- [217] F. Gao, Q. Peng, X. Feng, B. Gao, and Y. Zheng, “Single-wavelength blood oxygen saturation sensing with combined optical absorption and scattering,” *IEEE Sensors Journal* **16**, 1943–1948 (2015).
- [218] A. von Chong, M. Terosiet, A. Histace, and O. Romain, “Towards a novel single-LED pulse oximeter based on a multispectral sensor for IoT applications,” *Microelectronics Journal* **88**, 128–136 (2019).
- [219] L. Frey, P. Parrein, L. Virot, C. Pellé, and J. Raby, “Thin film characterization for modeling and optimization of silver-dielectric color filters,” *Applied Optics* **53**, 1663–1673 (2014).
- [220] L. Frey, L. Masarotto, L. El Melhaoui, S. Verrun, S. Minoret, G. Rodriguez, A. André, F. Ritton, and P. Parrein, “High-performance silver-dielectric interference filters for RGBIR imaging,” *Optics Letters* **43**, 1355–1358 (2018).
- [221] L. Tu, L. Huang, and W. Wang, “A novel micromachined Fabry-Perot interferometer integrating nano-holes and dielectrophoresis for enhanced biochemical sensing,” *Biosensors and Bioelectronics* **127**, 19–24 (2019).
- [222] O. Stenzel *et al.*, *The physics of thin film optical spectra* (Springer, 2015).
- [223] S. Boutami, Y. Desieres, L. Frey, and G. Grand, “Optical filter suitable for dealing with a radiation of variable incidence and detector including said filter,” (2015). US Patent 8,933,389.

- [224] L. Frey, L. Masarotto, M. Armand, M.-L. Charles, and O. Lartigue, “Multispectral interference filter arrays with compensation of angular dependence or extended spectral range,” *Optics Express* **23**, 11799–11812 (2015).
- [225] J. Correia, M. Bartek, and R. Wolffenbuttel, “High-selectivity single-chip spectrometer for operation at visible wavelengths,” in “International Electron Devices Meeting 1998,” (IEEE, 1998), pp. 467–470.
- [226] L. Frey and B. Mourey, “Optical filtering device including Fabry-Perot cavities comprising first and second structured layers,” (2020). US Patent 10,571,612.
- [227] T. Yamaguchi, S. Kasuga, T. Murata, and K. Orita, “Solid-state imaging device, manufacturing method for solid-state imaging device, and camera using the same,” (2007). US Patent App. 10/566,671.
- [228] Raspberry Pi Foundation, “Camera module,” (2020). (www.raspberrypi.org; accessed: 2020.03.10).
- [229] R. M. A. Azzam, “Stokes-vector and Mueller-matrix polarimetry,” *Journal of the Optical Society of America A* **33**, 1396 (2016).
- [230] A. van Amerongen, J. Rietjens, M. Smit, D. van Loon, H. van Brug, W. van der Meulen, M. Esposito, and O. Hasekamp, “SPEX the Dutch roadmap towards aerosol measurement from space,” *Proc. SPIE* **10562**, 105621O (2017).
- [231] H. Knopf, N. Lundt, T. Bucher, S. Höfling, S. Tongay, T. Taniguchi, K. Watanabe, I. Staude, U. Schulz, C. Schneider *et al.*, “Integration of atomically thin layers of transition metal dichalcogenides into high-Q, monolithic Bragg-cavities: An experimental platform for the enhancement of the optical interaction in 2D-materials,” *Optical Materials Express* **9**, 598–610 (2019).
- [232] T. Siefke, S. Kroker, K. Pfeiffer, O. Puffky, K. Dietrich, D. Franta, I. Ohlídal, A. Szeghalmi, E.-B. Kley, and A. Tünnermann, “Materials pushing the application limits of wire grid polarizers further into the deep ultraviolet spectral range,” *Advanced Optical Materials* **4**, 1780–1786 (2016).
- [233] J. M. Bennett, E. Pelletier, G. Albrand, J.-P. Borgogno, B. Lazarides, C. K. Carniglia, R. Schmall, T. H. Allen, T. Tuttle-Hart, K. H. Guenther *et al.*, “Comparison of the properties of titanium dioxide films prepared by various techniques,” *Applied Optics* **28**, 3303–3317 (1989).
- [234] P. Johnson and R. Christy, “Optical constants of transition metals: Ti, V, Cr, Mn, Fe, Co, Ni, and Pd,” *Physical Review B* **9**, 5056 (1974).
- [235] K. Meyer, H.-J. Tiller, E. Welz, and W. Kühn, “Modifizierung von SiO₂-Oberflächen mit Hilfe von Plasmen Teil I-EPR-Spektroskopische Untersuchung der Defektzentren und der Einfluß des Plasma-trärgases auf deren Bildung,” *Zeitschrift für Chemie* **14**, 146–150 (1974).
- [236] L. Novotny and B. Hecht, *Principles of nano-optics* (Cambridge University Press, 2012).

- [237] T. Ceccotti, *Integration and modeling of a metasurface spectropolarimeter for space applications* (Delft University of Technology, 2020).
- [238] S. J. Orfanidis, *Electromagnetic waves and antennas* (Rutgers University - New Brunswick, 2016).
- [239] Y. K. Zhong, S. M. Fu, S. L. Yan, P. Y. Chen, and A. Lin, “Arbitrarily-Wide-Band Dielectric Mirrors and Their Applications to SiGe Solar Cells,” *IEEE Photonics Journal* **7**, 1–12 (2015).
- [240] M. Shaheen, J. Gagnon, and B. Fryer, “Laser ablation of iron: A comparison between femtosecond and picosecond laser pulses,” *Journal of Applied Physics* **114**, 083110 (2013).
- [241] D. Bäuerle, *Laser processing and chemistry* (Springer Science & Business Media, 2013).
- [242] H. Wada and T. Kamijoh, “Thermal conductivity of amorphous silicon,” *Japanese Journal of Applied Physics* **35**, L648 (1996).
- [243] H. Webber, A. Cullis, and N. Chew, “Computer simulation of high speed melting of amorphous silicon,” *Applied Physics Letters* **43**, 669–671 (1983).
- [244] C. Ong, H. Tan, and E. Sin, “Calculations of melting threshold energies of crystalline and amorphous materials due to pulsed-laser irradiation,” *Materials Science and Engineering* **79**, 79–85 (1986).
- [245] W. Sinke and F. Saris, “Evidence for a self-propagating melt in amorphous silicon upon pulsed-laser irradiation,” *Physical Review Letters* **53**, 2121 (1984).
- [246] J. Thorstensen and S. Erik Foss, “Temperature dependent ablation threshold in silicon using ultra-short laser pulses,” *Journal of Applied Physics* **112**, 103514 (2012).
- [247] J. Liu, “Simple technique for measurements of pulsed gaussian-beam spot sizes,” *Optics Letters* **7**, 196–198 (1982).
- [248] X. Zhu, M. K. Hedayati, S. Raza, U. Levy, N. A. Mortensen, and A. Kristensen, “Digital resonant laser printing: Bridging nanophotonic science and consumer products,” *Nano Today* **19**, 7–10 (2018).
- [249] E. Donovan, F. Spaepen, D. Turnbull, J. Poate, and D. Jacobson, “Heat of crystallization and melting point of amorphous silicon,” *Applied Physics Letters* **42**, 698–700 (1983).
- [250] Z. Iqbal, S. Vepřek, A. Webb, and P. Capezzuto, “Raman scattering from small particle size polycrystalline silicon,” *Solid State Communications* **37**, 993–996 (1981).
- [251] I. Theodorakos, I. Zergioti, V. Vamvakas, D. Tsoukalas, and Y. Raptis, “Picosecond and nanosecond laser annealing and simulation of amorphous silicon thin films for solar cell applications,” *Journal of Applied Physics* **115**, 043108 (2014).
- [252] C. Becker, D. Amkreutz, T. Sontheimer, V. Preidel, D. Lockau, J. Haschke, L. Jogschies, C. Klimm, J. J. Merkel, P. Plocica *et al.*, “Polycrystalline silicon thin-film solar cells: Status and perspectives,” *Solar Energy Materials and Solar Cells* **119**, 112–123 (2013).

- [253] J. Lian, L. Wang, X. Sun, Q. Yu, and R. C. Ewing, "Patterning metallic nanostructures by ion-beam-induced dewetting and rayleigh instability," *Nano Letters* **6**, 1047–1052 (2006).
- [254] J. D. Fowlkes, L. Kondic, J. Diez, Y. Wu, and P. D. Rack, "Self-assembly versus directed assembly of nanoparticles via pulsed laser induced dewetting of patterned metal films," *Nano Letters* **11**, 2478–2485 (2011).
- [255] J. Ye and C. V. Thompson, "Templated solid-state dewetting to controllably produce complex patterns," *Advanced Materials* **23**, 1567–1571 (2011).
- [256] E. Hecht, *Optics* (Pearson Education, San Francisco, 2002), 4th ed.
- [257] A. Maznev, T. Crimmins, and K. Nelson, "How to make femtosecond pulses overlap," *Optics Letters* **23**, 1378–1380 (1998).
- [258] B. N. Chichkov, C. Momma, S. Nolte, F. Von Alvensleben, and A. Tünnermann, "Femtosecond, picosecond and nanosecond laser ablation of solids," *Applied Physics A* **63**, 109–115 (1996).
- [259] S.-S. Wellershoff, J. Hohlfeld, J. Güdde, and E. Matthias, "The role of electron-phonon coupling in femtosecond laser damage of metals," *Applied Physics A* **69**, S99–S107 (1999).
- [260] T. Kondo, S. Matsuo, S. Juodkazis, V. Mizeikis, and H. Misawa, "Multiphoton fabrication of periodic structures by multibeam interference of femtosecond pulses," *Applied Physics Letters* **82**, 2758–2760 (2003).
- [261] A. Sabbah and D. M. Riffe, "Femtosecond pump-probe reflectivity study of silicon carrier dynamics," *Physical Review B* **66**, 165217 (2002).
- [262] F. Millot, V. Sarou-Kanian, J.-C. Rifflet, and B. Vinet, "The surface tension of liquid silicon at high temperature," *Materials Science and Engineering: A* **495**, 8–13 (2008).
- [263] T. Young, "III. An essay on the cohesion of fluids," *Philosophical transactions of the royal society of London* pp. 65–87 (1805).
- [264] F. B. Wyart and J. Daillant, "Drying of solids wetted by thin liquid films," *Canadian Journal of Physics* **68**, 1084–1088 (1990).
- [265] E. Jiran and C. Thompson, "Capillary instabilities in thin films," *Journal of Electronic Materials* **19**, 1153–1160 (1990).
- [266] M. El-Khoury, B. Voisiat, T. Kunze, and A. F. Lasagni, "Utilizing fundamental beam-mode shaping technique for top-hat laser intensities in direct laser interference patterning," *Journal of Laser Micro Nanoengineering* **13**, 268–272 (2018).
- [267] M. Domke, L. Nobile, S. Rapp, S. Eiselen, J. Sotrop, H. P. Huber, and M. Schmidt, "Understanding thin film laser ablation: The role of the effective penetration depth and the film thickness," *Physics Procedia* **56**, 1007–1014 (2014).

- [268] D. Pierce and W. E. Spicer, “Electronic structure of amorphous Si from photoemission and optical studies,” *Physical Review B* **5**, 3017 (1972).
- [269] S. Moss and J. Graczyk, “Evidence of voids within the as-deposited structure of glassy silicon,” *Physical Review Letters* **23**, 1167 (1969).
- [270] Light Conversion, “Ultrafast lasers & systems for science,” (2020). (www.lightcon.com; accessed: 2020.04.10).
- [271] Y. H. Ko and R. Magnusson, “Wideband dielectric metamaterial reflectors: Mie scattering or leaky Bloch mode resonance?” *Optica* **5**, 289–294 (2018).
- [272] N. A. Butakov and J. A. Schuller, “Designing multipolar resonances in dielectric metamaterials,” *Scientific Reports* **6**, 38487 (2016).
- [273] A. E. Miroshnichenko, A. B. Evlyukhin, Y. F. Yu, R. M. Bakker, A. Chipouline, A. I. Kuznetsov, B. Luk’yanchuk, B. N. Chichkov, and Y. S. Kivshar, “Nonradiating anapole modes in dielectric nanoparticles,” *Nature Communications* **6**, 1–8 (2015).
- [274] E. D. Palik, *Handbook of Optical Constants of Solids*, vol. 3 (Academic Press, 1998).
- [275] L. Frey, “Interference filter,” (2018). US Patent App. 15/920,349.
- [276] A. Fernandez and D. W. Phillion, “Effects of phase shifts on four-beam interference patterns,” *Applied Optics* **37**, 473–478 (1998).
- [277] Y. Nakata, K. Murakawa, K. Sonoda, K. Momoo, N. Miyanaga, and T. Hiromoto, “Designing of interference pattern in ultra-short pulse laser processing,” *Applied Physics A* **112**, 191–196 (2013).
- [278] K. Momoo, K. Sonoda, Y. Nakata, and N. Miyanaga, “Generation of new nanostructures in designed matrix by interfering femtosecond laser processing,” *Proc. SPIE* **8243**, 82431E (2012).
- [279] B. Voisiat, J. Ströbel, K. Du, and A. F. Lasagni, “How to improve throughput in direct laser interference patterning: Top-hat beam profile and burst mode,” *Proc. SPIE* **11268**, 112680Y (2020).
- [280] A. F. Lasagni, C. Gachot, K. E. Trinh, M. Hans, A. Rosenkranz, T. Roch, S. Eckhardt, T. Kunze, M. Bieda, D. Günther, V. Lang, and F. Mücklich, “Direct laser interference patterning, 20 years of development: From the basics to industrial applications,” *Proc. SPIE* **10092**, 1009211 (2017).
- [281] O. Žukovskaja, S. Agafilushkina, V. Sivakov, K. Weber, D. Cialla-May, L. Osminkina, and J. Popp, “Rapid detection of the bacterial biomarker pyocyanin in artificial sputum using a SERS-active silicon nanowire matrix covered by bimetallic noble metal nanoparticles,” *Talanta* **202**, 171–177 (2019).
- [282] C. Escobedo, “On-chip nanohole array based sensing: A review,” *Lab on a Chip* **13**, 2445–2463 (2013).

- [283] A.-P. Blanchard-Dionne and M. Meunier, "Sensing with periodic nanohole arrays," *Advances in Optics and Photonics* **9**, 891–940 (2017).
- [284] E. P. Ivanova, J. Hasan, H. K. Webb, G. Gervinskas, S. Juodkazis, V. K. Truong, A. H. Wu, R. N. Lamb, V. A. Baulin, G. S. Watson *et al.*, "Bactericidal activity of black silicon," *Nature Communications* **4**, 1–7 (2013).
- [285] G. Jellison Jr, "Optical functions of GaAs, GaP, and Ge determined by two-channel polarization modulation ellipsometry," *Optical Materials* **1**, 151–160 (1992).
- [286] D. E. Aspnes and A. Studna, "Dielectric functions and optical parameters of Si, Ge, GaP, GaAs, GaSb, InP, InAs, and InSb from 1.5 to 6.0 eV," *Physical Review B* **27**, 985 (1983).
- [287] D. Aspnes, S. Kelso, R. Logan, and R. Bhat, "Optical properties of $\text{Al}_x\text{Ga}_{1-x}\text{As}$," *Journal of Applied Physics* **60**, 754–767 (1986).
- [288] A. Ciesielski, L. Skowronski, M. Trzcinski, E. Górecka, P. Trautman, and T. Szoplik, "Evidence of germanium segregation in gold thin films," *Surface Science* **674**, 73–78 (2018).
- [289] A. D. Rakić, "Algorithm for the determination of intrinsic optical constants of metal films: Application to aluminum," *Applied Optics* **34**, 4755–4767 (1995).

Appendix A

Refractive index database

This appendix serves as a collection of materials used in this work. The refractive indices are an essential part of accurate numerical simulations. Some of the materials used in this work possess wavelength-dependent dispersion. The list of such materials includes Si, as well as other high-index and plasmonic materials. They are graphically represented in the following subsections.

Silicon

Si is the most frequently used high-index material. Often, c-Si is referred, but the direct growth of c-Si on top of a foreign substrate such as a glass is not possible. Hence, other types of Si are preferred: a-Si and a-Si:H. Their refractive indices are shown in Figure A.1. The properties of a-Si and a-Si:H were measured, while the refractive index of c-Si was taken from a database [274]. The real part of the refractive index n for all three varieties are similar. However, the imaginary part (extinction coefficient) k for c-Si is much lower in the visible spectral range than for the others. Regardless of that, most of the experimental demonstrations in this work were done using a-Si.

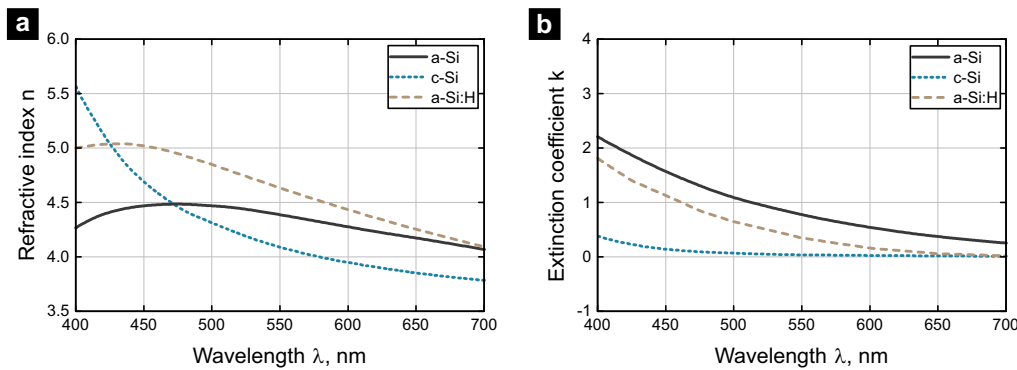


Figure A.1: Refractive index and extinction coefficient of different types of silicon: (a) refractive index n , (b) extinction coefficient k . The solid black line depicts the refractive index of a-Si, the blue dotted line – c-Si [274], and the dashed brown line – a-Si:H.

Other high-index materials

Besides Si, there are a number of other high-index materials worth considering in the field of nanophotonics; such a list includes but is not limited to TiO₂, GaP, InP, GaAs, and Ge. In particular, TiO₂ was implemented in Chapter 2. The refractive indices of TiO₂ (taken from [232]), GaP (taken from [285]), InP (taken from [286]), GaAs (taken from [287]), and Ge (taken from [286]), are shown in Figure A.3.

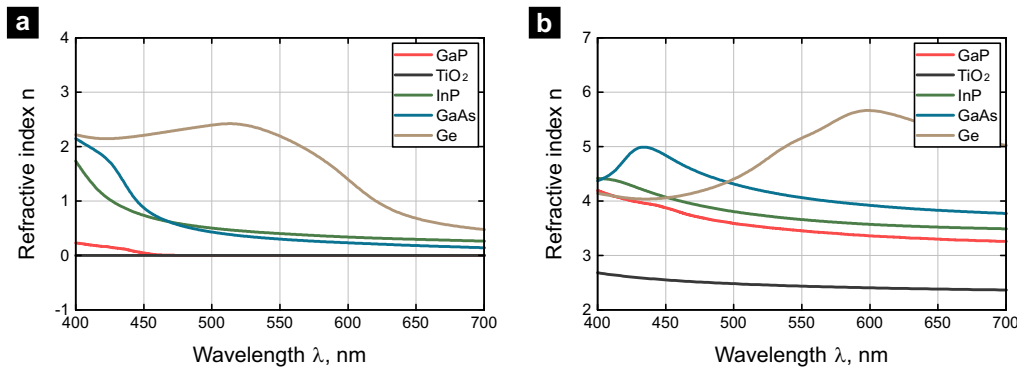


Figure A.2: Refractive index and extinction coefficient of various high-index materials: TiO₂ [232], GaP [285], InP [286], GaAs [287], and Ge [286]. (a) refractive index n , (b) extinction coefficient k .

Plasmonic materials

Despite the focus on dielectrics, this work involves several plasmonic materials. Au is used in the initial dielectric vs. plasmonic comparison; see Section 1.1.1. Then several metals such as Ag, Au, and Al are utilized as mirrors for the best performance of FP filters; see Section 2.2.3. Finally, Cu was used in the contamination analysis of FP filters; see Section 2.3.3. The refractive indices of Au (taken from [288]), Ag (measured), Al (taken from [289]), and Cu (taken from [234]), are given in Figure A.3.

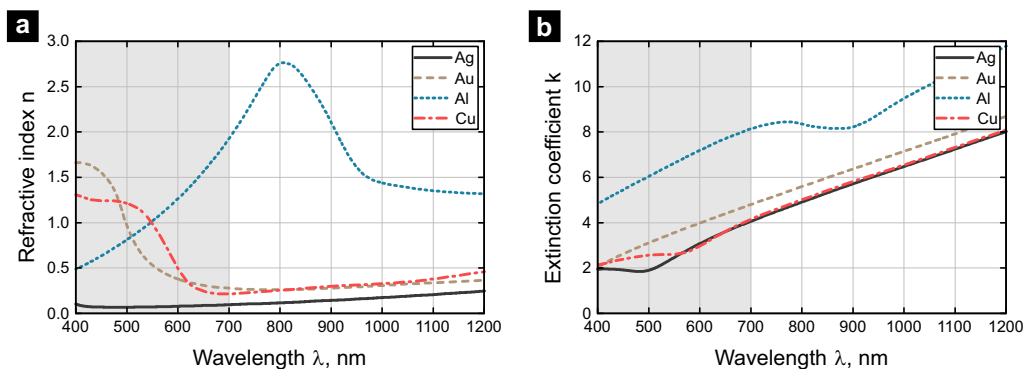


Figure A.3: Refractive index and extinction coefficient of Au [288], Ag (measured), Al [289], and Cu [234]: (a) refractive index n , (b) extinction coefficient k . Grey area highlights the visible spectral range.

Laser-tailored silicon

Chapter 3 highlights the change of the refractive index of Si due to thermal effects during the laser-induced tailoring of Si nanostructures and single-pulse laser interference patterning of Si films; Section 3.1 and Section 3.2, respectively.

The first part of Section 3.1 presents the laser tailoring of metasurfaces with their resonances in the visible spectral range. These metasurfaces were made from a commercial a-Si layer (Tafelmaier Dünnschicht-Technik GmbH); see Figure A.4(a,b) for the measured refractive index in comparison to c-Si data from literature [274]. Furthermore, the second part of Section 3.1 discusses the metasurface sample with its resonances in infrared. The sample was structured from an a-Si film. Its real part of the refractive index n was taken from the same commercial a-Si. The extinction coefficient k was fitted via comparison of the measured and simulated transmittance; see refractive index n and extinction coefficient k in Figure A.4(c,d).

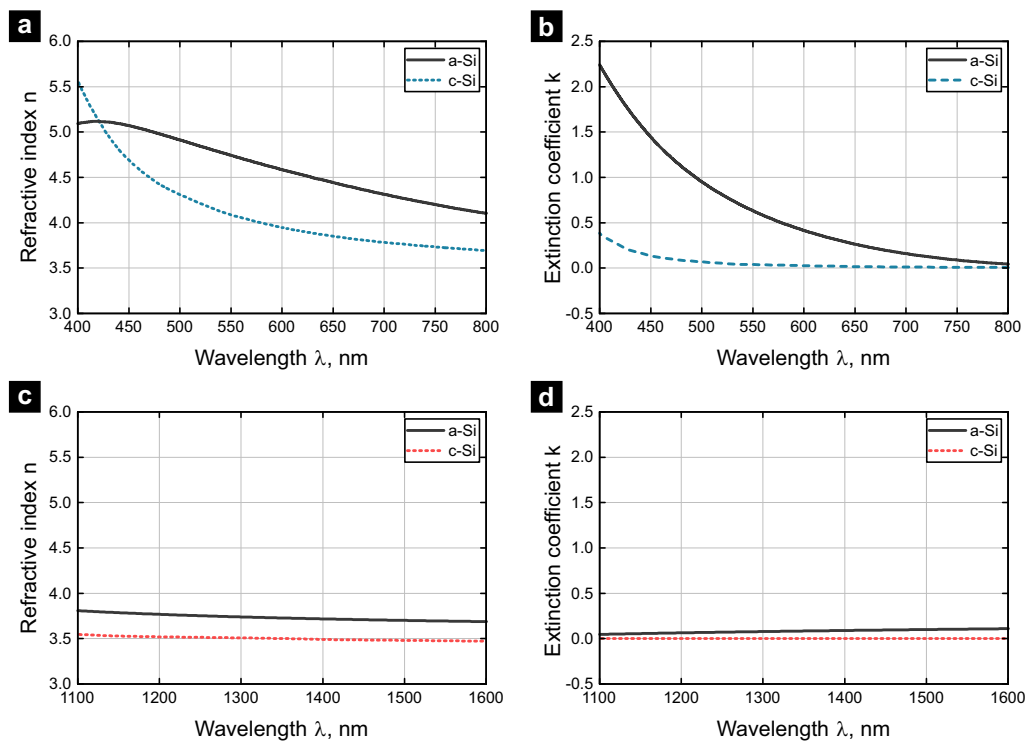


Figure A.4: Refractive index and extinction coefficient of Si samples before and after laser-induced tailoring. Sample in the visible spectral range: (a) refractive index n , (b) extinction coefficient k , where the blue dashed line depicts a-Si, and c-Si is shown in solid black line. Sample in the infrared spectral range: (c) refractive index n , (d) extinction coefficient k , where a-Si is shown in solid black line, and c-Si – red dotted line.

Laser-patterned silicon

The dispersion parameters of the initial Si films in Section 3.2 were obtained from goniometric measurements, see in Figure A.5. The dispersion parameters of the patterned Si were calculated, accounting for the refractive index dependence on the crystallization [S8, S10]. Similarly, this was done by fitting the numerically obtained spectra to the measured spectral data while varying the refractive index of Si between

the measured a-Si index before the patterning and the c-Si from a database [274] – after. The obtained real part n and extinction coefficient k of the refractive index of Si after the patterning is shown in Figure A.5(a) and Figure A.5(b), respectively.

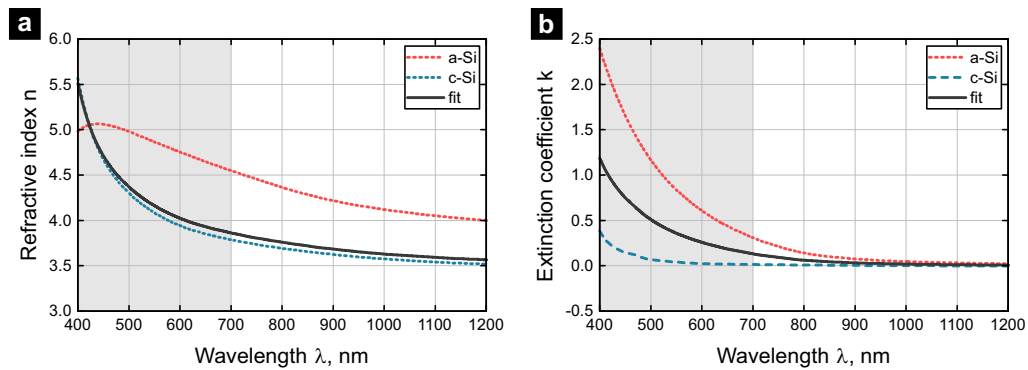


Figure A.5: Refractive index and extinction coefficient of Si film prior- and post-patterning. (a) refractive index n , (b) imaginary part (extinction coefficient) k . The blue line depicts the refractive index of the initial a-Si film, the black dashed line shows the c-Si refractive index, while the red dotted line shows the fitted refractive index of the patterned Si nanostructures.

Abbreviations

ALD – atomic layer deposition
BFAST – broadband fixed angle source technique
CMOS – complementary metal–oxide–semiconductor
CMY – cyan, magenta and yellow
CW – continuous wave
DOE – diffractive optical element
EBL – electron-beam lithography
ED – electric dipole
EQ – electric quadrupole
FDTD – finite-difference time-domain
FEM – finite element method
FIB – focused ion beam
FP – Fabry–Pérot
FWHM – full width at half maximum
HSV – hue, saturation, value
IR – infrared spectral range
MD – magnetic dipole
MQ – magnetic quadrupole
NA – numerical aperture
NIR – near-infrared
PBC – periodic boundary condition
PECVD – plasma-enhanced chemical vapor deposition
PIAD – plasma-ion-assisted deposition
PML – perfectly matched layer
RGB – red, green, blue
SEM – scanning electron microscope
SNIP – statistics-sensitive non-linear iterative peak-clipping
SNR – signal-to-noise ratio
SNOM – scanning near-field optical microscope
TE – transverse electric
TM – transverse magnetic
VIS – visible spectral range

Deutschsprachige Zusammenfassung

Zweidimensionale Anordnungen von Subwellenlängen-Nanostrukturen, Metaoberflächen, sind eine neue Generation der Optik. Materialien mit hohem Brechungsindex wie Silizium (Si) sind in der Nanophotonik eine Alternative zu plasmonischen Materialien geworden.

Insbesondere verlustarme Dielektrika mit hohem Brechungsindex ermöglichen neue Konzepte mit effizienten photonischen Komponenten Vorrichtungen für Bildgebung, Detektion und Fokussierung, Lichtemission, -steuerung, -führung und -schaltung und viele andere Anwendungen. Dielektrische Nanostrukturen, sogenannte Mie-Resonatoren, unterstützen elektrische und magnetische Resonanzen, die eine wellenlängenabhängige optische Response ermöglichen, die durch Variation der Form und Größe der Elemente auf eine bestimmte Funktionalität zugeschnitten ist. Die physikalischen Phänomene, die die Wechselwirkung zwischen Licht und Nanostruktur bestimmen, stehen im Mittelpunkt dieser Arbeit, um die Metaoberflächen den realen Anwendungen näher zu bringen.

Kapitel 1 analysiert Mie-Resonanzen und ihre Anwendbarkeit bei der Spektralfilterung. Dielektrische Nanostrukturen mit hohem Index, die elektrische und magnetische Resonanzen aufweisen, liefern eine wellenlängenabhängige spektrale Antwort, die die Realisierung von Farbfilterarrays ermöglichte. Die Nanostrukturen können zu flexiblen und Miniatur-Spektralfiltern zusammengesetzt werden. Als Ergebnis wurden RGB-Filter mit einer lateralen Größe von nur 0,5 μm realisiert.

Der Fabry-Perot-Resonator ist ein weiteres optisch resonantes System. Es wurde gezeigt, dass das Medium zwischen den zwei Reflektoren als effektives Medium moduliert werden kann, um multispektrale Filter zu erzeugen und das Konzept sogar auf polarisationempfindliche Strukturen auszudehnen. Die vorgeschlagene Architektur – Fabry-Perot-Resonator mit eingebettetem Material mit hohem Index - umfasst nur einen einzigen Lithographieschritt. Die in Kapitel 2 vorgestellte spektrale Auflösung von Systemen ist nur durch das Reflexionsvermögen der Spiegeln begrenzt, wodurch die Systeme äußerst kompakt, aber leistungsstark sind.

Die auf Nanostrukturen basierenden optischen Systeme eröffnen neue Horizonte in der Optik und könnten herkömmliche optische Komponenten ersetzen. Sie bleiben jedoch ihren herkömmlichen Gegenständen oft unterlegen: nicht aufgrund der Leistung, sondern aufgrund der Größe und der komplexen Herstellung. In Kapitel 3 werden zwei laserbasierte Fertigungstechniken vorgestellt, mit denen Metaoberflächen in auf großen Oberflächen hergestellt werden können. Damit wird der Weg frei gemacht, Metaoberflächen einzusetzen in Geräten, die in größeren Stückzahlen gefertigt werden.

Es wird nicht erwartet, dass diese Arbeit die Optik revolutioniert. Dennoch ist diese Arbeit in der Hoffnung geschrieben, einen kleinen Schritt in der Entwicklung der Nanophotonik und ihrer Anwendbarkeit in realen Anwendungen beizutragen.

Ehrenwörtliche Erklärung

Ich erkläre hiermit ehrenwörtlich, dass ich die vorliegende Arbeit selbständig, ohne unzulässige Hilfe Dritter und ohne Benutzung anderer als der angegebenen Hilfsmittel und Literatur angefertigt habe. Die aus anderen Quellen direkt oder indirekt übernommenen Daten und Konzepte sind unter Angabe der Quelle gekennzeichnet.

Bei der Auswahl und Auswertung folgenden Materials haben mir die nachstehend aufgeführten Personen in der jeweils beschriebenen Weise unentgeltlich geholfen:

Kapitel 1

- Stefan Fasold strukturierte die Nanostrukturen mithilfe der Elektronenstrahlolithographie
- Koen van Erve und Prof. Dr. Giampiero Gerini lieferten Modenzerlegungsspektren

Kapitel 2

- Jan Sperrhake arbeitete an der Idee von Filtern für die Blutmessung mit
- Stefan Fasold strukturierte die Nanostrukturen mithilfe der Elektronenstrahlolithographie
- Markus Walther, Carsten Stock und Dr. Thomas Siefke haben den Filter für die Blutmessung auf dem CMOS-Chip integriert
- L. Pjotr Stoevelaar, Dr. Fabrizio Silvestri, Prof. Dr. Giampiero Gerini und Dr. Stefan Bäumer haben zur Idee des Spektropolarimeters beigetragen
- L. Pjotr Stoevelaar führte die mathematische Analyse des Spektropolarimeters durch
- Heiko Knopf und Dr. Falk Eilenberger haben Bragg-Reflektoren hinterlegt

Kapitel 3

- Dr. Simonas Indrišiūnas und Dr. Paulius Gečys stellten die Laserausrüstung zur Verfügung und unterstützten die Experimente
- Dr. Olga Žukovskaja, Prof. Dr. Dana Cialla-May führten Raman-Spektroskopiemessungen durch
- Michael Steinert führte SEM- und AFM-Messungen durch
- Koen van Erve, Dr. Arvind Nagarajan und Prof. Dr. Giampiero Gerini lieferten Modendekompositionsspektren

Weitere Personen waren an der inhaltlich-materiellen Erstellung der vorliegenden Arbeit nicht beteiligt. Insbesondere habe ich hierfür nicht die entgeltliche Hilfe von Vermittlungs- bzw. Beratungsdiensten (Promotionsberater oder andere Personen) in Anspruch genommen. Niemand hat von mir unmittelbar oder mit-

telbar geldwerte Leistungen für Arbeiten erhalten, die im Zusammenhang mit dem Inhalt der vorgelegten Dissertation stehen.

Die Arbeit wurde bisher weder im In- noch im Ausland in gleicher oder ähnlicher Form einer anderen Prüfungsbehörde vorgelegt. Die geltende Promotionsordnung der Physikalisch-Astronomischen Fakultät ist mir bekannt. Ich versichere ehrenwörtlich, dass ich nach bestem Wissen die reine Wahrheit gesagt und nichts verschwiegen habe.

Jena, 05. Januar 2021

Jonas Berzinš